



## Development of Three-Dimensional Graphene Biocatalysts for Enzymatic Biofuel Cells

Tang, Jing

*Publication date:*  
2019

*Document Version*  
Publisher's PDF, also known as Version of record

[Link back to DTU Orbit](#)

*Citation (APA):*  
Tang, J. (2019). *Development of Three-Dimensional Graphene Biocatalysts for Enzymatic Biofuel Cells*. Technical University of Denmark.

---

### General rights

Copyright and moral rights for the publications made accessible in the public portal are retained by the authors and/or other copyright owners and it is a condition of accessing publications that users recognise and abide by the legal requirements associated with these rights.

- Users may download and print one copy of any publication from the public portal for the purpose of private study or research.
- You may not further distribute the material or use it for any profit-making activity or commercial gain
- You may freely distribute the URL identifying the publication in the public portal

If you believe that this document breaches copyright please contact us providing details, and we will remove access to the work immediately and investigate your claim.

# Development of Three-Dimensional Graphene Biocatalysts for Enzymatic Biofuel Cells

Jing Tang

Ph.D. Thesis

February 2019

**Development of Three-Dimensional Graphene Biocatalysts for Enzymatic Biofuel Cells**

Ph.D. Thesis

February 29<sup>th</sup>, 2019

**Jing Tang**

jita@kemi.dtu.dk

Supervisor

**Prof. Jingdong Zhang** and **Prof. Jens Øllgaard Duus**

Co-supervisor

**Dr. Christian Engelbrekt** and **Prof. Jens Ulstrup**

NanoChemistry group

Department of Chemistry

Technical University of Denmark

---

# Preface and Acknowledgments

The thesis is submitted to Technical University of Denmark (DTU) in partial fulfilment of the requirements for the degree of Doctor of Philosophy (Ph.D.). The work was carried out at the NanoChemistry group at DTU Chemistry from March 2017 to February 2020, under the supervision of Prof. Jingdong Zhang, Prof. Jens Øllgaard Duus, Dr. Christian Engelbrekt and Prof. Jens Ulstrup. The Ph.D. project “Development of Three-Dimensional Graphene Biocatalysts for Enzymatic Biofuel Cells” was part of an Independent Research Fund Denmark (IRFD)/YDUN project and involved collaboration with Prof. Ulla Wollenberger and Prof. Silke Leimkühler from the Institute of Biochemistry and Biology, University of Potsdam (UP), Germany. This YDUN project (DFE 4093-00297) is greatly acknowledged for my Ph.D. work and the external stay in UP.

First of all, I would like to thank my supervisor Prof. Jingdong Zhang for offering me the opportunity to pursue a Ph.D. degree at DTU Chemistry, and for her great help, enthusiastic motivation and valuable advice during the last three years. She taught me to grow as a scientific researcher. I am greatly thankful to my supervisors Prof. Jens Ulstrup and Dr. Christian Engelbrekt for giving me constructive scientific input and guidance during my study. Great thanks to my supervisor Prof. Jens Øllgaard Duus for providing me great support especially at the end of my study. I would like to thank Prof. Ulla Wollenberger for her strong support in both my work and life during my stay in Potsdam.

I am grateful to the whole NanoChemistry group for their support in both my work and life as well as creating a friendly and active scientific atmosphere. In particular, I would like to express my deep gratitude to Dr. Xinxin Xiao for sharing rich experience in biofuel cells as well as giving me invaluable scientific inspiration and suggestions. Thanks to Dr. Rebecka Maria Larsen Werchmeister for introducing the electrochemical experiment skills to me at the beginning of my Ph.D. study. I would like to thank Dr. Nedjeljko Seselj and Dr. Minwei Zhang for introducing me how to operate a fuel cell station and synthesize graphene oxide, respectively.

I would like to express my appreciation to Dr. Xiaorong Zhang and Dr. Loredana Preda’s great support during my stay in Potsdam. Thanks to Lars Nilausen Cleemann and Chao Pan at DTU Energy Conversion and Storage for giving me access to their hot-pressing instrument for membrane cathode assembly. I would like to thank Sara Nørgaard Sørensen at DTU Environment for help with Zeta potential measurements and Prof. Anders Egede Daugaard at DTU Chemical Engineering for assistance with contact angle measurements. I would also like to thank many people at Department of Chemistry especially laboratory technicians David Frej Nielsen, Johanne Marie Nielsen and Marie

---

Koefoed as well as Ph.D. coordinator Mette Hansen, and receptionist Jette Berg Nestén for their great help to me during the last three years.

Last but not least, Thanks to my parents, sister, and my boyfriend Wei Huang and other friends for their immense understanding and support.

February 2019, Kgs. Lyngby

---

Jing Tang

---

# Abstract

Biofuel cell technology offers sustainable and environmentally friendly solutions for energy production for the alleviation of the global energy crisis. Enzymatic biofuel cells (EBFCs), a subclass of biofuel cells, can produce electrical power from renewable fuels by employing biodegradable catalysts (*i.e.* enzymes), and have therefore attracted interest. Further, graphene arranged in three-dimensional (3D) structures with excellent electric conductivity and high surface area has been widely used in bioelectrode fabrication for EBFC applications. The aim of this Ph.D. project is to develop EBFCs by utilizing 3D graphene-based electrodes as supports for enzyme immobilization to convert chemical energy directly into electrical energy.

In this Ph.D. project, we have constructed graphene-based 3D electrodes by depositing graphene oxide (GO) nanosheets on 3D porous carbon paper (CPG electrodes) *via*  $\pi$ - $\pi$  interactions. The improved hydrophilicity of the carbon paper after functionalization with GO ensured the uniform immobilization of aqueous graphene-based nanomaterials and enzymes. The optimized CPG was chosen as the substrate for the following bioelectrode fabrications.

The as-prepared CPG electrodes was first applied to design *human* sulfite oxidase (*hSO*) bioanodes for sulfite/ $O_2$  EBFCs by drop-casting graphene-polyethylenimine (G-P) composites onto the CPG (CPG/G-P), and further immobilization of the negatively charged enzyme *hSO* through electrostatic interaction with the positively charged G-P matrix leading to a good enzyme orientation for electron transfer. Notably, electroreduction of GO in the CPG/G-P electrodes before enzyme loading led to a 9-fold increase of the saturation catalytic current density for sulfite oxidation compared to the bioelectrode without electroreduction treatments reaching  $24.4 \pm 0.3 \mu\text{A cm}^{-2}$ . The increased electron transfer rate played a dominating role in the enhancement of direct enzymatic current because of the improved electric contact of *hSO* with the electrode. The assembly of the *hSO* bioanode and a commercial platinum biocathode allowed the construction of sulfite/ $O_2$  EBFCs with flowing fuels. The optimized EBFC displayed an open-circuit voltage (OCV) of  $0.64 \pm 0.01 \text{ V}$  and a maximum power density of  $61 \pm 6 \mu\text{W cm}^{-2}$  at  $30 \text{ }^\circ\text{C}$ , which exceeds the best reported value by more than six times.

*Myrothecium verrucaria* bilirubin oxidase (*MvBOx*) biocathodes based on the CPG was fabricated for glucose/ $O_2$  EBFCs. The electroreduction of GO to reduced GO (RGO) and introduction of 4-aminobenzoic acid (4-ABA), achieved by applying successively electrochemical negative and positive potentials pulses, significantly improved the bioelectrocatalytic performance of the bioelectrodes toward dioxygen reduction reaching catalytic current densities as high as  $193 \pm 4 \mu\text{A cm}^{-2}$ . The grafting of 4-ABA was important roles both in the orientation of BOx and in the alleviation of RGO aggregation.

---

The bioelectrode showed an outstanding operational stability in comparison to other reported DET-type BOx bioelectrodes with the half-lifetime of 55 h mainly due to the strong covalent bond between the enzyme and electrode surface. The fabricated bioelectrodes were finally exploited in a gas diffusion electrode (GDE) configuration producing catalytic current densities ( $60 \mu\text{A cm}^{-2}$ ) larger than traditional bioelectrodes. Finally, an EBFC was constructed with the BOx biocathode and a glucose oxidase bioanode. The glucose/O<sub>2</sub> EBFCs delivered a maximum power density of  $22 \mu\text{W cm}^{-2}$  with an OCV of 0.51 V.

---

# Abstract in Danish

Biobrændselsceller repræsenterer en bæredygtig og miljøvenlig mulighed for energiproduktion og afhjælpning af den globale energikrise. Enzymatiske biobrændselsceller (EBFCer), en underklasse af biobrændselsceller, kan producere strøm fra vedvarende brændsler ved at anvende bionedbrydelige katalysatorer (dvs. enzymer) og har derfor tiltrukket betydelig interesse. Ydermere er grafen arrangeret i tredimensionelle (3D) strukturer med fremragende elektrisk ledningsevne og stort overfladeareal blevet anvendt bredt til fremstilling af bioelektroder til EBFCer. Målet med dette Ph.D.-projekt er at udvikle EBFCer ved at benytte 3D grafen-baserede elektroder som supportmateriale for enzym-immobilisering til omdannelsen af kemisk energi direkte til elektrisk energi.

I dette Ph.D.-projekt har vi konstrueret grafen-baserede 3D elektroder ved at deponere grafenoxid (GO) på 3D, porøst kulstofpapir (CPG elektroder) via  $\pi$ - $\pi$  vekselvirkninger. Den forbedrede hydrofilicitet af kulstofpapiret efter funktionalisering med GO sikrede en ensartet immobilisering af grafen-baserede nanomaterialer og enzymer i vandig opløsning. Den optimerede CPG blev valgt som underlag for den efterfølgende bioelektrodefremstilling.

De fremstillede CPG elektroder blev først anvendt til at designe *human* sulfioxidase (*hSO*) bioanoder til sulfid/ $O_2$  EBFCer ved at dryp-støbe grafen-polyethenimin (G-P) kompositter på CPG (CPG/G-P) og videre immobilisere det negativt ladede enzym *hSO* gennem elektrostatiske vekselvirkninger med den positivt ladede G-P matrix, hvilket medførte en fordelagtig enzymorientering for elektronoverførsel. Bemærkelsesværdigt førte elektroreduktion af GO i CPG/G-P elektroderne før enzymimmobilisering til en 9 gange højere specifik katalytisk strøm ved sulfioxidering sammenlignet med elektroder uden elektroreduktionsbehandling, der nåede  $24.4 \pm 0.3 \mu\text{A cm}^{-2}$ . Den øgede elektronoverførselshastighed spillede en dominerende rolle i forbedringen af direkte enzymatisk strøm pga. en bedre elektrisk kontakt mellem *hSO* og elektroden. Kombinationen af *hSO* bioanoden og en kommerciel platinkatode gjorde det muligt at samle en sulfid/ $O_2$  EBFC med gennemstrømmende brændsel. Den optimerede EBFC præsterede en åbent kredsløbsspænding (OCV) på  $0.64 \pm 0.01 \text{ V}$  og en maksimal effekt på  $61 \pm 6 \mu\text{W cm}^{-2}$  ved  $30 \text{ }^\circ\text{C}$ , hvilket overgår de bedste rapporterede værdier mere end seks gange.

*Myrothecium verrucaria* bilirubinoxidase (*MvBOx*) biokatoder baseret på CPG blev fabrikeret til glukose/ $O_2$  EBFCer. Elektroreduktion af GO til reduceret GO (RGO) og tilføjes af 4-aminobenzosyre (4-ABA), som blev opnået ved at påføre på hinanden følgende negative og positive elektrokemiske potentialepulser, medførte en væsentlig forbedring af bioelektrodernes bioelektrokatalytiske ydeevne over for iltreduktion, som

---

nåede specifikke katalytiske strømme op til  $193 \pm 4 \mu\text{A cm}^{-2}$ . Overfladefunktionalisering med 4-ABA spiller en vigtig rolle både for orientering af BOx og for at modvirke RGO aggregering. Bioelektroden udviste exceptionel driftsstabilitet sammenlignet med andre DET-type BOx bioelektroder med en halveringstid på 55 timer, hvilket hovedsageligt skyldtes den stærke kovalente binding mellem enzym og elektrodeoverflade. De fremstillede bioelektroder blev til ydermere anvendt i et gas-diffusions-elektrode (GDE) system, som producerede større specifikke katalytiske strømme ( $60 \mu\text{A cm}^{-2}$ ) end traditionelle bioelektroder. Til slut blev en EBFC konstrueret med BOx biokatoden samt en glukoseoxidase bioanode. Glukose/O<sub>2</sub> EBFCer producerede en maksimum effekt på  $22 \mu\text{W cm}^{-2}$  med en OCV på 0.51 V.

---

# Motivation

Depletion of fossil fuels along with a rapid increase in energy demand drives the development of sustainable energy conversion technologies. Biologically renewable resources such as sugars, lignin, alcohol and glycerol have become alternative fuels for energy production. Electrochemical techniques are furthermore considered to directly convert chemical energy of renewable fuels into electrical energy in an environmentally friendly way. Based on the power and energy densities, commonly used electrochemical energy devices are presented in a Ragone plot which includes batteries, fuel cells, capacitors and supercapacitors.

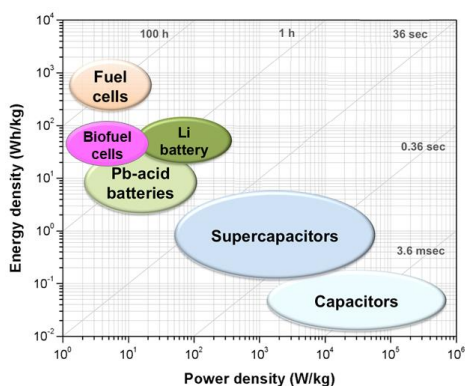


**Figure 1.** Ragone plot illustrating the performances of specific power vs specific energy for different energy conversion/storage devices. Times shown in the plot are the discharge time. Reprinted with permission from ref.<sup>[1]</sup>. Copyright 2014 American Chemical Society.

Among these electrochemical energy conversion/storage devices, biofuel cells as a subclass of fuel cells have become attractive in recently years. Compared to conventional fuel cells that use costly and scarce noble metals and/or their alloys as catalysts, biofuel cells (BFCs) such as enzymatic biofuel cells (EBFCs) employ biological renewable enzymes for the oxidation of fuels at the anode and the reduction of the oxidant at the cathode. The mild operating conditions of EBFCs such as room temperature and neutral pH make them promising electrochemical devices. Furthermore, EBFCs do not require expensive ion-exchange membranes for the separation of oxidation and reduction reactions into individual compartments such as conventional fuel cells do. Despite rapid developments of EBFCs, the open circuit voltage (OCV), power output and stability of EBFCs cannot yet afford practical applications but moving towards such goals aiming at improving the electrocatalytic activity and stability of the biocatalyst on the electrodes.

---

# Synopsis

The project aims at developing enzymatic bioelectrodes for enzymatic biofuel cells. Graphene especially arranged in three dimensions with excellent electric conductivity and high surface area are used to improve the enzyme loading, electrocatalytic activity and stability. The purpose of this Ph.D. project is specifically to develop three-dimensional (3D) graphene-based electrodes as supports for enzyme immobilization. The resulting bioelectrodes are then assembled in EBFCs for energy conversion from chemical into electrical energy.

The Ph.D. thesis is composed of six chapters, including the introduction of research background, methodologies, experimental details, results, discussion, conclusions and perspectives.

**Chapter 1** is a general introduction to enzymatic biofuel cells (EBFCs) and graphene-based bioelectrodes with concepts, theory and typical applications reviewed. The overview of the EBFCs is presented first, including major achievements of EBFCs over the last 20 years. Fundamentals and developments of the electrocatalysis on enzymatic bioelectrodes and surface chemistry in enzymatic bioelectrode design are then introduced, followed by the application of graphene as an excellent electrode material in EBFCs and its perspectives. Parts of this chapter, specifically the sections 1.2 Electrocatalysis on enzymatic bioelectrodes, 1.4 Features of graphene for bioelectrochemistry and 1.5 Graphene-based electrodes for enzymatic biofuel cells have been included in the review “Development of graphene-based enzymatic biofuel cells: A minireview”, submitted to *Bioelectrochemistry* (January 2020).

**Chapter 2** summarizes the methodology and techniques used for characterization of electrode materials and for the performance evaluation of enzymatic electrodes and enzymatic biofuel cells. It describes the principles of the methods employed.

**Chapter 3** focuses on fabrication and characterization of graphene-loaded three-dimensional carbon paper electrodes including the graphene synthesis. The hydrophilicity and electrochemical performance of graphene-based carbon paper electrodes are investigated in detail. Parts of this chapter, including the preparation of graphene and graphene-based carbon electrodes, as well as the characterization of morphology and hydrophilicity, are included in the paper “Three-dimensional sulfite oxidase bioanodes based on graphene functionalized carbon paper for sulfite/O<sub>2</sub> biofuel cells” published in *ACS Catal.*, 2019, and the manuscript “Direct electron transfer of orientated bilirubin oxidase on three-dimensional carbon paper with reduced graphene aggregation” (in preparation).

---

**Chapter 4** describes the fabrication of the 3D sulfite oxidase bioelectrode with the graphene-based carbon papers as supports, and its applications as a bioanode for EBFCs. The electrocatalytic processes on the bioanode are discussed in detail. The performance of the EBFCs was tested and compared to other published work. The results presented in this chapter are also included in the article “Three-dimensional sulfite oxidase bioanodes based on graphene functionalized carbon paper for sulfite/O<sub>2</sub> biofuel cells” published in *ACS Catal.*, 2019.

**Chapter 5** describes the fabrication of a 3D bilirubin oxidase bioelectrode based on the graphene-based carbon papers and its application as a biocathode for EBFCs. The stability, including long-term operation and storage stability, of the biocathode was investigated thoroughly, and compared with other published bilirubin oxidase bioelectrodes. The performance of the EBFCs with the biocathode and a glucose oxidase bioanode was characterized. The results presented in this chapter are also included in the manuscript “Direct electron transfer of orientated bilirubin oxidase on three-dimensional carbon paper with reduced graphene aggregation” (in preparation).

**Chapter 6** summarizes conclusions of the entire Ph.D. thesis and offers perspectives of the three-dimensional graphene-based biocatalysts for EBFC applications.

---

# Acronyms and instructional notes

**2D:** 2-Dimensional

**3D:** 3-Dimensional

**3-NTB:** 3-P-naphthoyl-Toluidine Blue O

**4-ABA:** 4-Aminobenzoic acid

**ABTS:** 2,2'-azinobis-(3-ethylbenzthiazoline-6-sulfonate)

**ADH:** Alcohol dehydrogenase

**AFM:** Atomic force microscopy

**Ag/AgCl:** Saturated silver/silver chloride

**Al:** Aluminum

**AldDH:** Aldehydedehydrogenase

**An:** Anthracene

**APTES:** Aminopropyltriethoxysilane

**AuNPs:** Au nanoparticles

**BE:** Binding energy

**BET:** Brunauer, Emmett and Teller

**BFC:** Biofuel cell

**BOx:** Bilirubin oxidase

**BQ:** 1,4-Benzoquinone

**BSA:** Bovine serum albumin

**CA:** Chronoamperometry

**CaM:** Calmodulin chimer

**CDH:** Cellobiose dehydrogenase

**CE:** Counter electrode

**CFC:** Carbon fiber cloth

**CMC:** N-cyclohexyl-N'-(2-morpholinoethyl) carbodiimide metho-p-toluenesulfonate

**CP:** Carbon paper

**CPE:** Constant phase element

X

**CPG:** Carbon paper coated with graphene oxide

**CoPc:** Cobalt phthalocyanine

**CNP:** Carbon nanoparticle

**CNT:** Carbon nanotube

**CV:** Cyclic voltammetry

**CVD:** Chemical vapor deposition

**DET:** Direct electron transfer

**DMFc:** 1,1-Dimethyl ferrocene

**DTU:** Technical University of Denmark

**DTSP:** Dithio-bis(N-hydroxysuccinimidyl propionate)

**EBFC:** Enzymatic biofuel cell

**ECSA:** Electrochemical surface area

**EDS:** Energy-dispersive X-ray spectroscopy

**EIS:** Electrochemical impedance spectroscopy

**E<sub>p</sub>:** Peak potential

**ET:** Electron transfer

**ETD:** Everhart-Thornley Detector

**FAD:** Flavin adenine dinucleotide

**FaLDH:** Formaldehyde dehydrogenase

**Fc:** Ferrocene

**FcCOOH:** Ferrocene carboxylic acid

**Fc-C<sub>6</sub>-LPEI:** Hexylferrocenyl linear polyethylenimine

**FDH:** Fructose dehydrogenase

**FePc:** Iron phthalocyanine

**FoDH:** Formate dehydrogenase

---

|   |  |
|---|--|
| <b>FC:</b> Fuel cell                                | <b>MbBOx:</b> <i>Myrothecium verrucaria BOx</i>  |
| <b>GA:</b> Graphene aerogel                         | <b>NAD:</b> Nicotinamide adenine dinucleotide  |
| <b>GDBE:</b> Gas diffusion bioelectrode             | <b>NG:</b> Nitrogen-doped graphene   |
| <b>GCE:</b> Glassy carbon electrode                 | <b>NGA:</b> Nitrogen-doped graphene aerogel  |
| <b>GDH:</b> Glucose dehydrogenase                   | <b>NP:</b> Nanoparticle  |
| <b>GDE:</b> gas diffusion electrode                 | <b>NPG:</b> Nanoporous gold  |
| <b>GO:</b> Graphene oxide                           | <b>OCP:</b> Open circuit voltage   |
| <b>GOx:</b> Glucose oxidase                         | <b>OCV:</b> Open circuit voltage   |
| <b>G-P:</b> Reduced graphene oxide-polyethylenimine | <b>ORR:</b> Oxygen reduction reaction  |
| <b>GQD:</b> Graphene quantum dot                    | <b>Os:</b> Osmium  |
| <b>ITO:</b> Indium tin oxide                        | <b>Os(bpy)<sub>2</sub>PVI:</b> Os(2,2'-bipyridine) <sub>2</sub> (polyvinylimidazole) <sub>10</sub> |
| <b>HCP:</b> Hydrophobic carbon paper                | <b>P<sub>max</sub>:</b> Maximum power density  |
| <b>hSO:</b> Human sulfite oxidase                   | <b>PANI:</b> Polyaniline   |
| <b>HOPG:</b> Highly oriented pyrolytic graphite     | <b>PBSE:</b> 1-Pyrenebutanoic acid succinimidyl ester  |
| <b>KB:</b> Ketjen Black                             | <b>PEDOT:</b> Poly(3,4-ethylenedioxythiophene)   |
| <b>LDH:</b> Lactate dehydrogenase                   | <b>PEI:</b> Polyethylenimine   |
| <b>LED:</b> Light-emitting diode                    | <b>PEGDGE:</b> Poly(ethylene glycol)diglycidyl ether   |
| <b>LOx:</b> Lactate oxidase                         | <b>PPy:</b> Polypyrrole  |
| <b>LPEI:</b> Linear Polyethylenimine                | <b>PLL:</b> Polylysine   |
| <b>LSV:</b> Linear sweep voltammetry                | <b>PQQ:</b> Pyrroloquinoline quinone   |
| <b>MB:</b> Meldola blue                             | <b>PSS:</b> Poly(styrene-b-isoprene-b-styrene)   |
| <b>MBFC:</b> Microbial fuel cells                   | <b>Pt:</b> Platinum  |
| <b>MCO:</b> Multicopper oxidase                     | <b>PTCA:</b> 3,4,9,10-Perylene tetracarboxylic acid  |
| <b>MET:</b> Mediated electron transfer              | <b>PTFE:</b> Polytetrafluoroethylene   |
| <b>MG:</b> Methylene green                          | <b>RE:</b> Reference electrode   |
| <b>MPA:</b> Mercaptopropionic acid                  | <b>RHE:</b> Reversible hydrogen electrode  |
| <b>MW:</b> Molecule weight                          | <b>RGO:</b> Reduced graphene oxide   |
| <b>MWCNT:</b> Multi-walled carbon nanotube          | <b>R.T.:</b> Room temperature  |
| <b>MFcOH:</b> Hydroxy methyl ferrocene              |  |
| <b>Mo:</b> Molybdenum                               |  |

---

|  |   |
|--|---|
| <b>SCE:</b> Saturated calomel electrode      | <b>THF:</b> Tetrahydrofuran                     |
| <b>SEM:</b> Scanning electron microscopy     | <b>TTF:</b> Tetrathiafulvalene                  |
| <b>SHE:</b> Standard hydrogen electrode      | <b>UP:</b> University of Potsdam                |
| <b>SPE:</b> Screen-printed electrode         | <b>UV-vis:</b> Ultraviolet-visible spectroscopy |
| <b>SWCNT:</b> Single-walled carbon nanotube  | <b>VFc:</b> Vinyl ferrocene                     |
| <b>TBAB:</b> Tetrabutylammonium bromide      | <b>WE:</b> Working electrode                    |
| <b>TBO:</b> Toluidine Blue                   | <b>XPS:</b> X-ray photoelectron spectroscopy    |
| <b>TEM:</b> Transmission electron microscopy |   |

### *Instructional notes*

Acronyms of terms ending in -microscopy, -chemistry, -voltammetry or -spectroscopy, refer to -microscope, -chemical, -voltammogram and -spectrum/spectra, as well. Abbreviations are used in plural form by adding “s”. Figures and Equations are abbreviated to “Fig.” and “Eq.” respectively in the text.

---

## Table of Contents

|  |      |
|--|------|
| Preface and Acknowledgments .....  | I    |
| Abstract .....   | III  |
| Abstract in Danish .....   | V    |
| Motivation .....   | VII  |
| Synopsis .....   | VIII |
| Acronyms and instructional notes.....                                    | X    |
| Chapter 1 Enzymatic biofuel cells and graphene-based bioelectrodes ..... | 1    |
| 1.1 Introduction to enzymatic biofuel cells .....                        | 1    |
| 1.2 Electrocatalysis on enzymatic bioelectrodes .....                    | 4    |
| 1.2.1 Electron transfer between enzymes and electrodes.....              | 4    |
| 1.2.2 Enzymatic bioanodes.....   | 7    |
| 1.2.3 Enzymatic biocathodes.....   | 8    |
| 1.3 Surface chemistry in enzymatic bioelectrode design.....              | 9    |
| 1.3.1 Enzyme immobilization techniques.....                              | 10   |
| 1.3.2. Electrode modification with nanomaterials .....                   | 12   |
| 1.4 Features of graphene for bioelectrochemistry .....                   | 14   |
| 1.5 Graphene-based electrodes for enzymatic biofuel cells.....           | 17   |
| 1.5.1 Graphene-based electrodes .....                                    | 17   |
| 1.5.2 Graphene-based enzymatic biofuel cells .....                       | 22   |
| 1.6 Perspectives of enzymatic biofuel cells .....                        | 30   |
| 1.6.1 Application of EBFCs.....  | 30   |
| 1.6.2 Challenges and perspectives.....                                   | 31   |
| 1.7 Conclusions .....  | 32   |
| Chapter 2 Methodology.....   | 33   |
| 2.1 Microscopic techniques .....   | 33   |
| 2.1.1 Atomic force microscopy .....                                      | 33   |
| 2.1.2 Scanning electron microscopy.....                                  | 34   |
| 2.2 Spectroscopic techniques .....                                       | 35   |
| 2.2.1 Ultraviolet-visible spectroscopy.....                              | 35   |
| 2.2.2 X-ray photoelectron spectroscopy .....                             | 37   |
| 2.2.3 Raman spectroscopy.....  | 37   |
| 2.2.4 Energy-dispersive X-ray spectroscopy.....                          | 38   |
| 2.3 Electrochemical techniques .....                                     | 38   |
| 2.3.1 Cyclic voltammetry.....  | 39   |

---

|   |    |
|---|----|
| 2.3.2 Linear sweep voltammetry.....   | 40 |
| 2.4.3 Polarization and power curves for enzymatic biofuel cells.....                            | 40 |
| 2.3.4 Chronoamperometry.....  | 41 |
| 2.3.5 Electrochemical impedance spectroscopy.....   | 42 |
| Chapter 3 Preparation and characterization of graphene-based 3D carbon papers.....              | 44 |
| 3.1 Introduction.....   | 44 |
| 3.2 Experimental.....   | 45 |
| 3.2.1 Chemicals and materials.....  | 45 |
| 3.2.2 Synthesis of graphene oxide.....  | 45 |
| 3.2.3 Pre-treatment of carbon paper.....  | 48 |
| 3.3 Results and discussion.....   | 49 |
| 3.3.1 Morphology and structure characterization of GO.....                                      | 49 |
| 3.3.2 Hydrophilicity of functionalized carbon papers.....                                       | 50 |
| 3.3.3 Electrochemical characterizations of functionalized carbon papers.....                    | 52 |
| 3.3.4 Effects of sonication time on carbon papers with GO.....                                  | 53 |
| 3.3.5 Electroactive surface area calculation of carbon papers with GO.....                      | 57 |
| 3.4 Conclusions.....  | 58 |
| Chapter 4 3D sulfite oxidase graphene-based bioanode for sulfite/O <sub>2</sub> fuel cells..... | 59 |
| 4.1 Introduction.....   | 59 |
| 4.2 Experimental.....   | 62 |
| 4.2.1 Chemicals and materials.....  | 62 |
| 4.2.2 Synthesis of polyethylenimine-modified graphene nanomaterials.....                        | 62 |
| 4.2.3 Fabrication of <i>h</i> SO modified bioelectrodes.....                                    | 63 |
| 4.2.4 Electrochemical measurements of the bioelectrodes.....                                    | 64 |
| 4.2.5 Activity assay of bioelectrodes.....  | 65 |
| 4.2.6 Construction and characterization of sulfite/O <sub>2</sub> enzymatic biofuel cells.....  | 66 |
| 4.3 Results and discussion.....   | 68 |
| 4.3.1 Characterization of electrode materials.....  | 68 |
| 4.3.2 Electrochemical characterization of modified electrodes.....                              | 71 |
| 4.3.3 Electrocatalysis of bioelectrodes.....  | 75 |
| 4.3.4 Effect of electroreduction on biocatalysis.....   | 76 |
| 4.3.5 Optimization of bioelectrodes.....  | 78 |
| 4.3.6 Evaluation of bioelectrodes.....  | 82 |
| 4.3.7 Application of bioanodes in enzymatic biofuel cells.....                                  | 85 |
| 4.4 Conclusions.....  | 87 |

---

|   |     |
|---|-----|
| Chapter 5 3D bilirubin oxidase graphene-based biocathode for glucose/O <sub>2</sub> biofuel cells | 88  |
| 5.1 Introduction  | 88  |
| 5.2 Experimental  | 89  |
| 5.2.1 Chemicals and materials   | 89  |
| 5.2.2 Fabrication of the BOx modified bioelectrodes   | 90  |
| 5.2.3 Electrochemical characterization of the modified electrodes                                 | 91  |
| 5.2.4 Determination of the amount of active enzymes on electrodes                                 | 92  |
| 5.2.5 Construction and characterization of gas diffusion bioelectrodes                            | 92  |
| 5.2.6 Characterization of glucose/O <sub>2</sub> enzymatic biofuel cells                          | 94  |
| 5.3 Results and discussion  | 94  |
| 5.3.1 Characterization of electrode materials   | 94  |
| 5.3.2 Electrochemical characterization of modified electrodes                                     | 99  |
| 5.3.3 Electrocatalysis of BOx Bioelectrodes   | 101 |
| 5.3.4 Kinetic analysis of performance of bioelectrodes  | 104 |
| 5.3.5 Stability evaluation of bioelectrodes   | 107 |
| 5.3.6 Applications as gas diffusion bioelectrodes and biocathodes                                 | 110 |
| 5.4 Conclusions   | 111 |
| Chapter 6 Conclusions   | 112 |
| Bibliography  | 115 |
| Appendix  | i   |



# Chapter 1

## Enzymatic biofuel cells and graphene-based bioelectrodes

---

---

This chapter gives an introduction to enzymatic biofuel cells and graphene-based enzymatic bioelectrodes. Part of the chapter has been submitted to the journal *Bioelectrochemistry* as a review entitled “Development of graphene-based enzymatic biofuel cells: A minireview”, coauthored by J. Tang, X. Xiao, X. Yan, C. Engelbrekt, J. Ulstrup, E. Magner and J. Zhang.

---

### 1.1 Introduction to enzymatic biofuel cells

Due to increasing demands for clean and sustainable energy sources, biologically renewable resources such as polysaccharide and lignin have become alternative fuels for energy production. Compared to traditional combustion power generation, fuel cells (FCs) are considered as environmentally friendly electrochemical devices that directly convert chemical energy to electrical energy. Typically, conventional FCs use noble metals (*e.g.*, platinum (Pt), ruthenium, palladium, *etc.*) and/or their alloys as catalysts for the oxidation of pure fuels (*e.g.*, hydrogen or methanol) at the anode and the reduction of the oxidant (*e.g.* dioxygen in air) at the cathode, in basic and/or acidic electrolytes, resulting in a very high efficiency.<sup>[2]</sup> However, noble metals are costly and scarce. The use of strongly acidic/alkaline electrolytes, together with the requirement for expensive ion-exchange membranes to separate reactions into individual compartments, poses additional challenges.

Biofuel cells, a subclass of FCs, include enzymatic biofuel cells (EBFCs) and microbial biofuel cells (MBFCs) categorized based on the type of biocatalyst used. EBFCs employ enzymes to catalyze the oxidation of fuel molecules and/or the reduction of oxygen or peroxide for energy conversion to electricity (Fig. 1.1A), while MBFCs use living cells or microorganisms as catalysts at the cathode and/or anode. Although current MBFCs have certain advantages over EBFCs, such as long lifetimes (up to five years)<sup>[3-4]</sup> and the ability

of complete oxidation of simple sugars to carbon dioxide,<sup>[5]</sup> they are fraught with low power densities owing to slow electron transfer (ET) across cellular membranes to electrodes.<sup>[3, 6]</sup> In contrast, EBFCs typically can produce a relatively high power because of faster ET between the active sites of enzyme and electrode surface. EBFCs can operate under mild conditions (*i.e.*, ambient temperature and neutral pH), as opposed to strongly acidic/alkaline environment needed in conventional FCs.<sup>[2]</sup> Furthermore, an abundance of substrates can be used as fuels for EBFCs such as conventional fuels (*e.g.*, dihydrogen,<sup>[7]</sup> methanol<sup>[8-9]</sup> and ethanol<sup>[10]</sup>), carbohydrates (*e.g.*, starch,<sup>[11]</sup> glucose,<sup>[12-13]</sup> fructose,<sup>[14]</sup> and lactate<sup>[15-17]</sup>) and even inorganic salts (*e.g.* sulfite<sup>[18]</sup>). The oxidation of some molecules cannot be achieved by inorganic catalysts, while specific enzymes can accomplish this task. For example, the oxidation of starch is very sluggish if catalyzed by Pt, but efficiently facilitated using enzymatic catalysts.<sup>[19]</sup> Since enzymes generally show high specificity toward their substrates, membrane separators can be avoided if the enzymes are immobilized, simplifying fuel cell device design.<sup>[13, 20]</sup> EBFCs are thus well suited for applications such as self-powered biosensors using power outputs as analytical signals,<sup>[17, 21]</sup> implantable<sup>[22-23]</sup> and wearable<sup>[24-25]</sup> power sources fueled by endogenous substances, as well as portable power sources,<sup>[26-27]</sup> Fig. 1.1 B-D.

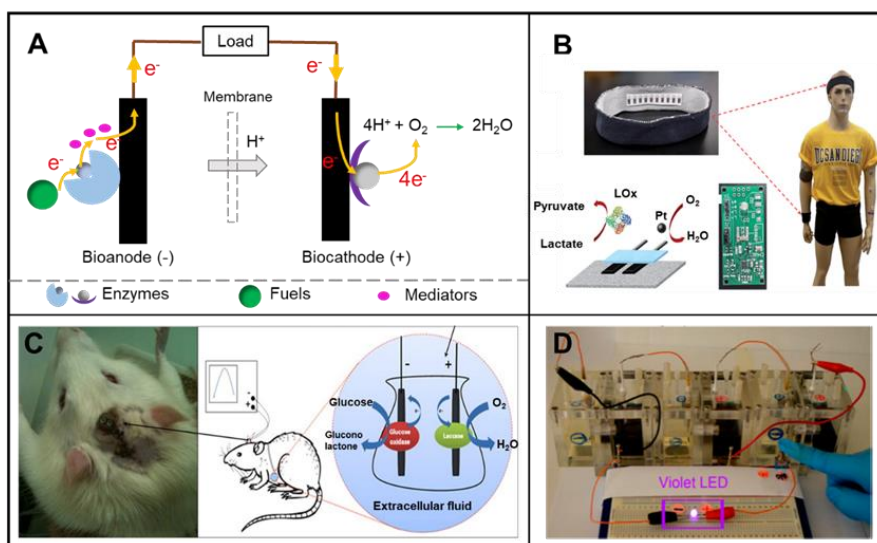
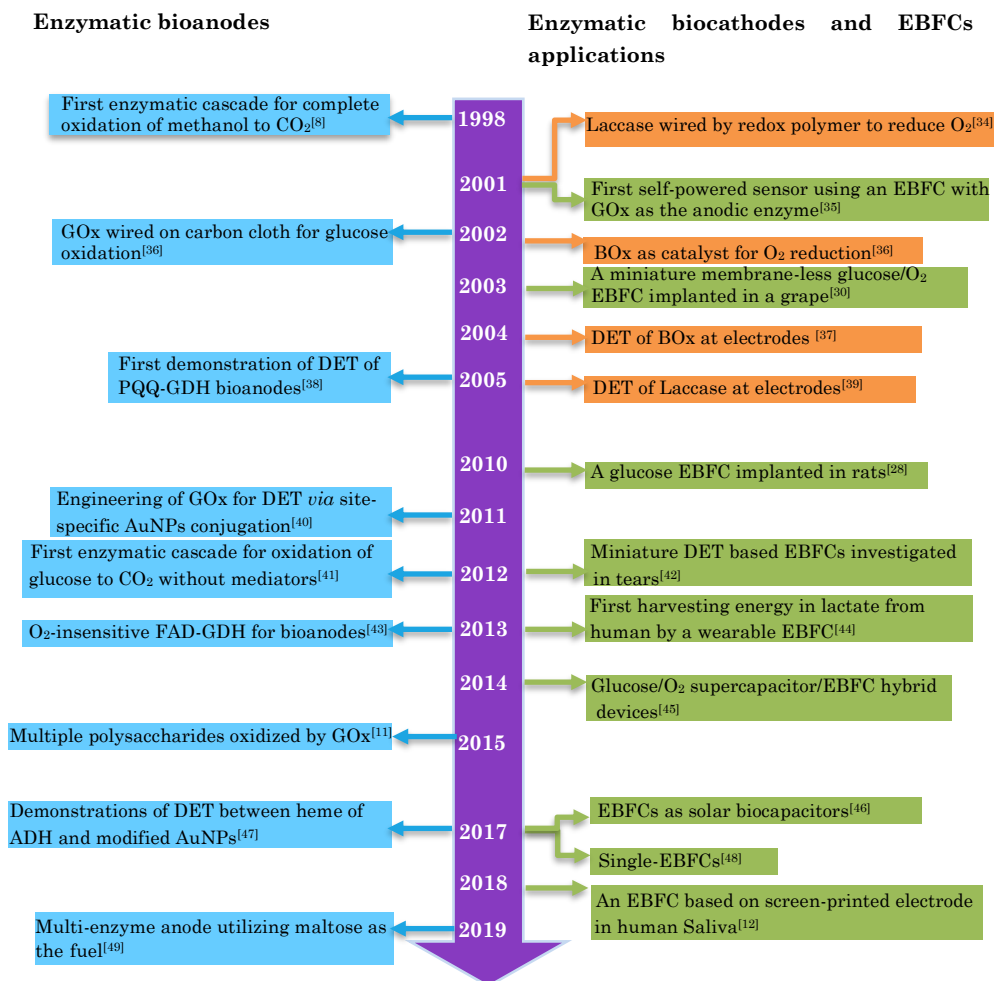


**Figure 1.1** (A) Schematic illustration of an EBFC with a bioanode operating by mediated electron transfer (MET), and a biocathode operating by direct electron transfer (DET). EBFC applications as (B) wearable,<sup>[24]</sup> (C) implantable and<sup>[28]</sup> portable power sources.<sup>[27]</sup> Reprinted with permission from refs.<sup>[24, 27-28]</sup>. Copyright 2014 Royal Society of Chemistry; Copyright 2013 Springer Nature; Copyright 2014 American Chemical Society.

---

In 1964, Kimble and co-workers first introduced an EBFC using glucose oxidase (GOx) or D-amino acid oxidase to catalyze anodic reactions.<sup>[29]</sup> By the late 1990s, Palmore and Whitesides reported that an enzymatic cascade employing alcohol dehydrogenase (ADH), formaldehyde dehydrogenase (FaDH), and formate dehydrogenase (FoDH) could be used for complete oxidation of methanol to carbon dioxide.<sup>[8]</sup> In 2003, a miniaturized membrane-less glucose/O<sub>2</sub> EBFC were reported, where both the bioanode and biocathode were implanted in a grape reaching a power density of 47  $\mu\text{W cm}^{-2}$  at 0.52 V.<sup>[30]</sup> The significant developments in EBFCs over the past few decades are outlined in Scheme 1.1. More recently, EBFCs as biosupercapacitors have been shown to achieve both energy conversion and charge storage using the same device.<sup>[31-33]</sup> Despite these rapid developments of EBFCs, the open circuit voltage (OCV), power output and stability of the state-of-the-art EBFCs cannot yet afford commercial production mainly due to limited efficiency and poor stability of the biocatalyst. To solve these obstacles, it is important to understand the following fundamental issues: (1) how to ensure efficient electronic communication between active centers of enzymes and the electrode; (2) how to maintain the electrocatalytic activity of enzymes immobilized on an inorganic substrate over time. The ET between the active site of enzymes and the electrode surface is here crucial. Understanding the mechanisms of ET and enzyme immobilization on electrodes in EBFCs are thus essential.



**Scheme 1.1** Timeline showing recent major achievements in the development of enzymatic anodes (indicated in blue) and cathodes (orange) as well as EBFCs (green). ADH: alcohol dehydrogenase. Ps: Au nanoparticles. BOx: bilirubin oxidase. FAD-GDH: Flavin adenine dinucleotide-dependent glucose dehydrogenase. PQQ: pyrroloquinoline quinone.

## 1.2 Electrocatalysis on enzymatic bioelectrodes

### 1.2.1 Electron transfer between enzymes and electrodes

ET is the key process that links solid-state electron donors or acceptors to the enzyme active sites. Depending on whether foreign redox molecules are involved, the process can be divided into mediated electron transfer (MET) and direct electron transfer (DET) (Fig.

1.2). MET describes systems in which a mediator molecule is oxidized or reduced by reacting with the enzyme active site, and subsequently diffuses to the electrode surface where a rapid ET takes places to regenerate the mediator for another cycle. Characteristic requirements for mediator species include stability and selectivity of both oxidized and reduced forms, as well as a need for reversible redox chemistry to ensure low overpotentials.<sup>[50]</sup> A suitable mediator should provide driving force for ET between enzyme active site and electrode. The redox potential of the mediator should be more positive for oxidative biocatalysis or more negative for reductive biocatalysis than that of the enzyme active sites.<sup>[51]</sup> Mediators studied include organic dyes, and transition metal complexes such as tetrathiafulvalene (TTF), osmium (Os) complexes, ferrocene (Fc) and quinone derivatives, Table 1.1.<sup>[51-57]</sup> Mediators are often required for nicotinamide adenine dinucleotide (NAD<sup>+</sup>) and flavin adenine dinucleotide (FAD)-dependent enzymes as the distance between these enzyme active sites and electrode surface is too far for DET.

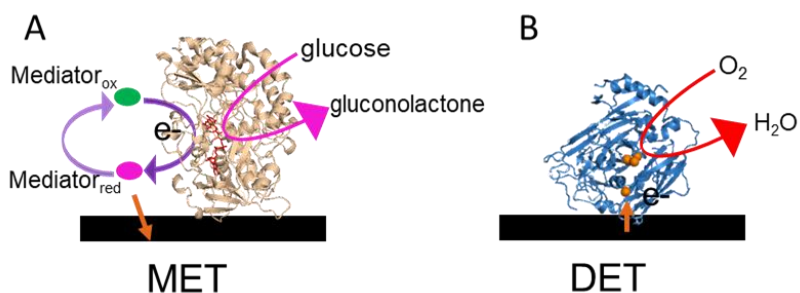


**Figure 1.2** Scheme of representative ET processes between the enzyme and the electrode surface at the enzymatic bioelectrodes: (A) MET from the bioanode surface through redox mediators to GOx (PDB: 1cf3), and (B) DET from a biocathode surface to BOx (PDB: 2xxl), catalytic copper centers are highlighted by orange color.

**Table 1.1.** A summary of commonly studied mediators and their redox reactions and corresponding redox potentials (vs. saturated calomel electrode, SCE).

| Mediator                            | Redox reaction   | Redox potential<br>(mV vs. SCE) | Ref. |
|-------------------------------------|--|---------------------------------|------|
| TBO                                 | $\text{TBO}^+ + \text{H}^+ + \text{e}^- \rightleftharpoons \text{TBOH}$  | -285 (pH 7.0)                   | [56] |
| MB                                  | $\text{MBH} \rightleftharpoons \text{MB}^+ + \text{e}^-$   | -160                            | [58] |
| 3-NTB                               | $3\text{-NTB}^+ + \text{H}^+ + \text{e}^- \rightleftharpoons 3\text{-NTBH}$                                      | -135 (pH 7.0)                   | [56] |
| BQ                                  | $\text{BQ}^+ + 2\text{H}^+ + 2\text{e}^- \rightleftharpoons \text{BQH}_2$  | 39 (pH 7.0)                     | [55] |
| DMFc                                | $\text{DMFc} \rightleftharpoons \text{DMFc}^+ + \text{e}^-$  | 100                             | [51] |
| Fc                                  | $\text{Fc} \rightleftharpoons \text{Fc}^+ + \text{e}^-$  | 165                             | [51] |
| $[\text{Fe}(\text{CN})_6]^{4-}$     | $[\text{Fe}(\text{CN})_6]^{4-} \rightleftharpoons [\text{Fe}(\text{CN})_6]^{3-} + \text{e}^-$                    | 180                             | [51] |
| MFcOH                               | $\text{MFcOH} \rightleftharpoons \text{MFc}^+\text{OH} + \text{e}^-$   | 185                             | [51] |
| VFc                                 | $\text{VFc} \rightleftharpoons \text{VFc}^+ + \text{e}^-$  | 250                             | [51] |
| $\text{Os}(\text{bpy})_2\text{PVI}$ | $[\text{Os}(\text{bpy})_2\text{PVI}]^+ \rightleftharpoons [\text{Os}(\text{bpy})_2\text{PVI}]^{2+} + \text{e}^-$ | 265                             | [54] |
| FcCOOH                              | $\text{FcCOOH} \rightleftharpoons \text{Fc}^+\text{COOH} + \text{e}^-$   | 275                             | [51] |
| TTF                                 | $\text{TTF} \rightleftharpoons \text{TTF}^+ + \text{e}^-$  | 300                             | [51] |
| ABTS                                | $\text{ABTS} \rightleftharpoons \text{ABTS}^+ + \text{e}^-$  | 517                             | [57] |

*3-NTB: 3-P-naphthoyl-Toluidine Blue O. ABTS: 2,2'-azinobis-(3-ethylbenzthiazoline-6-sulfonate). BQ: 1,4-Benzoquinone. DMFc: 1,1-dimethyl ferrocene. FcCOOH: Ferrocene carboxylic acid. MB: Meldola blue. MFcOH: Hydroxy methyl ferrocene. Os(bpy)<sub>2</sub>PVI: Os(2,2'-bipyridine)<sub>2</sub>(polyvinylimidazole)<sub>10</sub>. TBO: Toluidine Blue. VFc: Vinyl ferrocene.*

Compared to an unbound mediator, an immobilized mediator on the electrode surface is more desirable for practical applications. In recent years, mediator-derived redox polymers or DNA redox hydrogels are becoming more prevalent within bioelectrochemical applications due to the facile exchange of electrons between enzyme redox centers along the backbone of polymers or DNA<sup>[59-61]</sup>. For example, Merchant *et al.* synthesized two ferrocene-based linear polyethylenimine(LPEI) redox polymers with three-carbon (Fc-C<sub>3</sub>-LPEI) and six-carbon (Fc-C<sub>6</sub>-LPEI) backbones. Both redox polymers were able to exchange electrons with the FAD centers in GOx.<sup>[62]</sup> For MET systems, lower potential losses and greater mediator stability are the current development directions.

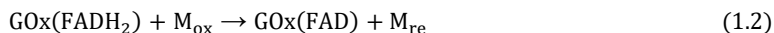
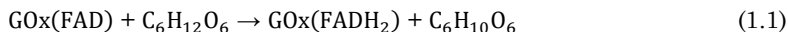
Unlike MET systems, DET systems entail direct transfer of electrons between the enzymes and the electrode without the help of external redox mediators, thus reducing potential losses resulting from the potential difference between the enzyme cofactor/active site and the mediator. DET is an electron-tunneling phenomenon between the active site or relay center of the enzyme and the electrode surface at short distances. Some enzymes containing redox active metal centers which are close to the surfaces are capable of DET. For example, pyrroloquinoline quinone (PQQ)-dependent enzymes containing a heme group in the oxidized state that can accept electrons from the oxidation

---

of substrates like alcohol, aldehyde, and glucose at the active site.<sup>[38, 63]</sup> Although DET is among the goals for EBFCs, most EBFCs in the literature utilize MET since such systems typically result in higher current densities.<sup>[64]</sup> Low current densities in DET systems mainly arise from sluggish ET flow. This is commonly caused by poor control of enzyme orientation on the electrode, and the fact that multiple layers (rather than a monolayer) of DET active enzymes are deposited on the electrode surface. Accurate control of the enzyme immobilization for proper DET and a three-dimensional (3D) structure of the enzyme-electrode assembly can thus lead to superior performance of DET systems.

### 1.2.2 Enzymatic bioanodes

Typically, electrocatalysis of oxidation at the anode is more versatile than the reduction at the cathode because of the diversity of fuels such as glucose, alcohols and sucrose, while the most popular oxidant for EBFCs at cathodes is O<sub>2</sub>. Widely studied fuels and relevant enzymes are outlined in Table 1.2. Among these fuels, oxidation of glucose on bioanodes has been extensively investigated and a representative mediated bioelectrocatalytic reaction with FAD-dependent-GOx (FAD-GOx) is shown in Eq. 1.1–1.3, where “M<sub>red</sub>” and “M<sub>ox</sub>” represent the reduced and oxidized forms of mediators, respectively. It is worth noting that a commercial GOx with great substrate promiscuity can oxidize many mono-, di-, tri-, and polysaccharides.<sup>[11]</sup> Such non-selective activity, though being an issue in biosensor applications, can be a great advantage in EBFCs.



During substrate catalysis, cofactors of enzymes at the active sites, change oxidation state. A variety of natural organic and inorganic oxidoreductase cofactors and ET relays are investigated including NAD<sup>+</sup>, nicotinamide adenine dinucleotide phosphate (NADP), FAD, PQQ, hemes, ironsulfur clusters, coenzyme Q, coenzyme F420, flavin mononucleotide (FMN) and molybdenum (Mo) clusters.<sup>[65-66]</sup> Some types of dehydrogenases such as NAD<sup>+</sup>-dependent,<sup>[67]</sup> heme-containing,<sup>[68]</sup> PQQ-dependent,<sup>[69]</sup> and FAD-dependent dehydrogenases<sup>[43]</sup> are good candidates for anode enzymes, because they are not sensitive to oxygen, and the side reaction of O<sub>2</sub> reduction to H<sub>2</sub>O<sub>2</sub> will not happen at the anodes. These enzymes may avoid the need for external diffusional mediators.<sup>[43, 68-69]</sup> The chemical environments at the anode and cathode do not therefore need to be separated by selective membranes leading to simpler device structures.

**Table 1.2** A summary of commonly studied biofuels and relevant single enzymes as well as cofactor redox reactions.

| Biofuel  | Enzyme | Cofactor         | Redox reaction  | Ref. |
|----------|--------|------------------|---|------|
| Glucose  | GOx    | FAD              | Glucose + GOx(FAD) → Gluconolactone + GOx(FADH <sub>2</sub> )                   | [70] |
|          | GDH    | FAD              | Glucose + GDH(FAD) → Gluconolactone + GDH(FADH <sub>2</sub> )                   | [43] |
|          | GDH    | PQQ              | Glucose + GDH(PQQ <sub>ox</sub> ) → Gluconolactone + GDH(PQQ <sub>red</sub> )   | [71] |
|          | GDH    | NAD              | Glucose + GDH(NAD <sup>+</sup> ) → Gluconolactone + GDH(NADH)                   | [72] |
|          | CDH    | Heme-FAD         | Glucose + CDH(FAD) → Gluconolactone + CDH(FADH <sub>2</sub> )                   | [68] |
| Methanol | ADH    | NAD <sup>+</sup> | Methanol + ADH(NAD <sup>+</sup> ) → Formaldehyde + ADH(NADH)                    | [9]  |
|          | FalDH  |                  | Formaldehyde + FalDH(NAD <sup>+</sup> ) → Formic acid + FalDH(NADH)             |      |
|          | FoDH   |                  | Formic acid + FoDH(NAD <sup>+</sup> ) → CO <sub>2</sub> + FoDH(NADH)            |      |
| Ethanol  | ADH    | NAD <sup>+</sup> | Ethanol + ADH(NAD <sup>+</sup> ) → Acetaldehyde + ADH(NADH)                     | [73] |
|          | ADH    | Heme-PQQ         | Ethanol + ADH(PQQ <sub>ox</sub> ) → Acetaldehyde + ADH(PQQ <sub>red</sub> )     | [74] |
|          | AldDH  |                  | Acetaldehyde + AldDH(PQQ <sub>ox</sub> ) → Acetate + AldDH(PQQ <sub>red</sub> ) |      |
| Lactate  | LOx    | FAD              | Lactate + LOx(FAD) → Pyruvate + LOx(FADH <sub>2</sub> )                         | [44] |
|          | LDH    | NAD <sup>+</sup> | Lactate + LDH(NAD <sup>+</sup> ) → Pyruvate + LDH(NADH)                         | [75] |
| Fructose | FDH    | Heme-FAD         | Fructose + FDH(FAD) → 5-Keto-D-Fructose + FDH(FADH <sub>2</sub> )               | [76] |
| Glycerol | ADH    | Heme-PQQ         | Glycerol + ADH(PQQ <sub>ox</sub> ) → Glyceraldehyde + ADH(PQQ <sub>red</sub> )  | [77] |

*CDH: cellobiose dehydrogenase. AldDH: aldehyde dehydrogenase. LOx: lactate oxidase. LDH: lactate dehydrogenase.*

### 1.2.3 Enzymatic biocathodes

The oxygen reduction reaction (ORR) is the main priority in the field of biocathode research since most EBFC applications rely on dioxygen in air or biological fluids as

oxidant. To date, Multicopper oxidases (MCOs) such as laccase and BOx have been utilized at the biocathode to directly or indirectly catalyze the reduction of dioxygen to water.<sup>[39, 78]</sup> The active center of MCOs contains four Cu atoms located in three different regions classified as T1, T2 and T3 (Fig. 1.3B). The Cu<sub>T1</sub> site, a hydrophobic pocket near the surface of the protein, is able to accept electrons. Electrons then tunnel to the Cu<sub>T2/T3</sub> site formed by a trinuclear cluster, where dioxygen can be efficiently reduced to water in a four-electron mechanism, Fig. 1.3. <sup>[78-79]</sup>

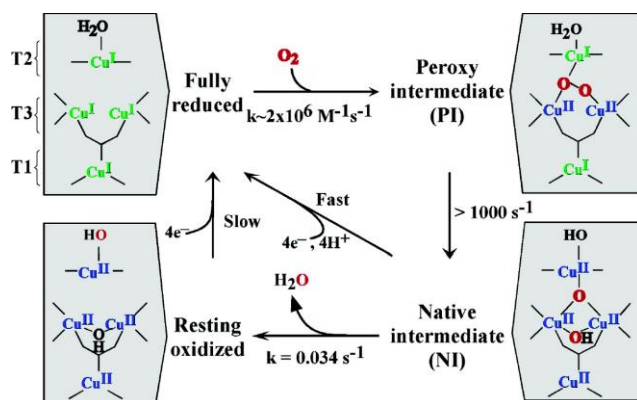


**Figure 1.3** Mechanism of O<sub>2</sub> reduction to H<sub>2</sub>O by the MCOs. Reprinted with permission from ref.<sup>[79]</sup>. Copyright 2007 American Chemical Society

The NI, different from the resting form, is a fully oxidized form of the enzyme. The transformation of NI to the resting state is very slow due to the reorganization of oxygen atoms, so it is typically not in the catalytic cycle, whereas the reduction of NI is fast (> 1000 s<sup>-1</sup>) and this is the catalytically relevant fully oxidized form of the MCOs.

Laccase is one of the most widely used enzymes for ORR.<sup>[78]</sup> The key characteristic of laccase is the standard redox potentials of the T1 site. The values in different laccases have been found to be between 430 and 790 mV vs. normal hydrogen electrode (NHE) due to various coordination conditions.<sup>[39]</sup> Aside from laccase, BOx has also been investigated for ORR catalysis with similar redox centers and catalytic mechanisms.<sup>[37, 80]</sup> BOx with the redox potential of BOx Cu<sub>T1</sub> (490 mV vs. NHE at pH 5.3) has the ability to catalyze ORR in near neutral solutions.<sup>[37]</sup> This is notable compared to laccase typically showing optimized catalytic current in slightly acidic solutions (less than pH 5.0).

### 1.3 Surface chemistry in enzymatic bioelectrode design

In order to achieve high performance of enzymatic bioelectrodes, recent research has implemented protein engineering, immobilization techniques and nanostructured materials to improve the biocatalysts-hosting capability of the electrode. Protein

---

engineering is a method for enzyme stabilization, requiring considerable knowledge of enzyme structures and delicate techniques, and is thus associated with significant cost.<sup>[81]</sup> In this part, we only focus on the surface chemistry in enzymatic bioelectrodes in terms of immobilization technique and electrode scaffold modification.

### 1.3.1 Enzyme immobilization techniques

Enzyme immobilization on electrodes is complicated, as a number of factors should be considered including enzyme properties such as size, isoelectric point and the hydrophobic or hydrophilic nature of the enzyme surface, as well as the composition, structure and charge of electrode surface. Each of these properties are related to different strategies for enzyme immobilization. The main types of enzyme immobilization are adsorption, covalent binding, and entrapment/encapsulation. Fig. 1.4 outlines these techniques with a general schematic representation.

Adsorption refers to enzyme immobilization on electrode surfaces *via* different types of non-covalent interactions such as van der Waals interactions, hydrogen bonding and electrostatic interactions.<sup>[82]</sup> For example, enzymes with a large lipophilic surface area interact well with a hydrophobic electrode surface. Sugar residues of glycosylated enzymes can ensure adsorption *via* hydrogen bonding.<sup>[82-83]</sup> Properties like enzyme charge and polarity are therefore crucial to ensure high coverage of enzymes on the electrode. This is typically a mild immobilization method, but a disadvantage is that enzymes tend to leach readily from the electrode over time.<sup>[81]</sup>

Covalent binding of enzymes to electrode surfaces has the advantage that the enzyme is tightly fixed. Enzyme leaching in aqueous media is thus minimized. The amino groups of the enzyme are nucleophilic, and can attack for instance an epoxide or aldehyde group. In the case of the aldehyde, an imine is formed which subsequently can be reduced, ensuring irreversible immobilization.<sup>[82]</sup> Carbodiimides can also be used to crosslink an amine of the enzyme with an acid group on the electrode or vice versa, forming an amide bond.<sup>[84]</sup> Additionally, other functional groups on the enzyme surface can be utilized, including sugar residues,<sup>[85]</sup> carboxylic acid<sup>[86]</sup> and exposed thiols (cysteine residues).<sup>[87-88]</sup> However, covalent binding of enzymes can sometimes be harsh, resulting in enzyme denaturation. It is therefore important to consider the chemical microenvironment and maintain the 3D structure and activity of the enzyme.<sup>[81]</sup> A more elegant covalent bonding is site-directed immobilization of engineered enzymes, which has appeared recently, potentially giving precise control of the orientation and environment of the enzyme attached to the electrode surface.<sup>[89-91]</sup> For example, an optimized CDH bioelectrode prepared by this method was able to retain its catalytic currents for at least two months.<sup>[91]</sup>

---

Entrapment is a process of using polymers to trap enzymes on a surface.<sup>[81]</sup> Both traditional and electropolymerization have been employed for entrapping enzymes. Sol-gel methods are also commonly used for entrapment. Heller *et al.* wired many enzymes to sol-gel materials, some of which contained redox moieties (Os or Fc-based complexes) as mediators embedded within the polymer to facilitate ET.<sup>[92]</sup> It is important to ensure that the chemical environment of the polymerization solution does not denature the enzyme, and that the pore size and interconnectivity of the pores in the polymer allows substrates and products to diffuse in and out of the polymer while withholding the enzymes.<sup>[93]</sup> Polymers including polyaniline (PANI),<sup>[63]</sup> polypyrrole,<sup>[94]</sup> polyethylenimine (PEI),<sup>[94-95]</sup> or their composites with other nanomaterials<sup>[69, 96-97]</sup> have been extensively used for enzyme entrapment. PEI, a positively charged polymer, can also trap GOx within the polymer electrostatically since GOx is negatively charged in neutral solution. Additionally, PEI can covalently trap enzymes by taking advantage of its free amino groups.<sup>[98-99]</sup> Recently, newly emerged conducting polymers like poly(3,4-ethylenedioxythiophene) (PEDOT) have also been used to entrap enzymes.<sup>[13, 32]</sup> Electron mediator-functionalized polymers have also been demonstrated to enhance the ET efficiency between the electrode and entrapped enzymes<sup>[13, 95, 100]</sup>. Polymer entrapment has been common, because it seldomly results in significant decrease in enzyme activity after immobilization.<sup>[101]</sup> However, leaching is frequently a problem.

Encapsulation is similar to entrapment in that the enzyme is confined within a polymeric matrix, but the matrix has “pockets” or “pores” for immobilizing enzymes.<sup>[81]</sup> Micellar polymers are an example of polymers that can encapsulate enzymes. The polymer micelles are swelled and the enzyme allowed to intercalate into the micellar pockets/aggregates followed by solvent evaporation. The polymer membrane provides a chemical microenvironment similar to a cellular microenvironment that can provide temperature, pH, and organic solvent to improve the stability of the enzyme. Minter *et al.* have attempted to tailor the micellar pore size of a tetrabutylammonium bromide-modified Nafion polymer for the encapsulation of a six-enzyme cascade on carbon papers (CPs). Impressively, this bioanode could oxidize glucose all the way to carbon dioxide *via* DET.<sup>[41]</sup> In addition, chitosan<sup>[102-103]</sup> and nanoporous materials<sup>[104-105]</sup> have also been modified for enzyme encapsulation.

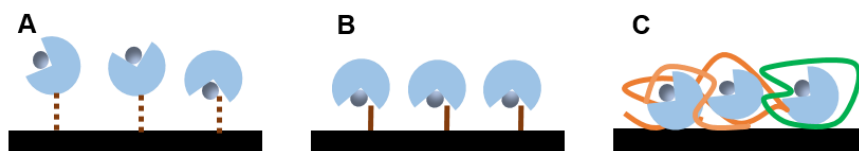


**Figure 1.4** Scheme of three main enzyme immobilization techniques, (A) adsorption, (b) covalent binding, and (C) entrapment (red wire)/encapsulation (green wire).

---

### 1.3.2. Electrode modification with nanomaterials

Modification of the electrode substrate with nanomaterials or direct utilization of nanostructured material as electrodes provides sustainable and efficient solutions for extended lifetime and performance of EBFCs due to the unique properties of nanostructured materials. Conducting nanomaterials can supply a favourable connection with biocatalysts by non-covalent or covalent binding, which ensures efficient ET between the enzyme active sites and the electrodes. In addition, nanostructured materials possess large surface areas for enzyme loading, and may provide open porous structures for sufficient diffusion of mediators and fuel molecules. A suitable microenvironment can also be offered to potentially preserve the activity of the biocatalysts. Significant progress in EBFCs has thus been made using various nanostructured materials, such as carbon-based materials, polymers and metal/metal oxides. Each of these will be addressed in detail in the following sections.

#### 1.3.2.1 Carbon-based materials

Carbon materials have attracted a great deal of interest in the field of EBFCs due to their good electrical conductivity and biocompatibility. Furthermore, their excellent mechanical performance and chemical stability also play important roles in the long-term operation of EBFCs. With the rapid development of advanced nanotechnologies and methodologies, carbon materials that possess various nanostructures, such as nanoparticles, nanotubes, nanowires, nanofibers and nanosheets, have been widely fabricated and used as electrode materials in EBFCs. The different nanostructures of carbon materials can provide various charge diffusion lengths and immobilization structures for biocatalysts, thereby changing the efficiency of ET. As a two-dimensional (2D) sheet formed with  $sp^2$  hybridized carbon atoms, graphene is an attractive electrode material for electrochemical devices, especially providing new opportunities for EBFCs. Graphene has unique properties such as high electrical conductivity ( $2-65 \text{ S cm}^{-1}$ ),<sup>[106-109]</sup> extremely high theoretic specific surface area (up to  $\sim 2600 \text{ m}^2 \text{ g}^{-1}$ )<sup>[110]</sup> and mechanical robustness (Young's modulus around  $0.98 \text{ TPa}$ ).<sup>[111]</sup> This will be described in detail in sections 1.4 and 1.5. Presently we discuss two other carbon materials, *i.e.*, carbon nanotubes (CNTs) and carbon nanoparticles (CNPs) and their derivatives are discussed to explore the function of carbon materials in enzymatic bioelectrodes.

CNTs are cylindrically shaped hollow nanomaterials with diameters less than  $100 \text{ nm}$  with large specific surface areas (usually a few hundreds to  $1300 \text{ m}^2 \text{ g}^{-1}$ ), high mechanical strength and excellent conductivity, becoming one of the most promising electrode materials. CNTs as catalyst supports in EBFCs have attracted attention, showing excellent properties such as significant enhancement ET rate at the electrode interfaces. CNTs have been widely used to modify different kinds of substrate electrodes in the field of EBFCs. For instance, Mao *et al.* presented the fabrication of one-compartment

glucose/O<sub>2</sub> EBFCs with a CNT-based bioelectrode.<sup>[112]</sup> CNTs served as the support for laccase to facilitate DET in the reduction of O<sub>2</sub> at the cathode. However, the power output was only 9.5 μW cm<sup>-2</sup>. In order to facilitate ET, many efforts have been made to tune the gap between the nanotube and active sites of the enzymes. A successful approach is to attach the enzyme molecules in a controlled orientation. Salimi and co-workers developed a new strategy to immobilize BOx in a glucose/O<sub>2</sub> EBFC by coupling DNA and CNTs as the supporting materials on glassy carbon electrode (GCE), Fig. 1.5.<sup>[113]</sup> In the system, a CNT-based electrode with bound DNA and thus negative surface charge could control the orientation of BOx by specifically interacting with a positively charged patch on the BOx surface close to the Cu<sub>T1</sub> site. The resulting electrodes showed excellent electrocatalytic activity for oxygen reduction with an onset potential of 0.57 V vs. Ag/AgCl (3 M KCl) and a maximum current density of 277 μA cm<sup>-2</sup>. Another general approach to achieve close proximity between CNT-based electrodes and enzymes is to use mechanical compression. Cosnier and co-workers created a bioelectrode of a mediator-less glucose EBFC by compressing the mixture of enzymes and multi-walled CNTs (MWCNTs) with a hydraulic press.<sup>[114]</sup> The fabricated EBFC delivered a high power density up to 1.3 mW cm<sup>-2</sup> and an OCV of 0.95 V. Additionally, carbon nanotube “forests”<sup>[115]</sup> and 3D porous CNT-based bioelectrodes<sup>[116]</sup> have also been used to improve the performance of EBFCs. For further study on CNTs-based EBFCs especially for implantable devices, the toxicity of CNTs however need be taken into account.

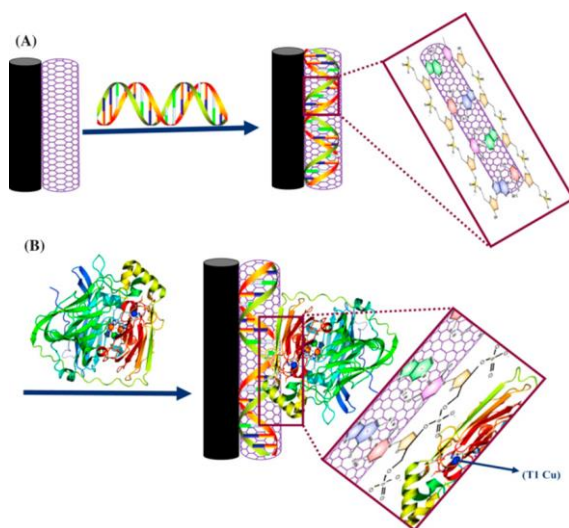


**Figure 1.5** (A) Scheme of DNA adsorption on GCE/MWCNT modified electrode, and (B) directing immobilization of BOx enzyme molecule onto the GCE/MWCNTs/DNA electrode. The DNA was adsorbed on CNTs *via* π-π stacking interaction between π-electrons of stacked base pairs in DNA structure and aromatic-like structure of CNTs. Reprinted with permission from ref.<sup>[113]</sup>. Copyright 2015 Elsevier.

---

Besides CNTs, CNPs have the advantages of high short-range conductivity, good biocompatibility, ease of functionalization and high surface area. Ketjen Black (KB) EC300J, a commercial porous CNP ((diameter:  $\sim 78$  nm) with specific surface area of  $800 \text{ m}^2 \text{ g}^{-1}$  from *Lion Specialty Chemicals Co., Ltd*, has been widely used to modify electrodes for enzyme immobilization.<sup>[117-119]</sup> For example, FDH adsorbed on KB particles modified CPs exhibited a maximum direct catalytic current density of ca.  $4.0 \text{ mA cm}^{-2}$ .<sup>[117]</sup> Together with laccase modified CP biocathodes, the efficient FDH bioelectrodes served as the anodes in one-compartment fructose/ $\text{O}_2$  EBFC, which delivered a maximum power density ( $P_{\text{max}}$ ) of  $850 \text{ } \mu\text{W cm}^{-2}$  with OCV of  $0.79 \text{ V}$ . In addition, Willner *et al.* designed an EBFC system based on enzyme-capped mesoporous CNP modified electrodes.<sup>[120]</sup> Redox mediators, MeFcOH or ABTS, were first loaded into the  $6.3 \text{ nm}$  pores of the  $< 500 \text{ nm}$  CNPs before capping these pores with GOx and BOx, respectively. The resulting EBFC provide a power output of  $\sim 95 \text{ } \mu\text{W cm}^{-2}$ . Another kind of CNPs, carbon nanodots ( $50\text{-}60 \text{ nm}$ ) were used as immobilization supports and electron carriers to promote DET of GOx and BOx, and a mediator-free glucose/air EBFC with OCV of  $0.93 \text{ V}$  and  $P_{\text{max}}$  of  $48 \text{ } \mu\text{W cm}^{-2}$  was fabricated.<sup>[121]</sup>

### 1.3.2.2 Metal/metal oxides

In the last decades, metals and metal oxides have attracted significant attention because they can be prepared with high surface area, catalytic activity, and conductivity. AuNPs have been the most widely used candidate for enzymatic bioelectrode design since they can act as electron relays between enzyme and electrode surface.<sup>[122]</sup> Moreover, DET can be achieved *via* site-specific conjugation between genetically modified GOx and AuNPs ( $1.2 \text{ nm}$ ).<sup>[40]</sup> AuNPs decorated on carbon-based nanomaterials or conducting polymers can provide more electroactive sites and improve conductivity.<sup>[123]</sup> Other metal nanoparticles (NPs), for example, Pt,  $\text{Pt}_{0.75}\text{Sn}_{0.25}$  and Ag NPs have also been used for enzymatic bioelectrode fabrication.<sup>[124-125]</sup> However, due to the drawbacks of these noble metals (*e.g.*, high price and scarcity), abundant transition metal/ metal oxides such as Fe-<sup>[126]</sup> and Ni-based materials<sup>[123]</sup> have been alternative matrices for bioelectrodes.  $\text{Fe}_3\text{O}_4$ <sup>[127]</sup> and  $\text{Fe}_2\text{O}_3$ <sup>[128]</sup> NPs with good biocompatibility and low toxicity can mediate ET between immobilized enzymes and electrode surfaces. Magnetic NPs are particularly widely investigated because of their strong magnetic property and easy separation.<sup>[126-127, 129-130]</sup>  $\text{Fe}_3\text{O}_4$  NPs can electrostatically adsorb positively charged horseradish peroxidase and the resulting protein- $\text{Fe}_3\text{O}_4$  film showed a sensitivity of  $3.5 \text{ } \mu\text{A mM}^{-1}$  in a linear range from  $50$  to  $36 \text{ } \mu\text{M}$ .<sup>[127]</sup>

## 1.4 Features of graphene for bioelectrochemistry

Graphene as an electrode material has excellent features for applications in many fields including energy storage and conversion,<sup>[31]</sup> sensors,<sup>[131]</sup> and bioremediation.<sup>[132]</sup> High electronic conductivity and mechanical strength of graphene are essential properties for

---

electrode materials. Under ambient conditions, the charge mobility of graphene can reach  $15000 \text{ cm}^2 \text{ V}^{-1} \text{ s}^{-1}$ , ten-fold higher than the charge mobility of silicon.<sup>[133]</sup> In addition, the electronic conductivity of graphene is almost 2-60 times higher than that of single-walled carbon nanotubes (SWCNTs)<sup>[134]</sup> with a similar mechanical hardness (Young's moduli around 0.98 TPa).<sup>[111]</sup> An early attempt employing silica sol-gel immobilized graphene sheet/enzyme composite electrodes for EBFC application was reported in 2010, demonstrating that the catalytic efficiency of graphene-based GOx anodes is twice that of SWCNT-based anodes, Fig. 1.6A.<sup>[20]</sup> As a result, the performance of graphene-based EBFC was also doubled, Fig. 1.6B. With a high optical transparency ( $\sim 97\%$ ) and a wide electrochemical window, graphene films are potential alternatives of widely used indium tin oxide (ITO) transparent electrodes in spectro-electrochemistry.<sup>[135-136]</sup>

In contrast to other carbon-based nanomaterials, graphene, consisting of 2D structures, has attracted considerable attention due to its unique layered structure. The thickness of monolayer graphene film can be very thin (ranging from 0.34 to 1.6 nm).<sup>[137]</sup> The remarkable flexibility and lightness are key for sensing or wearable bioelectronics.<sup>[138]</sup> Chemically synthesized reduced graphene oxide (RGO) assembled with crumpled sheets due to the interaction between the thin layers, Fig. 1.6C, showed good electrocatalytic activity for NADH oxidation a 330 mV decrease of the overpotential than bare GCE.<sup>[135]</sup> Furthermore, a graphene paper as a carrier for enzyme immobilization (*i.e.*, GDH and BOx) has been used to fabricate EBFCs, Fig. 1.6D. The resulting glucose/O<sub>2</sub> EBFC displayed a satisfactory power output (OCV: 0.665 V,  $P_{\text{max}}$ :  $4 \mu\text{W cm}^{-2}$ ), Fig. 1.6E, without obvious changes in power output upon bending up to 180 degree due to the notable mechanical flexibility of graphene paper, Fig. 1.6F.<sup>[139]</sup> This kind of flexible graphene-based EBFC holds great promise to activate low-power biomedical and bioanalytical microelectronics in particular for wearable applications.

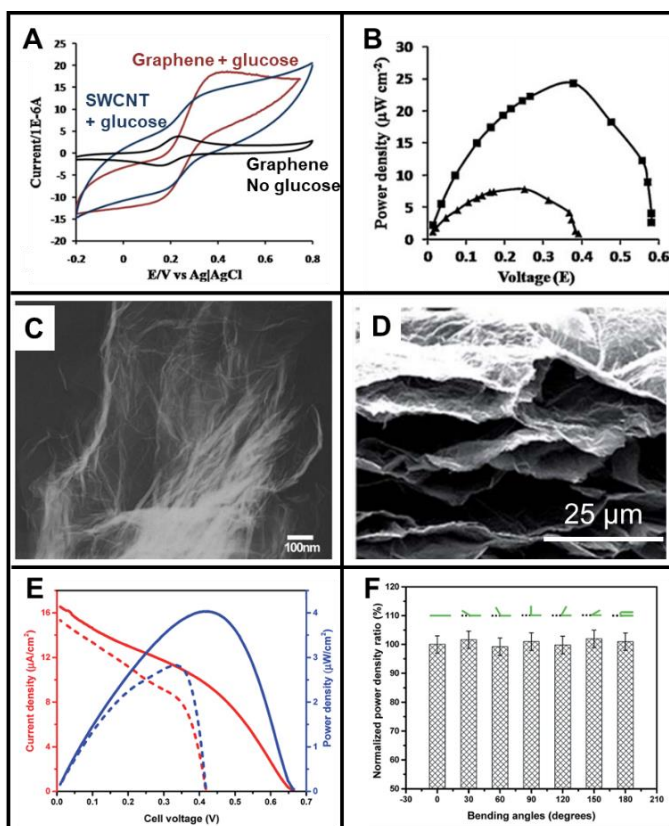


**Figure 1.6** (A) Cyclic voltammograms of graphene- or SWCNT-based anode in 100 mM glucose solution and graphene-based anode in phosphate buffer solution (PBS, pH 7.4) without glucose (scan rate:  $500 \text{ mV s}^{-1}$ ), where the redox wave originates from the mediator ferrocenemethanol in PBS.<sup>[20]</sup> (B) Power density profiles for (■) graphene-based EBFC and (▲) SWCNT-based EBFC in 100 mM glucose solution.<sup>[20]</sup> (C) Transmission electron microscopic (TEM) images of reduced graphene sheets.<sup>[135]</sup> (D) Cross-section scanning electron microscopic (SEM) images of the layered assembly of graphene papers.<sup>[139]</sup> (E) Polarization (red) and power curves (blue) obtained from the graphene paper supported GDH bioanode and BOx biocathode in air saturated buffer containing 6.4 mM glucose, solid and dashed curves for pure PBS and blood simulated buffer, respectively, and (F) power density ratio of the EBFCs after bending to various angles.<sup>[139]</sup> Reprinted with permission from ref.<sup>[20, 135, 139]</sup> with modification. Copyright 2010 Elsevier; Copyright 2009 John Wiley and Sons; Copyright 2019 Royal Society of Chemistry.

Graphene-based aerogels (GAs) constructed by the assembly of individual graphene sheets display high porosity (*i.e.*, light weight and high surface area) and high performance in both strength and electrical conductivity.<sup>[140-141]</sup> Surface areas for an aerogel fiber, measured by the Brunauer, Emmett and Teller (BET) technique, is as high

as  $884 \text{ m}^2 \text{ g}^{-1}$ ,<sup>[141]</sup> higher than those of CNTs ( $512$  to  $790 \text{ m}^2 \text{ g}^{-1}$ ).<sup>[142-143]</sup> Furthermore, Qian *et al.* prepared aerogels with a weight density as low as  $3.2 \text{ mg cm}^{-3}$  and a surface area of  $1019 \text{ m}^2 \text{ g}^{-1}$ .<sup>[140]</sup> A 3D N-doped graphene (NG) aerogel (3D-NGA) incorporated with dopamine can serve as a highly efficient electrocatalyst for  $\text{H}_2\text{O}_2$  reduction, Fig. 1.7, exhibiting a detection limit of  $0.05 \text{ mM}$  and a linear detection range up to  $35 \text{ mM}$ .<sup>[144]</sup> In addition, a GOx biosensor was developed based on the GA/AuNPs hybrid materials through a simple hydrothermal route.<sup>[145]</sup> The porous structure of the hybrid enabled a platform for GOx immobilization for glucose biosensors, exhibiting a remarkable sensitivity of  $258 \mu\text{A mM}^{-1} \text{ cm}^{-2}$  in a linear range from  $50$  to  $450 \mu\text{M}$ , and a detection limit of  $0.6 \mu\text{M}$ .<sup>[145]</sup>

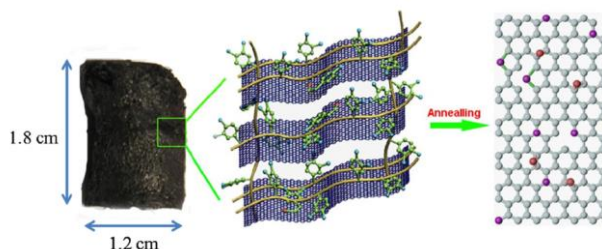


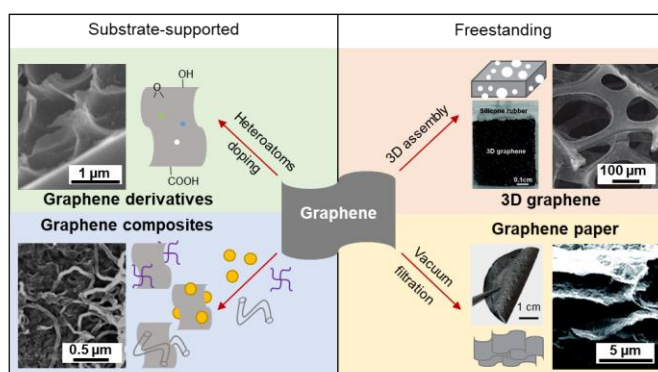
**Figure 1.7** Digital photo of 3D-NGA and the schematic illustration of its preparation. To construct an electrode, the 3D-NGA was cut into a ( $1.0 \text{ cm} \times 0.50 \text{ cm}$ ,  $0.30 \text{ mm}$  thick) piece. The piece was fixed onto a glass slide, and an electrical lead made by copper paste and copper wire insulated with silicone rubber. Reprinted with permission from ref.<sup>[144]</sup>. Copyright 2016 Elsevier.

## 1.5 Graphene-based electrodes for enzymatic biofuel cells

### 1.5.1 Graphene-based electrodes

As a 2D sheet with  $\text{sp}^2$  hybridized carbon atoms, the unique properties of structurally perfect graphene such as high electronic conductivity, large specific surface area (up to  $\sim 2600 \text{ m}^2 \text{ g}^{-1}$ ) and strong mechanical robustness, make it an attractive electrode material for electrochemical devices.<sup>[146-147]</sup> The properties of graphene materials depend on preparation method. Mechanical exfoliation,<sup>[148]</sup> epitaxial growth,<sup>[149]</sup> chemical vapor deposition (CVD),<sup>[150-153]</sup> un-zipping of CNTs,<sup>[154]</sup>  $\text{Ni}^{2+}$ -exchange/KOH activation,<sup>[155-156]</sup> and reduction of graphene oxide (GO)<sup>[157]</sup> are general routes for graphene production. Mechanical exfoliation is the first reported method to isolate graphene sheets from pyrolytic graphite, but is not suitable for large-scale production.<sup>[158]</sup> CVD is attractive since it can produce “pure” and high-quality graphene with large area and functionalized with heteroatoms or groups on solid surfaces but with a quite high cost.<sup>[151]</sup> Un-zipping of CNTs and  $\text{Ni}^{2+}$ -exchange/KOH activation are delicate processes and not applied widely in bioelectrochemistry. A highly cost-effective and easy-handling fabrication method is

chemical graphene, *i.e.*, reduction of GO obtained from the oxidation and subsequent exfoliation of graphite.<sup>[133]</sup> After a thermal,<sup>[159]</sup> chemical<sup>[160]</sup> or electrochemical<sup>[161]</sup> reduction process, the conductivity of GO can be enhanced by restoring the conjugated  $sp^2$  bonds responsible for graphene's conductivity. The resulting RGO nanosheets can also be produced on the surface of carbon fibers by *in situ* electrochemical procedures consisting of oxidative and reductive steps to yield surface supported RGO, Fig. 1.8.<sup>[162]</sup> RGO sheets possess considerable amounts of defects and disordered structures, which are different from the "ideal" graphene. The direct utilization of graphene in bioelectrochemistry applications suffers from irreversible  $\pi$ - $\pi$  stacking aggregations and thus loss of active surface area. Surface modification of graphene with grafted functional groups is necessary to achieve specific properties. Physicochemical properties such as hydrophilicity/hydrophobicity and surface charge influence the performance of enzymatic bioelectrodes. Freestanding graphene electrodes have emerged recently as promising supportive materials for wearable and implantable biomedical devices due to their mechanical robustness and flexibility, Fig. 1.8.



|                      | Preparation methods   | Advantages   |
|----------------------|---|--|
| Graphene derivatives | CVD; chemical GO reduction; oxidation of carbon fiber                                       | Biocompatibility; dispersibility; electrocatalytic activity                  |
| Graphene composites  | Noncovalent or covalent bonding; modification with nanoparticles                            | Bi-functionality; biocompatibility; high enzyme loading; high dispersibility |
| 3D graphene          | CVD; Ni <sup>2+</sup> -exchange/KOH activation; chemical GO reduction; vacuum freeze-drying | Flexibility; easy of fabrication   |
| Graphene paper       | CVD; GO assembly with reduction   | High surface area; high porosity for diffusion; high enzyme loading          |

**Figure 1.8** Strategies of designing graphene-based electrodes, including graphene derivatives and graphene modified electrodes as well as freestanding graphene electrodes. Representative scanning electron microscopy (SEM) images (top left: graphene nanosheets on carbon fibers of CPs,<sup>[162]</sup> top right: graphene/MWCNT,<sup>[163]</sup> bottom left: 3D graphene foam,<sup>[156]</sup> bottom right: graphene paper<sup>[139]</sup>). Preparation methods and advantages are summarized. Reprinted with permission from ref. <sup>[139, 156, 162-163]</sup> with modifications. Copyright 2016 John Wiley and Sons; Copyright 2011, 2012 American Chemical Society; Copyright 2019 Royal Society of Chemistry.

---

### 1.5.1.1 Graphene derivatives

Pristine graphene has not been widely exploited for bioelectrode construction which may be explained by the lack of functional groups such as oxygenated groups to anchor the enzymes to the electrode.<sup>[164]</sup> RGO is a graphene derivative with residual oxygenated species making it suitable for construction of enzymatic bioelectrodes. For example, Zhou *et al.* modified a GCE by drop-casting chemically produced RGO and then GOx, showing a better electrochemical response for the detection of glucose compared to graphite/GCE-based bioelectrodes.<sup>[165]</sup> It was suggested that the high density of edge-plane like defects on RGO may provide favorable sites for accelerating the redox reaction of H<sub>2</sub>O<sub>2</sub> generated on the electrode surface. Unnikrishnan *et al.* prepared a similar GOx/RGO-based bioelectrode *via* a one-step process.<sup>[131]</sup> It was demonstrated that RGO ensured high stability of GOx and thus a stable response. However, the aggregation of RGO could result in a decrease of surface area for high enzyme loading and therefore a low electrocatalytic current. It has been reported that a larger amount of laccase can be wired on anthraquinone-modified RGO/MWCNT (75 μg cm<sup>-2</sup>) than on the similarly aggregated RGO-based matrix (41 μg cm<sup>-2</sup>).<sup>[166]</sup> This implies that modification of RGO sheets with functional groups can ensure specific adsorption of enzyme, prevent aggregation and preserve high surface area for enzyme immobilization with MWCNT.<sup>[10, 166]</sup> Modifications of GO derivatives will be detailed in section 1.5.1.2.

Elemental doping is a versatile method of tuning the electronic structure of graphene. Actually GO and RGO can be regarded as a type of O-doped graphene. Recent attempts on doping graphene with other elements aim to tailor the electronic properties of graphene. Heteroatom-doped graphenes mainly include nitrogen, phosphorous, boron, sulfur, and fluorine doped graphene. Among them, nitrogen-doped graphene (NG) has been widely studied in electrochemistry. Compared to graphene and RGO, NG exhibits much better electrocatalytic activity<sup>[101]</sup> because of a relatively high positive partial charge density on carbon atoms adjacent to N-doping sites,<sup>[167-168]</sup> and beneficial physical and chemical properties such as enhanced electrical conductivity<sup>[169]</sup> and ET efficiency.<sup>[170]</sup> A NG modified gold electrode has been used to immobilize FoDH and a 500 mV decrease in oxidation overpotential of NADH on NG compared to the non-doped graphene was found.<sup>[171]</sup> The regeneration of the NAD<sup>+</sup> cofactor was thus accelerated, leading to an improved formate oxidation process with an onset potential of ca. -0.25 V vs. SCE. Additionally, a membraneless glucose/O<sub>2</sub> EBFC with a NG modified GOx-based bioanode showed an enhanced power output (85.91 μW cm<sup>-2</sup>) over a similar RGO-based EBFC (59.45 μW cm<sup>-2</sup>).<sup>[172]</sup>

Phosphorous and boron doped graphenes have been reported as promising electrode materials for supercapacitors,<sup>[173]</sup> batteries<sup>[174]</sup> and electrocatalysis,<sup>[175-176]</sup> but not widely applied in bioelectrochemistry yet. Sulfur and fluorine-doped graphenes have been studied for biomolecular sensing, holding promise for bioelectrochemistry

---

applications.<sup>[177-179]</sup> Sulfur-doped graphene, with abundant micropores and mesopores, showed high electrocatalytic activity towards the oxidation of dopamine, with high selectivity, a high sensitivity of  $3.94 \mu\text{M } \mu\text{A}^{-1}$ , and a low detection limit of  $1.5 \times 10^{-8} \text{ M}$ .<sup>[177]</sup> An electrochemical fluorine-doped RGO/GCE sensor for histamine showed a detection limit of 7 nM, because fluorine-atoms provided highly active catalytic sites and fast ET.<sup>[179]</sup> The electrocatalytic performance of controllably fluorine-doped graphene for NADH oxidation, decreasing the overpotential of NADH oxidation by 0.25 V in comparison to a bare GCE has also been investigated.<sup>[178]</sup>

#### 1.5.1.2 Graphene composites

Most bioelectrochemical applications of graphene involve functionalized graphene composites. Graphene has been functionalized to form hydrophilic/hydrophobic or positively/negatively charged groups on its surface. The formation of new bonds on the graphene layers alters their physico-chemical properties. Precise control over the functionalization reaction is therefore required. These functional groups introduced on the graphene layers are particularly important for enzyme attachment, affecting the reproducibility and performance of the resulting bioelectrodes.

Covalent bonding and noncovalent interactions are two ways to functionalize graphene. Organic covalent functionalization reactions of graphene include two general routes: (a) the transformation of  $\text{sp}^2$  carbon of pristine graphene to  $\text{sp}^3$  hybridization with free radicals or dienophiles and (b) the formation of covalent bonds between organic functional groups and the oxygenated groups of GO.<sup>[180]</sup> Organic groups can be grafted on graphene with the help of diazonium salts, nitrophenyls, peroxides and hydroxylated aryl groups etc.<sup>[133]</sup> Bari and co-workers prepared DET-type enzymatic electrodes by covalently anchoring BOx and laccase to a RGO-based GCE with the assistance of two different diazonium salts, showing high catalytic currents (up to  $1.0 \text{ mA cm}^{-2}$  under rotation).<sup>[86]</sup> Covalent functionalization changes the properties of graphene dramatically. For example, graphene sheets treated with diazonium salts showed a decrease in conductivity with increasing grafting density.<sup>[181]</sup> Similarly, the covalent attachment of nitrophenyls to pristine graphene sheets resulted in the introduction of a band gap.<sup>[182]</sup> Graphene derivatives such as GO and RGO with considerable amounts of oxygenated groups can be grafted with polymer chains with reactive species such as hydroxyls and amines. Most of these polymers, e.g., poly(ethylene glycol),<sup>[183]</sup> polylysine (PLL),<sup>[184]</sup> polyallylamine<sup>[185]</sup> and poly(vinyl alcohol),<sup>[186]</sup> are biocompatible and can also be used to immobilize proteins. For example, a PLL/RGO nanostructure with immobilized horseradish peroxidase was used as a  $\text{H}_2\text{O}_2$  biosensor, exhibiting a 2.7-fold higher reduction currents over the blank control (at  $-0.3 \text{ V vs. Ag/AgCl}$ ).<sup>[184]</sup> These composites show synergetic properties: the polymeric part leads to high dispersion of graphene, while graphene offers the electrical conductivity and reinforcement of the mechanical properties.

Noncovalent functionalization includes polymer wrapping,<sup>[187-188]</sup> adsorption of surfactants such as sodium and lithium dodecyl sulfate,<sup>[189]</sup> direct interactions with nanomaterials<sup>[27, 80, 190]</sup> or small aromatic molecules.<sup>[139]</sup> Interactions between these modifiers and graphene usually are physical interactions such as  $\pi$ - $\pi$ , van der Waals, hydrophobic interactions, and electrostatic forces. Various noncovalent modifiers such as PEI,<sup>[191]</sup> chitosan,<sup>[192]</sup> PANI,<sup>[185]</sup> methylene green (MG),<sup>[193-194]</sup> AuNPs<sup>[12, 123]</sup> and CNTs<sup>[27, 80]</sup> have further been used to modify graphene.<sup>[133, 180]</sup> Depending on the nature of the modifier, noncovalent functionalization significantly changes the dispersibility, conductivity and other properties of graphene. For instance, the use of chitosan ensured the formation of homogeneous graphene suspensions<sup>[192]</sup> and biocompatibility for enzyme immobilization.<sup>[195]</sup> Liu and co-workers<sup>[194]</sup> functionalized graphene with a water-soluble aromatic electroactive dye, MG, and MWCNT through layer-by-layer chemistry,<sup>[163]</sup> Fig. 1.9. The resulting MG functionalized graphene nanostructure on a GCE had lower charge-transfer resistances and better electrocatalytic activities towards NADH oxidation than pristine graphene, making it suitable for immobilization of NAD-dependent GDH. Some composites are based on entrapping graphene sheets within the polymer PEDOT or dispersing AuNPs on graphene for improved electrical conductivity.<sup>[196]</sup>

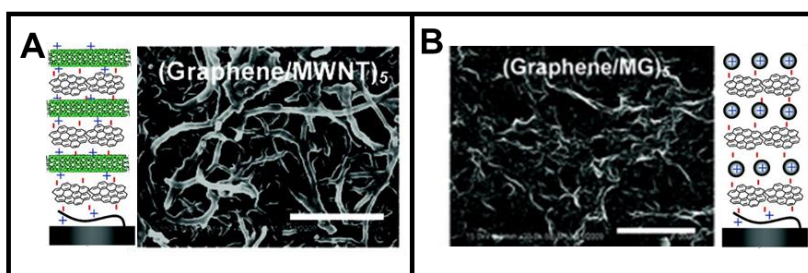


**Figure 1.9** Schematic illustration of the formation of electrochemically functional (A) (graphene/SWCNT)<sub>5</sub> and (B) (graphene/MG)<sub>n</sub>-based nanostructures through a layer-by-layer method and corresponding SEM images. 5 represents the number of graphene layer and the scale bar is 1  $\mu\text{m}$ . Reprinted with permission from ref.<sup>[163]</sup> with modification. Copyright 2011 American Chemical Society.

### 1.5.1.3 Freestanding graphene

Supportive electrodes (*e.g.*, GCE, graphite and Au electrodes) are usually needed to support graphene and its composites for enzyme immobilization. Alternatively, freestanding graphene-based electrodes are under rapid development. Graphene has been used as freestanding electrode hosts for enzyme immobilization taking advantages of its outstanding mechanical robustness, and its chemical and thermal stability. Graphene paper is one of the most promising freestanding electrodes for practical application, since it exhibits very high flexibility and stability. Shen *et al.* have engineered a graphene paper *via* a low-cost solution-processing procedure and the enzymes adsorbed on the graphene

---

exhibited high performance and stability, Fig. 1.8.<sup>[31, 139]</sup> Additionally, 3D graphene platelets and graphene gel have appeared recently. For example, Campbell and co-workers have constructed a freestanding 3D graphene/SWCNT cogel as a BOx bioelectrode.<sup>[80]</sup> The cogel electrode had a large surface area ( $\sim 800 \text{ m}^2 \text{ g}^{-1}$ ) ensuring high enzyme loading, as well as high porosity for substrate diffusion and a moderate conductivity ( $\sim 0.2 \text{ S cm}^{-1}$ ). Another type of freestanding graphene-based electrode is the CVD-derived 3D graphene foam comprising continuous conduction networks, with a large surface area ( $670 \text{ m}^2 \text{ g}^{-1}$ ) for high laccase loading, Fig. 1.8.<sup>[27, 156]</sup>

### 1.5.2 Graphene-based enzymatic biofuel cells

Due to the aforementioned properties of graphene, graphene-based EBFCs are promising with improved power output and lifetime compared to the EBFCs without graphene modifications. The development of graphene-based EBFCs over the last five years evaluated in terms of  $P_{\max}$ , OCV, and stability is summarized in Table 1.3.<sup>[2]</sup>  $P_{\max}$  is typically normalized to geometric area of the electrode, while the mass or volume of the cell has not received wide attention.<sup>[2]</sup> Stability measured in a time course of OCV is not an effective method, because the stored charges in the capacitive matrix will maintain the OCV at a high level as revealed by the recent progress on supercapacitor/EBFC hybrid devices.<sup>[2]</sup> Most graphene-based EBFCs were constructed in a similar way as CNT-based EBFCs without exploiting their full potential. Probably due to the lack of precise control over the architecture of graphene, only a few reported EBFCs using graphene can exceed a  $P_{\max}$  of  $1.0 \text{ mW cm}^{-2}$ . For example, a membrane-less NG based formic acid/ $\text{O}_2$  EBFC with a  $P_{\max}$  of  $1.96 \pm 0.13 \text{ mW cm}^{-2}$  and an OCV of  $0.95 \pm 0.05 \text{ V}$  was fabricated. Effective recycling of  $\text{NAD}^+/\text{NADH}$  cofactor was achieved at a NG/AuNPs/FoDH bioanode and NG played a key role in decreasing the NADH oxidation overpotential.<sup>[171]</sup> A detailed evaluation of graphene-based bioanodes and biocathodes for EBFCs is provided in sections 1.5.2.1 and 1.5.2.2.

**Table 1.3** Graphene based EBFCs.

| Graphene materials        | Anode                            | Cathode                          | Note            | OCV (V) | $P_{\max}$ ( $\mu\text{W cm}^{-2}$ ) | Stability  | Ref.  |
|---------------------------|----------------------------------|----------------------------------|-----------------|---------|--------------------------------------|--|-------|
| Graphene based full EBFCs |                                  |                                  |                 |         |                                      |  |       |
| Commercial graphene       | CDH/AuNPs/graphene SPEs          | Laccase/AuNPs/graphene SPEs      | Two-compartment | 0.74    | 5.16                                 | 90% decrease of $P_{\max}$ after 8 h                           | [12]  |
|                           | DET                              | DET                              |                 |         |                                      |  |       |
|                           | 5 mM glucose, 150 mM NaCl        | Air-saturated                    |                 |         |                                      |  |       |
| Commercial graphene       | GOx/graphene-carboxylated PSS/Au | BOx/graphene-carboxylated PSS/Au | One-compartment | 0.72    | 20                                   | -  | [187] |
|                           | DET                              | DET                              |                 |         |                                      |  |       |
|                           | 300 mM glucose                   | Air-equilibrated                 |                 |         |                                      |  |       |
| Graphene                  | GOx/graphene-3D micropillar      | Laccase/graphene-3D micropillar  | One-compartment | 0.91    | 136                                  | 49% decrease of $P_{\max}$ for the 2nd measurement after 7 day | [197] |
|                           | DET                              | DET                              |                 |         |                                      |  |       |
|                           | 100 mM glucose                   | Air-saturated                    |                 |         |                                      |  |       |
| RGO; chemical method      | GOx/RGO-CoPc/GCE                 | RGO-FePc/GCE                     | One-compartment | 0.35    | 23                                   | 80% retain of $P_{\max}$ after one month                       | [198] |
|                           | DET                              | -                                |                 |         |                                      |  |       |
|                           | 15 mM glucose                    | Air-equilibrated                 |                 |         |                                      |  |       |

*SPEs: screen-printed electrodes; PSS: poly(styrene-*b*-isoprene-*b*-styrene); CoPc: cobalt phthalocyanine; FePc: iron phthalocyanine.*

**Table 1.3** Continued.

| Graphene materials  | Anode                                       | Cathode  | Note            | OCV (V)         | $P_{\max}$ ( $\mu\text{W cm}^{-2}$ ) | Stability                                  | Ref.  |
|---|---|--|-----------------|-----------------|--------------------------------------|--|-------|
| Graphene based full EBFCs   |   |  |                 |                 |                                      |  |       |
| RGO;<br>chemical method   | GOx/RGO-SWCNT aerogels                      | BOx/RGO-SWCNT aerogels                           | One-compartment | 0.61            | 190                                  | ~20% retain of $P_{\max}$ after 15 h       | [80]  |
|   | DET   | DET  |                 |                 |                                      |  |       |
|   | 100 mM glucose; stirring                    | Air-saturated                                    |                 |                 |                                      |  |       |
| RGO;<br>chemical method   | MWCNT-GOx-Nafion/RGO                        | BOx/PBSE/RGO                                     | One-compartment | -               | 70                                   | -  | [199] |
|   | DET   | DET  |                 |                 |                                      |  |       |
|   | 50 mM glucose                               | Air-saturated                                    |                 |                 |                                      |  |       |
| Graphene nanosheets;<br>electrochemically produced <i>in situ</i> | GDH/SiO <sub>2</sub> NPs/PEI/MB/graphene CP | GOx/SiO <sub>2</sub> NPs/hemin/graphene CP       | One-compartment | 0.50;<br>(0.53) | 18; (4)                              | -; (decreased by less than 15% after 12 h) | [200] |
|   | MET, 0.02 mM NAD <sup>+</sup>               | DET  |                 |                 |                                      |  |       |
|   | 5 mM glucose; (human serum solution)        | O <sub>2</sub> -equilibrated; (air-equilibrated) |                 |                 |                                      |  |       |
| Graphene nanosheets;<br>electrochemically produced <i>in situ</i> | LDH/SiO <sub>2</sub> NPs/PEI/MB/graphene CP | LOx/SiO <sub>2</sub> NPs/hemin/graphene CP       | One-compartment | 0.87;<br>(0.79) | 380;<br>(225)                        | -  | [16]  |
|   | MET, 2 mM NAD <sup>+</sup>                  | DET  |                 |                 |                                      |  |       |
|   | 14 mM lactate; (real sweat)                 | Air-equilibrated                                 |                 |                 |                                      |  |       |

*PBSE: 1-pyrenebutanoic acid succinimidyl ester; MB: Meldola blue.*

**Table 1.3** Continued.

| Graphene materials  | Anode  | Cathode                    | Note            | OCV (V) | $P_{\max}$ ( $\mu\text{W cm}^{-2}$ ) | Stability   | Ref.  |
|---|--|----------------------------|-----------------|---------|--------------------------------------|---|-------|
| Graphene based full EBFCs   |  |                            |                 |         |                                      |   |       |
| Graphene nanosheets; electrochemically produced <i>in situ</i>      | PQQ-GDH-CaM/PBSE/graphene CP                         | GOx/hemin/ graphene CP     | One-compartment | ~0.50   | ~70                                  | -   | [201] |
|   | DET  | DET                        |                 |         |                                      |   |       |
|   | 20 mM glucose, 100 mM $\text{Ca}^{2+}$ , 100 mM NaCl | Air-equilibrated           |                 |         |                                      |   |       |
| Graphene nanosheets; electrochemically produced <i>in situ</i>      | PQQ-GDH/PBSE/graphene CP                             | Laccase/PBSE/graphene CP   | One-compartment | 0.41    | 5.5                                  | -   | [202] |
|   | DET  | DET                        |                 |         |                                      |   |       |
|   | 20 mM glucose  | Air-equilibrated           |                 |         |                                      |   |       |
| NG; chemically produced   | FoDH/AuNPs/NG/Au                                     | Laccase/AuNPs/NG/Au        | One-compartment | 0.95    | 1960                                 | -   | [171] |
|   | MET, 5 mM $\text{NAD}^{+}$                           | MET, 0.5 mM ABTS           |                 |         |                                      |   |       |
|   | 50 mM formic acid                                    | $\text{O}_2$ -equilibrated |                 |         |                                      |   |       |
| Graphene paper; assembly of GO sheet followed by chemical reduction | PQQ-GDH/MB/graphene paper                            | BOx/graphene paper         | One-compartment | 0.67    | 4.0                                  | 35% and 55% retain of $P_{\max}$ after 100 min under static or stirring, respectively | [139] |
|   | MET  | DET                        |                 |         |                                      |   |       |
|   | 6.4 mM glucose                                       | Air-equilibrated           |                 |         |                                      |   |       |

*CaM: calmodulin chimera.*

**Table 1.3** Continued.

| Graphene materials  | Anode                                       | Cathode                                      | Note            | OCV (V) | $P_{\max}$ ( $\mu\text{W cm}^{-2}$ ) | Stability  | Ref.  |
|---|---|--|-----------------|---------|--------------------------------------|--|-------|
| Graphene based full EBFCs                                     |   |  |                 |         |                                      |  |       |
| Graphene paper; assembly of GO followed by chemical reduction | PQQ-GDH/cytochrome <i>c</i> /graphene paper | BOx/cytochrome <i>c</i> /graphene paper      | One-compartment | 0.38    | 0.29                                 | -  | [31]  |
|   | MET   | DET  |                 |         |                                      |  |       |
|   | 3 mM glucose                                | Air-equilibrated                             |                 |         |                                      |  |       |
| Graphene-CFC; CVD method                                      | GOx/Fc/graphene-CFC                         | BOx/graphene-CFC                             | One-compartment | ~0.63   | 34.3                                 | $P_{\max}$ higher than 5 $\mu\text{W cm}^{-2}$ after 24 h function | [203] |
|   | MET   | DET  |                 |         |                                      |  |       |
|   | 200 mM glucose                              | Air-equilibrated                             |                 |         |                                      |  |       |
| 3D graphene; Ni <sup>2+</sup> -exchange/KOH activation method | Nafion/GOx/Fc/3D-graphene/GCE               | Nafion/Laccase/3D-graphene-PTCA-dopamine/GCE | One-compartment | 0.40    | 112                                  | ~84% retain of initial current after 72-h continuous discharging   | [155] |
|   | MET   | MET  |                 |         |                                      |  |       |
|   | 10 mM glucose                               | O <sub>2</sub> -equilibrated                 |                 |         |                                      |  |       |

*CFC: carbon fiber cloth; Fc: ferrocene; PTCA: 3,4,9,10-perylene tetracarboxylic acid.*

**Table 1.3** Continued.

| Graphene materials                | Anode  | Cathode                                     | Note                | OCV (V) | $P_{\max}$ ( $\mu\text{W cm}^{-2}$ ) | Stability   | Ref.  |
|-----------------------------------|--|---|---------------------|---------|--------------------------------------|---|-------|
| Graphene based bioanode for EBFCs |  |   |                     |         |                                      |   |       |
| GO nanosheets;<br>chemical method | GDH-BSA/GDH/NAD <sup>+</sup> /GO<br>nanosheets/GCE | Polydopamine/Lacase<br>nanoflowers/AuNPs/Au | One-<br>compartment | 0.86    | 400                                  | -   | [204] |
|                                   | MET  | MET   |                     |         |                                      |   |       |
|                                   | 10 mM glucose                                      | Air-saturated                               |                     |         |                                      |   |       |
| RGO;<br>CVD method                | GOx/TTF/RGO/AuNPs/N-<br>doped CNTs/Ni foam         | Pt  | One-<br>compartment | 0.32    | 235                                  | $j_{\max}$ on the anode<br>at 0.25 V retained<br>above 60% after 15<br>days | [123] |
|                                   | MET  | -   |                     |         |                                      |   |       |
|                                   | 60 mM glucose                                      | Air-equilibrated                            |                     |         |                                      |   |       |
| NG;<br>CVD method                 | GOx/Fc-C <sub>6</sub> -LPEI/NG/CP                  | BOx/An-MWCNT/TBAB-<br>Nafion/CP             | One-<br>compartment | 0.55    | 355                                  | -   | [172] |
|                                   | MET  | MET   |                     |         |                                      |   |       |
|                                   | 100 mM glucose                                     | O <sub>2</sub> -equilibrated                |                     |         |                                      |   |       |

*BSA: bovine serum albumin; TTF: tetrathiafulvalene; Fc-C<sub>6</sub>-LPEI: hexylferrocenyl linear polyethylenimine; An-MWCNT: anthracene-modified MWCNT; TBAB: tetrabutylammonium bromide.*

### 1.5.2.1 Graphene based bioanodes

Various graphene materials have been applied in GOx bioanode fabrication for glucose/O<sub>2</sub> EBFCs, including chemically produced 2D graphene sheets,<sup>[80, 198]</sup> graphene papers,<sup>[31, 139]</sup> NG sheets,<sup>[172]</sup> 3D graphene.<sup>[197]</sup> Glucose/O<sub>2</sub> EBFCs functionalized with 3D graphene showed high power outputs ( $P_{\max}$  ranging from 112 to 136  $\mu\text{W cm}^{-2}$ ), Table 1.3. Furthermore, a commercial GOx showing broader substrate response than most other common bioanode enzymes can oxidize a range of mono-, di-, tri-, and polysaccharides.<sup>[11]</sup> Other enzymes such as GDH<sup>[139]</sup> and CDH<sup>[12]</sup> have also been successfully used as the biocatalysts for glucose oxidation at the graphene-based bioanode. Due to the insensitivity to O<sub>2</sub>, dehydrogenases can perform in a one-compartment cell where the O<sub>2</sub> reduction takes place at the biocathode surface. For instance, PQQ dependent GDH modified 2D graphene paper showed good electrocatalytic activity in air-saturated electrolytes.<sup>[139]</sup> The resulting bioanode was assembled with a BOx graphene-based cathode into a one-compartment EBFC, displaying an acceptable power output in an air-saturated phosphate buffer containing 6.4 mM glucose, with an OCV of 0.665 V and a  $P_{\max}$  of ca. 4.0  $\mu\text{W cm}^{-2}$ .

Although most graphene based EBFCs have utilized glucose as the fuel, other fuels need to be investigated. Lactate, with a concentration of up to 60 mM in sweat,<sup>[205]</sup> has been catalytically oxidized on graphene-based bioanodes, allowing wearable lactate/O<sub>2</sub> EBFCs<sup>[16, 25, 206]</sup> externally located on skin instead of surgically implanted devices located inside a body. Koushanpour *et al.* constructed a graphene-based lactate/H<sub>2</sub>O<sub>2</sub> EBFC using a lactate dehydrogenase (LDH) bioanode and a LOx/hemin biocathode, Fig. 1.10.<sup>[16]</sup> An electrode functionalized with graphene nano-sheets was achieved by *in situ* electrochemically produced graphene flakes on the carbon fiber, resulting in an EBFC registering a  $P_{\max}$  of 380 and 225  $\mu\text{W cm}^{-2}$  operated in mimicked human sweat (14 mM lactate) and real human sweat, respectively.

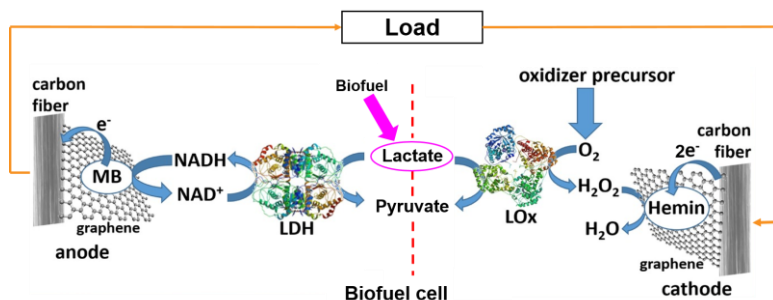


**Figure 1.10** A scheme of the lactate/H<sub>2</sub>O<sub>2</sub> graphene-based biofuel cell. NADH and H<sub>2</sub>O<sub>2</sub> formed by the enzymes are consumed through electrocatalytic reactions by Meldola's blue (MB) and hemin, respectively. Reprinted with permission from ref.<sup>[16]</sup>. Copyright 2017 John Wiley and Sons.

---

### 1.5.2.2 Graphene-based biocathodes

Laccase and BOx have been widely utilized at biocathodes to catalyze the four-electron reduction of dioxygen to water.<sup>[27, 39, 78]</sup> The performance of these biocathodes can be improved when immobilized on different graphene architectures. An electrochemically produced graphene-based laccase biocathode reached a DET catalytic current density plateau of  $1.0 \text{ mA cm}^{-2}$  under rotation at 1500 rpm.<sup>[86]</sup> Graphene sheet composites are the most studied substrates for enzyme immobilization compared to other graphene materials. For EBFC applications, laccase on NG-AuNPs, and graphene-3D micropillars have been reported for MET ( $P_{\text{max}}: 1,960 \text{ } \mu\text{W cm}^{-2}$ ),<sup>[171]</sup> and DET-type biocathodes ( $P_{\text{max}}: 136 \text{ } \mu\text{W cm}^{-2}$ ),<sup>[197]</sup> respectively. Most BOx biocathodes used in EBFCs can directly receive electrons from the electrode surface, such as BOx is physically adsorbed on RGO-SWCNT aerogels and assembled in an EBFC ( $P_{\text{max}}: 190 \text{ } \mu\text{W cm}^{-2}$ ) together with a GOx bioanode.<sup>[80]</sup> Hierarchical 3D graphene-based structures are also promising supports for laccase and BOx immobilization due to their high surface area. Recently, laccase was immobilized on 3D graphene networks produced with a  $\text{Ni}^{2+}$ -exchange/KOH activation combination method. With the help of an immobilized mediator (dopamine), this biocathode was coupled to a GOx bioanode in a glucose/ $\text{O}_2$  EBFC leading to a  $P_{\text{max}}$  of  $112 \text{ } \mu\text{W cm}^{-2}$ .<sup>[155]</sup> BOx immobilized on flexible 3D graphene coated fiber cloth was applied in a glucose EBFC with a GOx bioanode, resulting in a  $P_{\text{max}}$  of  $34.4 \text{ } \mu\text{W cm}^{-2}$  at  $0.43 \text{ V}$ .<sup>[203]</sup>

Besides  $\text{O}_2$ , *in-situ* generated  $\text{H}_2\text{O}_2$  can be reduced at the biocathode through catalytic reactions. Koushanpour *et al.* fabricated FAD-dependent oxidases, *i.e.*, GOx<sup>[200-201]</sup> and LOx,<sup>[16]</sup> on hemin modified graphene CP biocathodes. GOx and LOx produce  $\text{H}_2\text{O}_2$  during the catalyzed oxidation of glucose and lactate, respectively, in the presence of oxygen. The immobilized hemin can then electrocatalytically reduce the generated  $\text{H}_2\text{O}_2$  by accepting electrons from the CP electrode, Fig. 1.9. These GOx and LOx immobilized hemin/graphene CP biocathodes can be incorporated in an EBFC with a GDH and LDH bioanode, respectively. Although a small number of high-performance graphene-based EBFCs ( $P_{\text{max}} > 1.0 \text{ mW cm}^{-2}$ ) has been reported, the half-lifetime of the EBFCs ranges from several hours to days, Table 1.3. Stability is therefore the main issue for EBFC applications resulting from the fragile enzymes and so far not fully developed immobilization techniques for graphene-based electrodes. Improvement of the performance of graphene-based bioanodes and biocathodes especially the long-term stability is thus an essential step for development of EBFCs. Two perspectives of graphene-based EBFCs can here be proposed. (1) Graphene quantum dots (GQDs) may be a suitable platform for enzyme immobilization because the carboxylic acid moieties at the edge of GQD are easy to functionalize with various groups.<sup>[207]</sup> (2) The interconnected porous structures of 3D graphene-based electrodes must be precisely controlled because these meso- and micro- pores are beneficial for enzyme accommodation and substrate diffusion, respectively.

---

## 1.6 Perspectives of enzymatic biofuel cells

### 1.6.1 Application of EBFCs

Unlike MBFCs as large-scale biological reactors, EBFCs are mostly considered as micro-power sources for miniature biodevices.<sup>[36, 92]</sup> The first miniature membrane-less EBFC, consisting of two carbon fibers (diameter 7.0  $\mu\text{m}$ , length: 2.0 cm) respectively coated with GOx and an Os-redox polymer at the anode and laccase and a second Os-redox polymer at the cathode, was reported by Heller et al.<sup>[208]</sup> The  $P_{\text{max}}$  reached 137  $\mu\text{W cm}^{-2}$  at 0.4 V in a pH 5 aqueous solution containing 15 mM glucose at 37  $^{\circ}\text{C}$ . Soon after, a similar miniature EBFC operated successfully in a physiological buffer.<sup>[36]</sup> Ever since, the number of EBFCs operating in bodily fluids have been growing exponentially due to the promising application under these conditions.

As a proof of concept of possible implantation in media containing glucose and  $\text{O}_2$ , EBFCs have been first inserted in a grape.<sup>[30]</sup> In this study, the glucose/ $\text{O}_2$  EBFC consisting of a GOx anode and a BOx cathode within the grape could generate a  $P_{\text{max}}$  of 2.4  $\mu\text{W cm}^{-2}$  at 0.52 V. Until now, EBFCs have been successfully implanted in other fruits (*e.g.*, oranges and apples)<sup>[117]</sup> and animals (*e.g.*, rats,<sup>[28]</sup> rabbits<sup>[209]</sup> and snails<sup>[210]</sup>). Although there have been numerous examples of EBFCs operating in bovine or human serum, experiments in human blood have been rare.<sup>[211]</sup> Cadet *et al.* reported the highest  $P_{\text{max}}$  to date (129  $\mu\text{W cm}^{-2}$  at 0.38 V) of an EBFC in undiluted blood containing 8.2 mM glucose.<sup>[212]</sup> The first *ex vivo* evaluation of an EBFC in human blood was reported in 2016 and demonstrated that a biocompatible and safe bio-device could be implanted in superficial human veins.<sup>[213]</sup> The first real *in vivo* experiment has yet to be done due to considerations such as biocompatibility and cytotoxicity. In addition, EBFCs have also been operated in other human fluids such as saliva,<sup>[214]</sup> urine,<sup>[214]</sup> or tears.<sup>[42]</sup>

Considering the general properties such as low current/power density and miniature size, another application of EBFCs as portable power sources is to power electronic devices such as light-emitting diodes (LEDs) and music devices.<sup>[2]</sup> There are many demonstrations of EBFCs as portable power sources for LEDs or for digital clocks.<sup>[27, 215]</sup> *Akerman Inc.* has demonstrated that an EtOH/air EBFC stack could power an iPod.<sup>[26, 216]</sup> Moreover, *Sony Corporation* demonstrated that a stack of glucose/ $\text{O}_2$  EBFCs ( $1.45 \pm 0.24$  mW  $\text{cm}^{-2}$  at 0.3 V for single EBFC) could power a music device in 2007,<sup>[2]</sup> and the operation of radio-controlled car in 2009, Fig. 1.11.<sup>[217]</sup>

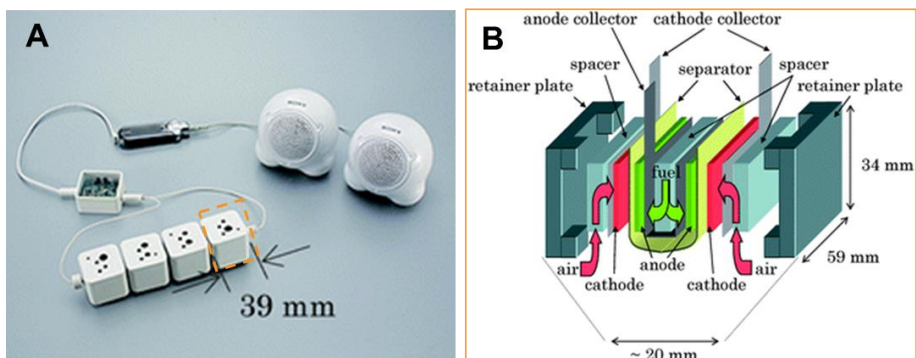


**Figure 1.11** (A) Digital images of a stack of glucose/O<sub>2</sub> EBFCs as power sources to operate a music device together with a pair of passive-type speakers. (B) Schematic view of a multi-stacked biofuel cell unit composed of two biofuel cells connected in parallel. Reprinted with permission from ref.<sup>[217]</sup>. Copyright 2009 Royal Society of Chemistry.

Wearable electronics and especially wearable electrochemical sensors have attracted much attention recently. Wearable biodevices should be flexible and biocompatible with human skin or eyes.<sup>[211]</sup> The first EBFC with a bioanode and a Pt cathode attached to human skin could harvest biochemical energy from lactate generated by human perspiration.<sup>[44]</sup> Power densities during non-invasive on-body studies ranged from 5 to 70  $\mu\text{W cm}^{-2}$ , holding considerable promise as a facile autonomous power source for wearable electronics. An EBFC with a FDH anode and a BO<sub>x</sub> cathode immobilized on skin was developed for transdermal iontophoresis, registering an OCV of 0.75 V and a maximum current density 300  $\mu\text{A cm}^{-2}$ .<sup>[218]</sup>

These implantable, portable or wearable EBFCs can further be used as self-powered sensing bio-devices. This kind of sensing device does not need an external power source since the target of the sensor also acts as the fuel in the EBFC, and the power output is usually proportional to the concentration of the analyzed substrate. In 2001, Katz and Willner invented the first self-powered system as a biosensor for glucose determination using an EBFC with a GO<sub>x</sub> anode and a O<sub>2</sub>-reducing cathode.<sup>[219]</sup> Furthermore, EBFCs have also been used for self-powered immune sensors,<sup>[219]</sup> lactate<sup>[17]</sup> and antibiotic<sup>[220]</sup> sensors.

### 1.6.2 Challenges and perspectives

Significant progress has been made in the field of EBFCs, but several issues still need to be addressed for successful commercialization. Advances in terms of increased OCV, current density or power density should be developed in two major directions: (1) to improve the electrical connection between enzymes and the electrode surface by electrode modifications, irrespective of MET or DET, and (2) to increase the enzyme loadings on

---

sophisticated nanostructured porous electrodes with appropriate modification techniques. An inspiring advance is that multi-enzyme anodes in EBFCs can completely oxidize fuels.<sup>[41, 221-222]</sup> How to control the diffusion and transport of reactants and cascade intermediates to enhance overall biochemical energy conversion is a huge challenge.<sup>[223]</sup> Stability of EBFCs is another inevitable obstacle that needs be addressed. The combination of biotechnology strategies, such as enzyme engineering, and materials engineering could improve the stability of enzymes and the chemical microenvironment for enzymes at electrode surfaces. However, these strategies for enzyme stabilization frequently result in lower catalytic activity.<sup>[65]</sup> The mutual restriction between stabilization and catalytic activity in enzyme immobilization is thus still problematic.

The studies discussed showing EBFCs successfully applied in *ex vivo* human blood set fundamental milestones. Meanwhile, new challenges such as biocompatibility and cytotoxicity issues, have arisen.<sup>[211]</sup> To minimize the foreign body reaction, biocompatible materials in EBFC assemblies, for instance protective coatings or membranes, will be required. Different configurations of EBFCs such as biosupercapacitors,<sup>[220, 224-225]</sup> solar biosupercapacitors<sup>[46]</sup> and single-enzyme biofuel cells,<sup>[48]</sup> also have attracted much attention. These new concepts will represent a paradigm shift in EBFC design for environmental applications including energy storage and carbon capture.

## 1.7 Conclusions

In this chapter, we have introduced the fundamentals of EBFCs and summarized current research progress in graphene-based EBFCs. In particular, we described graphene-based electrodes for enzyme immobilization, including electrodes modified with graphene derivatives and graphene composites, as well as freestanding graphene electrodes. The introduction of graphene can improve the performance of EBFCs due to its properties such as high conductivity, mechanical flexibility, large surface area, though the stability and power output remains significantly lower than that of conventional FCs. To make high-performance graphene-based EBFCs, the precise control of electrode materials synthesis (such as the functional surface groups and hierarchical structures) and enzymes immobilization on electrode surfaces, as well as enzyme engineering, need to be further explored.

# Chapter 2

## Methodology

---

---

This chapter is an overview of techniques used for the Ph.D. project. Fundamental principles of techniques employed are described to support the discussions in the following chapters. Methodology is divided into three segments: microscopic, spectroscopic, and electrochemical techniques.

---

### 2.1 Microscopic techniques

#### 2.1.1 Atomic force microscopy

Atomic-force microscopy (AFM) is a high-resolution type (in principle down to the atomic level) of scanning probe microscopy. An Agilent Technologies 5500 AFM was used to characterize the surface morphology of the materials. The AFM principle is based on a cantilever/tip assembly (the probe) that interacts with the sample surface through a raster scanning motion, Fig. 2.1.<sup>[226-227]</sup> The up/down and side to side motion of the AFM cantilever as it scans along the sample surface is monitored through a laser beam reflected by the cantilever. A position sensitive photodiode detector tracks the reflected laser beam. The morphology of the sample surface can therefore be imaged by recording the signal from the photodetector. AFM can also record other sample features such as elastic properties and force-distance correlations.

AFM can be conducted in either tapping or contact mode. Tapping is gentler to the sample surface than contact mode and was therefore used in this project. The specific type of tapping mode used on the 5500 AFM is called acoustic alternating contact (AAC) mode. In this mode, the cantilever is brought to vibrate close to its resonant frequency near the sample surface. Due to the tip-surface interaction, the frequency, amplitude and phase of the oscillating signal on the photodetector change with the cantilever sample distance  $d$ . The amplitude can be used as a feedback channel, in order to image with a constant tapping force. At a certain amplitude set-point, for example, the feedback loop will adjust the tip-sample distance to keep the amplitude constant. The cantilever sample distance

is recorded as a function of the lateral position of the tip with respect to the sample, and the scanned height essentially represents the surface topography.

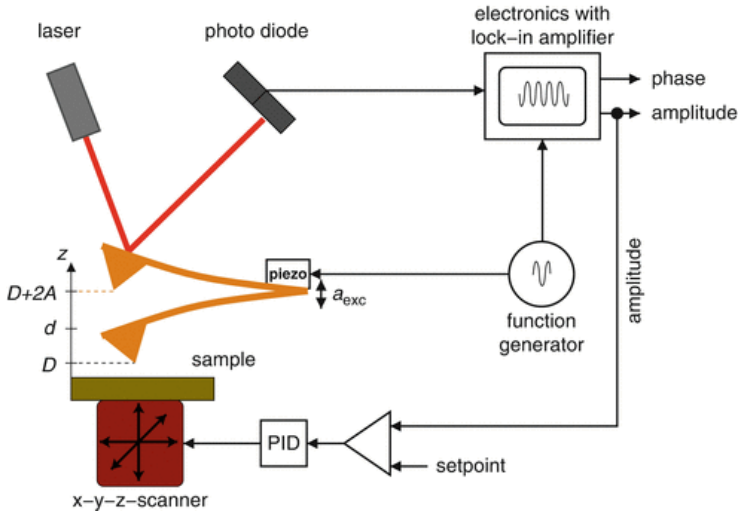


**Figure 2.1** Scheme of the experiment setup of an AFM in the ACC mode.<sup>[227]</sup>

### 2.1.2 Scanning electron microscopy

In a scanning electron microscope (SEM), a sample is scanned with a focused electron beam to generate images. The SEM, used in this project for morphology and nanostructure characterization of samples, was a Quanta FEG 200 ESEM with the Everhart-Thornley Detector (ETD) from FEI. Fig. 2.2 shows the working principle of a SEM.<sup>[228]</sup> An electron gun located at the top of the column emits electrons. Under the action of an accelerating voltage, the generated electrons are converged while passing through the condenser lens and the objective lens, forming an electron beam with a diameter of just a few nanometers on the specimen. Three basic types of electron signals, including back scatter electrons, secondary electrons, and X-rays, are generated by the beam-specimen interaction processes when the electron beam hits the specimen surface. While the electron beam raster scans over the specimen surface, the electron signals are collected by the detector, and counts are converted into brightness of the corresponding points of the image. The corresponding electron image is recorded and displayed on a video screen.

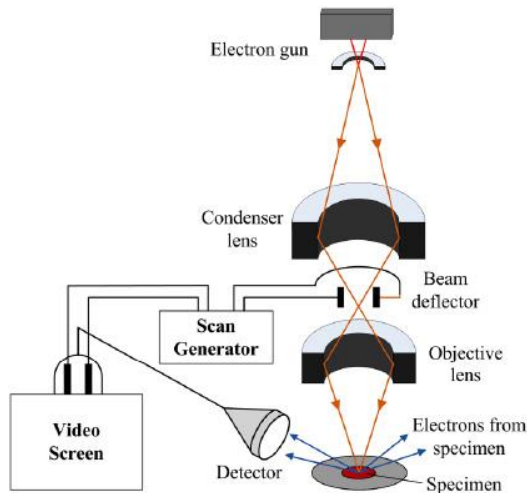


**Figure 2.2** Schematic representation of the SEM working principle.<sup>[228-229]</sup>

## 2.2 Spectroscopic techniques

### 2.2.1 Ultraviolet-visible spectroscopy

Ultraviolet-visible spectroscopy or ultraviolet-visible spectrophotometry (UV-vis) is a technique in which light absorption by solution, transparent solids and gaseous samples is measured in the visible and adjacent (near-UV and near-infrared) electromagnetic spectrum. A scheme of the basic working principle of a UV-vis spectrophotometer is shown in Fig. 2.3. Depending on the monochromator, light with fixed wavelength ( $\lambda$ ) or the entire spectrum of visible light can be generated to illuminate the sample. The UV-vis spectrophotometer compares the light intensity before ( $I_0$ ) and after ( $I$ ) passing through the sample. Transmittance, the ratio between these two signals ( $I/I_0$ ), and absorbance have a relationship described by Lambert-Beer's law:<sup>[230]</sup>

$$A = -\log\left(\frac{I}{I_0}\right) = \varepsilon \cdot l \cdot c \quad (2.1)$$

where  $\varepsilon$  is the molar absorptivity in  $\text{M}^{-1} \text{cm}^{-1}$ ,  $l$  is the light path length (dimension of the cuvette containing the sample) in cm and  $c$  is the analyte concentration in  $\text{mol L}^{-1}$ .<sup>[230]</sup> When the analyte is excited by a light source, specific wavelengths are absorbed while the rest are transmitted and recorded by the detector. Absorbance, converting from transmittance through Eq. 2.1, is often presented as a function of wavelength. The peaks in a UV-vis spectrum, representing the wavelength dependence of the absorbance, are specific to the analyzed species and can therefore be used to distinguish different chemicals.

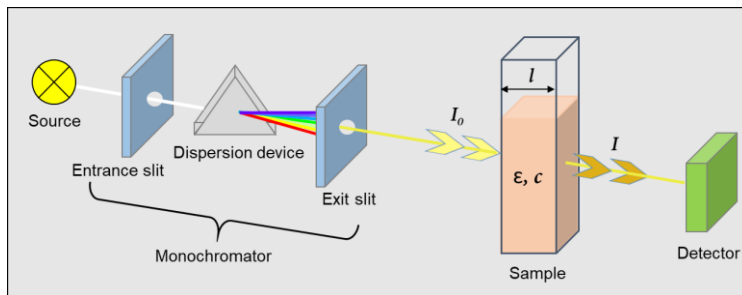


**Figure 2.3** Scheme of UV-vis absorption measurement principle.

The analyte concentration can be determined based on the absorbance ( $A$ ) according to Eq. 2.1, providing that the  $\epsilon$  for the composition of the sample and the light path distance  $d$  are known. However, the Lambert-Beer's law has its limitation especially for high analyte concentrations, since deviations of  $\epsilon$  occur due to interactions between molecules in close proximity.<sup>[231]</sup> To avoid these limitations, proper sample dilution and calibration are required.

In this Ph.D. project, the UV-vis spectra of graphene-based materials dispersed in water were obtained by an Agilent 8453 UV-vis spectrophotometer. GO, the graphene precursor, possesses two distinguishable absorption peaks, the main peak at 231 nm, originating from  $\pi$ - $\pi^*$  bonds in  $sp^2$  hybrid regions, and the other peak at  $\sim 303$  nm due to  $\sigma$ - $\pi^*$  bonds from  $sp^3$  hybridized orbitals.<sup>[232]</sup> Upon full reduction of GO, graphene exhibits observable changes in the absorption spectrum with a red-shift of the  $sp^2$  hybrid orbitals to 270 nm.<sup>[233]</sup>

Enzyme activities were determined using a UV-vis spectrophotometric assay (UV-2401PC, SHIMADZU). The basic principle of enzyme assay is to measure either the consumption of substrate or production of product over time, Eq. 2.2. The commonly used unit for enzyme activity is U (micromoles of substrate converted per min). In the assay process, the course of the enzyme-substrate reaction is followed by measuring the absorbance change, corresponding to a change in analyte concentration in solution based on Eq. 2.1 and 2.3.

$$\text{Enzyme activity (micromoles of substrate converted per minute)} = \frac{\Delta c}{\Delta t} \times V_r \quad (2.2)$$

$$\frac{\Delta c}{\Delta t} = \frac{\Delta A}{\Delta t} \times \frac{1}{\epsilon \cdot l} \quad (2.3)$$

where  $\frac{\Delta A}{\Delta t}$  and  $\frac{\Delta c}{\Delta t}$  are the value of the change of absorbance and concentration ( $\text{mmol L}^{-1}$ ) per minute, respectively, at the specific wavelength of consumed substrate or produced product.  $V_r$  is the reaction volume in mL.  $\epsilon$  in  $\text{mM}^{-1} \text{cm}^{-1}$  and  $l$  in cm have the same meanings as in Eq. 2.1.

---

### 2.2.2 X-ray photoelectron spectroscopy

The elemental composition of graphene modified electrodes was analyzed by a Thermo Scientific X-ray photoelectron spectroscopy (XPS) system with Avantage as the operating and analysis software. XPS as a quantitative, surface-sensitive spectroscopic technique can be used to measure elemental compositions, empirical formulae, chemical state and electronic states of the elements within a material. The sample is submitted to X-ray irradiation by a high-energy source, where the photoelectrons produced from only 1-10 nm under the surface can escape, permitting the surface analysis, Fig. 2.4.<sup>[234]</sup> When an irradiated atom absorbs the X-rays, it will produce electrons with binding energies lower than the photon (X-ray) energy including K-shell electrons with a kinetic energy. The kinetic energy is related to the energy of the incident beam ( $h\nu$ ), the electron binding energy (BE) and the work function ( $\phi$ ) of the spectrometer. The XPS detector counts the number of electrons with the same BE that is proportional to the number of corresponding atoms in the sample. This enables determining the atomic percentage of different elements in the sample. The standard detection limit range is about 100 ppm for nearly all elements (except hydrogen). In this Ph.D. project, XPS is employed to characterize elemental composition and functionalization of graphene-based electrode materials based on the intensities obtained at specific binding energies.

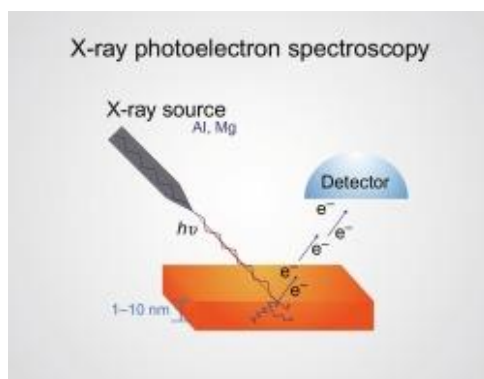


**Figure 2.4** Scheme of the measurement principle XPS.<sup>[234]</sup>

### 2.2.3 Raman spectroscopy

Raman spectra of graphene-based electrode materials were recorded by a Renishaw InVia Raman spectrometer using a 633 nm laser source. Raman spectroscopy is commonly used to provide structural fingerprints based on inelastic light scattering (*i.e.* Raman scattering) that enable the identification of organic molecules and inorganic phases. The sample is excited by an intense and monochromatic light, usually from a laser in the visible, near infrared, or near ultraviolet range. The scattered light contains photons with different frequencies (*i.e.*, the excitation frequency  $\nu_0$ , Stokes shifted frequency  $\nu_0 - \nu_{\text{vib}}$

and Anti-Stokes shifted frequency  $\nu_0 + \nu_{\text{vib}}$  are collected by a detector, Fig. 2.5.<sup>[235]</sup> The difference ( $\nu_{\text{vib}}$ ) between the shifted and excitation frequency equals the frequency of the irradiated molecular or crystal-lattice vibration.

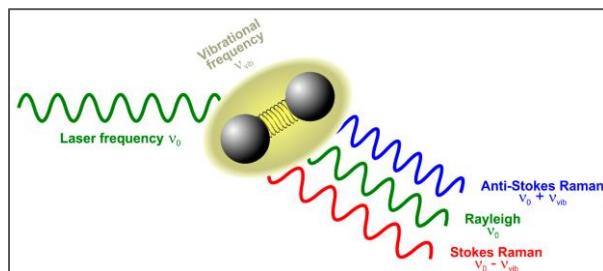


**Figure 2.5** Basic concept of elastic (Rayleigh) and inelastic (Raman) scattering of light when irradiated on molecules or crystals.<sup>[235]</sup> A monochromatic laser beam with a frequency  $\nu_0$  excites a characteristic vibration of a chemical compound having the frequency  $\nu_{\text{vib}}$ . The light can be either Rayleigh scattered resulting in light of the same frequency  $\nu_0$ , or Raman scattered yielding either Stokes ( $\nu_0 - \nu_{\text{vib}}$ ) or Anti-Stokes shifted ( $\nu_0 + \nu_{\text{vib}}$ ) photons.

### 2.2.4 Energy-dispersive X-ray spectroscopy

Energy-dispersive X-ray spectroscopy (EDS) is an analytical technique for the elemental analysis and chemical characterization of a sample. The main principle of EDS is that each element has a unique atomic structure therefore allowing a unique set of peaks in its electromagnetic emission spectrum. After bombarding a sample with high-energy electrons within an electron microscope, the generated X-rays from the sample can be detected with an energy-dispersive spectrometer that distinguishes element-specific X-ray energies. Because the amount of X-rays emitted by each element in the sample is proportional to the density of the element as a mass or atomic fraction, EDS is particularly suitable for elemental percentage determination. In addition, combining computer-assisted imaging and X-ray spectroscopy, the local elemental distribution can be obtained through a process of X-ray mapping, which is a full qualitative and quantitative analysis of a studied sample.<sup>[236]</sup> In this Ph.D. study, EDS-mapping technique was used together with SEM imaging in order to identify the elemental distribution of the graphene-based electrode materials.

## 2.3 Electrochemical techniques

In order to study the electrochemical process such as ET and heterogeneous catalyzed redox reactions on an electrode surface, different electroanalytical techniques presented below were utilized. Potentiostats including an Autolab (PGSTAT12 or PGSTAT30) or a

CHI 650B electrochemical workstation were used to characterize the electrochemical process.

### 2.3.1 Cyclic voltammetry

Cyclic voltammetry (CV) is a widely applied electrochemical technique used to investigate the kinetics and reversibility of an electrochemical redox reaction, as well as the electrochemical properties of molecules in solution. This involves sweeping the electrode potential from  $E_1$  to  $E_2$  and then reversing back to  $E_1$  at a certain scan rate. The sweep potential can then be terminated, again reversed or alternatively continued to a different value  $E_3$ , Fig. 2.6A. The CV curve is the current response at the electrode versus the applied potential, Fig. 2.6B. A positive wave represents an oxidation reaction on the working electrode (WE), and its parameters include anodic peak current ( $I_p^a$ ), anodic peak potential ( $E_p^a$ ). The negative wave corresponding to a reduction process in the system can be characterized by parameters such as cathodic peak current ( $I_p^c$ ) and cathodic peak potential ( $E_p^c$ ). CV can, therefore, disclose useful information about redox potentials and electrochemical reaction rates, diffusion coefficients of redox molecules if in solution, etc. A three-electrode system is mostly employed, with a WE as the studied electrode, a reference electrode (RE) against which the WE potential is controlled, and a counter electrode (CE) closing the current circuit in the electrochemical cell.

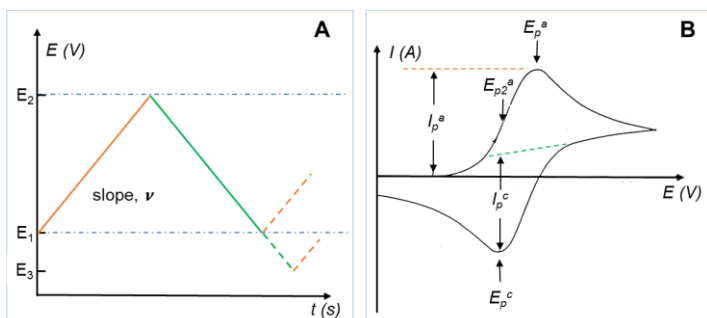


**Figure 2.6** (A) Profiles of potential versus time for CV. (B) Typical reversible cyclic voltammogram where  $I_p^a$  and  $I_p^c$  represent the anodic and cathodic peak currents respectively at corresponding  $E_p^a$  and  $E_p^c$  peak potentials.<sup>[237]</sup>

The electrodes are usually positioned in an unstirred solution during CV. Provided that ET at the working electrode is fast and the current limited by diffusion of analyte species from bulk solution to the WE surface, the peak current will be proportional to the square root of the scan rate. This is expressed in the Randles-Sevcik equation:<sup>[237]</sup>

$$i_p = 0.4463nFAC \left( \frac{nFA\nu D}{RT} \right)^{1/2} \quad (2.4)$$

where  $n$  is the number of transferred electrons,  $F$  is Faraday's constant ( $96\,485\text{ C mol}^{-1}$ ), and  $A$  the geometrical area of the electrode in  $\text{cm}^2$ .  $C$  is the concentration of analyte in  $\text{mol cm}^{-3}$  and  $D$  the diffusion coefficient for the species in  $\text{cm}^2\text{ s}^{-1}$ .  $\nu$  is the scan rate in  $\text{V s}^{-1}$ ,  $R$  the gas constant ( $8.314\text{ J K}^{-1}\text{ mol}^{-1}$ ), and  $T$  the temperature in K.

In this Ph.D. study, CV was used to characterize electrochemical properties of graphene modified carbon paper electrode as well as the catalytic mechanisms of the prepared bioanode and biocathode.

### 2.3.2 Linear sweep voltammetry

Linear sweep voltammetry (LSV) a simple potential sweep technique because the electrode potential is only swept from  $E_1$  to  $E_2$  at a defined scan rate, Fig. 2.7A. The resulting current response on the electrode is plotted as a function of the applied potential, Fig. 2.7B. If the system is applied with a very slow linear potential sweep such as  $1.0\text{ mV s}^{-1}$ , the recorded voltammogram will appear like a steady state  $I$  vs  $E$  curve.<sup>[237]</sup> In the Ph.D. study, LSV was used to characterize the biocathode for the catalysis of  $\text{O}_2$  reduction and polarization discharge curves for EBFCs.

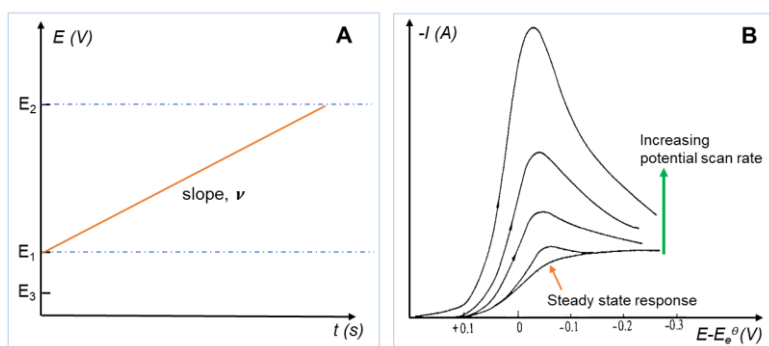


**Figure 2.7** (A) A profile of potential versus time for LSV. (B) A series of linear sweep voltammograms for the reduction reaction  $\text{O} + \text{e}^- \rightarrow \text{R}$ , at several potential scan rates.  $E^{\circ}$  is the standard potential of the redox couple.<sup>[237]</sup>

### 2.4.3 Polarization and power curves for enzymatic biofuel cells

In this Ph.D. study, the EBFC performance is assessed by polarization and power curves which describe the generation of power density at given current density values, Fig. 2.8. These curves are typically obtained using a two-electrode system with a biocathode and a bioanode as the combined reference/counter and working electrodes, respectively. Typically, OCV can be determined as the experimentally measured difference of the open circuit potentials (OCPs) between the biocathode and the bioanode when no current is passing and a stabilized OCP is reached. This value strongly depends on the properties

of catalysts and mediators. During polarization, the real voltage of an EBFC under operation  $E_{cell}$  can be described as Eq. 2.5.<sup>[238-239]</sup>

$$E_{cell} = OCV - \eta_{act} - \eta_{ohm} - \eta_{conc} \quad (2.5)$$

where  $\eta_{act}$  the activation overpotential, related to the kinetics of the electrochemical redox reactions at the interfaces between the bioanode/biocathode and electrolyte,  $\eta_{ohm}$  the ohmic overpotential corresponding to resistance of all cell components, and  $\eta_{conc}$  the concentration overpotential due to mass transport limitations during cell operation.<sup>[238-239]</sup>

The power output of an EBFC can be defined as:<sup>[2, 239]</sup>

$$P = E_{cell} \times I \quad (2.6)$$

where  $I$  is the electric current in A. For comparison between different EBFC devices, current and power are given as current density and power density, respectively, based on the electrode geometric surface area of the electrode.<sup>[239]</sup> EBFC power density increases with increasing current density, reaches a maximum value ( $P_{max}$ ), and then starts decreasing with further increase of current density due to the mass transport limitation, Fig. 2.8.

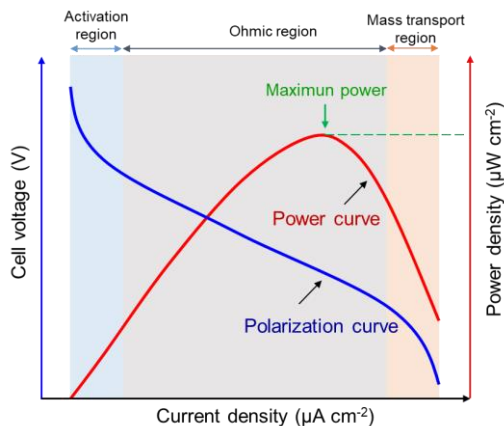


**Figure 2.8** Polarization ( $E$  vs.  $i$ , blue) and power ( $P$  vs.  $i$ , red) curves scheme with highlighted activation (light blue), ohmic (grey) and mass transport (light orange) regions.

### 2.3.4 Chronoamperometry

Chronoamperometry (CA) is another useful electrochemical technique. In the process, the WE potential is stepped from  $E_1$ , where no electrochemical reaction occurs, to  $E_2$  to initiate the electrode reaction of interest, and the current response is recorded as a function of time, Fig. 2.9.

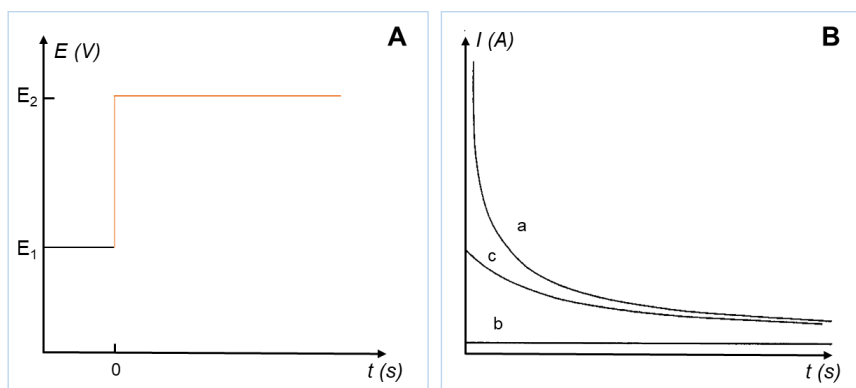


**Figure 2.9** (A) A profile of potential versus time for CA. (B) Current-time profiles for single potential step experiments. The potential  $E_2$  is chosen to achieve the (a) diffusion-controlled, (b) kinetically-controlled, and (c) mixed-controlled reaction.<sup>[237]</sup>

CA was used to functionalize graphene-based electrode with redox molecules and investigate the stability of bioelectrodes in the Ph.D. project. By applying a potential to the graphene-based electrode, the polymerization of redox molecules on the electrode surface was achieved. CA can be utilized to monitor electrodes current at the defined potential over a period of time, reflecting the stability of the bioelectrodes.

### 2.3.5 Electrochemical impedance spectroscopy

Electrochemical impedance spectroscopy (EIS) is usually measured by applying an AC potential to the WE while recording the cell current. Normally a small AC potential amplitude is applied, so that the cell's response is pseudo-linear. In a linear (or pseudo-linear) system, the current response to a sinusoidal potential will be a sinusoid at the same frequency but shifted in phase (Fig. 2.10), and the electric impedance ( $Z$ ) in  $\Omega$  of the system based on Ohm's Law can be expressed as the following equation:<sup>[240]</sup>

$$Z = |Z| e^{-j\varphi} \quad (2.7)$$

where  $j$  is the imaginary number equal to  $(-1)^{1/2}$  and  $|Z|$  the modulus of the applied potential divided by current related to the measured phase shift ( $\varphi$ ). If the system exhibits pure resistor behavior (impedance independent of frequency),  $\varphi$  equals to 0 (*i.e.*  $0^\circ$ ). In contrast, a pure capacitor has the  $\varphi$  with  $\pi/2$  (*i.e.*  $90^\circ$ ).<sup>[240]</sup>

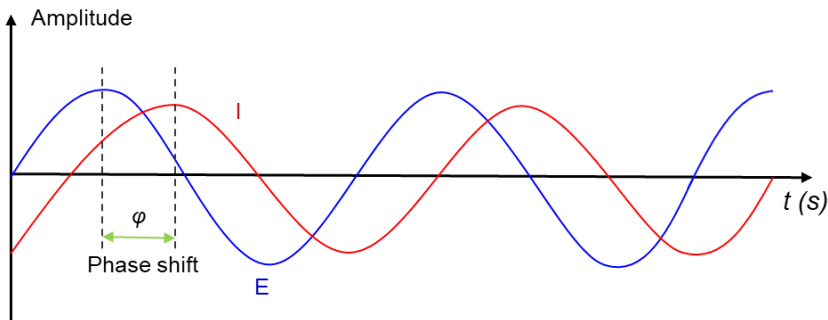


**Figure 2.10** AC circuit time dimension shows phase shift between applied voltage and resulting current.

Electrochemical systems can be expressed by series and parallel configurations of resistors and capacitors. Polarization of the electrode can cause current to flow *via* electrochemical reactions at the electrode surface. The amount of current is controlled by the kinetics of the reactions and the diffusion of reactants/products towards/away from the electrode. A typical overall admittance  $Y$  (an inverse of  $Z$  in S) can be expressed as follows.<sup>[240]</sup>

$$Y(\omega) = \frac{1}{R_s} + \frac{1}{R_p} (1 + j\omega C_{dl}) \quad (2.8)$$

where  $R_s$  and  $R_p$  are the solution and polarization resistance in  $\Omega$ , respectively.  $\omega$  is the angular frequency in  $\text{rad s}^{-1}$  and  $C_{dl}$  is the double layer capacitor in F. However, most real systems cannot simply be expressed as a classic model as Eq. 2.8, since the overall impedance due to both frequency and energy (different oxidation/reduction levels) dispersions needs to be described by a non-classic model of imperfect capacitors, namely constant phase element (CPE). CPE can model semi-infinite linear diffusion processes such as Warburg impedance (a special case), pure resistor and capacitor. This versatile element is nowadays widely used in EIS fitting mainly due to its robust approximation of porosity for electrodes.<sup>[241-242]</sup> In this Ph.D. study, EIS was used to characterize the interfacial charge transfer resistance of graphene-based electrodes.

# Chapter 3

## Preparation and characterization of graphene-based 3D carbon papers

---

---

This chapter describes the synthesis of graphene oxide, fabrication of three-dimensional graphene-based carbon paper electrodes and characterization of prepared electrodes. Part of this chapter was included in the published article “Three-Dimensional sulfite Oxidase Bioanodes Based on Graphene Functionalized Carbon Paper for Sulfite/O<sub>2</sub> Biofuel Cells” in *ACS Catalysis* co-authored by J. Tang, R. M. L. Werchmeister, L. Preda, W. Huang, Z. Zheng, S. Leimkühler, U. Wollenberger, X. Xiao, C. Engelbrekt, J. Ulstrup, and J. Zhang, as well as in the manuscript “Direct electron transfer of orientated bilirubin oxidase on three-dimensional carbon paper with reduced graphene aggregation” (in preparation).

---

### 3.1 Introduction

Electrode materials are essential in the development of high-performance of EBFCs, since their chemical and physical properties as well as their structure are key factors affecting enzyme immobilization and electrocatalytic activity of fabricated enzymatic electrodes. Recent research on electrode construction for practical applications focus on designing 3D porous electrodes, as they ensure the high enzyme loading and efficient mass-transfer diffusion due to the large surface area and micro-/macro- porous structures, respectively.<sup>[243-245]</sup> In addition, the confinement effects of the porous electrodes are suitable for the enzyme orientation and redox polymer modification compared to planar electrodes.<sup>[2]</sup> CP assembled with carbon fibers, one of the most attractive 3D electrodes, has been widely used as electrode substrates for enzyme immobilization.<sup>[162]</sup> This robust and porous supporting electrode can sustain after strong chemical modification without changing the original 3D structure.

Graphene, a carbon nanomaterial with high conductivity and large surface area, holds great promise as electrode materials. 3D graphene electrodes have been used for EBFC

---

applications, but the strategies for immobilizing enzyme on the 3D graphene electrode are limited to non-specific physical adsorption.<sup>[27, 155]</sup> To anchor enzyme on perfect graphene is thus difficult due to the lack of functional groups such as oxygenated groups on the surface.<sup>[244]</sup> In particular, a proper orientation of enzyme on the electrode surface is important to achieve efficient ET for DET-type bioelectrodes undergoing direct electric communication between the enzyme and electrode surface. Graphene-functionalized 3D electrodes are therefore required. CP, the aforementioned 3D-conducting electrode substrate suitable for practical applications, was used to support functionalized graphene-based materials in this Ph.D. project.

Since CP is hydrophobic, it is hard to uniformly immobilize nanomaterials and enzymes suspended in aqueous solution on the electrode surface. In this chapter, several protocols including boiling in strong acid or alkaline and sonicated in GO solution were proposed to make CP hydrophilic. The pre-treatment of CP and characterization of the resulting CP electrode are described in detail. The application of optimized pre-treated CP electrodes for enzyme orientations will be described in Chapter 4 and 5.

## 3.2 Experimental

### 3.2.1 Chemicals and materials

Potassium permanganate ( $\text{KMnO}_4$ ,  $\geq 99.9\%$ ) and potassium hexacyanoferrate(II) ( $\text{K}_4[\text{Fe}(\text{CN})_6] \cdot 3\text{H}_2\text{O}$ , 99.0-102.0%) was from Merck (Germany). Graphite powder ( $< 20 \mu\text{m}$ ), hydrogen peroxide ( $\text{H}_2\text{O}_2$ , 34.5-36.5%), sulfuric acid ( $\text{H}_2\text{SO}_4$ , 95-97%), hydrochloric acid (HCl, 37%), nitric acid ( $\text{HNO}_3$ ,  $\geq 65\%$ ) potassium persulfate ( $\text{K}_2\text{S}_2\text{O}_8$ ,  $\geq 99\%$ ), potassium chloride (KCl,  $\geq 99.0\%$ ), sodium hydroxide (NaOH, 97%), phosphorous pentoxide ( $\text{P}_2\text{O}_5$ ,  $\geq 98\%$ ) were from Sigma-Aldrich (USA). Ethanol (96% vol.) was obtained from VWR Chemicals (USA). CP (product No. EC-TP1-060, thickness of  $190 \mu\text{m}$ ) composed of carbon fibers with diameters of 6-8  $\mu\text{m}$  was purchased from Quintech (Germany). Glue gun (PKP 18 E) and hot melt adhesive (polyvinyl chloride, PVC) used to block CP were from BOSCH (Germany). All the solutions were prepared with 18.2 M $\Omega$  cm Millipore water.

### 3.2.2 Synthesis of graphene oxide

GO was in-house prepared according to a modified Hummer's method.<sup>[246-247]</sup> As shown in Fig. 3.1, briefly, 5.0 g graphite powder was first pre-oxidized by heating 15.0 mL concentrated  $\text{H}_2\text{SO}_4$  containing 2.5 g  $\text{P}_2\text{O}_5$  and 2.5 g  $\text{K}_2\text{S}_2\text{O}_8$  at 80 °C in an oil bath under stirring for 3 h under refluxing. 120 mL Millipore water was then slowly added into the hot solution along the flask wall to dilute and cool down the solution. The cooled solution was filtered and washed by Millipore water until neutral pH of the filtrate. The product, pre-oxidized graphite, was dried at 50 °C overnight and then grounded for use, Fig. 3.2.

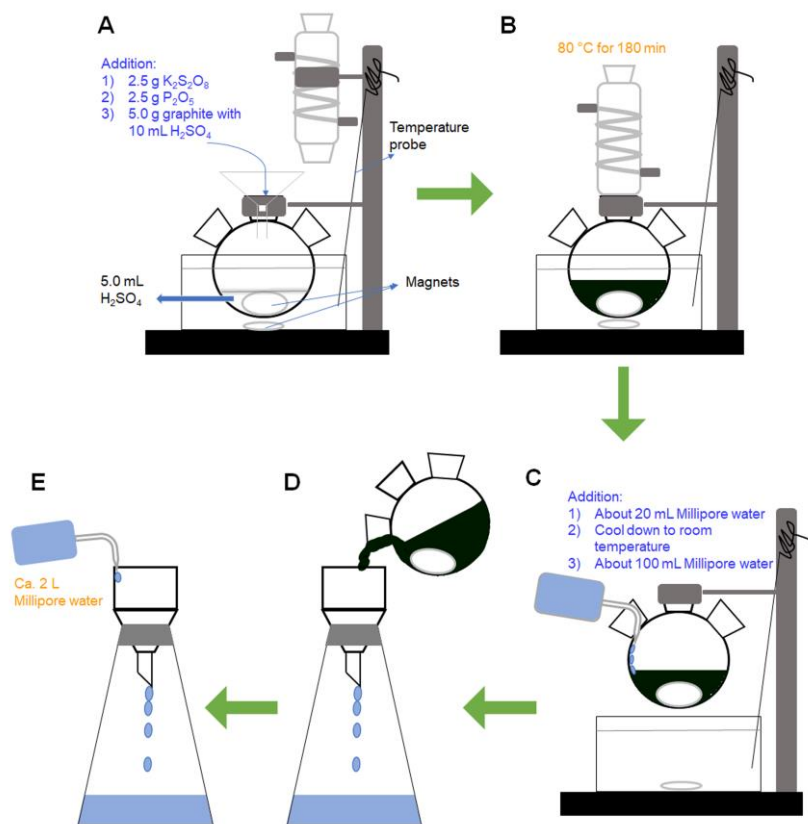


**Figure 3.1** Schematic drawing of the synthesis of pre-oxidized graphite: (A) addition of 5.0 mL  $H_2SO_4$ , 2.5 g  $K_2S_2O_8$ , 2.5 g  $P_2O_5$  and 5.0 g graphite with 10 mL  $H_2SO_4$  into the flask, (B) the pre-oxidation process, (C) addition of Millipore water, (D) vacuum filtration of pre-oxidized graphite solution, and (E) washing pre-oxidized graphite using Millipore water.

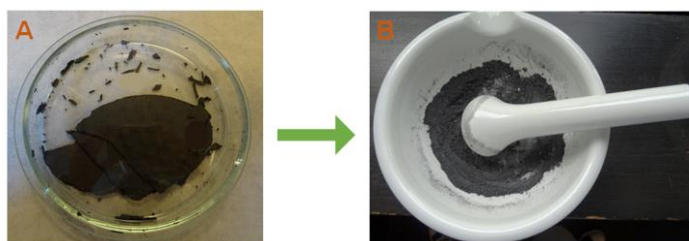


**Figure 3.2** Digital pictures of (A) dried and (B) ground pre-oxidized graphite.

As schemed in Fig. 3.3, 1.0 g of the resulting pre-oxidized graphite powder was dispersed in 23.0 mL concentrated  $H_2SO_4$ , and 3.0 g  $KMnO_4$  was slowly added. The reaction was

maintained with magnetic stirring at 35 °C for 2 h. 200 mL Millipore water and ~2 mL H<sub>2</sub>O<sub>2</sub> were then slowly added sequentially into the solution until no further bubble generation.

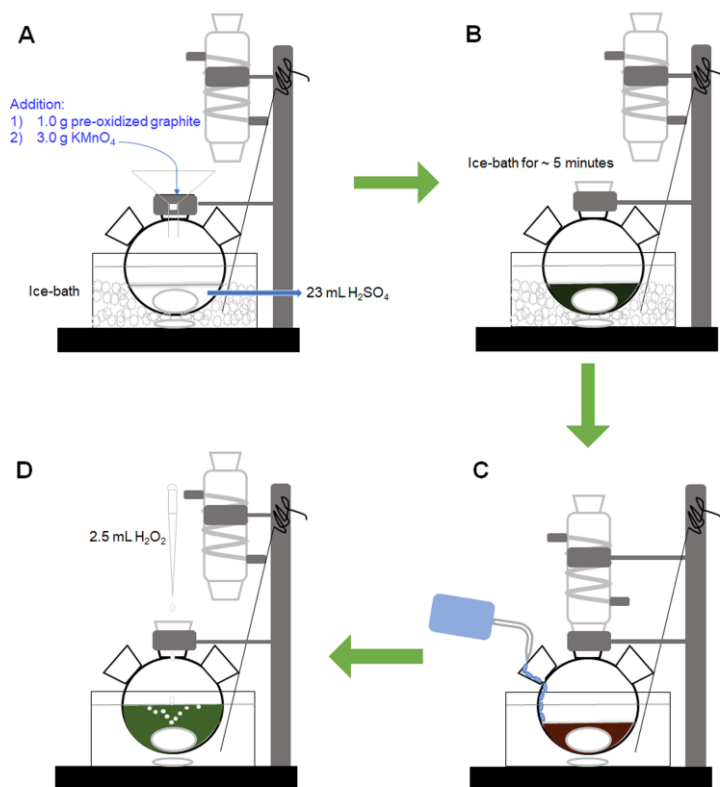


**Figure 3.3** Scheme drawing of the synthesis of raw graphene oxide: (A) addition of 23 mL H<sub>2</sub>SO<sub>4</sub>, 1.0 g pre-oxidized graphite and 3.0 g KMnO<sub>4</sub> into the flask and (B) ice-bath reaction for 5.0 min. (C) After two-hour reaction in oil-bath at 35 °C, 46 mL Millipore water was added and the solution left for ~15 min. 140 mL Millipore water was then added and kept for 5.0 min. (D) ~2.5 mL H<sub>2</sub>O<sub>2</sub> was added into the flask until no bubbles appeared.

The resulting GO was purified as shown in Fig. 3.4. First, the raw GO was filtrated with 250 mL 1.0 M HCl. The GO residues obtained were dispersed in 200 mL Millipore water and sonicated for ~2 h. Medium size GO sheets were concentrated by a two-step centrifugation: a 500-rpm centrifugation was first used to separate the graphite from appropriate GO supernatant with the resulting GO solution centrifuged at 12000 rpm to collect the residues. GO sheets with medium sizes were dialyzed in a dialysis bag (cut-off: 12000-14000 Da) with fresh Millipore water every day for one week.

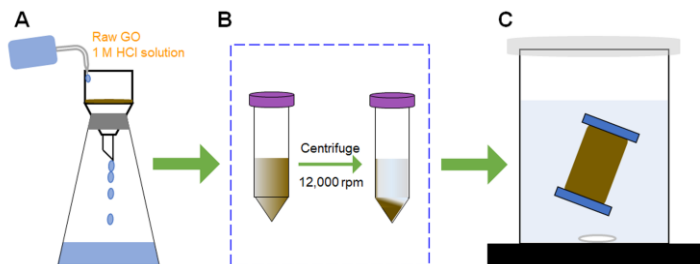


**Figure 3.4** Schemes of purification of raw graphene oxide: (A) vacuum filtration, (B) centrifugation and (C) GO dialysis.

### 3.2.3 Pre-treatment of carbon paper

Coating hydrophilic nanomaterials on CP can increase its wettability. GO with abundant hydrophilic oxygen-containing groups could be an ideal modifier, since it can be attached on CP *via*  $\pi$ - $\pi$  interactions.<sup>[248]</sup> Before GO was coated on CP (CPG), the T-shape electrode was first cut from CP with a working surface area of  $0.50 \times 0.50 \text{ cm}^2$  defined with hot melt adhesive using a glue gun, Fig. 3.5, blocking the one side with the melted glue.

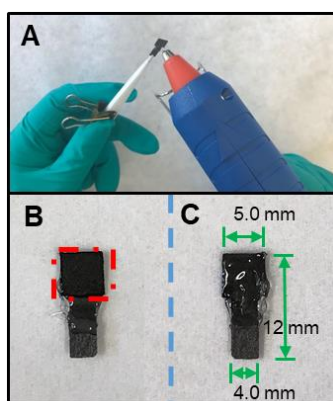


**Figure 3.5** Digital photos of (A) the fixed T-shape CP blocked on one side with hot melt adhesive by a glue gun, and glued T-shape CP (B) from a front view and (C) view from the back. The active area was  $0.25 \text{ cm}^2$ , marked with a red dashed-square in (B).

The working surface of the prepared T-shape CP was immersed in  $1.0 \text{ mg mL}^{-1}$  GO solution for sonication in an ice bath, Fig. 3.6A and B. The sonication time varied from 10, 30, 60, 90 to 120 min and the resulting electrodes were labelled as CPG10, CPG30, CPG60, CPG90 and CPG120, respectively. This step ensured to improve the hydrophilicity of CP, allowing aqueous solution to be uniformly spread on CPG electrodes, Fig. 3.6C. The control electrode (CP- $\text{H}_2\text{O}$ ) was immersed in Millipore water for 10-min sonication.

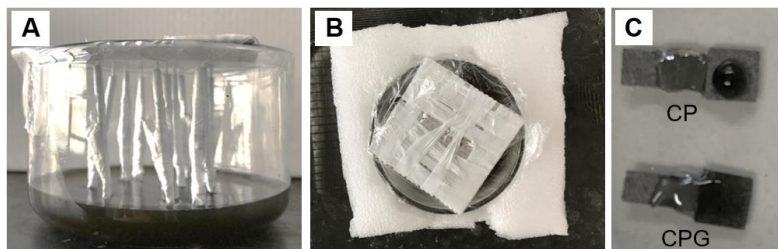


**Figure 3.6** Digital photos of (A) the fixed T-shape CP immersed in  $1.0 \text{ mg mL}^{-1}$  GO solution, (B) the sonication process from a top view and (C) comparison of the hydrophilicity of CP and CPG by dropping water on them.

CP can also be activated with strong acid or alkali, achieved by boiling  $6.0 \times 1.20 \text{ cm}^2$  CP in 15 %  $\text{HNO}_3$  or 1.0 M NaOH solution for 10 min. After that, the activated CPs (CP- $\text{HNO}_3$  and CP-NaOH) were dried at room temperature overnight, and cut into T-shape with dimension  $0.50 \times 1.20 \text{ cm}^2$ . The working surface area is  $0.50 \times 0.50 \text{ cm}^2$ , defined with hot melt adhesive using a glue gun, Fig. 3.5.

### 3.3 Results and discussion

#### 3.3.1 Morphology and structure characterization of GO

The morphology of GO was probed by tapping mode AFM with a Tap300Ai-G silicon tip from Budget Sensors.  $20 \mu\text{L}$  GO solution ( $61 \mu\text{g mL}^{-1}$ ) was dropped onto a mica sheet ( $10.0 \times 10.0 \text{ mm}^2$ , thickness 0.1 to 0.2 mm) which was freshly cleaved with a tape and allowed to dry at room temperature. GO sheets are clearly visible in Fig. 3.7A. The thickness of single-layered sheets is ca. 1.0 nm and the lateral dimensions range from several hundred nanometers to three micrometers, Fig. 3.7A and B. The UV-vis spectra of GO solutions with different concentration are presented in Fig. 3.7C. The two GO-characteristic adsorption peaks are observed, *i.e.*, the broad absorption band at 233 nm corresponding to  $\pi \rightarrow \pi^*$  transition of aromatic C–C and C=C bonds, and the 304 nm peak attributed to the  $n \rightarrow \pi^*$  transitions of C=O.<sup>[232]</sup> All these observations suggest the successful synthesis of GO.

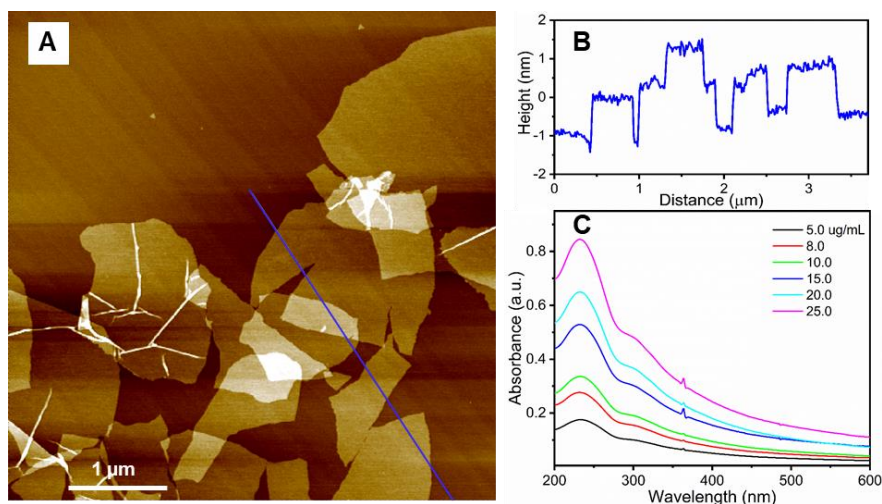


**Figure 3.7** (A) AFM image of GO with (B) a cross section topography profile of the line in (A). (C) UV-vis spectra of GO solutions with different concentrations.

### 3.3.2 Hydrophilicity of functionalized carbon papers

The hydrophilicity was characterized using a Contact Angle system (OCA Data Physics, Germany) to measure the water contact angle (WCA) of dried electrodes. It has been reported that material surfaces can be considered hydrophobic if the WCA is larger than  $50^\circ$ , otherwise hydrophilic.<sup>[249]</sup> The bare CP has a WCA of  $138.3^\circ$  (Fig. 3.8A), indicating a hydrophobic surface. Treatments of CP in boiling alkane and acidic solutions for 10 min do not change surface hydrophobicity significantly since their WCAs ( $133^\circ$  for CP- $\text{HNO}_3$  and  $134^\circ$  for CP-NaOH, Fig. 3.8B and C) are just slightly smaller than that of the bare CP.

However, Sonicating CP in GO solution for 10 min changes the surface remarkably to hydrophilic with a WCA of  $43.3^\circ$  for CPG10, Fig. 3.8D. As a control, the sonication of CP in  $\text{H}_2\text{O}$  has a negligible effect on CP, because the WCA of the result in CP- $\text{H}_2\text{O}$  ( $140^\circ$ ) is comparable to the value of bare CPs, Fig. 3.8E. The improved hydrophilicity, therefore, is mainly due to the presence of GO on carbon fibers of CP. To support the explanation, SEM images of bare CP and CPG120 electrodes were obtained, Fig. 3.9. Small flakes, regarded as GO sheets characterized by AFM (Fig. 3.7A), appear on the carbon fibers of CPG120 (Fig. 3.9C and D), in contrast to bare CPs (Fig. 3.9A and B). This indicates the hydrophilic GO is deposited on the carbon fibers *via*  $\pi$ - $\pi$  interactions and the original 3D structure is preserved.<sup>[248]</sup> In addition, prolonging the sonication time in GO solution to 120 min further decreases the WCA to  $27^\circ$  for CPG120, Fig. 3.8F. The above observations imply that the immobilization of GO on CP greatly enhances the wettability of electrode

substrate, which is good for the following functionalization using drop-casting aqueous nanomaterials and enzymes onto the electrodes.

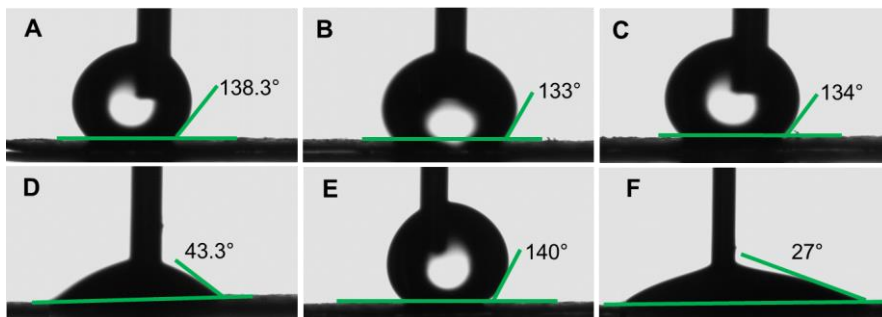


**Figure 3.8** WCAs of (A) bare CP, (B) CP-HNO<sub>3</sub>, (C) CP-NaOH, (D) CPG10, (E) CP-H<sub>2</sub>O and (F) CPG120.

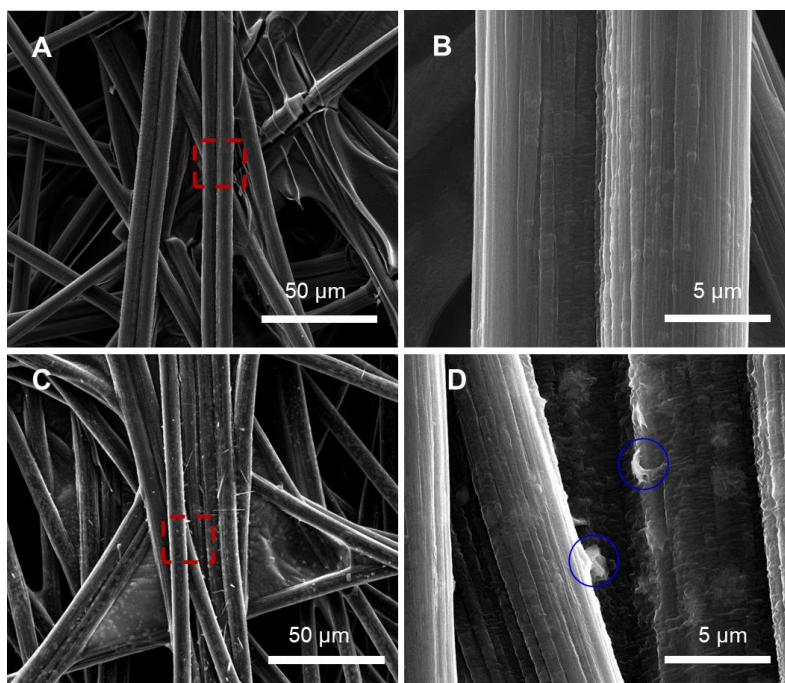


**Figure 3.9** SEM images of (A and B) bare CP and (C and D) CPG120. (B) and (D) is the magnified area (red dash-square in (A) and (C)) of CP and CPG120, respectively. Small white flakes, indicated with blue circles in (D), are recognized as GO sheets.

### 3.3.3 Electrochemical characterizations of functionalized carbon papers

Electrochemical performance of functionalized CPs, *i.e.*, the electrochemical responses in 1.0 mM  $\text{K}_4[\text{Fe}(\text{CN})_6]$  in 100 mM KCl electrolyte, was characterized by CV, Fig. 3.10. Since CP is quite hydrophobic, the redox probe  $[\text{Fe}(\text{CN})_6]^{3-/4-}$  is hard to get access to the electrode, and no  $[\text{Fe}(\text{CN})_6]^{3-/4-}$  redox peaks appear in the scan window (-0.2 to 0.7 V vs. Ag/AgCl), Fig. 3.10A. After CP treatment with boiling 15%  $\text{HNO}_3$  or 1.0 M NaOH for 10min,  $[\text{Fe}(\text{CN})_6]^{3-/4-}$  peaks on CP- $\text{HNO}_3$  and CP-NaOH start to appear, Fig. 3.10B and C. Notably, a series of well-defined redox peaks are observed at scan rates lower than 200  $\text{mV s}^{-1}$  on the CPG10, Fig. 3.10D. This is because CPG10 is more hydrophilic than CP- $\text{HNO}_3$  and CP-NaOH, confirmed by WCA measurements (section 3.3.2). Although a similar electrochemical response on CP- $\text{H}_2\text{O}$  is achieved (Fig. 3.10E), the property is temporary, and the dried CP- $\text{H}_2\text{O}$  turns to be hydrophobic again. Compared with CVs on GCE, the control electrode, Fig. 3.10F, CPG10 exhibits larger peak-peak separation ( $\Delta E_p$ ) at higher scan rates. For example,  $\Delta E_p$  on CPG10 reduces from  $0.35 \pm 0.05$  V at 100  $\text{mV s}^{-1}$  to  $0.13 \pm 0.02$  V at 10  $\text{mV s}^{-1}$ , while  $\Delta E_p$  on GCE reduces from  $0.079 \pm 0.004$  V at 100  $\text{mV s}^{-1}$ ,  $0.072 \pm 0.003$  V at 10  $\text{mV s}^{-1}$ , Fig. 3.11 and Table 3.1. These phenomena can be explained by the fact that the diffusion of the redox probe plays a dominating role in the electrochemical redox process on CPG10 at a high scan rate, which is not the case for GCE.

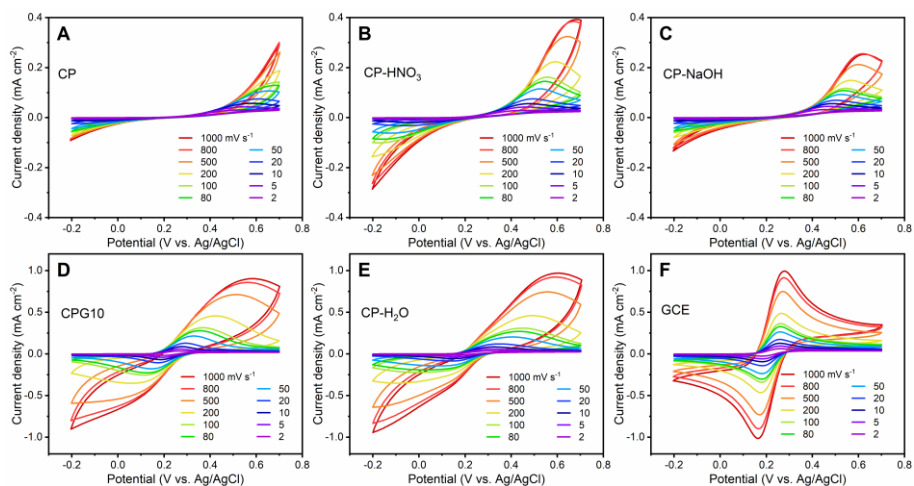


**Figure 3.10** CVs of (A) bare CP, (B) CP- $\text{HNO}_3$ , (C) CP-NaOH, (D) CPG10, (E) CP- $\text{H}_2\text{O}$  and (F) GCE in 100 mM KCl solution containing 1.0 mM  $\text{K}_4[\text{Fe}(\text{CN})_6]$  with different scan rates (1000, 800, 500, 200, 100, 80, 50, 20, 10, 5 and 2  $\text{mV s}^{-1}$ ).

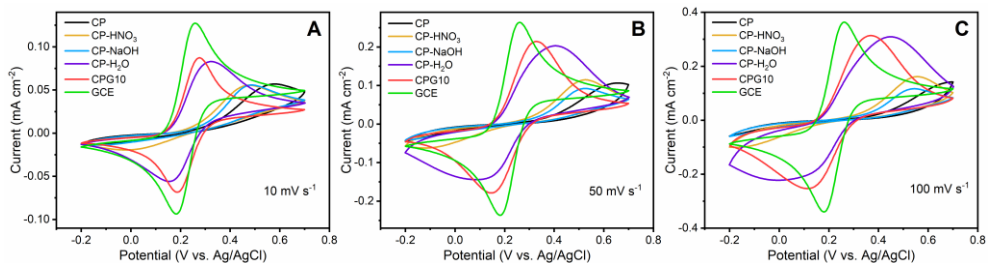


**Figure 3.11** Comparisons of CVs of bare CP, CP-HNO<sub>3</sub>, CP-NaOH, CP-H<sub>2</sub>O, CPG10 and GCE in 100 mM KCl solution containing 1.0 mM K<sub>4</sub>[Fe(CN)<sub>6</sub>] with scan rates of (A) 100, (B) 50 or (C) 10 mV s<sup>-1</sup>.

### 3.3.4 Effects of sonication time on carbon papers with GO

CVs of CP120, CPG10 and GCE with a series of scan rates are shown in Fig. 3.12, Fig. 3.10D and Fig. 3.10F, respectively. Electrochemical parameters of CVs of GCE and CPG with different sonication times are summarized in Table 3.1. For both CPG and GCE electrodes,  $\Delta E_p$  at higher scan rates is much larger than at lower scan rates, suggesting partial kinetic control.  $\Delta E_p$  of CPG electrodes with the same scan rate decreases with increasing sonication time, *i.e.*, from  $0.13 \pm 0.02$  V for CPG10 to  $0.081 \pm 0.007$  V for CPG120 at 10 mV s<sup>-1</sup>. In addition, the  $\Delta E_p$  value for CPG120 electrodes is quite close to that for GCE at scan rate lower than 10 mV s<sup>-1</sup>. In general, the anodic and cathodic current densities for CPG electrodes increase with longer sonication time due to the enhanced hydrophilicity of CP, Table 3.1.

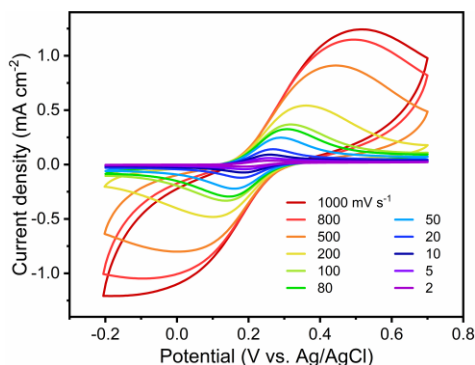


**Figure 3.12** CVs of a CPG120 electrode in 100 mM KCl solutions containing 1.0 mM K<sub>4</sub>[Fe(CN)<sub>6</sub>] with different scan rates.

**Table 3.1** Electrochemical parameters of CVs of CPG with different sonication times and GCE in 100 mM KCl solution containing 1.0 mM  $K_4[Fe(CN)_6]$ .

| Electrode | $\nu$ (mV s <sup>-1</sup> ) | $E_p^a$ (V)*  | $i_p^a$ ( $\mu$ A cm <sup>-2</sup> ) | $E_p^c$ (V)*   | $i_p^c$ ( $\mu$ A cm <sup>-2</sup> ) | $ \Delta E_p $ (V) | $ i_p^a / i_p^c $ |
|-----------|-----------------------------|---------------|--------------------------------------|----------------|--------------------------------------|--------------------|-------------------|
| CPG10     | 1000                        | 0.55 ± 0.02   | 478 ± 226                            | -0.08 ± 0.02   | -384 ± 182                           | 0.63 ± 0.04        | 1.25 ± 0.04       |
|           | 800                         | 0.56 ± 0.03   | 482 ± 17                             | -0.09 ± 0.03   | -372 ± 34                            | 0.65 ± 0.06        | 1.30 ± 0.07       |
|           | 500                         | 0.52 ± 0.02   | 440 ± 8                              | -0.06 ± 0.02   | -336 ± 18                            | 0.59 ± 0.04        | 1.32 ± 0.07       |
|           | 200                         | 0.48 ± 0.03   | 294 ± 69                             | -0.01 ± 0.04   | -216 ± 54                            | 0.48 ± 0.07        | 1.37 ± 0.03       |
|           | 100                         | 0.42 ± 0.02   | 222 ± 45                             | 0.07 ± 0.02    | -167 ± 37                            | 0.35 ± 0.05        | 1.33 ± 0.03       |
|           | 80                          | 0.40 ± 0.02   | 199 ± 37                             | 0.08 ± 0.02    | -151 ± 32                            | 0.31 ± 0.04        | 1.32 ± 0.04       |
|           | 50                          | 0.37 ± 0.02   | 155 ± 27                             | 0.11 ± 0.02    | -123 ± 25                            | 0.25 ± 0.03        | 1.27 ± 0.06       |
|           | 20                          | 0.32 ± 0.02   | 98 ± 14                              | 0.15 ± 0.01    | -83 ± 14                             | 0.17 ± 0.03        | 1.18 ± 0.04       |
|           | 10                          | 0.30 ± 0.01   | 69 ± 8                               | 0.170 ± 0.009  | -60 ± 8                              | 0.13 ± 0.02        | 1.14 ± 0.02       |
|           | 5                           | 0.28 ± 0.01   | 48 ± 5                               | 0.181 ± 0.008  | -43 ± 5                              | 0.10 ± 0.02        | 1.11 ± 0.02       |
| 2         | 0.28 ± 0.01                 | 30 ± 2        | 0.185 ± 0.006                        | -29 ± 2        | 0.09 ± 0.02                          | 1.04 ± 0.02        |                   |
| CPG30     | 1000                        | 0.537 ± 0.007 | 673 ± 80                             | -0.069 ± 0.006 | -535 ± 60                            | 0.61 ± 0.01        | 1.26 ± 0.02       |
|           | 800                         | 0.521 ± 0.004 | 639 ± 65                             | -0.03 ± 0.02   | -511 ± 58                            | 0.55 ± 0.02        | 1.25 ± 0.03       |
|           | 500                         | 0.482 ± 0.003 | 608 ± 49                             | 0.01 ± 0.03    | -490 ± 59                            | 0.48 ± 0.03        | 1.25 ± 0.06       |
|           | 200                         | 0.44 ± 0.05   | 410 ± 107                            | 0.04 ± 0.06    | -331 ± 79                            | 0.4 ± 0.1          | 1.23 ± 0.05       |
|           | 100                         | 0.39 ± 0.04   | 310 ± 59                             | 0.10 ± 0.04    | -264 ± 49                            | 0.29 ± 0.08        | 1.18 ± 0.03       |
|           | 80                          | 0.37 ± 0.04   | 283 ± 49                             | 0.11 ± 0.03    | -242 ± 43                            | 0.26 ± 0.07        | 1.17 ± 0.02       |
|           | 50                          | 0.34 ± 0.03   | 221 ± 35                             | 0.14 ± 0.02    | -198 ± 32                            | 0.20 ± 0.05        | 1.12 ± 0.02       |
|           | 20                          | 0.30 ± 0.02   | 137 ± 16                             | 0.17 ± 0.02    | -126 ± 16                            | 0.13 ± 0.03        | 1.09 ± 0.02       |
|           | 10                          | 0.28 ± 0.01   | 93 ± 8                               | 0.18 ± 0.01    | -87 ± 8                              | 0.10 ± 0.02        | 1.07 ± 0.01       |
|           | 5                           | 0.27 ± 0.01   | 63 ± 4                               | 0.19 ± 0.008   | -59 ± 4                              | 0.08 ± 0.02        | 1.06 ± 0.02       |
| 2         | 0.267 ± 0.005               | 37 ± 2        | 0.19 ± 0.004                         | -37 ± 2        | 0.074 ± 0.009                        | 1.02 ± 0.01        |                   |

**Table 3.1** Continued.

| Electrode | $\nu$ (mV s <sup>-1</sup> ) | $E_p^a$ (V)*  | $i_p^a$ ( $\mu\text{A cm}^{-2}$ ) | $E_p^c$ (V)*  | $i_p^c$ ( $\mu\text{A cm}^{-2}$ ) | $ \Delta E_p $ (V) | $ i_p^a / i_p^c $ |
|-----------|-----------------------------|---------------|-----------------------------------|---------------|-----------------------------------|--------------------|-------------------|
| CPG60     | 1000                        | 0.54 ± 0.02   | 597 ± 67                          | -0.07 ± 0.02  | -501 ± 41                         | 0.61 ± 0.05        | 1.19 ± 0.08       |
|           | 800                         | 0.53 ± 0.02   | 580 ± 90                          | -0.06 ± 0.02  | -484 ± 42                         | 0.58 ± 0.04        | 1 ± 0.1           |
|           | 500                         | 0.50 ± 0.02   | 563 ± 80                          | -0.04 ± 0.02  | -457 ± 40                         | 0.54 ± 0.04        | 1.23 ± 0.08       |
|           | 200                         | 0.43 ± 0.02   | 443 ± 50                          | 0.06 ± 0.02   | -350 ± 32                         | 0.37 ± 0.03        | 1.26 ± 0.04       |
|           | 100                         | 0.38 ± 0.01   | 320 ± 33                          | 0.10 ± 0.01   | -265 ± 24                         | 0.27 ± 0.004       | 1.21 ± 0.03       |
|           | 80                          | 0.36 ± 0.01   | 282 ± 28                          | 0.117 ± 0.009 | -239 ± 22                         | 0.24 ± 0.02        | 1.18 ± 0.02       |
|           | 50                          | 0.335 ± 0.009 | 214 ± 23                          | 0.139 ± 0.008 | -191 ± 17                         | 0.20 ± 0.02        | 1.12 ± 0.03       |
|           | 20                          | 0.299 ± 0.005 | 130 ± 13                          | 0.167 ± 0.005 | -118 ± 10                         | 0.13 ± 0.01        | 1.10 ± 0.02       |
|           | 10                          | 0.282 ± 0.004 | 87 ± 7                            | 0.180 ± 0.003 | -81 ± 6                           | 0.102 ± 0.007      | 1.08 ± 0.02       |
|           | 5                           | 0.272 ± 0.003 | 58 ± 4                            | 0.188 ± 0.004 | -55 ± 4                           | 0.083 ± 0.006      | 1.07 ± 0.02       |
| 2         | 0.267 ± 0.002               | 35 ± 2        | 0.192 ± 0.003                     | -34 ± 2       | 0.076 ± 0.005                     | 1.03 ± 0.01        |                   |
| CPG90     | 1000                        | 0.52 ± 0.02   | 658 ± 61                          | -0.07 ± 0.02  | -599 ± 28                         | 0.50 ± 0.03        | 1.12 ± 0.06       |
|           | 800                         | 0.51 ± 0.02   | 656 ± 53                          | -0.05 ± 0.02  | -542 ± 27                         | 0.57 ± 0.04        | 1.21 ± 0.06       |
|           | 500                         | 0.48 ± 0.02   | 617 ± 47                          | -0.02 ± 0.03  | -498 ± 34                         | 0.51 ± 0.05        | 1.24 ± 0.02       |
|           | 200                         | 0.42 ± 0.02   | 459 ± 31                          | 0.08 ± 0.02   | -373 ± 31                         | 0.34 ± 0.04        | 1.23 ± 0.03       |
|           | 100                         | 0.37 ± 0.02   | 330 ± 23                          | 0.12 ± 0.01   | -282 ± 25                         | 0.25 ± 0.03        | 1.17 ± 0.03       |
|           | 80                          | 0.35 ± 0.02   | 294 ± 23                          | 0.13 ± 0.01   | -255 ± 24                         | 0.23 ± 0.03        | 1.16 ± 0.03       |
|           | 50                          | 0.33 ± 0.02   | 227 ± 20                          | 0.15 ± 0.01   | -202 ± 20                         | 0.19 ± 0.02        | 1.12 ± 0.02       |
|           | 20                          | 0.30 ± 0.01   | 134 ± 12                          | 0.172 ± 0.009 | -123 ± 12                         | 0.13 ± 0.02        | 1.09 ± 0.02       |
|           | 10                          | 0.28 ± 0.01   | 87 ± 8                            | 0.183 ± 0.009 | -82 ± 9                           | 0.10 ± 0.02        | 1.09 ± 0.02       |
|           | 5                           | 0.28 ± 0.02   | 58 ± 5                            | 0.189 ± 0.008 | -54 ± 6                           | 0.09 ± 0.02        | 1.08 ± 0.03       |
| 2         | 0.27 ± 0.02                 | 34 ± 2        | 0.191 ± 0.007                     | -33 ± 2       | 0.08 ± 0.02                       | 1.03 ± 0.01        |                   |

**Table 3.1** Continued.

| Electrode | $\nu$ (mV s <sup>-1</sup> ) | $E_p^a$ (V)*  | $i_p^a$ ( $\mu\text{A cm}^{-2}$ ) | $E_p^c$ (V)*  | $i_p^c$ ( $\mu\text{A cm}^{-2}$ ) | $ \Delta E_p $ (V) | $ i_p^a / i_p^c $ |
|-----------|-----------------------------|---------------|-----------------------------------|---------------|-----------------------------------|--------------------|-------------------|
| CPG120    | 1000                        | 0.50 ± 0.02   | 726 ± 143                         | -0.07 ± 0.02  | -636 ± 154                        | 0.57 ± 0.03        | 1.16 ± 0.07       |
|           | 800                         | 0.49 ± 0.02   | 724 ± 141                         | -0.03 ± 0.02  | -616 ± 149                        | 0.52 ± 0.04        | 1.19 ± 0.06       |
|           | 500                         | 0.46 ± 0.02   | 692 ± 132                         | 0.01 ± 0.04   | -571 ± 132                        | 0.46 ± 0.05        | 1.22 ± 0.05       |
|           | 200                         | 0.40 ± 0.01   | 511 ± 88                          | 0.09 ± 0.01   | -424 ± 90                         | 0.31 ± 0.03        | 1.22 ± 0.05       |
|           | 100                         | 0.35 ± 0.01   | 366 ± 59                          | 0.128 ± 0.008 | -320 ± 60                         | 0.22 ± 0.02        | 1.15 ± 0.03       |
|           | 80                          | 0.339 ± 0.009 | 327 ± 50                          | 0.138 ± 0.006 | -290 ± 51                         | 0.20 ± 0.02        | 1.13 ± 0.03       |
|           | 50                          | 0.315 ± 0.008 | 252 ± 36                          | 0.154 ± 0.005 | -231 ± 37                         | 0.16 ± 0.01        | 1.10 ± 0.02       |
|           | 20                          | 0.285 ± 0.005 | 150 ± 17                          | 0.178 ± 0.003 | -140 ± 18                         | 0.106 ± 0.009      | 1.07 ± 0.02       |
|           | 10                          | 0.270 ± 0.004 | 98 ± 9                            | 0.189 ± 0.003 | -93 ± 9                           | 0.081 ± 0.007      | 1.062 ± 0.007     |
|           | 5                           | 0.263 ± 0.003 | 64 ± 4                            | 0.195 ± 0.002 | -61 ± 4                           | 0.067 ± 0.005      | 1.042 ± 0.004     |
| 2         | 0.261 ± 0.003               | 38 ± 2        | 0.194 ± 0.002                     | -37 ± 2       | 0.066 ± 0.004                     | 1.013 ± 0.008      |                   |
| GCE       | 1000                        | 0.272 ± 0.005 | 1116 ± 38                         | 0.166 ± 0.004 | -1153 ± 26                        | 0.105 ± 0.009      | 0.98 ± 0.01       |
|           | 800                         | 0.269 ± 0.002 | 1014 ± 29                         | 0.169 ± 0.007 | -1042 ± 22                        | 0.101 ± 0.009      | 0.973 ± 0.009     |
|           | 500                         | 0.266 ± 0.003 | 830 ± 20                          | 0.173 ± 0.005 | -854 ± 13                         | 0.093 ± 0.008      | 0.972 ± 0.009     |
|           | 200                         | 0.261 ± 0.003 | 538 ± 8                           | 0.178 ± 0.001 | -550 ± 3                          | 0.083 ± 0.004      | 0.978 ± 0.008     |
|           | 100                         | 0.261 ± 0.002 | 398 ± 5                           | 0.182 ± 0.002 | -404 ± 2                          | 0.079 ± 0.004      | 0.984 ± 0.008     |
|           | 80                          | 0.258 ± 0.002 | 356 ± 4                           | 0.182 ± 0.002 | -362 ± 2                          | 0.077 ± 0.004      | 0.984 ± 0.008     |
|           | 50                          | 0.258 ± 0.002 | 283 ± 3                           | 0.183 ± 0.001 | -287 ± 2                          | 0.075 ± 0.003      | 0.987 ± 0.005     |
|           | 20                          | 0.257 ± 0.001 | 181 ± 2                           | 0.183 ± 0.001 | -182.6 ± 0.8                      | 0.073 ± 0.002      | 0.990 ± 0.005     |
|           | 10                          | 0.257 ± 0.001 | 129 ± 1                           | 0.184 ± 0.001 | -129.6 ± 0.4                      | 0.072 ± 0.001      | 0.992 ± 0.006     |
|           | 5                           | 0.257 ± 0.001 | 93.2 ± 0.3                        | 0.183 ± 0.001 | -92.8 ± 0.6                       | 0.073 ± 0.002      | 1.004 ± 0.003     |
| 2         | 0.257 ± 0.001               | 62.4 ± 0.2    | 0.182 ± 0.002                     | -60.8 ± 0.3   | 0.075 ± 0.003                     | 1.027 ± 0.002      |                   |

\* The potential refers to Ag/AgCl.

### 3.3.5 Electroactive surface area calculation of carbon papers with GO

The electroactive surface areas (ECSAs) of the GO modified CP (CPG) electrodes can be determined based on Eq. 3.1 using a specific capacitance ( $C_{sp}$ ,  $25 \mu\text{F cm}^{-2}$ )<sup>[250-251]</sup> typically for carbonaceous materials. According to Eq. 3.2, the capacitive current, obtained from CVs at different scan rates (0.002 to 0.010  $\text{V s}^{-1}$ ) in a potential window from 0 to 0.2 V vs Ag/AgCl in which no Faradic reactions are involved (Fig. 3.13), is linear with  $dE/dt$ . The value of  $C_{dl}$  used for ECSA calculation is the half of the slope.

$$ECSA = \frac{C_{dl}}{C_{sp}} \quad (3.1)$$

$$\Delta i = \frac{C_{dl}}{2} \times \frac{dE}{dt} \quad (3.2)$$

where the  $C_{dl}$  is the electrochemical double-layer capacitance in  $\mu\text{F}$ .  $\Delta i$  ( $\mu\text{A}$ ) is the difference between the anodic and cathodic capacitive current at the chosen potential of 0.15 V vs Ag/AgCl.  $dE/dt$  is the scan rate in  $\text{V s}^{-1}$ . The calculated ECSAs in  $\text{cm}^2$  are summarized in Table 3.2. The calculated ECSA increases significantly when the sonication time increases from 10 to 90 min, with the highest value of  $0.0860 \pm 0.0006 \text{ cm}^2$  at 120 min for CPG120 electrodes probably due to the enhanced hydrophilicity of electrodes. Thus, CPG120 was used as the electrode substrate for further enzymatic bioelectrode fabrication.

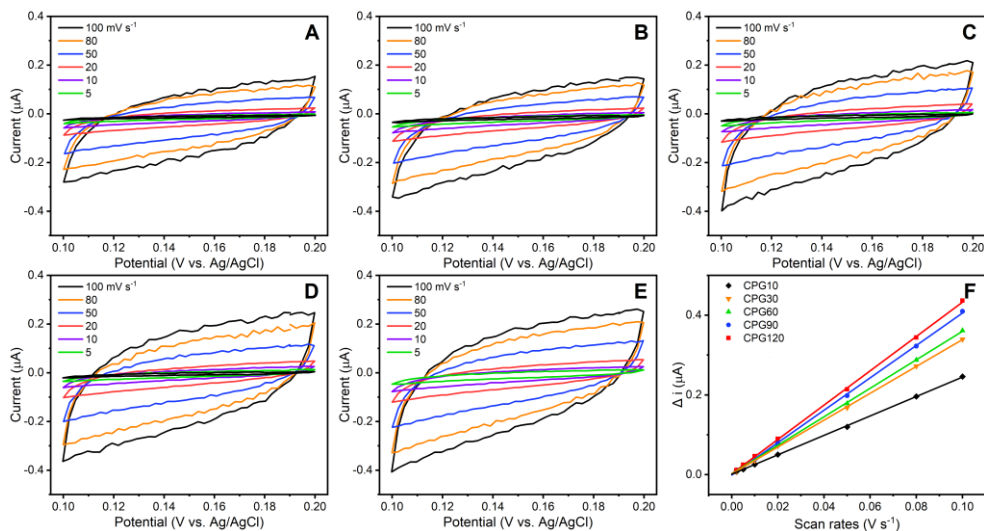


**Figure 3.13** CVs in 100 mM KCl for (A) CPG10, (B) CPG30, (C) CPG60, (D) CPG90 or (E) CPG120 at different scan rates; (F) corresponding capacitive currents plotted as a function of scan rate.

**Table 3.2** Summary of ECSAs of various CPG electrodes based on Fig. 3.13.

| Electrode | Slope in Fig. 3.13F | $C_{dl}$ ( $\mu\text{F}$ ) | ECSA ( $\text{cm}^2$ ) |
|-----------|---------------------|----------------------------|------------------------|
| CPG10     | $2.44 \pm 0.02$     | $1.22 \pm 0.01$            | $0.0488 \pm 0.0004$    |
| CPG30     | $3.37 \pm 0.02$     | $1.69 \pm 0.01$            | $0.0674 \pm 0.0004$    |
| CPG60     | $3.58 \pm 0.02$     | $1.79 \pm 0.01$            | $0.0716 \pm 0.0004$    |
| CPG90     | $4.07 \pm 0.04$     | $2.04 \pm 0.02$            | $0.0814 \pm 0.0008$    |
| CPG120    | $4.30 \pm 0.03$     | $2.15 \pm 0.02$            | $0.0860 \pm 0.0006$    |

### 3.4 Conclusions

Several methods including strong acid/alkaline activation and GO coating via sonication were carried out to make CP hydrophilic. It was found that synthesized GO sheets with coated CP exhibited the remarkably improved hydrophilicity with a WCA less than  $50^\circ$ , suitable for uniform immobilization of aqueous nanomaterials and enzymes. Based on morphology characterization with SEM, small flakes, regarded as GO sheets, were found on the carbon fibers of CPG120, in contrast to bare CP. This demonstrated that the enhanced hydrophilicity of modified CP was attributed to the deposition of GO *via*  $\pi$ - $\pi$  interactions.

Electrochemical performance of modified CP electrodes was characterized by recording CV responses towards the redox probe  $[\text{Fe}(\text{CN})_6]^{3-/4-}$ . CPG electrodes showed better performance with a smaller  $\Delta E_p$  value than other treated CP electrodes including CP- $\text{HNO}_3$ , CP- $\text{NaOH}$  and CP- $\text{H}_2\text{O}$ . Furthermore, the sonication time of coating GO onto CP was optimized and the  $\Delta E_p$  of CPG electrodes with the same scan rate decreased (*i.e.* increasing reversibility) with increasing sonication time. In particular, CPG120 with a 120-min sonication had the lowest  $\Delta E_p$  among CPG electrodes, *i.e.*,  $0.081 \pm 0.007$  V for at  $10 \text{ mV s}^{-1}$ , quite close to that of the standard carbon electrode (GCE) at the same scan rate. In addition, the calculated ECSA for CPG electrodes increased significantly when the sonication time increased from 10 to 90 min, achieving the maximum value at 120 min ( $0.0860 \pm 0.0006 \text{ cm}^2$  for CPG120). The 3D porous CPG120 electrode with the best performance and highest ECSA was therefore chosen to be the substrate for the following enzymatic bioelectrode fabrications and it is simplified as CPG in chapter 4 and 5.

# Chapter 4

## 3D sulfite oxidase graphene-based bioanode for sulfite/O<sub>2</sub> biofuel cells

---

---

This chapter describes the fabrication and characterization of a three-dimensional sulfite oxidase bioelectrode based on graphene functionalized carbon paper and its application as a bioanode for sulfite/O<sub>2</sub> biofuel cells. The chapter is part of the published article “Three-Dimensional sulfite Oxidase Bioanodes Based on Graphene Functionalized Carbon Paper for Sulfite/O<sub>2</sub> Biofuel Cells” in *ACS Catalysis* co-authored by J. Tang, R. M. L. Werchmeister, L. Preda, W. Huang, Z. Zheng, S. Leimkühler, U. Wollenberger, X. Xiao, C. Engelbrekt, J. Ulstrup, and J. Zhang.

---

### 4.1 Introduction

Most EBFCs exploit small organic and biological molecules as fuels, with less consideration on using small inorganic molecules. *Human* sulfite oxidase (*hSO*) catalyzes the oxidation of sulfite to sulfate,<sup>[252-253]</sup> which can be immobilized onto electrodes for bioanodes in sulfite/O<sub>2</sub> EBFCs.<sup>[18]</sup> Oxidation of sulfite occurs at the Mo containing co-factor, while a heme domain relays generated electrons from the Mo active site to the other natural redox partners, or to artificial electron acceptors.<sup>[18, 254-257]</sup> The electrons are transferred to an electrode either *via* heterogeneous DET where the electrode directly receives electrons or *via* MET with a redox mediator as the electron acceptor.<sup>[258-259]</sup> DET of *hSO* on electrode surfaces has been extensively studied.<sup>[257, 260]</sup> *hSO* is proposed to exist in two conformations switching between an “open” and “closed” state.<sup>[254, 256-257]</sup> In the “open” state, the heme group can react with an external electrode partner, but is unable to interact with the Mo co-factor. In the “close” state, internal, intramolecular ET is triggered, while external ET is blocked. This suggests that the conformational change and enzyme orientation strongly affect ET efficiency between the Mo co-factor and the electrode surface in a “gated” overall enzymatic ET process.<sup>[257]</sup>

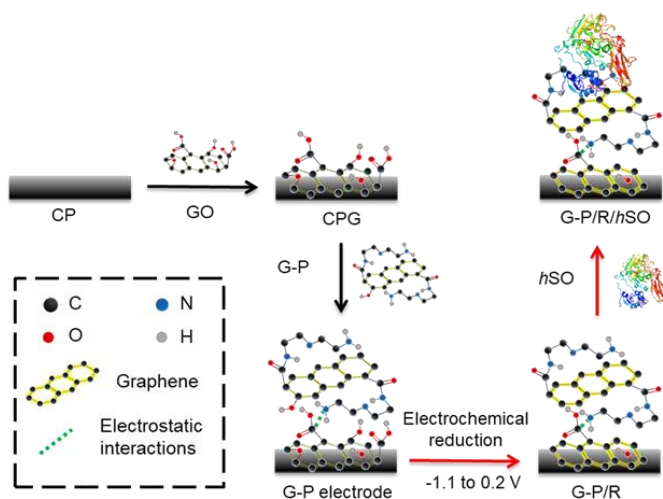
---

Positively charged electrode surface modifiers such as PEI have been adapted to promote adsorption of *h*SO (isoelectric point of  $\sim 5.5$ ) in a favorable orientation.<sup>[99, 260-262]</sup> The immobilized *h*SO on the electrodes can achieve DET with a low onset potential of the sulfite oxidation (ca.  $-0.2$  V vs. Ag/AgCl),<sup>[18]</sup> holding promise for sulfite/O<sub>2</sub> EBFCs with a high OCV. A sulfite/oxygen EBFC with an OCV of  $0.66$  V constructed with a *h*SO/PEI/thiol/AuNP/Au bioanode and a BO<sub>x</sub>/AuNP/Au based biocathode showing a  $P_{\max}$  of  $8 \mu\text{W cm}^{-2}$  was in fact reported recently.<sup>[18]</sup>

Design and preparation of electrode surfaces that can ensure that the stability and catalytic efficiency of the complex enzymes are retained or even improved on surface binding have been paramount in bioelectrochemical efforts.<sup>[245]</sup> The introduction of nanomaterials offers a strategy to promote the performance of *h*SO bioelectrodes. PEI-entrapped AuNPs covalently bound to a thiol-modified Au electrode have been successfully used for adsorption of *h*SO with improved electrocatalytic performance<sup>[99]</sup>. PEI-capped CdS QDs modified ITO is also proved to be a suitable matrix for *h*SO immobilization undergoing efficient DET with negligible competition from dioxygen reduction.<sup>[261]</sup> As noted, graphene has been widely applied in bioelectrode fabrication for EBFCs and biosensors due to its outstanding properties.<sup>[94, 263-264]</sup> RGOs obtained from the reduction of GOs have some structural defects, but offer good biocompatibility due to the presence of residual hydroxyl and carbonyl groups.<sup>[264]</sup> Both chemical and electrochemical reduction are efficient to obtain RGO from GO.<sup>[265]</sup> Compared to chemical reduction, electrochemical reduction is much more environmentally friendly due to the elimination of utilization of hazardous reducing agents (*e.g.*, hydrazine). The electrochemical reduction of GO is in fact an accumulative process.<sup>[266]</sup> The inner GO layers in direct contact with a conducting electrode can be electrochemically reduced wherever accessible to the electrolyte, while the outer GOs can be gradually reduced, once insulating GOs inside are converted to conductive RGO.<sup>[266]</sup> 3D graphene based electrodes such as graphene papers<sup>[267]</sup> and graphene foams<sup>[156]</sup> have emerged with considerable surface area for high-power-density FCs. This has prompted us to develop a 3D graphene substrate specifically for *h*SO immobilization,<sup>[27, 197]</sup> which is expected to gain enhanced bioelectrochemical signals compared to other reported *h*SO electrode materials due to a considerable surface area for the enzyme loading as well as local 3D environment to maintain the enzyme structure.<sup>[261, 268]</sup> Graphite electrodes have been used for the immobilization of *h*SO,<sup>[18, 268-269]</sup> but there are no reports on employing graphene to achieve DET between *h*SO and the electrodes.

In this work, we fabricated 3D *h*SO bioanodes based on graphene functionalized CP for sulfite/O<sub>2</sub> biofuel cells. As shown in Scheme 4.1, 3D graphene-based electrodes using CPs as supports coated with GO were designed. The pre-treated CP covered with GO (CPG) with improved surface hydrophilicity allow easier penetration and modification of the graphene-PEI (G-P) mixture. The CPG electrode covered with G-P (CPG/G-P) is further

electrochemically reduced (G-P/R) to increase the electroactive surface area and decrease the charge transfer resistance. *hSO* is drop-casted onto the electrode (G-P/R), on the basis that the polycation PEI induces favorable orientation of *hSO* *via* electrostatic binding to facilitate DET. The importance of electrochemical reduction of the modified electrodes was confirmed by control experiments. G-P composition, as well as pH and ionic strength of the electrolytes, were well optimized. Coupled with a Pt-based dioxygen reducing cathode, a two-compartment sulfite/O<sub>2</sub> EBFC was further built and tested. The *hSO* EBFC was fed with a flow of Na<sub>2</sub>SO<sub>3</sub> solution and dioxygen gas as fuels in the anodic and cathodic chambers, respectively.



**Scheme 4.1.** Schematic illustration of three-step construction process of a G-P/R/*hSO* on a CPG electrode. Stronger yellowish color is used to show the graphene with high conductivity. *hSO*, PDB:1SOX.

---

## 4.2 Experimental

### 4.2.1 Chemicals and materials

Potassium permanganate ( $\text{KMnO}_4$ ,  $\geq 99.9\%$ ) and potassium hexacyanoferrate(II) ( $\text{K}_4[\text{Fe}(\text{CN})_6] \cdot 3\text{H}_2\text{O}$ , 99.0-102.0%) were from Merck (Germany), acetic acid ( $\text{CH}_3\text{COOH}$ ,  $\geq 99.8\%$ ) from Riedel-deHaën (Germany). Sodium sulfite ( $\text{Na}_2\text{SO}_3$ ,  $\geq 98.0\%$ ), cytochrome *c* from bovine heart ( $\geq 95\%$ ), hexaammineruthenium(III) chloride ( $[\text{Ru}(\text{NH}_3)_6]\text{Cl}_3$ , 98%), graphite powder ( $< 20 \mu\text{m}$ ), tris(hydroxymethyl)aminomethane (Tris,  $(\text{HOCH}_2)_3\text{CNH}_2$ ,  $\geq 99.9\%$ ), hydrogen peroxide ( $\text{H}_2\text{O}_2$ , 34.5-36.5%), sulfuric acid ( $\text{H}_2\text{SO}_4$ , 95-97%), hydrochloric acid (HCl, 37%), potassium persulfate ( $\text{K}_2\text{S}_2\text{O}_8$ ,  $\geq 99\%$ ), phosphorous pentoxide ( $\text{P}_2\text{O}_5$ ,  $\geq 98\%$ ), branched polyethylenimine (PEI, molecule weight (MW) = 800 or 25000  $\text{g mol}^{-1}$ ), PEI solution (branched, 50% wt% in  $\text{H}_2\text{O}$ , MW = 1300 or 750000  $\text{g mol}^{-1}$ ), and the mediator N,N,N',N'-tetramethyl-p-phenylenediamine (TMPD, 99%) were from Sigma-Aldrich (USA). Branched PEI with a MW of 5000  $\text{g mol}^{-1}$  (Lupasol G 100) was from BASF (Germany). *hSO* (from the Department of Molecular Enzymology, University of Potsdam, Germany) was expressed in *Escherichia coli* TP1000 cells containing plasmid pTG718 and purified following a previous protocol.<sup>[252]</sup> Ethanol (96% vol.) was obtained from VWR Chemicals (USA). CP (product number EC-TP1-060, thickness of 190  $\mu\text{m}$ ) composed of carbon fibers with diameters of 6-8  $\mu\text{m}$ , Nafion membrane (perfluorinated ion exchange membrane, thickness 115  $\mu\text{m}$ ) and commercial platinum (Pt) cathodes (BC-H225-10F, the diameter of Pt nanoparticles: 5 nm, loaded onto activated carbon: 1.0  $\text{mg cm}^{-2}$ ) were purchased from Quintech (Germany). Glue gun (PKP 18 E) and hot melt adhesive (polyvinyl chloride, PVC) used to block CP were from BOSCH (Germany). All the solutions were prepared with 18.2  $\text{M}\Omega \text{ cm}$  Millipore water.

### 4.2.2 Synthesis of polyethylenimine-modified graphene nanomaterials

The detailed procedure of preparing GO by the modified Hummer's method<sup>[246-247]</sup> is described in section 3.2.2, Chapter 3. The G-P solution was produced by heating a solution containing 17.0 mL Millipore water, 2.0 mL GO solution (1.0  $\text{mg mL}^{-1}$ ), and 1.0 mL PEI (40  $\text{mg mL}^{-1}$ ) for 60 min at 95 °C. The color of GO solution changes from brownish yellow to black after reaction with PEI, Fig. 4.1, indicating that reduction of GO had taken place. The G-P mixtures were concentrated to 4.0 mL with a calculated concentration of 0.50  $\text{mg mL}^{-1}$  RGO and 10  $\text{mg mL}^{-1}$  PEI by centrifugation and kept at 4 °C for use. Unless otherwise specified, PEI with a MW of 25000  $\text{g mol}^{-1}$  was used as the optimum for all electrode modification.

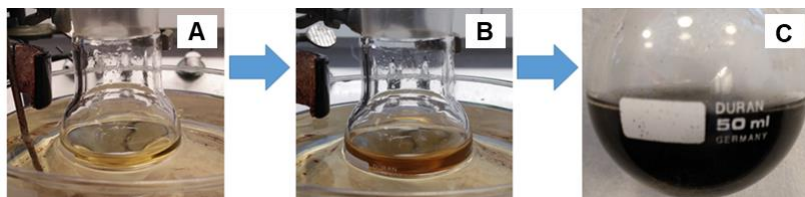


**Figure 4.1** Digital photos of (A) GO solution, (B) GO+PEI mixtures, and (C) G-P solutions.

#### 4.2.3 Fabrication of *h*SO modified bioelectrodes

Before modifications, the T-shape CP electrode with a working surface area ( $0.50 \times 0.50 \text{ cm}^2$ ) was prepared as described in section 3.2.3, Chapter 3. *h*SO bioelectrodes (G-P/R/*h*SO) were fabricated by a three-step procedure, Scheme 4.1, by the following recipe: 16  $\mu\text{L}$  G-P mixture was first drop-casted onto a  $0.25 \text{ cm}^2$  CPG electrode (labelled as G-P). After drying at room temperature, CPG/G-P was dipped ten times into deionized water to wash away any loosely bound nanomaterials. The CPG/G-P (or G-P electrode) was then reduced electrochemically by CV with 10 cycles at  $50 \text{ mV s}^{-1}$  in a potential window between  $-1.1$  and  $0.2 \text{ V}$  vs. Ag/AgCl (saturated KCl) in  $\text{N}_2$  saturated 15 mL Tris-acetate buffer solution (100 mM, pH = 7.0), resulting in CPG/G-P/-1.1R, simplified as G-P/R. Finally, 10  $\mu\text{L}$  of 10  $\mu\text{M}$  *h*SO in 0.5 mM pH 7.0 Tris-acetate buffer was drop-casted onto the moist G-P/R electrode. The resulting G-P/R/*h*SO electrode was dried in a petri dish for 2 to 3 h and then stored in a high-humid atmosphere at  $4 \text{ }^\circ\text{C}$ . The humid atmosphere was achieved with a wet tissue covered in a petri dish (diameter: 5.5 cm). Prior to electrochemical measurements, G-P/R/*h*SO electrodes were immersed ten times in 0.5 mM pH 7.0 Tris-acetate buffer to remove loosely bound *h*SO and to obtain the adsorption behavior of *h*SO on G-P/R electrodes. The amount of immobilized active *h*SO on the electrode is believed to be proportional to the catalytic response to the saturation concentration of substrate sulfite and the catalytic response of bioelectrodes obtained with different enzyme-incubation durations (from 5 to 180 min) was recorded. Specifically, the G-P/R electrode was incubated in 10  $\mu\text{L}$  of 10  $\mu\text{M}$  *h*SO in 0.5 mM pH 7.0 Tris-acetate buffer for 5, 10, 20, 40, 60, 120 or 180 min at  $4 \text{ }^\circ\text{C}$  and then washed with 0.5 mM pH 7.0 Tris-acetate buffer.

Control electrodes, including G-P/R/*h*SO using PEI with different MWs, PEI/R/*h*SO without RGO, and R/*h*SO without RGO and PEI, were prepared following the same procedure. G-P/R and G-P modified on CPG (CPG/G-P or G-P electrodes) without enzyme modification were also prepared. To optimize the electroreduction of G-P on CPG electrodes, the reduced electrodes with a potential window between  $-0.9$ ,  $-1.1$ ,  $-1.3$  or  $-1.5$  and  $0.2 \text{ V}$  vs. Ag/AgCl (saturated KCl) were obtained, labelled as G-P/-0.9R, G-P/-1.1R, G-P/-1.3R or G-P/-1.5R, respectively. Regarding to the fabrication of G-P/R/*h*SO, the electrochemical reduction step of the modified CP was carried out either before the drop-cast of G-P (labelled R/G-P/*h*SO), or both before and after the drop-cast (labelled as R/G-

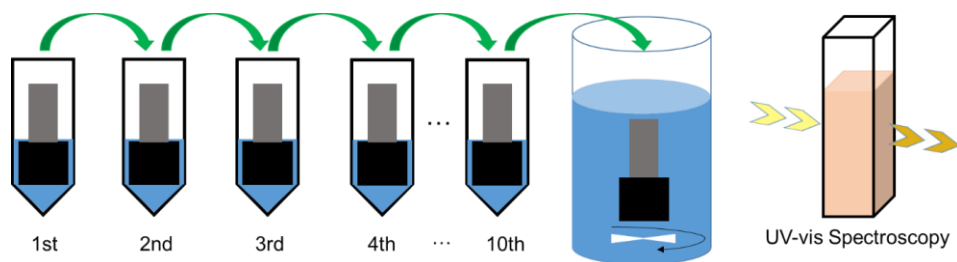


from the capacitive current values based on CV in dioxygen-free Tris-acetate buffer solution (750 mM, pH 8.4) in the absence of  $\text{Na}_2\text{SO}_3$ , similar to section 3.3.5, Chapter 3.

CV and chronoamperometry were carried out using a CHI 650B electrochemical workstation (CH Instruments, Inc., USA) or an Autolab PGSTAT12 (Eco Chemie, Netherlands), employing a three-electrode setup with a bioelectrode, a Pt wire, and Ag/AgCl (saturated KCl) as the working, counter, and reference electrode, respectively. All reported potentials are referred to the Ag/AgCl (saturated KCl) electrode. Unless otherwise stated, CV and chronoamperometry were recorded under stirring with a small magnet (10 mm diameter) at  $20 \pm 2$  °C. The electrolyte, 15 mL Tris-acetate buffer solution (750 mM, pH = 8.4), was purged with nitrogen gas for 30 min to remove dissolved dioxygen in prior to electrochemical tests.

#### 4.2.5 Activity assay of bioelectrodes

The dried G-P/R/*h*SO and G-P/*h*SO bioelectrodes were first immersed in 500  $\mu\text{L}$  of Tris-acetate buffer solution (pH 7.0, 0.5 mM) for 1 min to remove loosely bound *h*SO. The washed bioelectrode was then immersed into fresh 500  $\mu\text{L}$  of Tris-acetate buffer solution for another 1 min. This step was repeated 10 times, and thus a series of *h*SO bioelectrode washing buffer solutions (1st, 2nd 3rd, 4th ... and 10th) were obtained. The *h*SO activities of these washing solutions were determined from the rate of cytochrome *c* reduction using a spectrophotometer according to Eq. 4.1 and 4.2, Scheme 4.2. The cuvette contained 840  $\mu\text{L}$  of Tris-acetate buffer (pH 8.4, 50 mM), 50  $\mu\text{L}$  of cytochrome *c* (1.0 mM in Millipore water, stored in ice bath) and 10  $\mu\text{L}$  of  $\text{Na}_2\text{SO}_3$  (40 mM in 50 mM Tris-acetate buffer, pH 8.4). 100  $\mu\text{L}$  of the respective washing buffer solutions (1st, 2nd 3rd, 4th ... and 10th) was then added to the cuvette, with the absorbance change at 550 nm recorded for one minute.



**Scheme 4.2.** Schematic process of testing the activity assay by UV-vis spectroscopy of the bioelectrode washing solutions the 1st, 2nd 3rd, 4th ... and 10th time and the washed bioelectrode in the presence of indicator cytochrome *c* and substrate  $\text{Na}_2\text{SO}_3$ .



$$\text{Activity (U)} = \Delta A / \Delta t \times V_{\text{total}} \times V_{\text{washing buffer}} / (\epsilon \times L \times V_{\text{enzyme}}) \quad (4.2)$$

---

$\Delta A/\Delta t$  is the value of the absorbance change per minute at the wavelength 550 nm of reduced cytochrome *c*.  $\epsilon$  is the molar absorption coefficient (here,  $16.9 \text{ mM}^{-1} \text{ cm}^{-1}$ ) and  $L$  the light path of the cuvettes (1.0 cm).  $V_{total}$ ,  $V_{enzyme}$  and  $V_{washing\ buffer}$  are the volume of reaction solution (1.0 mL), added enzyme solution (0.10 mL) and the washing buffer solution (0.50 mL), respectively.

The washed bioelectrode was immersed in 5.0 mL solution which contained 4.7 mL Tris-acetate buffer (50 mM, pH 8.4), 250  $\mu\text{L}$  cytochrome *c* (1.0 mM in Millipore water) and 50  $\mu\text{L}$  40 mM  $\text{Na}_2\text{SO}_3$  (in 50 mM Tris-acetate buffer, pH 8.4) under stirring. At several time points, 500  $\mu\text{L}$  of the reaction solution was withdrawn and the absorbance of reduced cytochrome *c* determined at 550 nm. From the increase of reduced cytochrome *c* concentration, the catalytic activity of the immobilized *h*SO on electrodes was calculated, Eq. 4.3.

$$\text{Activity (U)} = \Delta A/\Delta t \times V_{total}/(\epsilon \times L) \quad (4.3)$$

where all parameters apart from  $V_{total}$  (here, 5.0 mL) have the same meanings and values as above.

#### 4.2.6 Construction and characterization of sulfite/ $\text{O}_2$ enzymatic biofuel cells

##### 4.2.6.1 Hot-pressing of Nafion membrane and the cathode

The membrane cathode assembly was composed of two components: a Nafion™ perfluorinated ion-exchange membrane ( $4.0 \times 4.0 \text{ cm}^2$ , 115  $\mu\text{m}$  thickness) and a commercial cathode. The membrane cathode assembly was assembled under hot-pressing at 135.0 °C and 120  $\text{kg cm}^{-2}$  pressure for 3 min.<sup>[247]</sup>

##### 4.2.6.2 Construction of enzymatic biofuel cells

The square-shaped G-P/R/*h*SO bioelectrode with a working surface area of  $1.0 \times 1.0 \text{ cm}^2$  was used as the bioanode of an EBFC ( $8.3 \times 8.3 \times 6.1 \text{ cm}^3$ ) together with a commercial Pt cathode separated by a Nafion membrane.<sup>[247]</sup> The EBFC was assembled with Teflon gaskets ( $60.0 \times 60.0 \text{ mm}^2$ , 185 to 220  $\mu\text{m}$  thickness) as mechanical protectors.<sup>[247, 270]</sup> Graphite blocks ( $60.0 \times 60.0 \text{ mm}^2$ , 12.0 mm thickness) were used for fuel or dioxygen supply, with Au-plates ( $60.0 \times 60.0 \text{ mm}^2$ , 990  $\mu\text{m}$  thickness) as current collectors. Teflon sheets ( $60.0 \times 60.0 \text{ mm}^2$ , 325  $\mu\text{m}$  thickness) were used as current-leaking protectors and aluminum (Al) blocks ( $84.0 \times 84.0 \text{ mm}^2$ , 10.0 mm thickness) as outer protectors, Fig. 4.3. Teflon gaskets were used to fix tightly the EBFC assembly of MCA/Nafion membrane and the *h*SO modified bioanode.

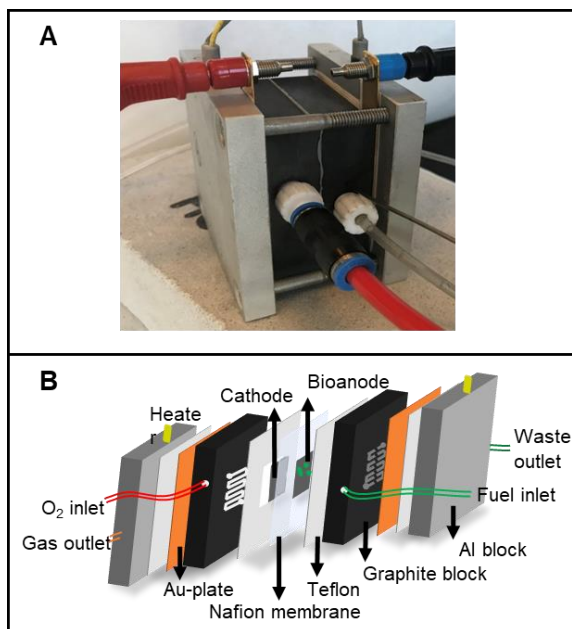
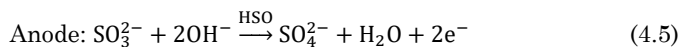


**Figure 4.3** (A) A digital photo and (B) schematic illustration of an EBFC.

#### 4.2.6.3 Electrochemical measurements of enzymatic biofuel cells

Prior to the tests, the Nafion membrane was wetted with Millipore water for 3-4 h using a peristaltic pump at  $2.0 \text{ mL min}^{-1}$ . Polarization and power density curves were recorded using an Autolab PGSTAT30 system (Eco Chemie, Netherlands) with the NOVA 1.1 software. These data were obtained using a two-electrode system with a bioanode (Eq. 4.5) and a cathode (Eq. 4.6) as the combined reference/counter and working electrodes, respectively. Fuel flow was controlled by a peristaltic pump (Minipuls 3, Gilson, French), while  $\text{O}_2$  flow ( $100 \text{ mL min}^{-1}$ ) and heating were fixed by a user interface panel designed by the LabVIEW 2015 software.<sup>[247]</sup> The electrocatalysis of the bioanode towards  $25 \text{ mM Na}_2\text{SO}_3$  oxidation operates in PBS ( $750 \text{ mM}$ ,  $\text{pH } 8.4$ ) with a constant flow rate of  $2.0 \text{ mL min}^{-1}$ .



## 4.3 Results and discussion

### 4.3.1 Characterization of electrode materials

CP electrodes, consisting of carbon fibers (6-8  $\mu\text{m}$  diameter), possess large surface areas in three dimensions suitable for high enzyme loading. However, as noted in Chapter 3, hydrophobic CP cannot disperse aqueous solution uniformly on the surface. Sonicating CP in a GO solution was verified to improve its hydrophilicity by coating with GO and the CPG was obtained, as described in Chapter 3. Larger thin flakes (added as G-P sheets) can therefore be uniformly immobilized on CPG, Fig. 4.4A. After electrochemical reduction, the coated nanomaterials aggregate, Fig. 4.4B, because the reduced GOs tend to restack by  $\pi$ - $\pi$  interactions.<sup>[266]</sup> The immobilization of *h*SO appears to result in further aggregation, due to the electrostatic interactions between negatively charged protein and positively charged G-P nanomaterials, Fig. 4.4C. As observed by EDS mapping, the distribution of nitrogen becomes non-uniform after *h*SO immobilization, implying that the observed aggregates contain PEI, Fig. 4.5.

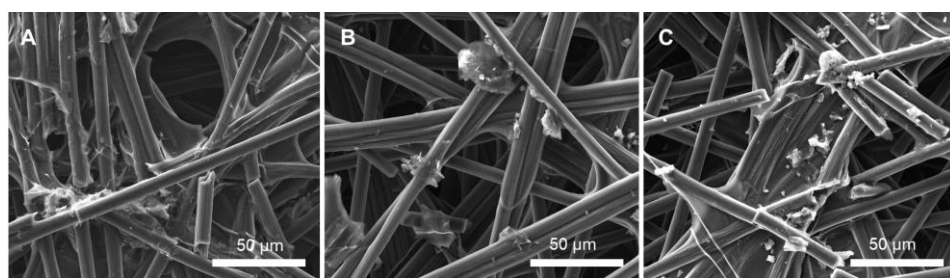


**Figure 4.4** SEM images of (A) CPG/G-P, (B) CPG/G-P/R and (C) G-P/R/*h*SO on CPG electrodes.

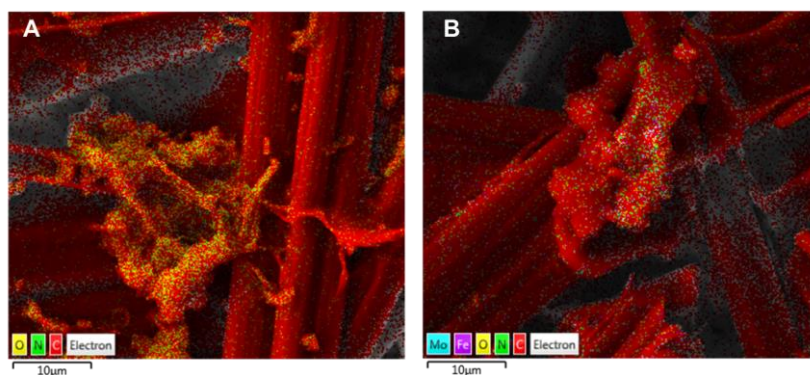


**Figure 4.5** SEM-EDX mapping of (A) G-P/R and (B) G-P/R/*h*SO on CPG electrodes.

XPS was used to examine the surface chemical composition, especially the carbon bonding states of the CP, CPG, CPG/G-P and CPG/G-P/R electrodes. The narrow spectra for C1s are well fitted into peaks at  $284.5 \pm 0.1$ ,  $285.0 \pm 0.1$ ,  $285.9 \pm 0.1$ ,  $286.6 \pm 0.1$ ,  $287.4 \pm 0.1$  and  $288.6 \pm 0.1$  eV, assigned to carbon atoms in C sp<sup>2</sup>, C sp<sup>3</sup>, C–N, C–O, C=O and COO<sup>–</sup>,<sup>[94, 267, 271]</sup> respectively, Fig. 4.6. The percent contribution of each carbon species, namely the relative peak area of each fitted component to the total carbon species, and values of the binding energy are summarized in Table 4.1. After coating of the CP by GO, the relative amount of oxygenated carbon species, *i.e.*, C–O, C=O and COO<sup>–</sup>, drastically increases from 4.0, 2.7 and 4.0% (of all carbon species) for CP to 20.7, 16.7 and 6.4% for CPG, respectively, Table 4.1. Such large amounts of oxygenated species originate from the GO film formed on the CP electrode.<sup>[271]</sup> The unexpected small amount of C–N species (Table 4.1) is likely from the inevitable impurities in CP. As expected, the presence of G-P nanomaterials increases the peak intensity of C–N by 14-fold (from 1.6 for CPG to 22.9% for CPG/G-P), indicating successful functionalization of CPG with G-P. After electrochemical reduction of the CPG/G-P electrode, only a 5.1% decrease for total oxygenated species, *i.e.*, C–O, C=O and COO<sup>–</sup>, was observed, Table 4.1. This might be because the electrochemical reduction step mainly affects GO coated on the CP by sonication. This GO is covered by the G-P nanocomposite, which dominates the XPS spectra, and is not affected by electroreduction, confirmed by the observation that electroreduction of CPG (CPG/R) leads to a 28.2% loss of total oxygenated species compared with the CPG electrode, Fig. 4.6, and Table 4.1.

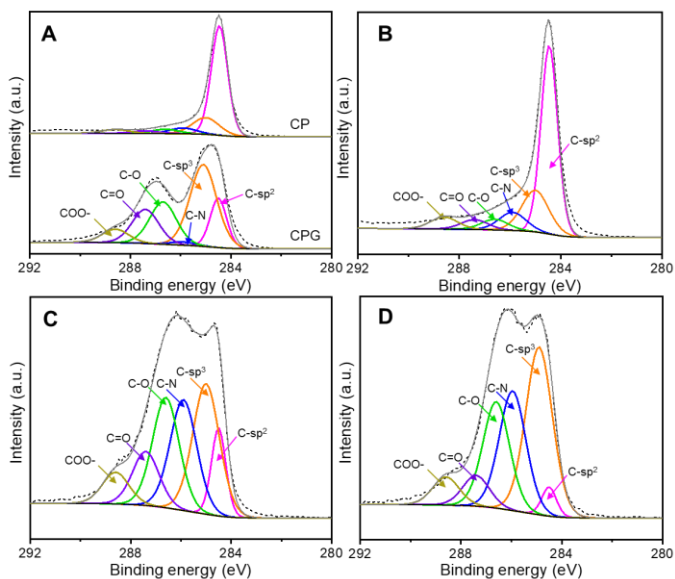


**Figure 4.6** C1s XPS spectra of (A) CP and CPG, (B) CPG/R, (C) CPG/G-P and (D) CPG/G-P/R. Black dot-curves are experimental data.

**Table 4.1** Relative peak area percentage of the carbon binding of all carbon species in CP, CPG, CPG/G-P, CPG/G-P/R and CPG/R electrodes determined by XPS (Fig. 4.5).

| Carbon status        | Binding energy (eV) | CP (eV) | CPG (eV) | CPG/R (eV) | CPG/G-P (eV) | CPG/G-P/R (eV) |
|----------------------|---------------------|---------|----------|------------|--------------|----------------|
| C sp <sup>2</sup>    | 284.5 ± 0.1         | 67.1    | 14.7     | 9.7        | 3.2          | 55.6           |
| C sp <sup>3</sup>    | 285.0 ± 0.1         | 16.8    | 39.8     | 27.0       | 36.0         | 20.0           |
| C–N                  | 285.9 ± 0.1         | 5.4     | 1.6      | 22.9       | 25.5         | 8.9            |
| C–O                  | 286.6 ± 0.1         | 4.0     | 20.7     | 22.9       | 22.7         | 5.0            |
| C=O                  | 287.4 ± 0.1         | 2.7     | 16.7     | 11.0       | 6.5          | 5.0            |
| COO–                 | 288.6 ± 0.1         | 4.0     | 6.4      | 6.5        | 6.1          | 5.6            |
| Total oxygen-species | -                   | 10.7    | 43.8     | 40.4       | 35.3         | 15.6           |

Raman spectra (Fig. 4.7) show the fingerprint signals of graphene. The D band is assigned to the disorders or defects in graphene or graphite materials, while the G band is associated with the vibration of sp<sup>2</sup> hybridized C–C bonds.<sup>[272]</sup> Fig. 4.7 shows that the I<sub>D</sub>/I<sub>G</sub> ratio of CPG/G-P (1.02) is higher than that of CPG (0.58), suggesting that the G-P nanomaterial coating on CPG has a more highly disordered structure. The highest I<sub>D</sub>/I<sub>G</sub> ratio (1.14) for CPG/G-P/R suggests the presence of a higher content of carbonaceous defects and disordered graphitized structure, resulting from the reduction of GOs to graphene sheets and their interactions with PEI.<sup>[273-274]</sup> XPS and Raman spectroscopy thus confirm that electrochemical treatment further increases the degree of GO reduction to graphene.

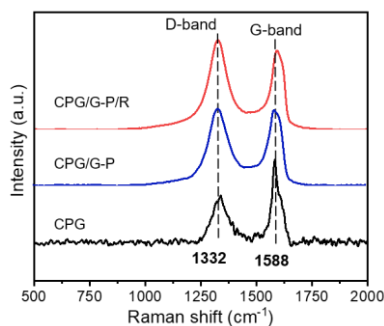


**Figure 4.7** Raman spectra of CPG, CPG/G-P and CPG/G-P/R electrodes.

The GO nanomaterials show a negative zeta potential ( $-7.8 \pm 0.2$  mV) in 750 mM Tris-acetate buffer solution (pH 8.4) because of the presence of oxygenated species, Table 4.2. Introduction of PEI with higher MWs increases the positive electrostatic charge of G-P nanomaterials except for G-P with the lowest MW (800 g mol<sup>-1</sup>), which might be due to the weaker dispersion of the short polymer chains for the reduced GO produced.

**Table 4.2**  $\zeta$  potentials of aqueous GO and G-P nanomaterials with different molecular weights (MWs) of PEI (*i.e.*, 800, 1,300, 5,000, 25,000, 750,000 g mol<sup>-1</sup>) in 750 mM Tris-acetate buffer (pH 8.4) determined by a Zetasizer Nano.

| Nanomaterial | $\zeta$ potential (mV) |
|--------------|------------------------|
| GO           | -7.8 ± 0.2             |
| G-P_MW800    | -8.5 ± 0.1             |
| G-P_MW1300   | 2.3 ± 0.2              |
| G-P_MW5000   | 8.2 ± 0.6              |
| G-P_MW25000  | 14 ± 1                 |
| G-P_MW750000 | 15 ± 1                 |

#### 4.3.2 Electrochemical characterization of modified electrodes

The electrochemical properties of the modified electrodes were first characterized by CV in a solution containing either negatively charged ( $K_4[Fe(CN)_6]$ ) or positively charged redox probes ( $[Ru(NH_3)_6]Cl_3$ ). After coating of G-P on the CPG electrodes, an increased peak current (3.41 mA cm<sup>-2</sup>) and a narrowed peak separation  $\Delta E_p$  (173 mV) were observed for  $[Fe(CN)_6]^{4-}$  (Fig. 4.8A), but a larger  $\Delta E_p$  (from 185 to 205 mV) for  $[Ru(NH_3)_6]^{3+}$  (Fig. 4.8B), Table 4.3. This is due to the addition of the polycationic PEI layer that alters the surface charge from negative to positive, consistent with the  $\zeta$  potential measurements. Upon electroreduction, both  $[Fe(CN)_6]^{4-}$  and  $[Ru(NH_3)_6]^{3+}$  give a reduced  $\Delta E_p$  due to the electrostatically more favourable ET.  $\Delta E_p$  increases after enzyme adsorption in both cases.

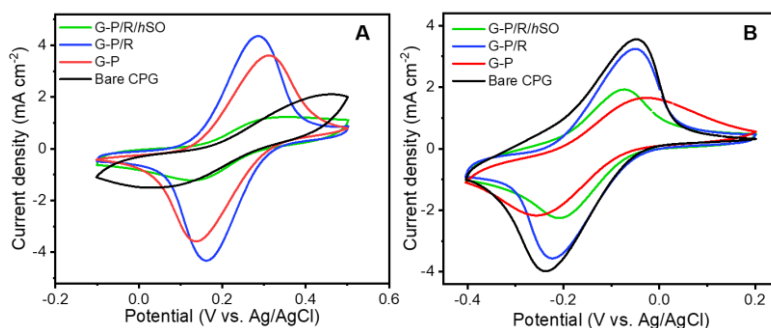


**Figure 4.8** CVs at 100 mV s<sup>-1</sup> of bare CPG, G-P, G-P/R and G-P/R/hSO electrodes recorded for oxygen-free KCl solution (100 mM) with 5.0 mM (A)  $K_4[Fe(CN)_6]$  or (B)  $[Ru(NH_3)_6]Cl_3$ .

**Table 4.3** Key voltammetry parameters of modified electrodes in 100 mM KCl in the presence of 5.0 mM  $K_4[Fe(CN)_6]$  or  $[Ru(NH_3)_6]Cl_3$  based on Fig. 4.8.

| Electrode | $K_4[Fe(CN)_6]$   |                              |                              | $[Ru(NH_3)_6]Cl_3$ |                              |                              |
|-----------|-------------------|------------------------------|------------------------------|--------------------|------------------------------|------------------------------|
|           | $\Delta E_p$ (mV) | $j_a$ (mA cm <sup>-2</sup> ) | $j_c$ (mA cm <sup>-2</sup> ) | $\Delta E_p$ (mV)  | $j_a$ (mA cm <sup>-2</sup> ) | $j_c$ (mA cm <sup>-2</sup> ) |
| Bare CPG  | 325               | 1.53                         | -0.62                        | 185                | 3.52                         | -3.43                        |
| G-P       | 173               | 3.41                         | -3.68                        | 205                | 1.51                         | -1.53                        |
| G-P/R     | 122               | 3.88                         | -4.17                        | 171                | 2.94                         | -3.42                        |
| G-P/R/hSO | 220               | 0.83                         | -0.66                        | 137                | 1.92                         | -2.07                        |

Furthermore, EIS studies of modified electrodes in 100 mM KCl containing 5.0 mM  $K_4[Fe(CN)_6]$  were carried out. The Nyquist plots are shown in Fig. 4.9. The equivalent circuit in Fig. 4.9B (inset) was fitted to the impedance spectra. As a certain degree of electrode roughness and inhomogeneity is evidenced according to SEM images, the use of a CPE instead of a capacitance is appropriate.<sup>[241-242, 275]</sup> Table 4.4 shows that CPG gives the highest charge transfer resistance ( $R_{ct}$ ) of 181  $\Omega$  among all the non-enzymatic electrodes, consistent with the CV curves which display the largest peak-peak separation  $\Delta E_p$  of 325 mV, and the smallest anodic peak current of 1.53 mA cm<sup>-2</sup> for the CPG electrode (black curve Fig. 4.8A and Table 4.3). This is due to the electrostatic repulsion between the negatively charged CPG surface and  $[Fe(CN)_6]^{3-/4-}$ , as well as the relatively low conductivity of GO. After coating of G-P on the CPG electrode, it is not surprising to observe a significant decrease of  $R_{ct}$  to 30.5  $\Omega$ . Additionally, an increased peak current (3.41 mA cm<sup>-2</sup>), and a narrowed peak-peak separation  $\Delta E_p$  (173 mV) were observed for  $[Fe(CN)_6]^{4-}$ , but a larger  $\Delta E_p$  (from 185 to 205 mV) for  $[Ru(NH_3)_6]^{3+}$ , Fig. 4.8 and Table 4.3. This is due to the addition of the polycationic PEI layer that alters the surface charge from negative to positive, consistent with the zeta potential measurements. The G-P on the CPG electrode was electrochemically reduced with increasing potential windows, *i.e.*, -0.9 to 0.2 V, -1.1 to 0.2 V, -1.3 to 0.2 V and -1.5 to 0.2 V.  $R_{ct}$  further drops from 19.4, 16.7, 15.8 to 12.6  $\Omega$  with the more negative potentials for reduction of GO, Fig. 4.9B and Table 4.4.

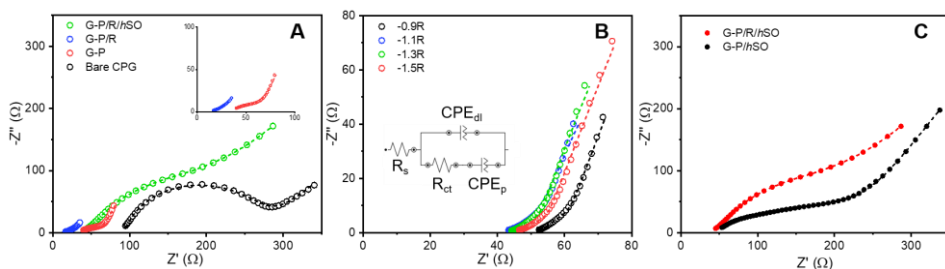


**Figure 4.9** EIS of (A) bare CPG, G-P, G-P/R and G-P/R/*h*SO, (B) G-P/-0.9R, -1.1R, -1.3R and -1.5R, (C) G-P/R/*h*SO and G-P/*h*SO electrodes recorded for 100 mM oxygen-free KCl with 5.0 mM  $\text{K}_4[\text{Fe}(\text{CN})_6]$ . Inset of (A): the magnified EIS of the G-P and G-P/R electrodes. Inset of (B): the equivalent circuit used to fit the impedance data.  $R_s$ : electrolyte solution resistance;  $R_{ct}$ : interfacial electron transfer resistance;  $\text{CPE}_{dl}$  and  $\text{CPE}_p$ : constant phase element of the electrode double layer and polarization, respectively.

**Table 4.4** Parameters obtained by fitting the impedance spectra based on the equivalent circuit (inset of Fig. 4.9B).

| Electrode          | $R_s$ ( $\Omega$ ) | $Y_{0,dl}$ ( $\text{S s}^{-\alpha_{dl}}$ ) | $\alpha_{dl}$ | $Y_{0,p}$ ( $\text{S s}^{-\alpha_p}$ ) | $\alpha_p$ | $R_{ct}$ ( $\Omega$ ) | $\chi \cdot 10^3$ |
|--------------------|--------------------|--|---------------|--|------------|-----------------------|-------------------|
| Bare CPG           | 93.6               | $4.72 \times 10^{-5}$                      | 0.868         | $6.96 \times 10^{-3}$                  | 0.525      | 181                   | 4.42              |
| G-P                | 38.5               | $1.59 \times 10^{-3}$                      | 0.632         | $1.59 \times 10^{-3}$                  | 0.750      | 30.5                  | 2.47              |
| G-P/-0.9R          | 53.1               | $8.85 \times 10^{-3}$                      | 0.707         | $9.65 \times 10^{-3}$                  | 0.892      | 19.4                  | 3.10              |
| G-P/-1.1R          | 15.0               | $6.00 \times 10^{-3}$                      | 0.461         | $9.20 \times 10^{-3}$                  | 0.582      | 16.7                  | 7.30              |
| G-P/-1.3R          | 44.7               | $9.00 \times 10^{-3}$                      | 0.684         | $1.22 \times 10^{-2}$                  | 0.898      | 15.8                  | 3.93              |
| G-P/-1.5R          | 46.8               | $5.26 \times 10^{-3}$                      | 0.706         | $1.12 \times 10^{-2}$                  | 0.850      | 12.6                  | 4.06              |
| G-P/R/ <i>h</i> SO | 43.0               | $7.96 \times 10^{-4}$                      | 0.679         | $3.81 \times 10^{-3}$                  | 0.595      | 258                   | 9.50              |
| G-P/ <i>h</i> SO   | 35.5               | $9.14 \times 10^{-4}$                      | 0.348         | $3.70 \times 10^{-3}$                  | 0.734      | 300                   | 7.47              |

On the other hand, larger electroreduction potential windows with more negative potentials result in smaller capacitive currents, Fig. 4.10, as indicated by the ECSA. The ECSAs of these reduced electrodes decrease from  $20 \pm 1$ ,  $18.6 \pm 0.7$ ,  $15.6 \pm 0.6$  to  $15 \pm 1$   $\text{cm}^2$  for the potential window -0.9 to 0.2 V, -1.1 to 0.2 V, -1.3 to 0.2 V and -1.5 to 0.2 V, respectively, Table 4.5. Since electrodes with lower  $R_{ct}$  and higher ECSA are usually more promising for bioelectrode fabrication, the potential window between -1.1 to 0.2 V was chosen for reduction of G-P and GO nanomaterials on the electrodes, Table 4.6. To simplify the abbreviation, the electrode CPG/G-P/-1.1R elsewhere denoted as G-P/R. Upon electroreduction, both  $[\text{Fe}(\text{CN})_6]^{4-}$  and  $[\text{Ru}(\text{NH}_3)_6]^{3+}$  give a reduced  $\Delta E_p$  due to the decreased electron transfer resistance, Table 4.3. After introduction of *h*SO on the G-P/R/*h*SO,  $R_{ct}$  increases dramatically to 258  $\Omega$ , reflecting that *h*SO is well immobilized on the electrode surface in accordance with the capacity measurements and reports on other enzyme electrodes.<sup>[276]</sup> In addition, the lower  $R_{ct}$  for G-P/R/*h*SO compared to G-P/*h*SO

indicates enhanced interfacial ET rate after the electroreduction treatment, Fig. 4.9C and Table 4.4.

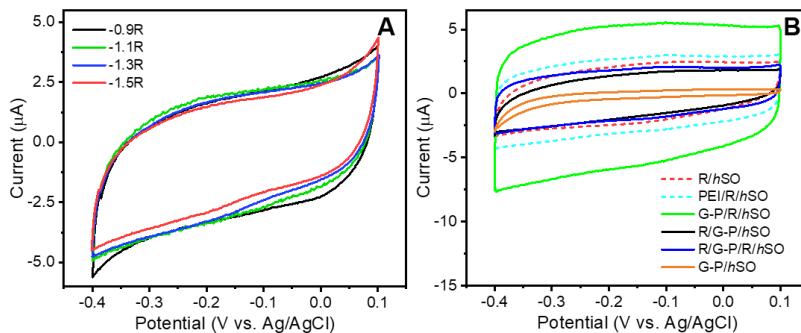


**Figure 4.10** Representative CVs of (A) G-P/R electrodes with different reduction windows (-0.9, -1.1, -1.3, or -1.5 to 0.2 V) and (B) various *hSO* bioelectrodes in oxygen-free Tris-acetate buffer solution (750 mM, pH 8.4) in the absence of  $\text{Na}_2\text{SO}_3$ ; scan rate:  $5 \text{ mV s}^{-1}$ .

**Table 4.5** Summary of ECSAs of G-P/R with different reduction windows (-0.9, -1.1, -1.3, or -1.5 to 0.2 V) and various *hSO* bioelectrodes based on Fig. 4.10.

| Electrode           | $\Delta i$ ( $\mu\text{A}$ ) | $C_{dl}$ ( $\mu\text{F}$ ) | ECSA ( $\text{cm}^2$ ) |
|---------------------|------------------------------|----------------------------|------------------------|
| G-P/-0.9R           | $4.9 \pm 0.3$                | $492 \pm 34$               | $20 \pm 1$             |
| G-P/-1.1R           | $4.6 \pm 0.2$                | $464 \pm 18$               | $18.6 \pm 0.7$         |
| G-P/-1.3R           | $3.9 \pm 0.1$                | $391 \pm 15$               | $15.6 \pm 0.6$         |
| G-P/-1.5R           | $3.9 \pm 0.3$                | $386 \pm 28$               | $15 \pm 1$             |
| R/ <i>hSO</i>       | $3.6 \pm 0.2$                | $355 \pm 18$               | $14 \pm 1$             |
| PEI/R/ <i>hSO</i>   | $5.7 \pm 0.6$                | $573 \pm 66$               | $23 \pm 2$             |
| G-P/R/ <i>hSO</i>   | $9.1 \pm 0.3$                | $910 \pm 30$               | $36 \pm 1$             |
| R/G-P/ <i>hSO</i>   | $2.5 \pm 0.5$                | $247 \pm 54$               | $10 \pm 2$             |
| R/G-P/R/ <i>hSO</i> | $3.4 \pm 0.1$                | $338 \pm 10$               | $13.5 \pm 0.4$         |
| G-P/ <i>hSO</i>     | $0.89 \pm 0.06$              | $89 \pm 6$                 | $3.6 \pm 0.2$          |

**Table 4.6** Comparisons of ECSAs and interfacial electron transfer resistance ( $R_{ct}$ ) of G-P/R with different reduction potential windows (-0.9, -1.1, -1.3, or -1.5 to 0.2 V) based on Fig. 4.9B and 4.10A.

| Electrode | ECSA ( $\text{cm}^2$ ) | $R_{ct}$ ( $\Omega$ ) |
|-----------|------------------------|-----------------------|
| G-P/-0.9R | $20 \pm 1$             | 19.4                  |
| G-P/-1.1R | $18.6 \pm 0.7$         | 16.7                  |
| G-P/-1.3R | $15.6 \pm 0.6$         | 15.8                  |
| G-P/-1.5R | $15 \pm 1$             | 12.6                  |

### 4.3.3 Electrocatalysis of bioelectrodes

The oxidation of sulfite on G-P/R/hSO electrodes was found to start at about -0.20 V vs. Ag/AgCl, in good agreement with previous reports.<sup>[18, 261]</sup> This potential is notably lower than that for the G-P/R electrode without hSO ( $\sim 0.02$  V vs. Ag/AgCl), Fig. 4.11A. This indicates that the immobilized hSO shows catalytic activity towards oxidation of  $\text{Na}_2\text{SO}_3$ , rather than the support electrode itself. The G-P/R/hSO bioelectrode shows 5.6-fold higher catalytic and 1.5-fold higher capacitive current compared to that of R/hSO (Fig. 4.11A and Table 4.5). The G-P modification therefore clearly increases the surface area for the amount of hSO capable of DET, which is supported by the higher estimated ECSA, increased from  $14 \pm 1 \text{ cm}^2$  for R/hSO to  $36 \pm 1 \text{ cm}^2$  for G-P/R/hSO, Table 4.5 and Fig. 4.10B. Similar phenomena were observed for G-P/hSO without electroreduction, Fig. 4.11B. Notably, the G-P/R/hSO bioelectrode exhibits both 9-fold higher catalytic oxidation of G-P/hSO bioelectrodes without electrochemical reduction, Fig. 4.11C, consistent to the 9-fold increased capacitive current and ECSA for G-P/R/hSO ( $36 \pm 1 \text{ cm}^2$ ) compared to G-P/hSO ( $3.6 \pm 0.2 \text{ cm}^2$ ) without the irreversible electrochemical reduction of GO on the electrodes, Fig. 4.12 and Table 4.5. The promoted electrochemical properties and catalytic activity are ascribed to the improved conductivity of the modified electrodes *via* electroreduction of GO on electrodes and thus the increased ECSA.

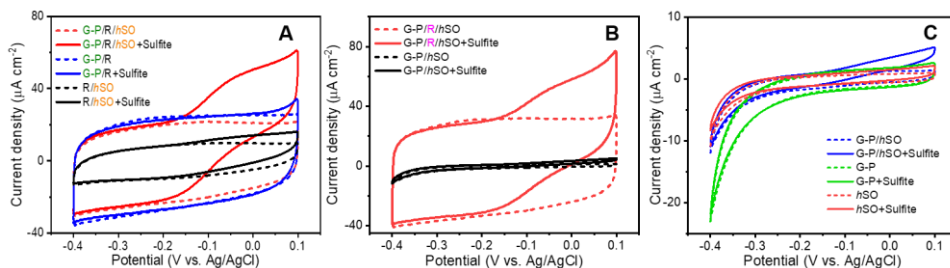


**Figure 4.11** CVs of the (A) G-P/R/hSO, G-P/R, and R/hSO electrodes, (B) G-P/R/hSO and G-P/hSO bioelectrodes, and (C) G-P/hSO, G-P and hSO on CPG electrodes in oxygen-free Tris-acetate buffer solutions (750 mM, pH 8.4) without (dashed) and with (solid) 1.0 mM  $\text{Na}_2\text{SO}_3$ ; scan rate:  $5 \text{ mV s}^{-1}$ .

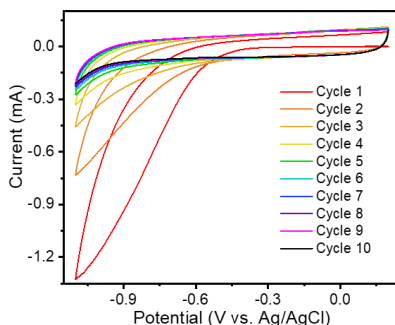


**Figure 4.12** Representative CVs for the reduction of G-P on CPG electrodes in oxygen-free Tris-acetate buffer solution (100 mM, pH 7.0) under stirring; scan rate: 50 mV s<sup>-1</sup>.

#### 4.3.4 Effect of electroreduction on biocatalysis

To further understand how the electroreduction treatment promotes the heterogeneous bioelectrocatalysis, the enzymatic activity of *h*SO in all washing buffer solution and the washed bioelectrodes was assayed, *cf.* section 4.2.5. It seems that the immobilization of *h*SO on aggregated substrate does not significantly change the activity, since the total relative enzyme activities (immobilized and detached) of G-P/R/*h*SO and G-P/*h*SO are 86 ± 5 and 97 ± 3% of the drop-casted enzyme, respectively, Table 4.7. The slightly lower activity for G-P/R/*h*SO is probably due to the inaccessibility inside the nanomaterials or the reduced accessibility of bound enzyme.

The enzyme activity in the solutions of ten successive washing steps is shown in Fig. 4.13A. The data show that the washing process can remove loosely bound enzyme from the bioelectrodes. Compared with the activity of all washing solutions for the bioelectrode without electroreduction (G-P/*h*SO, 0.048 ± 0.002 U), the washing solutions for the G-P/R/*h*SO electrode exhibit a 42% lower value (0.028 ± 0.001 U), Table 4.7. This implies that the G-P/R electrode substrate is more suitable for *h*SO immobilization. The washed G-P/R/*h*SO electrode (55 ± 4% of the total enzyme) shows 11% higher total enzymatic activity compared to the washed G-P/*h*SO (44 ± 1%), Fig. 4.13B and Table 4.7. This indicates that G-P/R/*h*SO carries only 11% more active *h*SO than G-P/*h*SO, even though the G-P/R modified electrode exhibits 9-fold higher estimated ECSA than the G-P modified electrode. Fig. 4.11B shows that the G-P/R/*h*SO bioelectrode shows 9-fold higher electrocatalytic oxidation current compared to G-P/*h*SO. This significantly enhanced DET response of G-P/R/*h*SO therefore proves that the increased interfacial electron transfer plays a decisive role. Furthermore, the estimated  $R_{ct}$  (258 Ω) of G-P/R/*h*SO is smaller than the value (300 Ω) of the bioelectrode without additional electrochemical reduction, an additional indication of enhanced contact between the electrode and electroactive

compounds, Fig. 4.9C. The reduction in  $R_{ct}$  might be caused by slight reduction of the amount of oxygenated species and thus less negative charge on the electrode surface.

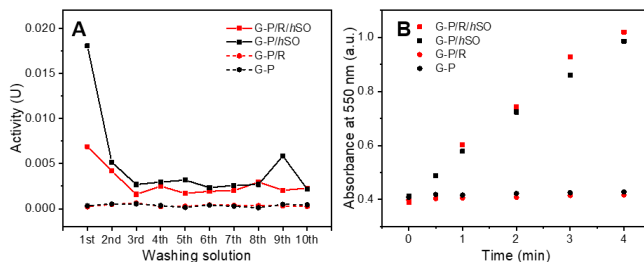


**Figure 4.13** (A) The enzyme activity of washing bioelectrode solutions based on the production of reduced cytochrome *c* (absorption wavelength = 550 nm) and (B) the absorbance value for reduced cytochrome *c* treated with the resulting washed bioelectrodes (G-P/R/*h*SO and G-P/*h*SO) in Tris-acetate buffer (pH 8.4, 50 mM) in the presence of substrate (0.40 mM  $\text{Na}_2\text{SO}_3$ ). G-P and G-P/R electrodes are controls.

**Table 4.7** The *h*SO activity in all washing solutions and immobilized on bioelectrodes (geometric area: 0.25  $\text{cm}^2$ ).

| Electrode  |                | $\Delta A_{550}/\Delta t$ ( $\text{min}^{-1}$ ) | Catalytic activity (U) | Percentage of total <i>h</i> SO (%) |
|--|----------------|---|------------------------|-------------------------------------|
| G-P/R/ <i>h</i> SO                               | Washed         | $0.110 \pm 0.003$                               | $0.028 \pm 0.001$      | $31 \pm 1$                          |
|  | immobilized    | $0.19 \pm 0.01$                                 | $0.050 \pm 0.004$      | $55 \pm 4$                          |
|  | In total       |   | $0.078 \pm 0.005$      | $86 \pm 5$                          |
| G-P/ <i>h</i> SO                                 | Washed         | $0.187 \pm 0.007$                               | $0.048 \pm 0.002$      | $53 \pm 2$                          |
|  | immobilized    | $0.157 \pm 0.001$                               | $0.040 \pm 0.001$      | $44 \pm 1$                          |
|  | In total       |   | $0.088 \pm 0.003$      | $97 \pm 3$                          |
| 10 $\mu\text{L}$ of 1 $\mu\text{M}$ <i>h</i> SO  |                | $0.179 \pm 0.007$                               | $0.0091 \pm 0.0003$    | 10                                  |
| 10 $\mu\text{L}$ of 10 $\mu\text{M}$ <i>h</i> SO | Applied amount |   | $0.091 \pm 0.003$      | 100                                 |

The oxidation current for the G-P/R/*h*SO electrode on increasing  $\text{Na}_2\text{SO}_3$  concentrations follows Michaelis-Menten kinetics and reaches saturation at 1.0 mM, Fig. 4.14. To evaluate the apparent oxidase activities of the bioelectrodes, the Michaelis-Menten parameters were calculated from variable  $\text{Na}_2\text{SO}_3$  concentrations based on Eq. 4.6.

$$v = \frac{V_m[S]}{K_m + [S]} \quad (4.6)$$

$$j = \frac{nFv}{A_G} \times 10^6 \quad (4.7)$$

where  $v$  can be expressed by the reaction rate in  $\text{mol s}^{-1}$ , corresponding to the bioelectrocatalytic current density  $j$  in  $\mu\text{A cm}^{-2}$ ,  $[S]$  is the concentration of the substrate

$\text{Na}_2\text{SO}_3$  in  $\mu\text{M}$ .  $\nu_m$  is the maximum reaction rate, and the related  $j_m$  is the saturation catalytic current density. The relationship between  $\nu$  and  $j$  is given by Eq. 4.7, where  $n$  is the number of electrons transferred in the electrochemical reactions (2 for sulfite oxidation), and  $F$  the Faraday constant ( $96485 \text{ C mol}^{-1}$ ).  $A_G$  is the geometric area of the electrodes, here  $0.25 \text{ cm}^2$ .

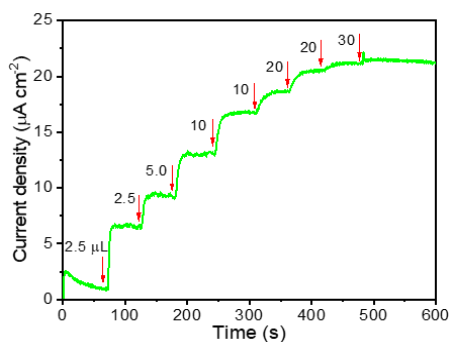


**Figure 4.14** Electrocatalytic responses of G-P/R/hSO bioelectrodes for increasing concentrations of  $\text{Na}_2\text{SO}_3$  on addition of different amounts of  $\text{Na}_2\text{SO}_3$  stock solutions (150 mM). All measurements were conducted in oxygen-free Tris-acetate buffer solution under stirring.

The Michaelis constant  $K_m$  in  $\mu\text{M}$  is the substrate concentration, at which the reaction rate is half of  $\nu_m$ . A smaller  $K_m$  for the free enzyme indicates a stronger binding affinity of enzyme to substrate and that the reaction rate approaches faster its maximum value. For  $h\text{SO}$  immobilized on the electrode surface, the apparent  $K_m$  is usually larger than in free solution due to the mass diffusion limitation.<sup>[268]</sup> The saturation values of the catalytic current density  $j_m$ , reaction rate  $\nu$ , and  $c$  apparent  $K_m$  of G-P/R/hSO are summarized in Table 4.8

#### 4.3.5 Optimization of bioelectrodes

Optimizations of (1) the electroreduction procedure, (2) graphene concentration in the G-P mixture, (3) effects of PEI with different MWs, (4) enzyme incubation durations, and (5) media (pH and ionic strength) were further conducted. Kinetic values for these bioelectrodes are summarized in Table 4.8 and 4.9.

**Table 4.8** Summary of enzyme kinetic parameters of various electrodes with different electroreduction procedures.

| Electrode   | $K_m$ ( $\mu\text{M}$ ) | $j_m$ ( $\mu\text{A cm}^{-2}$ ) | $v_m$ ( $\text{mol s}^{-1}$ )   |
|-------------|-------------------------|---------------------------------|---------------------------------|
| R/G-P/hSO   | $22 \pm 2$              | $3.42 \pm 0.04$                 | $4.43 \pm 0.05 \times 10^{-12}$ |
| R/G-P/R/hSO | $63 \pm 5$              | $12.7 \pm 0.2$                  | $1.64 \pm 0.02 \times 10^{-11}$ |
| G-P/R/hSO   | $111 \pm 5$             | $24.4 \pm 0.3$                  | $3.16 \pm 0.04 \times 10^{-11}$ |
| G-P/hSO     | $34 \pm 5$              | $2.46 \pm 0.06$                 | $3.19 \pm 0.08 \times 10^{-12}$ |

The catalytic performance of *h*SO electrodes with three different reduction procedures, *i.e.*, R/G-P/*h*SO, G-P/R/*h*SO, or R/G-P/R/*h*SO electrodes (the electrochemical reduction conducted before, after, or both before and after the drop-casting of G-P nanomaterials) is compared in Fig. 15A.  $j_m$  on G-P/R/*h*SO ( $24.4 \pm 0.3 \mu\text{A cm}^{-2}$ ) is seven times higher than that of R/G-P/*h*SO ( $3.42 \pm 0.04 \mu\text{A cm}^{-2}$ ), and twice higher than that of R/G-P/R/*h*SO ( $12.7 \pm 0.2 \mu\text{A cm}^{-2}$ ), Table 4.8. As can be seen from Table 4.9, to the best of our knowledge, G-P/R/*h*SO displays the highest  $j_m$  reported ( $24.4 \pm 0.3 \mu\text{A cm}^{-2}$ ) among all the reported *h*SO bioelectrodes.<sup>[18, 257, 261, 268]</sup> This is attributed to the high specific surface area of the RGO-based 3D electrode, enabling high enzyme loading. The electrochemical reduction of modified CPs before the drop-cast of G-P, however, might decrease the hydrophilic level of the CPG electrodes, leading to weaker interactions between the G-P and the electrode surface, and thus reduced electroactive surface area. This is supported by the calculated ECSAs for R/G-P/*h*SO and R/G-P/R/*h*SO, which are only 28% and 38% of the value of G-P/R/*h*SO, respectively, Table 4.5.

**Table 4.9** Comparison of catalytic performance ( $j_m$ ) of *h*SO immobilized on different modified electrodes with DET reported in literature.

| <i>h</i> SO on modified surface | Buffer              | pH  | $j_m$ ( $\mu\text{A cm}^{-2}$ ) | Ref.      |
|---------------------------------|---------------------|-----|---------------------------------|-----------|
| CPG/G-P/R                       | 750 mM Tris-acetate | 8.4 | $24.4 \pm 0.3$                  | This work |
| Au/AuNP/PEI                     | 750 mM Tris         | 8.4 | $0.37 \pm 0.02$                 | [99]      |
| ITO/CdS                         | 750 mM Tris-acetate | 8.4 | $1.0 \pm 0.1$                   | [261]     |
| Au/AuNP/thiol/PEI               | 750 mM Tris-acetate | 8.4 | 15                              | [18]      |
| Au/DTSP/AuNP                    | 750 mM Tris-acetate | 8.4 | $1.0 \pm 0.2$                   | [276]     |
| ITO/APTES                       | 750 mM Tris-acetate | 8.4 | $0.45 \pm 0.01$                 | [98]      |

*DTSP*: dithio-bis(*N*-hydroxysuccinimidyl propionate); *APTES*: aminopropyltriethoxysilane.

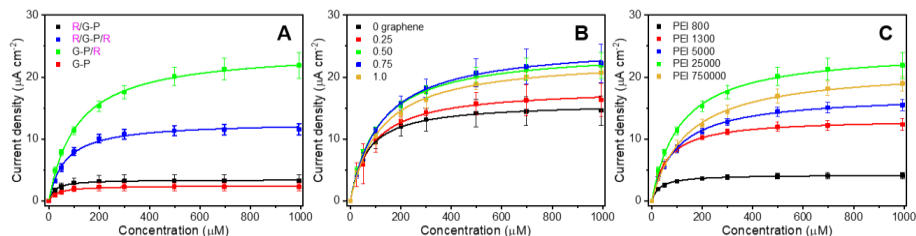


**Figure 4.15** The catalytic behavior of various bioelectrodes (A) fabricated by different electroreduction procedures, (B) with different amounts of graphene (RGO), and (C) with different MWs of PEI. The solid lines are Michaelis-Menten fitting curves. All measurements were conducted in oxygen-free Tris-acetate buffer solution under stirring.

**Table 4.10** Summary of enzyme kinetic parameters of G-P/R/*h*SO bioelectrodes with different graphene (reduced GO) concentrations ( $C_G$ ) and PEI MWs.

| $C_G$<br>(mg mL <sup>-1</sup> ) | PEI MWs<br>(g mol <sup>-1</sup> ) | $K_m$<br>( $\mu$ M) | $j_m$<br>( $\mu$ A cm <sup>-2</sup> ) | $\nu_m$<br>(mol s <sup>-1</sup> ) |
|---------------------------------|-----------------------------------|---------------------|---------------------------------------|-----------------------------------|
| 0                               | 25000                             | $65 \pm 2$          | $15.8 \pm 0.1$                        | $2.05 \pm 0.01 \times 10^{-11}$   |
| 0.25                            | 25000                             | $88 \pm 6$          | $18.2 \pm 0.3$                        | $2.36 \pm 0.4 \times 10^{-11}$    |
| 0.50                            | 25000                             | $111 \pm 5$         | $24.4 \pm 0.3$                        | $3.16 \pm 0.04 \times 10^{-11}$   |
| 0.75                            | 25000                             | $122 \pm 4$         | $25.4 \pm 0.2$                        | $3.29 \pm 0.03 \times 10^{-11}$   |
| 1.0                             | 25000                             | $118 \pm 6$         | $23.2 \pm 0.3$                        | $3.00 \pm 0.04 \times 10^{-11}$   |
| 0.50                            | 800                               | $32 \pm 1$          | $4.21 \pm 0.02$                       | $5.45 \pm 0.03 \times 10^{-12}$   |
| 0.50                            | 1300                              | $59 \pm 1$          | $13.2 \pm 0.1$                        | $1.72 \pm 0.09 \times 10^{-11}$   |
| 0.50                            | 5000                              | $100 \pm 3$         | $17.1 \pm 0.2$                        | $2.22 \pm 0.03 \times 10^{-11}$   |
| 0.50                            | 750000                            | $140 \pm 9$         | $21.5 \pm 0.4$                        | $2.78 \pm 0.05 \times 10^{-11}$   |

Here, graphene is crucial for enhancing the conductivity and surface area of CP. In the absence of graphene (RGO), PEI/R/*h*SO electrodes show smaller catalytic current compared to G-P/R/*h*SO, Fig. 4.15B. G-P nanomaterials with the concentrations 0.25, 0.5 and 1.0 mg mL<sup>-1</sup> graphene and 10 mg mL<sup>-1</sup> PEI, were used to optimize the amount of graphene for the *h*SO bioelectrodes. The saturation catalytic current increases with increasing graphene concentration up to 0.5 mg mL<sup>-1</sup>, Table 4.10.  $j_m$  of bioelectrodes with 0.75 mg mL<sup>-1</sup> ( $25.4 \pm 0.2 \mu$ A cm<sup>-2</sup>) and 1.0 mg mL<sup>-1</sup> graphene ( $23.2 \pm 0.3 \mu$ A cm<sup>-2</sup>) is comparable to that with 0.5 mg mL<sup>-1</sup> graphene ( $24.4 \pm 0.3 \mu$ A cm<sup>-2</sup>). 0.5 mg mL<sup>-1</sup> graphene is thus sufficient and used for the following experiments.

G-P nanomaterials were synthesized by partially reducing GO using PEI with MW of 800, 1300, 5000, 25000 or 750000 g mol<sup>-1</sup>. This is confirmed by the observation that the absorption peak of G-P corresponding to the  $\pi \rightarrow \pi^*$  transition of aromatic C–C bonds is red-shifted from 234 to 254 nm, indicative of the reduction of GO and the restoration of C=C bonds in the sheets (Fig. 4.16). However, the peak wavelength is lower than the

reported value of  $\sim 270$  nm for pure graphene,<sup>[233]</sup> likely due to incomplete reduction of GO. This is reasonable since G-P on electrodes can undergo further electrochemical reduction. The highest activity was found for the bioelectrodes with the PEI MW of  $25000 \text{ g mol}^{-1}$ , Table 4.10 and Fig. 4.15C. PEI with lower MW has been reported to weaken the immobilization strength for nanomaterials and enzyme compared to PEI with a larger MW,<sup>[277]</sup> resulting in aggregation of G-P nanomaterials and a lower current response. Further increasing the MW to  $750000 \text{ g mol}^{-1}$  gives a decreased signal (Fig. 4.15C), which can be explained by the significant drop of the conductivity.

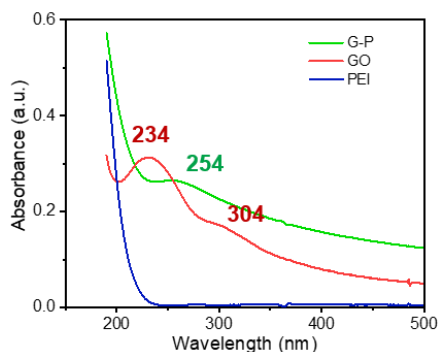


**Figure 4.16** UV-vis spectra of G-P (green), GO (red) and PEI (blue) nanomaterials in aqueous solution.

To investigate the adsorption behavior of *hSO* onto G-P/R modified electrode, the catalytic responses after variable durations of enzyme incubation were evaluated. A soaring catalytic current is obtained in the first 5 min, indicating quick adsorption of *hSO*, Fig. 4.17. After 120-min incubation, the catalytic current almost reaches a steady state. pH and ionic strength of supporting electrolyte were further optimized. The *hSO* bioelectrode shows the highest activity at pH 8.4 (Fig. 4.18A), close to the optimal pH (8.5) for *hSO* in solution.<sup>[268]</sup> The bioelectrocatalysis of *hSO* on modified CP depends strongly on the ionic strength of the electrolyte, which alters the flexible interaction between the built-in mediator heme *b<sub>5</sub>* domain and the catalytic Mo-containing unit.<sup>[257]</sup> The current density increases further with increasing buffer concentration up to 750 mM than that in the concentration range from 750 to 1000 mM, Fig. 4.18B. Because high ionic strength facilitates the flexible interaction between the built-in mediator heme *b<sub>5</sub>* domain, the catalytic Mo-containing unit and the electrode is facilitated, enabling higher electrocatalytic response of *hSO* bioelectrodes.<sup>[257, 260, 278]</sup> The rest of the electrochemical measurements were therefore carried out using a 750 mM pH 8.4 Tris-acetate buffer.

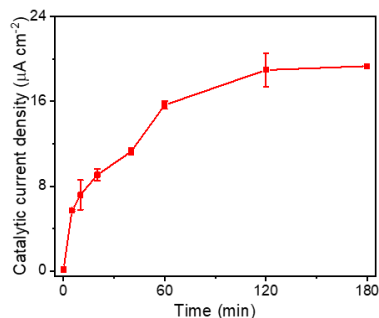


**Figure 4.17** Adsorption behavior of *hSO*: dependence of catalytic current towards 1.0 mM sulfite on the duration of incubation of the G-P/R electrode with 10 µL of 10 µM *hSO*. The enzyme was drop-casted and incubated for 0, 5, 10, 20, 40, 60, 120 or 180 min in high-humidity atmosphere at 4 °C. The catalytic response is recorded in oxygen-free Tris-acetate buffer solution (750 mM, pH 8.4) under stirring.

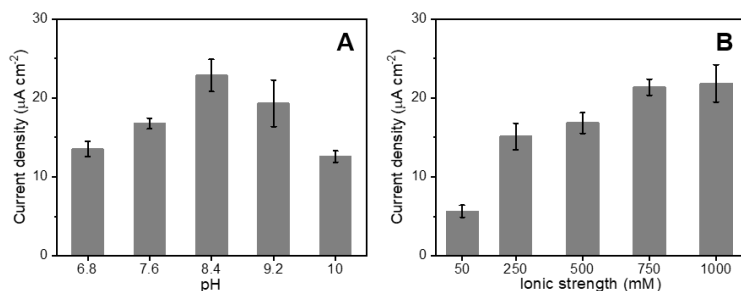


**Figure 4.18** Effects of (A) pH and (B) ionic strength of buffer on the performance of G-P/R/*hSO* bioelectrodes towards 1.0 mM Na<sub>2</sub>SO<sub>3</sub> operated at 0 V vs. Ag/AgCl. All measurements were conducted in oxygen-free Tris-acetate buffer solution under stirring.

#### 4.3.6 Evaluation of bioelectrodes

The *hSO* bioelectrodes show a fair stability in freshly changed electrolytes, Fig. 4.19A. After the initial five changes of electrolyte, the catalytic signal shows a rapid decrease, mainly due to enzyme detachment. The loss rate remains at 4 to 5% of the initial signal at each subsequent electrolyte exchange, implying that the immobilized *hSO* is gradually inactivated or further detached. In order to discriminate the denaturation from detachment of immobilized *hSO* from the electrodes, the catalytic responses on *hSO* bioelectrode (G-P/R/*hSO*) stored in high-humid atmosphere or immersed in Tris-acetate buffer solution (750 mM, pH 8.4) at room temperature for 3 h were measured. The control is a freshly prepared *hSO* bioelectrode. Bioelectrodes stored in high-humid atmosphere and buffer solution decreased by 6% and 17% of the original catalytic current,

respectively, Fig. 4.19B. This suggests that enzyme denaturation (6%) and enzyme detachment (11%) constitute a total 17% of the observed catalytic signal loss.

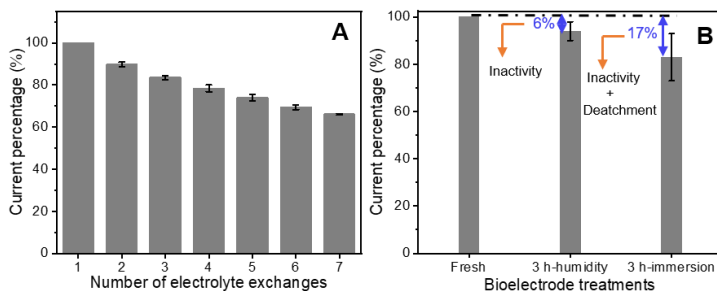


**Figure 4.19** (A) Stability of the G-P/R/*hSO* bioelectrodes in 1.0 mM  $\text{Na}_2\text{SO}_3$  operated at 0 V vs. Ag/AgCl. (B) Catalytic current percentage of G-P/R/*hSO* bioelectrodes stored in high-humidity atmosphere or immersed in Tris-acetate buffer solution (750 mM, pH 8.4) for 3 h at room temperature; the fresh bioelectrode as the control. The catalytic responses were recorded for oxygen-free Tris-acetate buffer solution (750 mM, pH 8.4) under stirring.

The stabilized *hSO* bioelectrode after five electrolyte exchanges was then used to evaluate the DET efficiency. The catalytic current of the *hSO* bioelectrodes undergoing MET was recorded using a mediator TMPD, Fig. 4.20. Notably, the catalytic current allows the first estimation of the fraction of immobilized *hSO* capable of DET. Based on the catalytic current ratio of DET to MET (Fig. 4.20B), 21% of the active *hSO* on the bioelectrode is thus capable of DET, while the rest cannot communicate with the electrode surface directly.

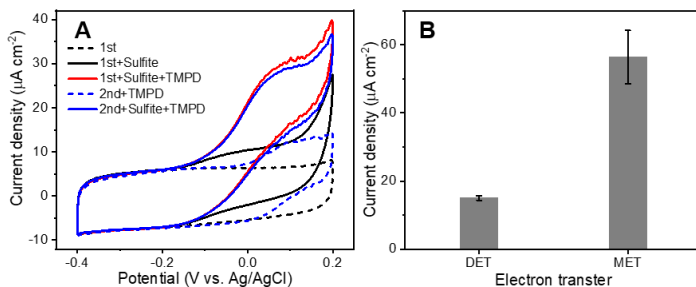


**Figure 4.20** (A) Evaluation of DET efficiency on the stabilized G-P/R/*hSO* bioelectrodes towards 1.0 mM  $\text{Na}_2\text{SO}_3$  in Tris-acetate buffer (750 mM, pH 8.4) under stirring. CVs at 5  $\text{mV s}^{-1}$ . 1st, 2nd, 3rd and 4th scan represent the measurement orders in fresh electrolytes. The concentration of the mediator TMPD for MET is 0.10 mM. (B) The corresponding current density with DET and MET. All measurements refer to oxygen-free Tris-acetate buffer (750 mM, pH 8.4).

In addition to the electrodes, O<sub>2</sub> can also be an external acceptor for the electrons generated from sulfite oxidation at the *h*SO co-factor. With the dioxygen reduction by the reduced enzyme, the catalytic current observed by CV thus decreases in air compared to N<sub>2</sub> atmosphere.<sup>[261]</sup> Two successive measurements each in freshly changed degassed electrolyte (1st+D and 2nd+D in Fig. 4.21) were first conducted to ensure that the expected stability of the bioelectrode was achieved. It turned out that the rate of catalytic current decrease (~ 5% of the original value) is consistent to the stability test (Fig. 4.21B). The catalytic activity of the same bioelectrode was then recorded in a non-degassed electrolyte (3rd+N in Fig. 4.21). Taking into account a 5% catalytic activity decrease expected from freshly changed degassed electrolyte, an additional ~10% reduced catalytic current in the non-degassed electrolyte was found, attributed to oxygen reduction by the reduced heme group co-factor. This is comparable to the value (~ 4%) of *h*SO on a CdS quantum dot modified ITO surface and much lower than the protein on a AuNP modified Au surface (40%).<sup>[261]</sup>

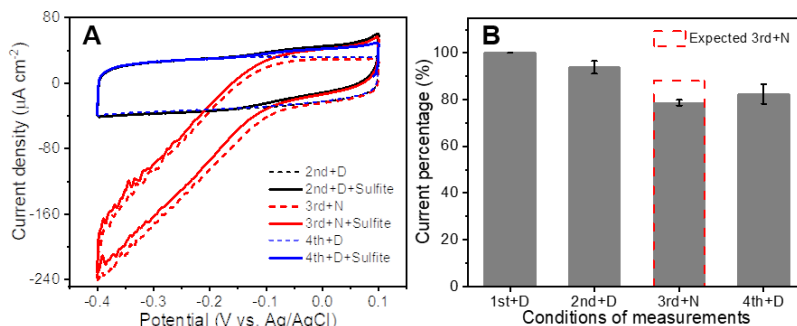


**Figure 4.21** (A) Effects of dioxygen competition of the G-P/R/*h*SO bioelectrodes in 1.0 mM Na<sub>2</sub>SO<sub>3</sub> operated at 0 V vs. Ag/AgCl. (B) The corresponding current density in the absence or presence of dioxygen. Except for the investigation on effects of dioxygen competition, all measurements refer to oxygen-free Tris-acetate buffer (750 mM, pH 8.4). D: degassed, N: non-degassed solution.

The storage lifetime of the *h*SO bioelectrode was investigated by storing the electrodes at 4 °C in a highly humid atmosphere. The bioelectrode activity has reduced by around 10% and 30% after one day and three days, respectively, Fig. 4.22A. After one week of storage, the current has dropped by 50%. A decrease of 34% of the initial response over 180 min operation was observed, Fig. 4.22B. The loss of activity (50%) during one-week storage is a consequence of enzyme inactivation and the detachment of immobilized *h*SO from the electrode surfaces.

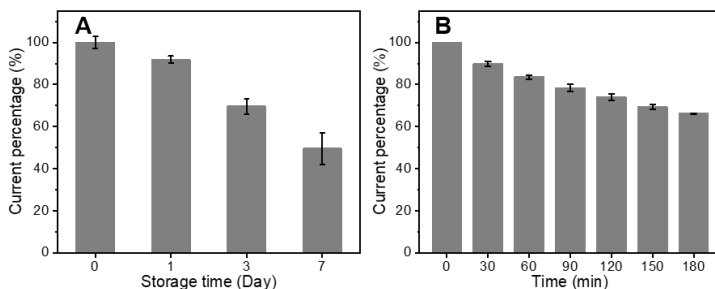


**Figure 4.22** (A) Storage and (B) operational stability of the G-P/R/*h*SO bioelectrodes in 1.0 mM Na<sub>2</sub>SO<sub>3</sub> operated at 0 V vs. Ag/AgCl. All measurements were carried out for oxygen-free Tris-acetate buffer solution (750 mM, pH 8.4) under stirring.

#### 4.3.7 Application of bioanodes in enzymatic biofuel cells

The *h*SO bioelectrodes were finally exploited as bioanodes in stacked FCs, coupled with a cathode based on commercial Pt catalysts. The sulfite concentration used was 25 mM, where the saturation current density was obtained for a three-electrode system under static conditions, Fig. 4.23. The control FC using a G-P/R electrode as the anode and the sulfite/O<sub>2</sub> EBFC were investigated by recording six consecutive polarization and power curves. The average polarization and power density curves are shown in Fig. 4.24A and B. The EBFCs with an OCV of  $0.64 \pm 0.01$  V reach a  $P_{\max}$  of  $61 \pm 6 \mu\text{W cm}^{-2}$  ( $122 \pm 14 \text{ mW m}^{-3}$ , normalized to the volume of the full FC), while the enzyme-free FCs show an OCV of  $0.40 \pm 0.06$  V and a  $P_{\max}$  of  $4 \pm 2 \mu\text{W cm}^{-2}$  ( $8 \pm 4 \text{ mW m}^{-3}$ ). Since *h*SO catalyzes the sulfite oxidation by reducing the onset potential and increasing the oxidation current, it is reasonable that the presence of *h*SO on the anode increases the OCV and thus the FC output power with the efficient commercial cathode. The  $P_{\max}$  decreases by 5% of the original value each time from the 3rd and 6th measurements, caused by the leakage of loosely bound *h*SO, as also observed for *h*SO bioelectrodes during electrolyte exchange, Fig. 4.19A. On the other hand, the OCV for the EBFCs is almost constant during consecutive measurements, fluctuating only from 0.63 to 0.65 V, Fig. 4.24C. Compared to EBFCs, the performance of the enzyme free control FCs consisting of a G-P/R anode (Fig. 4.24C) clearly degrades faster. The decrease in OCV by 41% and  $P_{\max}$  by 94% might be caused by a decrease in the amount of active sites and surface contamination.<sup>[279]</sup> Since the onset potential for sulfite oxidation by active *h*SO is stable in EBFCs, the OCV of EBFCs is between 0.63 and 0.65 V. The output  $P_{\max}$  only reduces by 30% during the six consecutive measurements.

Power outputs from the 3rd and 6th measurements were used to compare the performance of EBFCs at different temperatures, Fig. 4.24D. The OCV of EBFCs fluctuates from 0.57 to 0.68 V as the temperature rises, but without significant change. This is not surprising, as the stored charges in the capacitive matrix will maintain the

OCV at a high level.<sup>[32]</sup> However,  $P_{\max}$  increases from  $27 \pm 1$  to  $61 \pm 6 \mu\text{W cm}^{-2}$  ( $64 \pm 2$  to  $122 \pm 14 \text{ mW m}^{-3}$ ) when the temperature is increased from 15 to 30 °C, but drops to  $42 \pm 4 \mu\text{W cm}^{-2}$  ( $84 \pm 8 \text{ mW m}^{-3}$ ) at the further elevated temperature of 40 °C. The EBFCs with an OCV of  $0.64 \pm 0.01 \text{ V}$  reaches a  $P_{\max}$  of  $61 \pm 6 \mu\text{W cm}^{-2}$  at 30 °C, giving a 6.6-fold better output performance than previously reported sulfite/ $\text{O}_2$  EBFCs.<sup>[18]</sup> This phenomenon is different from our previously reported non-enzyme FCs which enhance the output performance with elevated temperatures up to 80 °C.<sup>[247]</sup> The temperature-dependent activity of the EBFCs is likely to come from the intrinsic properties of  $h\text{SO}$ ,<sup>[280]</sup> as free  $h\text{SO}$  in solution showed an optimal temperature of 30 °C, consistent with the observation here. The significantly enhanced performance compared to reported results of sulfite/ $\text{O}_2$  EBFCs<sup>[18]</sup> can be attributed to the high surface area for  $h\text{SO}$  loading and faster interfacial and intramolecular ET with concurrent strong electrocatalysis in the designed graphene based matrix.

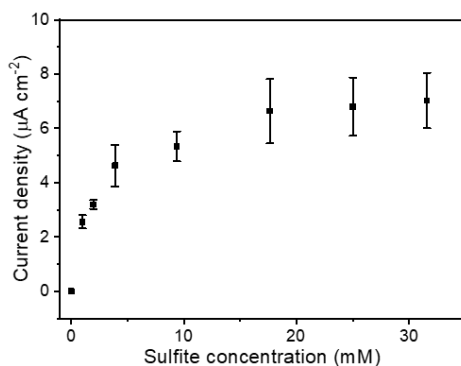


**Figure 4.23** Electrocatalytic response recorded by CA with G-P/R/ $h\text{SO}$  on  $1.0 \text{ cm}^2$  CPG electrodes under static conditions. After a quiescent period of 100 s, aliquots of  $\text{Na}_2\text{SO}_3$  (150 mM in 750 mM Tris-acetate buffer solution, pH 8.4) were added into the electrochemical cell to reach concentrations of 1.0, 2.0, 3.9, 9.4, 18, 25 and 32 mM in Tris-acetate buffer solution (750 mM, pH 8.4) in the present of dioxygen.  $E = 0 \text{ V}$  versus Ag/AgCl (saturated KCl).

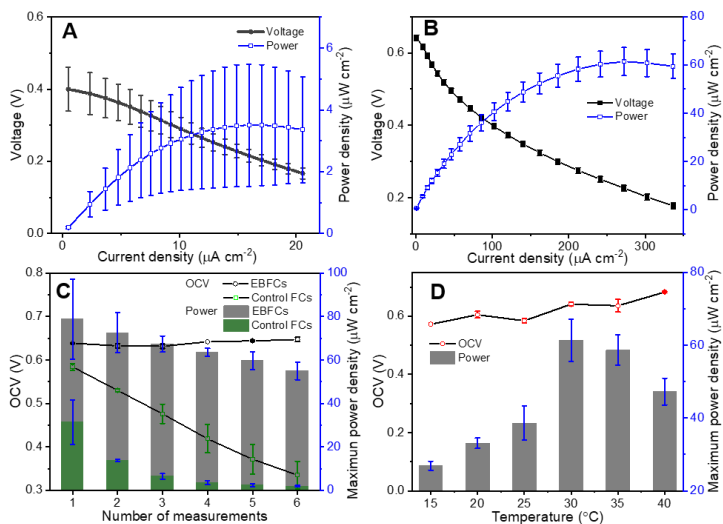


**Figure 4.24** Average polarization and power density curves of (A) control FCs and (B) EBFCs at 30 °C based on the 3rd to 6th measurements. (C) OCV and maximum power density of EBFCs and control FCs for six consecutive measurements at 30 °C. (D) Performance of EBFCs at different temperatures. All FCs were fed with Tris-acetate buffer (750 mM, pH 8.4) containing 25 mM  $\text{Na}_2\text{SO}_3$  ( $2.0 \text{ mL min}^{-1}$ ) in the presence of dioxygen at the bioanode and dioxygen ( $100 \text{ mL min}^{-1}$ ) at the cathode.

## 4.4 Conclusions

*h*SO bioanodes have been fabricated by electrostatic adsorption of *h*SO on the 3D graphene electrode surface modified by the polycation PEI. Electroreduction of the 3D graphene support improves significantly the catalytic performance of the bioelectrodes towards  $\text{Na}_2\text{SO}_3$  oxidation. The optimized saturation oxidation current ( $24.4 \pm 0.3 \mu\text{A cm}^{-2}$ ) is thus around 9 times higher than without electroreduction ( $2.48 \pm 0.08 \mu\text{A cm}^{-2}$ ). Electroreduction of GO on the 3D support can increase electronic conductivity of the electrode and decrease the interfacial electron transfer resistance between the electrode surface and electrolyte, showing enhanced contact of *h*SO with the electrode and therefore increased DET. Further, positively charged PEI can be an efficient DET promoter for *h*SO with proper orientation. The graphene-based *h*SO bioanodes developed combined with commercial Pt catalysts as cathodes were finally used to construct a sulfite/ $\text{O}_2$  based EBFC with a  $P_{\text{max}}$  of  $61 \pm 6 \mu\text{W cm}^{-2}$  ( $122 \pm 14 \text{ mW m}^{-3}$ ) and an OCV of  $0.64 \pm 0.01 \text{ V}$  at 30 °C. As a compact power generator or monitor, the stackable EBFC offers great potential for harvesting electrical energy from wastewater, foods and beverages containing sulfite.

# Chapter 5

## 3D bilirubin oxidase graphene-based biocathode for glucose/O<sub>2</sub> biofuel cells

---

This chapter describes the fabrication and characterization of a three-dimensional bilirubin oxidase bioelectrode based on graphene functionalized carbon paper and its application as a gas diffusion biocathode for glucose/O<sub>2</sub> biofuel cells. The chapter is included in the manuscript “Direct electron transfer of orientated bilirubin oxidase on three-dimensional carbon paper with reduced graphene aggregation” co-authored by J. Tang, X. Yan, W. Huang, C. Engelbrekt, J. Ulstrup, X. Xiao and J. Zhang (in preparation).

---

### 5.1 Introduction

Bilirubin oxidase (BOx) and laccase, in a family of MCOs, are interesting bioelectrocatalysts for four-electron ORR in mild pH solution.<sup>[119, 281]</sup> The active site of MCOs consists of four copper atoms, divided into three types as described in section 1.2: Cu<sub>T1</sub>, Cu<sub>T2</sub> and Cu<sub>T3</sub>.<sup>[282]</sup> During ORR, Cu<sub>T1</sub> receives electrons either from the oxidation of natural electron donors for MCO or from solid electrode surfaces (*i.e.* DET). The electrons are transferred to the trinuclear center including one Cu<sub>T2</sub> and two Cu<sub>T3</sub> atoms, in which O<sub>2</sub> is reduced to H<sub>2</sub>O.<sup>[89, 281]</sup> When the oxygen supply is sufficient, the electrocatalytic activity of MCO for DET on a solid electrode surface is determined by the rate of interfacial ET between the electrode and the Cu<sub>T1</sub> site of MCO. Theoretically, the distance for efficient electron tunneling should not exceed 1.5 nm,<sup>[283]</sup> highlighting the importance of proper orientation of MCO on the electrode. The modification of electrode surfaces with substrate-mimicking molecules is well accepted for achieving favorable orientation of MCO at the electrode surface.<sup>[284-286]</sup> The electrostatic and hydrophobic/hydrophilic micro-environment surrounding the Cu<sub>T1</sub> site should be taken into account when optimizing the orientation of MCO. For laccase, positively charged surface groups such as aminophenol groups can diminish the distance between the laccase Cu<sub>T1</sub> site and the electrode surface since aromatic amines belong to the natural substrates for laccase.<sup>[286]</sup> Laccase from

---

*Trametes versicolor* exhibits a hydrophobic domain in proximity to the Cu<sub>T1</sub> site, making  $\pi$ -extended hydrophobic groups such as anthraquinone, anthracene, naphthalene and pyrene promising candidates for immobilizing laccase for DET.<sup>[287]</sup> Widely-studied *Myrothecium verrucaria* BOx (*Mv*BOx) can efficiently undergo DET on negatively charged surfaces,<sup>[288]</sup> while *Bacillus pumilus* BOx prefers a positively charged electrode.<sup>[283]</sup> This highlights the importance of understanding the enzyme at a molecular level and electrode surface engineering. Moreover, enzyme engineering by site-directed mutation of *Magnaporthe oryzae* BOx provided surface-exposed cysteine residues which can be specifically linked to the electrode surface with maleimide groups *via* covalent binding.<sup>[89]</sup> Recently, it was reported that high DET bioelectrocatalytic current densities of BOx (up to  $\sim 0.2$  mA cm<sup>-2</sup> in static oxygen-saturated PBS solution) on electrochemically reduced GO based electrodes modified with negatively charged groups is achieved.<sup>[86]</sup> However, the system still suffered from the inevitable aggregation of the GO flakes (in a size of ca. 200  $\mu$ m).

In section 4.3.1, we described electrochemical GO reduction on 3D CPs. This, however, still leaves residual aggregation. Introducing hydrophilic surface groups such as sulfonic acid groups can also increase the dispersibility and separation of graphene layers in water.<sup>[289]</sup> To obtain well-dispersed graphene while maintaining high conductivity is thus paramount for bioelectrochemical applications. In order to overcome the problematic RGO aggregation, the work presented here employed 3D CPs as supports for RGO modified with a negatively charged molecule, 4-aminobenzoic acid (4-ABA), to enable the DET of *Mv*BOx.<sup>[119]</sup> The reduction of GO and grafting of 4-ABA were achieved simultaneously using an electrochemical pulse treatment applying negative and positive potentials alternately. Operational stability of the bioelectrode was investigated thoroughly. Finally, the fabricated bioelectrodes were applied in a gas diffusion electrode (GDE) configuration, and as a biocathode for glucose/O<sub>2</sub> EBFCs with a reported GOx bioanode.<sup>[290]</sup>

## 5.2 Experimental

### 5.2.1 Chemicals and materials

2,2'-Azino-bis(3-ethylbenzothiazoline-6-sulfonic acid) diammonium salt (ABTS,  $\geq 98\%$ ), potassium monohydrogen phosphate (K<sub>2</sub>HPO<sub>4</sub>,  $\geq 99.999\%$ ) and potassium dihydrogen phosphate (KH<sub>2</sub>PO<sub>4</sub>,  $\geq 99.999\%$ ) were from Fluka (Germany). Potassium hexacyanoferrate(II) (K<sub>4</sub>[Fe(CN)<sub>6</sub>]·3H<sub>2</sub>O, 99.0-102.0%) and potassium permanganate (KMnO<sub>4</sub>,  $\geq 99.9\%$ ) were obtained from Merck (Germany). Graphite powder (diameter of less than 20  $\mu$ m), phosphorous pentoxide (P<sub>2</sub>O<sub>5</sub>,  $\geq 98\%$ ), potassium peroxodisulfate (K<sub>2</sub>S<sub>2</sub>O<sub>8</sub>,  $\geq 99\%$ ), sulfuric acid (H<sub>2</sub>SO<sub>4</sub>, 95-97%), hydrogen peroxide (H<sub>2</sub>O<sub>2</sub>, 34.5-36.5%), hydrochloric acid (HCl, 37%), nitric acid (HNO<sub>3</sub>,  $\geq 65\%$ ), hexaammineruthenium(III)

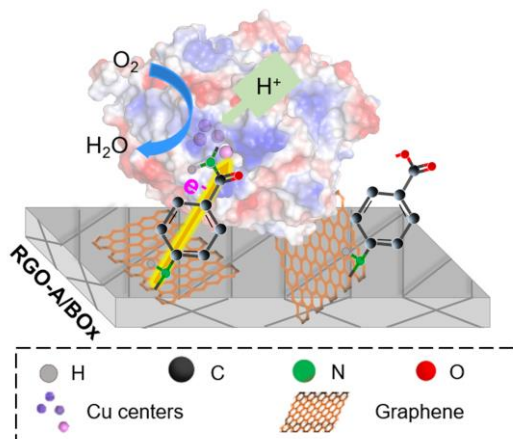
---

chloride ( $[\text{Ru}(\text{NH}_3)_6]\text{Cl}_3$ , 98%), N-cyclohexyl-N'-(2-morpholinoethyl) carbodiimide metho-p-toluenesulfonate (CMC, 95%), 4-ABA ( $\geq 99\%$ ) and poly(ethylene glycol)diglycidyl ether (PEGDGE) were from Sigma-Aldrich (USA). MbBOx (lyophilized powder, 15-65 unit  $\text{mg}^{-1}$  protein, molecule weight 60 kDa) was purchased from Sigma-Aldrich (USA) and used as received. Os(bpy)<sub>2</sub>PVI is kindly provided by Prof. Dónal Leech group in National University of Ireland Galway, synthesized according to an established procedure.<sup>[291-292]</sup> CP (product no. EC-TP1-060) with the thickness of 190  $\mu\text{m}$  was from Quintech (Germany). Hydrophobic CP (HCP, product no. HCP120, thickness 210  $\mu\text{m}$ ), the substrate of gas diffusion electrodes, was from Shanghai Hesun Electric Co. Ltd (China). Glue guns (Product no. PKP 18 E) with hot melt adhesive (*i.e.* polyvinyl chloride) used to fix the electrode geometric area were from BOSCH (Germany). All aqueous solutions were prepared with 18.2 M $\Omega$  cm Millipore water.

### 5.2.2 Fabrication of BOx modified bioelectrodes

The preparation of T-shaped CPG electrodes is described in section 3.2.3. BOx bioelectrodes (RGO-A/BOx), Scheme 5.1, on the CPG substrates were fabricated as follows: a 20  $\mu\text{L}$  GO suspension ( $3.0 \text{ mg mL}^{-1}$ ) was first drop-cast onto a  $0.25 \text{ cm}^2$  CPG electrode (labeled as CPG/GO electrode). After drying at room temperature, the CPG/GO electrode was then reduced and functionalized electrochemically by 15 cycles of alternating potential pulses  $-1.4 \text{ V}$  vs. Ag/AgCl (saturated KCl) for 10 s and  $1.4 \text{ V}$  for 5 s in a 15 mL Ar-saturated PBS (100 mM, pH 7.0) containing 5 mM 4-ABA. The functionalized electrodes, referred to as RGO-A, were then washed with Millipore water to remove loosely absorbed 4-ABA. The activation of  $-\text{COOH}$  groups was achieved by incubating the RGO-A electrode in 5 mM CMC aqueous solution for 2 h at  $4 \text{ }^\circ\text{C}$ . Finally, 10  $\mu\text{L}$  of  $1.25 \text{ mg mL}^{-1}$  BOx in 100 mM PBS (pH 7.0) was drop-cast onto the moist and activated RGO-A electrode. The prepared RGO-A/BOx electrodes were dried for *ca.* 12 h, and then stored at  $4 \text{ }^\circ\text{C}$  in a high-humidity atmosphere, *i.e.*, a plastic Petri dish (diameter: 5.5 cm) containing a wet tissue.

Controls, including electrodes without drop-cast GO suspension (R-A/BOx), electrodes where the CMC activation step was omitted and the BOx was physically adsorbed (RGO-A<sub>ads</sub>/BOx), as well as electrodes where electrochemical potential pulse treatment was done in the absence of 4-ABA in PBS (RGO/BOx), were prepared following the same procedure. To investigate the effect of the electrochemical potential pulse, bioelectrodes with different potential pulses of  $-1.4/0 \text{ V}$  (RGO-A(N)/BOx), and  $0/1.4 \text{ V}$  (GO-A/BOx) instead of the standard  $-1.4/1.4 \text{ V}$  (RGO-A/BOx) were prepared.



**Scheme 5.1** Schematic illustration of the prepared RGO-A/BOD on a CPG electrode and its bioelectrocatalysis process. A possible orientation of *Mv*BOD (PDB:2XXL), with surface charge distribution demonstrated with blue and red colour symbolizing positive and negative charges, respectively, is proposed. The left 4-ABA linker is occupied to form an amide bond with BOD, while the right 4-ABA with free -COO is still unreacted. Not drawn to real scale.

### 5.2.3 Electrochemical characterization of the modified electrodes

The basic electrochemical behavior of graphene modified electrodes without BOx modification was characterized by CV and electrochemical impedance spectroscopy (EIS) in 100 mM dioxygen-free PBS (pH 7.0) containing 5.0 mM  $K_4[Fe(CN)_6]$  or  $[Ru(NH)_6]Cl_3$ . EIS was conducted at 0.24 V vs. Ag/AgCl, with an applied alternating amplitude of 10 mV in the frequency range 0.1 to  $10^5$  Hz. CV was performed by scanning the potential from 0.00 to 0.65 V at a scan rate of  $50 \text{ mV s}^{-1}$ . CV in blank PBS at  $5 \text{ mV s}^{-1}$  was used to calculate the ECSA.

CV, in a potential window of 0.00 to 0.65 V at  $5 \text{ mV s}^{-1}$ , was used to characterize ORR performance of BOx bioelectrodes. Before electrochemical measurements, RGO-A/BOx bioelectrodes were immersed in 100 mM PBS (pH 7.0) for at least 30 min to remove loosely bound BOx molecules. A three-electrode setup was employed with BOx bioelectrodes, a Pt wire, and Ag/AgCl (saturated) as the working, counter, and reference electrodes, respectively. 15 mL 100 mM pH 7.0 PBS bubbled with either Ar or  $O_2$  for 30 min was used as the electrolyte for blank or ORR, respectively. The background-corrected ORR catalytic current density ( $\Delta j_{cat}$ ), normalized to a geometric area of  $0.25 \text{ cm}^2$ , is obtained based on the difference of cathodic currents at 0.2 V in Ar or  $O_2$  saturated solution. The operation stability of BOx bioelectrodes was evaluated by CA with an applied potential of 0.2 V in continuously air-bubbled PBS (100 mM, pH 7.0).

#### 5.2.4 Determination of the amount of active enzymes on electrodes

The amount of active BOx immobilized on electrodes was estimated from a standard calibration curve showing a linear relationship between the absorbance change rate of ABTS and the amount of BOx in solution. Briefly, the BOx bioelectrode was carefully washed with PBS (100 mM, pH 7.0) five times and then immersed in an air-equilibrated 100 mM PBS (pH 7.0) containing 0.50 mg mL<sup>-1</sup> ABTS with sufficient magnetic stirring. After certain soaking durations (*i.e.*, 1, 3, 5, 7, 10 min), 500 μL of the reaction solution was withdrawn, and its spectra in the range of 200 to 500 nm measured with an UV-vis spectrophotometer (UV-2401PC, SHIMADZU, Japan). The peak absorbance values were obtained at 420 nm

#### 5.2.5 Construction and characterization of gas diffusion bioelectrodes

The BOx bioelectrode was finally exploited as a gas diffusion bioelectrode (GDBE) with accelerated gaseous substrate supply. A commercial HCP, with one side treated with polytetrafluoroethylene (PTFE) which can prevent electrolyte leakage, was used as the gas diffusion support for RGO-A/BOx. The detailed fabrication of the GDBE is described as follows. One side of the HCP (1.0 × 1.2 cm<sup>2</sup>) was left without treatment, exposed to air and floating on 1.0 mg mL<sup>-1</sup> GO solution during 10 min of sonication. The hydrophilic side of the resulting HCP coated with GO sheets underwent further modification, onto which 80 μL of 3.0 mg mL<sup>-1</sup> GO solution was immediately drop-cast. The GO coating electrode was subsequently reduced and functionalized with 4-ABA by the electrochemical treatment. Finally, 40 μL of 1.25 mg mL<sup>-1</sup> BOx in 100 mM pH 7.0 PBS was drop-cast onto the activated side of the electrode. The prepared gas diffusion electrode was dried and then stored at 4 °C in a high-humidity atmosphere. For electrochemical characterization with a three-electrode system in an in-house built electrolyte cell (Fig. 5.1-5.3), the GDE was cut into a circle shape with a surface area of 0.33 cm<sup>2</sup>.

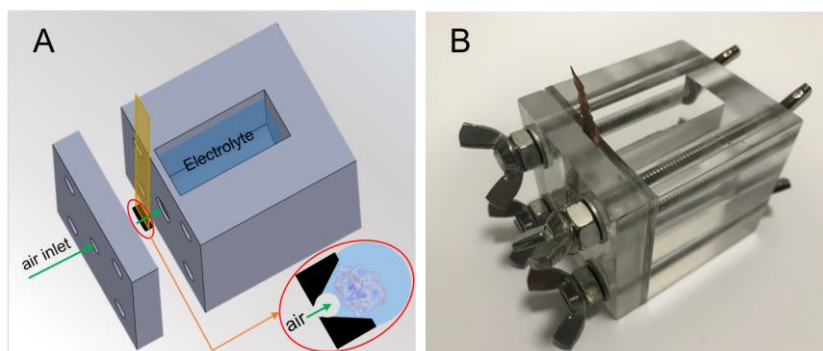


**Figure 5.1** (A) 3D view and (B) the digital photo of the in-house electrolyte cell.

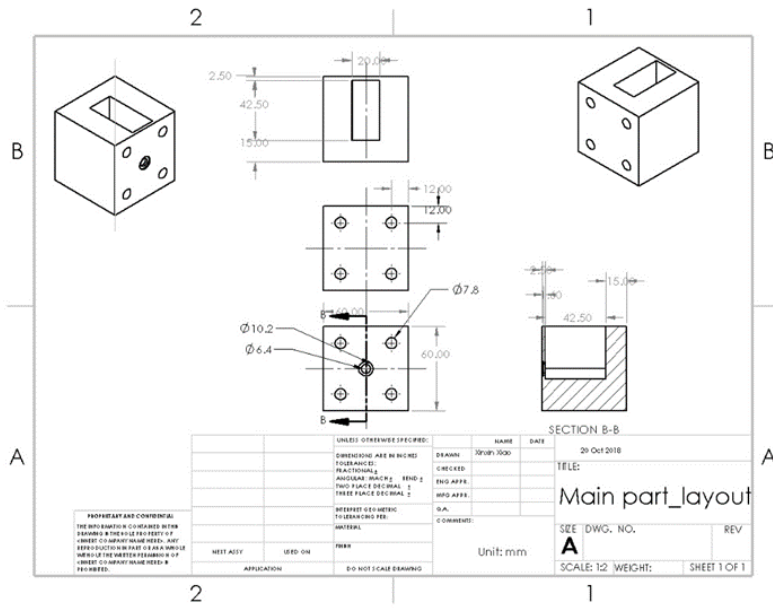


Figure 5.2 Layout of the main part of the in-house electrolyte cell (right part in Fig. 5.1A).

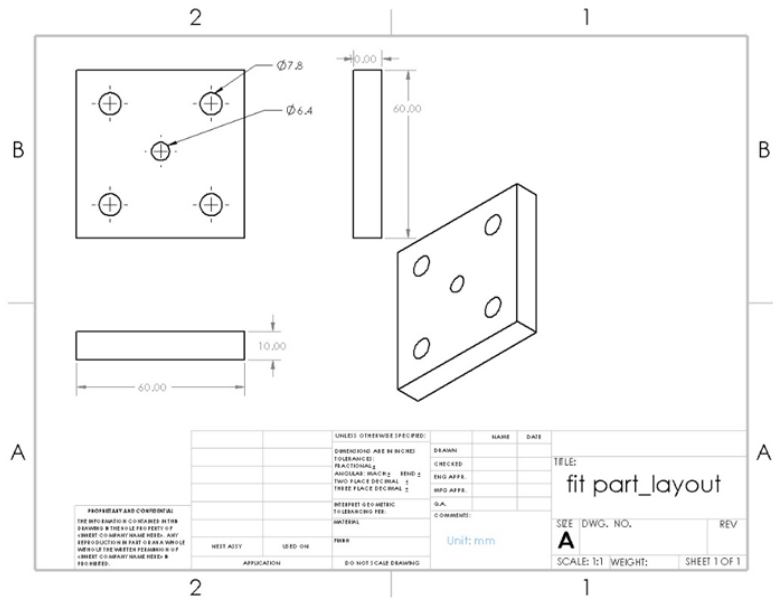


Figure 5.2 Layout of the fit part of the in-house electrolyte cell (right part in Fig. 5.1A).

---

### 5.2.6 Characterization of glucose/O<sub>2</sub> enzymatic biofuel cells

Prior to the GDE being applied as the biocathode in glucose/O<sub>2</sub> EBFCs, a GOx bioanode was prepared according to an established procedure.<sup>[290]</sup> Briefly, a 39.2  $\mu\text{L}$  of aqueous solution, containing 3.3  $\text{mg mL}^{-1}$  BOx, 2.0  $\text{mg mL}^{-1}$  PEGDGE, and 3.2  $\text{mg mL}^{-1}$  redox polymer, Os(bpy)<sub>2</sub>PVI, was drop-cast onto a nanoporous gold (NPG) electrode. After leaving the electrode in a vacuum desiccator for 20 min, the electrode was transferred to a refrigerator for drying overnight at 4 °C. For the electrochemical characterization of glucose/O<sub>2</sub> EBFCs, the GOx bioanode and the as prepared BOx GDE biocathode were immersed in 12 mL of PBS (100 mM, pH 7.0) in the in-house electrolyte cell and then connected to the electrochemical workstation as the working and reference/counter electrode, respectively. The GDE as the working electrode was fixed exactly at the middle hole on the side of the cell wall by tightening the screws firmly. After filling the air-equilibrated PBS electrolyte (100 mM, pH 7.0) above the middle hole, the catalytic performance was recorded with a three-electrode system. LSVs with a scan rate of 1  $\text{mV s}^{-1}$  were recorded to obtain polarization and power density curves.

## 5.3 Results and discussion

### 5.3.1 Characterization of electrode materials

CP consisting of carbon fibers arranged in three dimensions is suitable as an electrode substrate with high surface area.<sup>[293]</sup> GO is found to be uniformly coated on carbon fibers as seen by SEM images (Fig. 5.3A-B). After electrochemical pulse potential treatment in the absence of 4-ABA, the GO nanomaterials coated on CP aggregate because the resulting RGO sheets tend to stack due to  $\pi$ - $\pi$  interactions (Fig. 5.3E-F). Notably, the RGO-A shows the mildest aggregations compared to the RGO and RGO-A(N) (Fig. 5.3C-H). This is likely due to the presence of  $-\text{COO}^-$  (in neutral solutions) on RGO sheets introduced by the grafting of 4-ABA.<sup>[294-295]</sup> RGO-ABA with negative charges and thus relieves  $\pi$ - $\pi$  stacking due to electrostatic repulsion among the sheets.

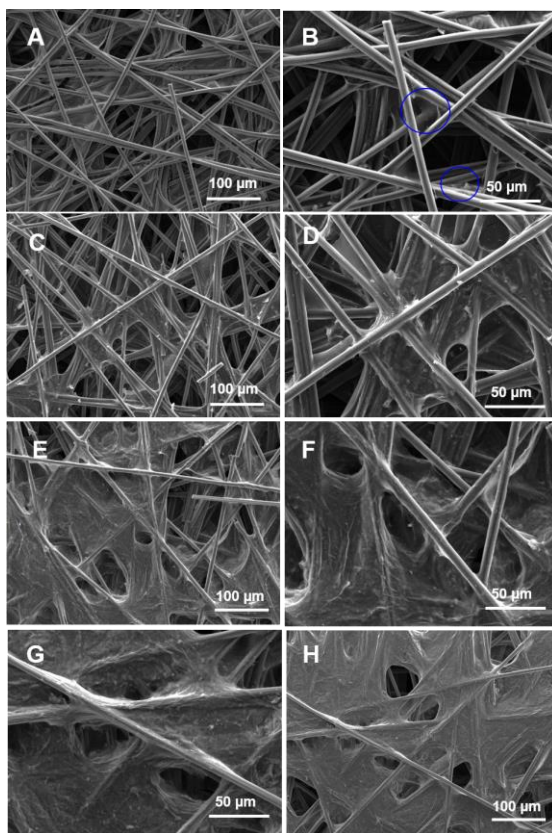


**Figure 5.3** SEM images of (A-B) CPG/GO, (C-D) RGO-A, (E-F) RGO, (G-H) RGO-A(N). Blue circles in (b) indicate the presence of GO sheets.

For further investigation, GO, RGO and RGO-A was immobilized on highly oriented pyrolytic graphite (HOPG) and characterized with AFM. To produce RGO or RGO-A from GO on HOPG, a narrower potential window (-1.0 and 0.8 V vs. Ag/AgCl), rather than -1.4 and 1.4 V vs. Ag/AgCl, was used to avoid any unwanted changes of the substrate HOPG, triggering the electrochemical oxidation of 4-ABA.<sup>[119]</sup> Excellent vertical resolution was obtained. It thus makes good sense that the thickness of GO ( $1.24 \pm 0.07$ ) measured is larger than that of RGO ( $0.78 \pm 0.03$ ) due to the removal of oxygenated groups *via* electroreduction, Fig. 5.4C-D and G-H, Fig. 5.5A-B and Table 5.1. RGO-A is  $\sim 2$  Å thicker than RGO (Fig. 5.4 E-F, Fig. 5.5B-C and Table 5.1), indicative of successful grafting of 4-ABA. 2 Å is, however, smaller than the distance ( $5.63$  Å) between the N atom of the  $\text{NH}_2$  group and the C atom of the COOH group of 4-ABA (Fig. 5.6), suggesting that the grafted 4-ABA is in a tilted orientation on the RGO surface.

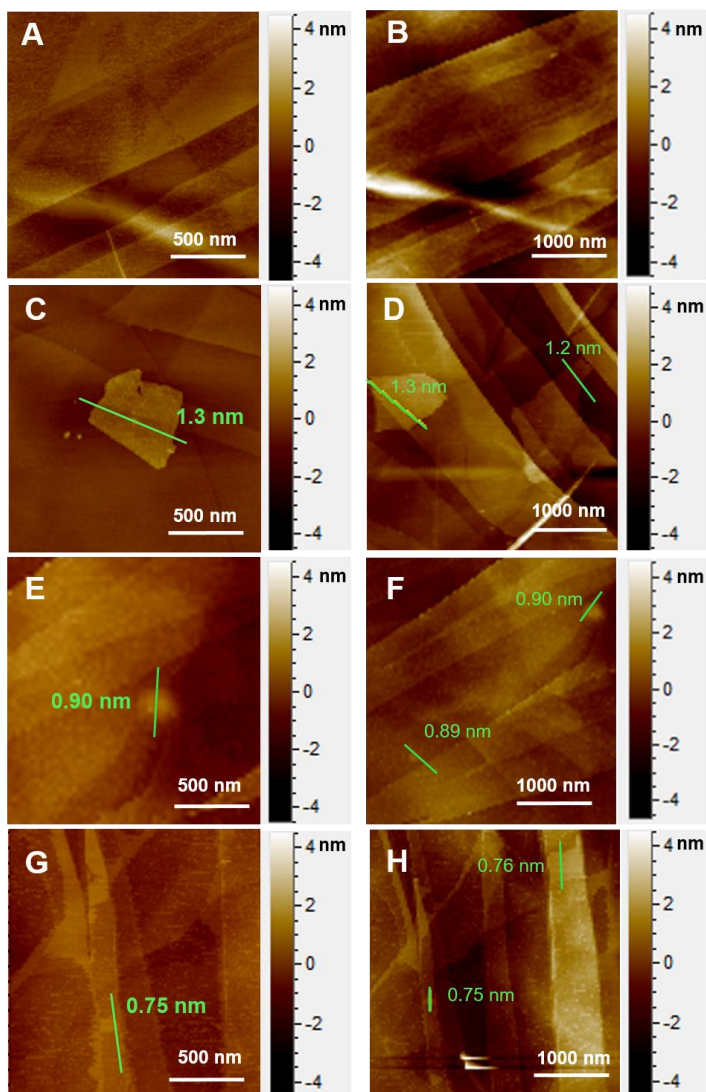


**Figure 5.4** Representative AFM images of (A-B) HOPG substrate and (C-D) GO, (E-F) RGO-A or (G-H) RGO on HOPG.

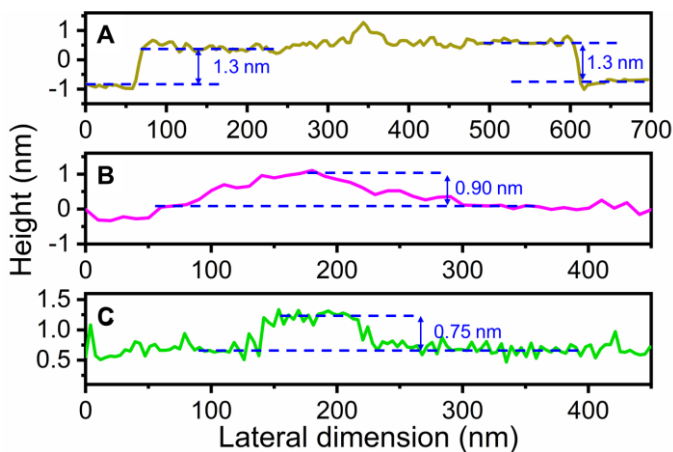


**Figure 5.5** AFM cross-section profiles for (A) GO in Fig. 5.4C, (B) RGO-A in Fig. 5.4E, and (C) RGO in Fig. 5.4G on HOPG, respectively.

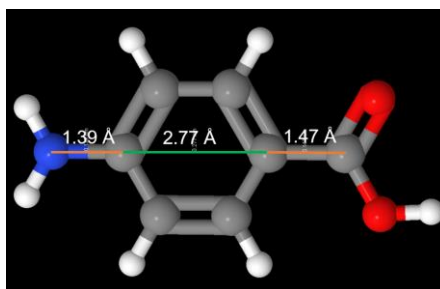


**Figure 5.6** 3D structure of 4-ABA molecule. The distances between the atoms are measured using Jmol software.<sup>[296]</sup>

**Table 5.1** Thickness of graphene-based materials on HOPG electrode, characterized by AFM.

| Graphene-based material | GO              | RGO             | RGO-A           |
|-------------------------|-----------------|-----------------|-----------------|
| Thickness (nm)          | $1.24 \pm 0.07$ | $0.78 \pm 0.03$ | $0.97 \pm 0.09$ |

XPS was chosen to investigate the surface chemical composition and the carbon bonding states of various modified electrodes. The percentages of each carbon species to the total species, based on the relative surface area of each fitted peak, Fig. 5.7B-F, with the corresponding binding energy are summarized in Table 5.2.<sup>[247]</sup> The trend of relative surface area of oxygenated carbon species for various electrodes is consistent with the O/C ratio in survey spectra, indicating a reasonable fitting, Table 5.2 and Fig. 5.7A. The relative amount of oxygenated carbon species including C–O, C=O and COO– drastically increases from 16.0%, 39.8% to 56.7% for bare CP, CPG and CPG/GO, respectively. This is due to the increased amount of immobilized GO with substantial oxygenated carbon

species on carbon fibers by coating GO under sonication (CPG) and further drop-casting GO on CP electrodes (CPG/GO). After treatment by electrochemical potential pulses, the total oxygenated species of CPG/GO electrodes notably decrease to 28.0%, 18.8% and 12.8% for RGO, RGO-A and RGO-A(N) electrodes, respectively. This is reasonable because the precursor electrode (*i.e.* CPG/GO) could be electrochemically reduced when applied with a negative potential pulse of -1.4 V, meaning that the GO on the electrode turns into RGO with fewer oxygenated groups. Compared to the RGO electrode, newly observed C–N species on RGO-A (16.3%) electrodes indicate the successful modification of 4-ABA undergoing electrochemical oxidation at 1.4 V. A small amount of C–N species (7.4%) can also be determined on RGO-A(N) due to the presence of physically adsorbed 4-ABA on the electrode. All these observations demonstrate that the electrochemical potential pulse of -1.4/1.4 V can achieve both the electroreduction of GO and the electro-oxidation of 4-ABA on CPG/GO electrode and thus the RGO-A electrode is obtained.

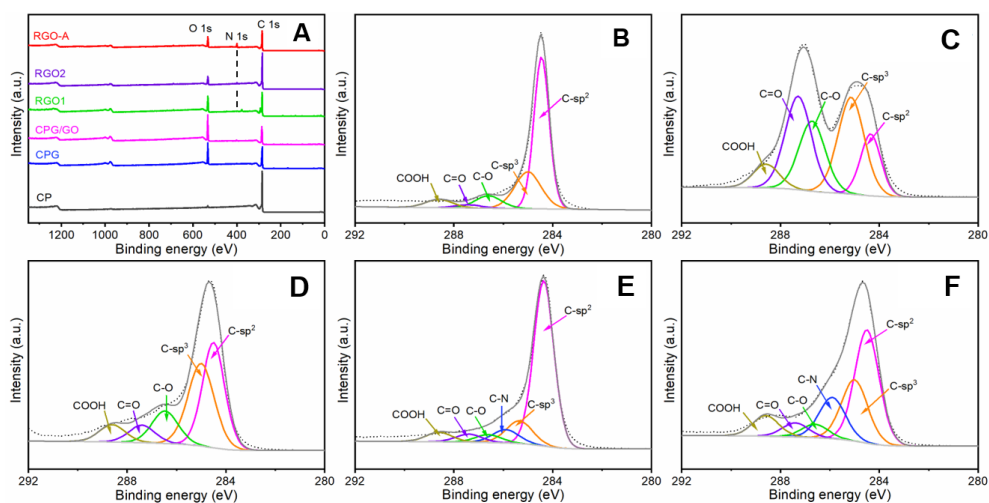


**Figure 5.7** (A) Survey spectra of different modified electrodes. XPS spectra of (B) CP, (C) CPG/GO, (D) RGO, (E) RGO-A(N) and (F) RGO electrodes.

**Table 5.2** Relative peak area percentage of the carbon bindings of all carbon species in CP, CPG, CPG/GO, RGO, RGO-A and RGO-A(N) electrodes determined by XPS.

| Carbon status        | Binding energy (eV) | CP (%) | CPG (%) | CPG/GO (%) | RGO (%) | RGO-A (%) | RGO-A(N) (%) |
|----------------------|---------------------|--------|---------|------------|---------|-----------|--------------|
| C sp <sup>2</sup>    | 284.5 ± 0.1         | 59.2   | 47.4    | 14.2       | 37.3    | 40.8      | 67.6         |
| C sp <sup>3</sup>    | 285.0 ± 0.1         | 24.8   | 12.8    | 29.1       | 34.7    | 24.1      | 12.2         |
| C–N                  | 285.9 ± 0.1         | -      | -       | -          | -       | 16.3      | 7.4          |
| C–O                  | 286.6 ± 0.1         | 8.3    | 32.2    | 21.2       | 13.4    | 5.3       | 4.0          |
| C=O                  | 287.4 ± 0.1         | 2.4    | 3.3     | 28.2       | 7.5     | 5.3       | 4.0          |
| COO–                 | 288.6 ± 0.1         | 5.3    | 4.3     | 7.3        | 7.1     | 8.2       | 4.7          |
| Total oxygen-species | -                   | 16.0   | 39.8    | 56.7       | 28.0    | 18.8      | 12.8         |

### 5.3.2 Electrochemical characterization of modified electrodes

Prior to enzyme immobilization, the various CP based electrodes were characterized electrochemically. EIS in 100 mM PBS (pH 7.0) containing 5.0 mM K<sub>4</sub>[Fe(CN)<sub>6</sub>] was first carried out. The impedance spectra were fitted using the equivalent circuit in Fig. 5.8A. The primary electrode (CPG/GO) gives a moderate charge transfer resistance ( $R_{ct}$ ) of 50.6  $\Omega$ , Table 5.3. GO-A shows the highest  $R_{ct}$  of 341  $\Omega$ , in good agreement with the largest peak separation ( $\Delta E_p$ ) of 286 mV and the smallest anodic peak current (0.50 mA cm<sup>-2</sup>) for the CV curves of [Fe(CN)<sub>6</sub>]<sup>3-/4-</sup>, Fig. 5.8B and Table 5.4. The significantly increased  $R_{ct}$  and  $\Delta E_p$  are mainly caused by the stronger electrostatic repulsion between the redox probe [Fe(CN)<sub>6</sub>]<sup>3-/4-</sup> and the increased amount of –COOH groups (mostly in –COO<sup>-</sup> form at pH 7.0), on electrode surface after electrochemical oxidation of 4-ABA. This is supported by a smaller  $\Delta E_p$  for positively charged [Ru(NH<sub>3</sub>)<sub>6</sub>]<sup>2+/3+</sup>, Fig. 5.8C and Table 5.4. On the other hand, negative potential pulses can reduce GO on the electrode surface and improves the electrode conductivity, supported by the  $R_{ct}$  decreasing from 50.6  $\Omega$  for CPG/GO to 29.0  $\Omega$  for the resulting RGO, together with lower  $\Delta E_p$  (from 146 to 105 mV, and from 166 to 107 mV) for both [Fe(CN)<sub>6</sub>]<sup>3-/4-</sup> and [Ru(NH<sub>3</sub>)<sub>6</sub>]<sup>2+/3+</sup>. When the CPG/GO was treated electrochemically with both negative and positive potential pulses, the resulting RGO-A electrode similarly shows a smaller  $R_{ct}$  of 32.6  $\Omega$  compared to the CPG/GO electrode, consistent with CV curves which display smaller  $\Delta E_p$  of 112 and 142 mV for [Fe(CN)<sub>6</sub>]<sup>3-/4-</sup> and [Ru(NH<sub>3</sub>)<sub>6</sub>]<sup>2+/3+</sup>, respectively. In addition, the  $R_{ct}$  and  $\Delta E_p$  for [Fe(CN)<sub>6</sub>]<sup>3-/4-</sup> at RGO-A are comparable to those at RGO and RGO-A(N). This is reasonable, as electroreduction of GO greatly enhances the electrochemical activity. Notably, RGO-A(N) shows the smallest  $\Delta E_p$  (105 mV) for [Ru(NH<sub>3</sub>)<sub>6</sub>]<sup>2+/3+</sup> probably due to the physically adsorbed 4-ABA efficiently attracting the positively charged redox probe molecules.

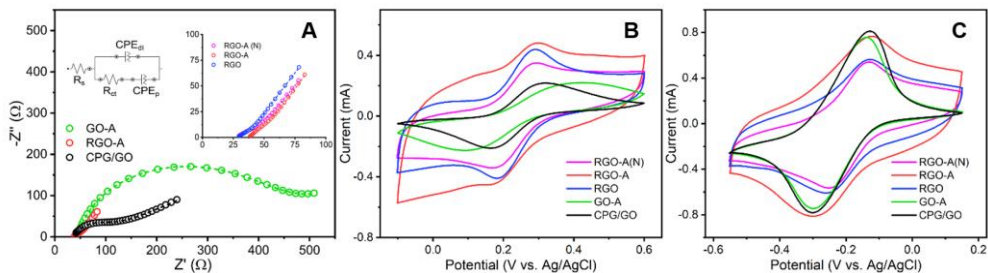


**Figure 5.8** (A) EIS of CPG/GO, RGO-A and GO-A electrodes recorded for 100 mM O<sub>2</sub>-free PBS (pH 7.0) with 5.0 mM K<sub>4</sub>[Fe(CN)<sub>6</sub>]. Inset right of (A): Magnified EIS of the RGO-A compared with RGO-A(N) and RGO electrodes. Inset left of (A): Equivalent circuit used to fit to the impedance data; R<sub>s</sub>: electrolyte solution resistance; R<sub>ct</sub>: interfacial electron transfer resistance; CPE<sub>dl</sub> and CPE<sub>p</sub>: constant phase element of the electrode double layer and polarization, respectively. CVs at 50 mV s<sup>-1</sup> of the CPG/GO, GO-A, RGO, RGO-A and RGO-A(N) electrodes in 100 mM O<sub>2</sub>-free PBS (pH 7.0) with 5.0 mM (B) K<sub>4</sub>[Fe(CN)<sub>6</sub>] or (C) [Ru(NH<sub>3</sub>)<sub>6</sub>]Cl<sub>3</sub>.

**Table 5.3** Parameters obtained by fitting the impedance spectra based on the equivalent circuit (inset of Fig. 5.8A).

| Electrode | R <sub>s</sub> (Ω) | Y <sub>0,dl</sub> (S s <sup>-α<sub>dl</sub></sup> ) | α <sub>dl</sub> | Y <sub>0,p</sub> (S s <sup>-α<sub>p</sub></sup> ) | α <sub>p</sub> | R <sub>ct</sub> (Ω) | χ • 10 <sup>3</sup> |
|-----------|--------------------|---|-----------------|---|----------------|---------------------|---------------------|
| CPG/GO    | 39.3               | 2.10 × 10 <sup>-5</sup>                             | 0.887           | 3.61 × 10 <sup>-3</sup>                           | 0.327          | 50.6                | 4.06                |
| GO-A      | 46.0               | 3.91 × 10 <sup>-3</sup>                             | 0.902           | 4.01 × 10 <sup>-3</sup>                           | 0.322          | 341                 | 1.58                |
| RGO-A     | 38.1               | 3.42 × 10 <sup>-3</sup>                             | 0.657           | 4.45 × 10 <sup>-3</sup>                           | 0.664          | 32.6                | 0.88                |
| RGO       | 28.9               | 4.85 × 10 <sup>-3</sup>                             | 0.549           | 3.12 × 10 <sup>-3</sup>                           | 0.755          | 29.0                | 0.24                |
| RGO-A(N)  | 28.4               | 2.43 × 10 <sup>-3</sup>                             | 0.558           | 4.00 × 10 <sup>-3</sup>                           | 0.658          | 31.2                | 0.98                |

**Table 5.4** Key voltammetry parameters of modified electrodes in 100 mM PBS (pH 7.0) containing 5.0 mM K<sub>4</sub>[Fe(CN)<sub>6</sub>] or [Ru(NH<sub>3</sub>)<sub>6</sub>]Cl<sub>3</sub> based on Fig. 5.8B and C.

| Electrode | K <sub>4</sub> [Fe(CN) <sub>6</sub> ] |                                       |                                       | [Ru(NH <sub>3</sub> ) <sub>6</sub> ]Cl <sub>3</sub> |                                       |                                       |
|-----------|---------------------------------------|---------------------------------------|---------------------------------------|---|---------------------------------------|---------------------------------------|
|           | ΔE <sub>p</sub> (mV)                  | j <sub>a</sub> (mA cm <sup>-2</sup> ) | j <sub>c</sub> (mA cm <sup>-2</sup> ) | ΔE <sub>p</sub> (mV)                                | j <sub>a</sub> (mA cm <sup>-2</sup> ) | j <sub>c</sub> (mA cm <sup>-2</sup> ) |
| CPG/GO    | 146                                   | 0.83                                  | -0.83                                 | 166   | 3.10                                  | -2.99                                 |
| GO-A      | 286                                   | 0.66                                  | -0.72                                 | 151   | 2.76                                  | -2.74                                 |
| RGO-A     | 112                                   | 0.50                                  | -0.95                                 | 142   | 1.18                                  | -1.18                                 |
| RGO       | 105                                   | 1.30                                  | -1.36                                 | 107   | 1.00                                  | -1.14                                 |
| RGO-A(N)  | 110                                   | 0.99                                  | -1.05                                 | 105   | 1.54                                  | -1.53                                 |

ECSAs of the modified carbon electrodes were determined from the capacitive currents based on CVs in PBS electrolyte, Fig. 5.9 and Table 5.5.<sup>[250]</sup> Bare CP shows the smallest ESCA of 0.010 ± 0.001 cm<sup>2</sup>, CPG shows 50-fold increased ESCA, and CPG/GO nearly further doubles the ESCA of CPG to 1.0 ± 0.2 cm<sup>2</sup> because of the improved hydrophilicity, Fig. 3.8. Electroreduction of GO to RGO results in a RGO electrode with an ESCA notably increasing to 45 ± 8 cm<sup>2</sup> due to the improved conductivity. The RGO-A electrode exhibits

the highest ECSA compared to other reduced electrodes (*i.e.*, RGO and RGO-A(N) electrodes), which can be explained by the SEM observation that the RGO-A electrode shows the mildest RGO sheet aggregation. Overall, the RGO-A electrode with improved  $R_{ct}$  and the highest ESCA could be an excellent matrix for BO<sub>x</sub> immobilizations. Both morphology and electrochemical studies thus show that grafting of 4-ABA is likely to alleviate RGO aggregation by electrostatic repulsion and thus attenuate  $\pi$ - $\pi$  stacking. After enzyme immobilization, similar trends were observed, whereas all ESCAs decrease by ca. 50% probably due to the presence of insulating protein (Table 5.5).

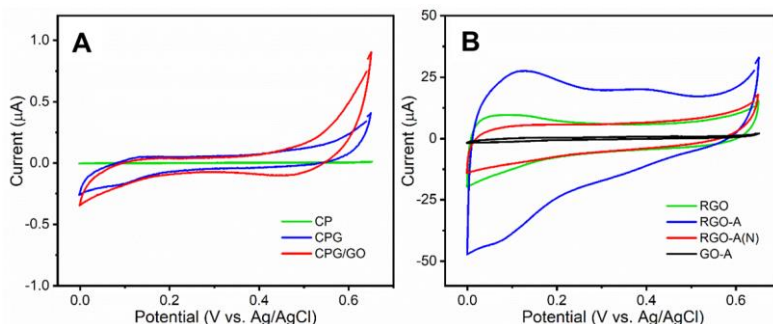


**Figure 5.9** Representative cyclic voltammograms (CVs) of (A) CP, CPG and CPG/GO electrodes and (B) various electrodes derived from CPG/GO with different electrochemical potential pulse treatments in O<sub>2</sub>-free PBS (100 mM, pH 7.0); scan rate: 5 mV s<sup>-1</sup>

**Table 5.5** ECSA of various electrodes based on Fig. 5.9, 5.11A, 5.11C and 5.13B.

| Electrode                | $\Delta i$ ( $\mu$ A) | $C_{dl}$ ( $\mu$ F) | ECSA ( $\text{cm}^2$ ) |
|--------------------------|-----------------------|---------------------|------------------------|
| CP                       | $0.0025 \pm 0.0003$   | $0.25 \pm 0.03$     | $0.010 \pm 0.001$      |
| CPG                      | $0.131 \pm 0.008$     | $13.1 \pm 0.9$      | $0.52 \pm 0.04$        |
| CPG/GO                   | $0.24 \pm 0.04$       | $24 \pm 4$          | $1.0 \pm 0.2$          |
| RGO                      | $11 \pm 2$            | $1131 \pm 209$      | $45 \pm 8$             |
| RGO-A                    | $20 \pm 2$            | $2058 \pm 238$      | $82 \pm 10$            |
| RGO-A(N)                 | $10 \pm 1$            | $1064 \pm 96$       | $42 \pm 4$             |
| GO-A                     | $0.71 \pm 0.05$       | $71 \pm 5$          | $2.8 \pm 0.2$          |
| RGO/BO <sub>x</sub>      | $6.4 \pm 0.2$         | $643 \pm 18$        | $25.7 \pm 0.7$         |
| RGO-A/BO <sub>x</sub>    | $11.9 \pm 0.8$        | $1188 \pm 77$       | $48 \pm 3$             |
| RGO-A(N)/BO <sub>x</sub> | $4.5 \pm 0.6$         | $446 \pm 59$        | $18 \pm 2$             |
| GO-A/BO <sub>x</sub>     | $0.53 \pm 0.07$       | $53 \pm 7$          | $2.1 \pm 0.3$          |
| R-A/BO <sub>x</sub>      | $2.6 \pm 0.3$         | $262 \pm 28$        | $10 \pm 1$             |

### 5.3.3 Electrocatalysis of BO<sub>x</sub> Bioelectrodes

The ORR on the RGO-A bioelectrodes with BO<sub>x</sub> immobilized was found to start at approximately 0.57 V vs. Ag/AgCl (Fig. 5.10 and 5.11A), consistent with reported observations.<sup>[119, 297]</sup> The limited catalytic current at 0 V is mainly due to the substrate

dioxygen supply constraint, confirmed by the observation that the addition of 5 mM ABTS hardly improves catalytic response, Fig. 5.10. ABTS is an efficient mediator allowing to address electrochemically the BOx molecules that are not optimally orientated.<sup>[298]</sup>

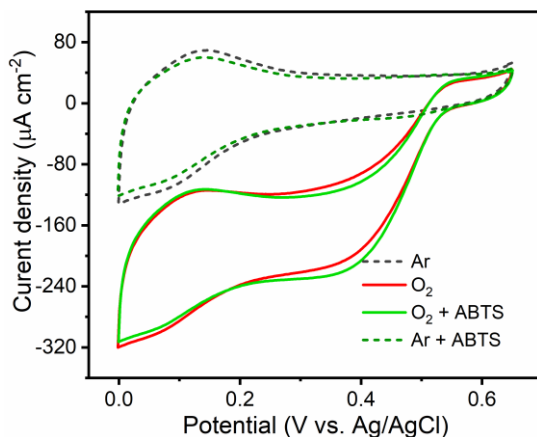


**Figure 5.10** Comparison of the catalytic performance on RGO-A/BOx bioelectrodes toward  $O_2$  reduction in 100 mM PBS (pH 7.0) in the absence or presence of the mediator ABTS (5 mM).

RGO-A/BOx bioelectrode ( $193 \pm 4 \mu A cm^{-2}$ ) shows 3.4-fold higher  $\Delta j_{cat}$  compared to R-A/BOx ( $44 \pm 5 \mu A cm^{-2}$ ), Fig. 5.11A. This can be explained by the more facile ET through the electrode due to the higher RGO content on RGO-A/BOx over R-A/BOx, revealed by the increased estimated ECSA from  $10 \pm 1 cm^2$  for R-A/BOx to  $48 \pm 3 cm^2$  for RGO-A/BOx (Fig. 5.11A and Table 5.6). This could be further verified by tuning the amount of drop-cast GO (*i.e.* the amount of resulting RGO) from 1.0 to 3.0  $mg mL^{-1}$  correspondingly reflected in  $\Delta j_{cat}$  of the BOx bioelectrodes, Fig. 5.11B. It is seen that  $\Delta j_{cat}$  increases with increasing concentration of drop-cast GO, reaching the maximum at 3  $mg mL^{-1}$ . However, further increasing the concentration of GO solution for electrode modification leads to a decreased  $\Delta j_{cat}$ , probably due to the limited diffusion of substrate  $O_2$  from bulk solution to the electrode surface.

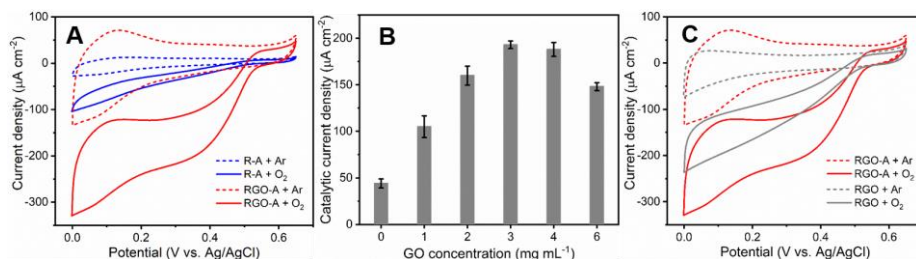


**Figure 5.11** CVs of the BOx bioelectrodes based on (A) R-A and RGO-A matrices, as well as (C) RGO-A and RGO matrices in 100 mM PBS (pH 7.0), scan rate:  $5 mV s^{-1}$ .

(B) Effect of the amount of drop-cast GO (20  $\mu\text{L}$ ) on the catalytic performance of RGO-A/BOx electrodes toward  $\text{O}_2$  reduction. All catalytic currents are obtained from the difference value of cathodic currents in the absence and presence of  $\text{O}_2$  at 0.2 V.

Compared to the RGO bioelectrode, the RGO-A bioelectrode shows a 1.4-fold catalytic response, Fig. 5.11C, highlighting the role of 4-ABA as a DET promotor grafted on the electrode surface by applying the positive potential pulse (Fig. 5.12 and 5.13A). This step is essential for favorable orientation of BOx, since the  $\text{Cu}_{\text{T1}}$  site of BOx, surrounded mainly by positively charges at neutral pH (illustrated in Scheme 5.1), is then close to the RGO-A electrode surface.<sup>[2]</sup> A large oxidation peak of the amino group of 4-ABA appears at around 0.85 V in the first cycle of CVs on the CPG/GO electrode, with the current gradually stabilizing in the following cycles, Fig. 5.12B, verifying the electrochemical modification of 4-ABA on the electrode surface. Comparable catalytic activities are observed on RGO-A/BOx bioelectrodes with different durations for electro-oxidation of 4-ABA, suggesting sufficient grafting of 4-ABA, Fig. 5.13A. The BOx bioelectrode based on the RGO-A(N) matrix obtained without positive potential pulse, *i.e.*, no grafting of 4-ABA, only exhibits  $\sim 34\%$  catalytic response on the RGO-A, Fig. 5.13B. Due to the smaller amount of physically adsorbed 4-ABA, concluded from a smaller amount of C–N on RGO-A(N) than a RGO-A based on XPS (Table 5.2), the RGO-A(N) matrix cannot strongly enough orientate BOx. In addition, RGO-A(N) suffers more serious RGO sheet aggregation in comparison to RGO-A. Only 2.6% catalytic activity was observed on the GO-A/BOx bioelectrode compared to the RGO-A/BOx, Fig. 5.13B, highlighting the importance of the electroreduction process for improved electrode conductivity. This is supported by the observation that the GO-A/BOx electrode shows only 4.4% ECSA compared to the RGO-A/BOx electrode, Table 5.5.

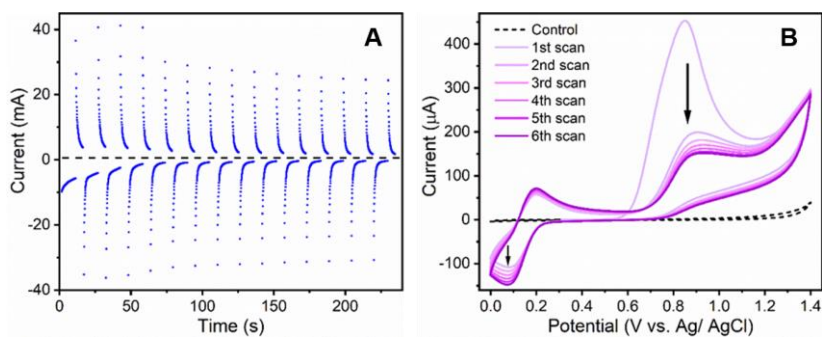


**Figure 5.12** (A) Electrochemical potential pulse treatment (alternatively, -1.4 V vs. Ag/AgCl for 10 s and 1.4 V for 5 s) of the CPG/GO electrode in Ar-saturated PBS (100 mM, pH = 7.0) containing 5 mM 4-ABA. (B) CVs of the CPG/GO electrode in the same electrolyte containing 5 mM 4-ABA. Scan rate 50  $\text{mV s}^{-1}$ . The control is obtained in absence of 4-ABA.

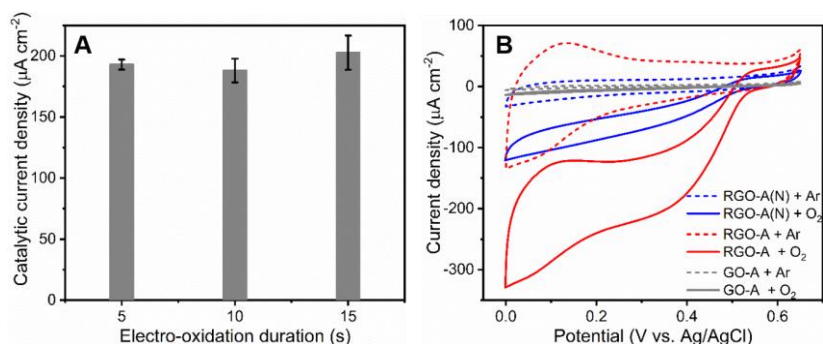


**Figure 5.13** (A) Effect of the duration of applied positive potential for electro-oxidizing 4-ABA on the catalytic performance of RGO-A/BOx electrodes toward  $\text{O}_2$  reduction. (B) CVs of the BOx bioelectrodes based on RGO-A, RGO-A(N) and GO-A matrices in 100 mM pH 7.0 PBS.

### 5.3.4 Kinetic analysis of performance of bioelectrodes

To achieve a better understanding on how 4-ABA functionalization promotes the DET of BOx, we undertook a more detailed kinetic analysis. The amount of active BOx immobilized on the electrode can be estimated by enzyme assay using a spectroscopic method, Fig. 5.14. The estimated surface coverage,  $\Gamma_{act}$  of active BOx on the RGO-A matrix ( $64 \pm 3 \text{ pmol cm}^{-2}$ ) is comparable to those on RGO ( $58.0 \pm 0.7 \text{ pmol cm}^{-2}$ ) and RGO-A(N) matrices ( $49.3 \pm 0.7 \text{ pmol cm}^{-2}$ ), although  $\Delta j_{cat}$  on these three electrode matrices varies somewhat, Table 5.6. The highest catalytic activity on RGO-A is therefore mainly due to higher ratio of BOx able of DET as a result of better enzyme orientation, rather than higher enzyme loading.

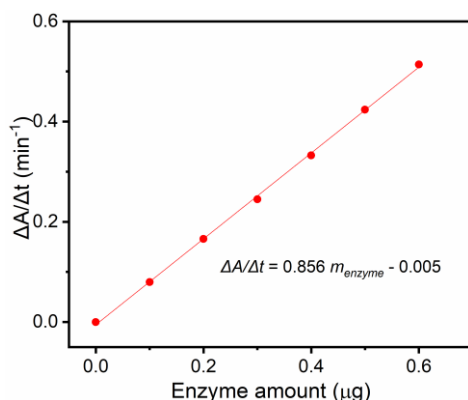


**Figure 5.14** Calibration curve showing the linear relationship between the rate of absorbance change with time at 420 nm and the BOx amount. The reaction solution is air-equilibrated PBS (100 mM, pH 7.0) containing  $0.20 \text{ mg mL}^{-1}$  ABTS as the electron donor and a certain amount of active BOx.

**Table 5.6** Kinetic parameters of DET-type bioelectrocatalytic reduction of dioxygen for different BOx bioelectrodes.

| BOx matrix | $k_{cat}/k_0^{max}$ | $\beta\Delta d$ | $k_{cat}\lambda\Gamma_{act}$ (mol cm <sup>-2</sup> s <sup>-1</sup> ) | $\Gamma_{act}$ (mol cm <sup>-2</sup> )<br># | $k_{cat}\lambda$ (s <sup>-1</sup> ) | $\Delta j_{cat}$ ( $\mu$ A cm <sup>-2</sup> ) |
|------------|---------------------|-----------------|--|---|-------------------------------------|---|
| RGO-A      | 1.6 ± 0.2           | 2.2 ± 0.2       | (4.53 ± 0.01) × 10 <sup>-10</sup>                                    | (6.4 ± 0.3) × 10 <sup>-11</sup>             | 7.1 ± 0.1                           | 193 ± 4                                       |
| RGO        | 4.5 ± 0.8           | 5.5 ± 0.6       | (2.9 ± 0.1) × 10 <sup>-10</sup>                                      | (5.80 ± 0.07) × 10 <sup>-11</sup>           | 5.0 ± 0.2                           | 134 ± 9                                       |
| RGO-A(N)   | 5.3 ± 0.1           | 3.4 ± 0.1       | (1.62 ± 0.01) × 10 <sup>-10</sup>                                    | (4.93 ± 0.07) × 10 <sup>-11</sup>           | 3.3 ± 0.1                           | 66 ± 8  |
| RGO-A_ads  | 2.0 ± 0.5           | 2.6 ± 0.4       | (5.19 ± 0.01) × 10 <sup>-10</sup>                                    | (7.1 ± 0.4) × 10 <sup>-11</sup>             | 7.3 ± 0.1                           | 195 ± 2                                       |

#  $\Gamma_{act}$  is the sum of surface coverage of active DET- and MET-type BOx, obtained from the activity assay.

Further, DET-type catalytic activity  $k_{cat}$  and/or the orientation factor  $\lambda$ ,<sup>[118-119]</sup> involved in the electrochemical communication between BOx and the electrode surface, are estimated based on the experimental data of the catalytic current ( $i$ ) vs. the electrode potential ( $E$ ) obtained from LSV. A steady-state model describing the  $i/i_{cat}^{lim}$  vs.  $E$  relationship ignoring the concentration depletion of the substrate and mainly considering the random orientation is expressed as follows:<sup>[118-119, 299]</sup>

$$\frac{i}{i_{cat}^{lim}} = \frac{1}{\beta\Delta d\{1+\exp(\varphi)\}} \ln \left| \frac{k_0^{max}\{1+\exp(\varphi)\} + \frac{k_{cat}}{k_0^{max}} \exp(\alpha\varphi)}{\exp(-\beta\Delta d)\{1+\exp(\varphi)\} + \frac{k_{cat}}{k_0^{max}} \exp(\alpha\varphi)} \right| \quad (5.1)$$

$$\varphi = \frac{nE}{RT} (E - E_E^{o'}) \quad (5.2)$$

where  $k_0^{max}$  is the standard rate constant of BOx with the best orientation (the closest approach,  $d_{min}$ ) and  $\Delta d$  the distance between the closest and farthest approach of DET-capable enzymes in various orientations, Fig. 5.15B.  $\alpha$  is the transfer coefficient and  $\beta$  is the long-range tunneling decay factor. The abbreviation  $\varphi$  is determined by  $n'E$ , the number of electrons in the rate-determining step of the electrocatalytic process (1 for the Cu<sub>T1</sub> site in BOx in this case).  $F$  is the Faraday constant,  $R$  the gas constant,  $T$  the absolute temperature and  $E_E^{o'}$  the formal potential of the Cu<sub>T1</sub> site of BOx that communicates with the electrode by DET (0.608 V vs. Ag/AgCl).<sup>[239, 300]</sup>

Following in previous reports,<sup>[118-119]</sup>  $k_{cat}/k_0^{max}$ ,  $\beta\Delta d$ , and  $k_{cat}\lambda\Gamma_{act}$  were used as adjustable parameters to fit the recorded LSV data with a non-linear regression by Excel©, Fig. 5.15A.  $k_{cat}\lambda\Gamma_{act}$  is positively relevant to the  $i_{cat}^{lim}$  where a specific enzyme immobilized on the electrode with the same surface area.  $\lambda$  is the surface concentration proportion of the DET-capable enzymes that can communicate with the electrode directly to the total amount of immobilized active enzymes. The catalytic rate constant for DET,  $k_{cat}$ , is

---

different from the solution activity ( $k_c$ ) because the value depends on the electron acceptor. The estimated the  $k_{cat}\lambda\Gamma_{act}$  for the RGO-A matrix ( $453 \pm 1 \text{ pmol cm}^{-2} \text{ s}^{-1}$ ) is much higher than for RGO ( $290 \pm 10 \text{ pmol cm}^{-2} \text{ s}^{-1}$ ) and RGO-A(N) matrices ( $162 \pm 1 \text{ pmol cm}^{-2} \text{ s}^{-1}$ ), in accordance with the trend of  $\Delta j_{cat}$  on these three electrode matrices, Table 5.6. Furthermore, assuming that the values for  $\Gamma_{act}$  obtained by the fitting and by the activity assay are comparable, the RGO-A bioelectrode gives a 1.4 fold and 2.2-fold higher  $k_{cat}\lambda$  ( $7.1 \text{ s}^{-1}$ ) than RGO and RGO-A(N) bioelectrodes, respectively. Assuming that the active BOx with comparable amounts on different graphene-based matrix shows a similar DET catalytic activity ( $k_{cat}$ ), the larger orientation parameters  $\lambda$  of RGO-A is then the main contributor to the improved catalytic performance.

$\beta\Delta d$  is evaluated as  $2.2 \pm 0.2$  for the RGO-A/BOx electrode, but  $5.5 \pm 0.6$  and  $3.4 \pm 0.1$  for the RGO/BOx and RGO-A(N)/BOx electrodes, respectively, Table 5.6. If the value of  $\beta$  is taken to be  $1.0\text{-}1.4 \text{ \AA}^{-1}$  for all the electrodes,<sup>[301]</sup> then  $\Delta d$  is  $1.6\text{-}2.2 \text{ \AA}$  for RGO-A/BOx, *i.e.*, lower than  $3.9\text{-}5.5 \text{ \AA}$  and  $2.4\text{-}3.4 \text{ \AA}$  for RGO/BOx and RGO-A(N)/BOx, respectively.  $\Delta d$  is also lower than the reported value ( $2.6 \pm 0.2 \text{ \AA}$ ) for BOx orientated on a planar electrode,<sup>[119]</sup> indicative of more favourable BOx orientation on RGO-A electrode. Taking into account that the BOx size is  $4\text{-}6 \text{ nm}$ ,<sup>[119]</sup> most of the DET-capable BOx would then be orientated with the  $\text{Cu}_{T1}$  site quite close to the electrode surface. The best orientated immobilization of BOx is achieved for the RGO-A matrix due to the abundance of negatively charged aromatic groups. Without 4-ABA modification, BOx on the RGO matrix seems to be in a less-ordered orientation. Finally,  $k_{cat}/k_0^{max}$  for RGO-A is estimated as  $1.6 \pm 0.2$ , around one third of the value for RGO and RGO-A(N) bioelectrodes, reflecting that the highest  $k_0^{max}$  is found at the RGO-A/BOx bioelectrode. Based on the kinetic analysis, the promoted DET-type biocatalysis on the RGO-A matrix is concluded to be due to the better orientation of BOx (the highest orientation parameter  $\lambda$ , smallest  $\Delta d$  and largest  $k_0^{max}$ ) promoted by the negatively-charged aromatic 4-ABA groups on the electrode surface.

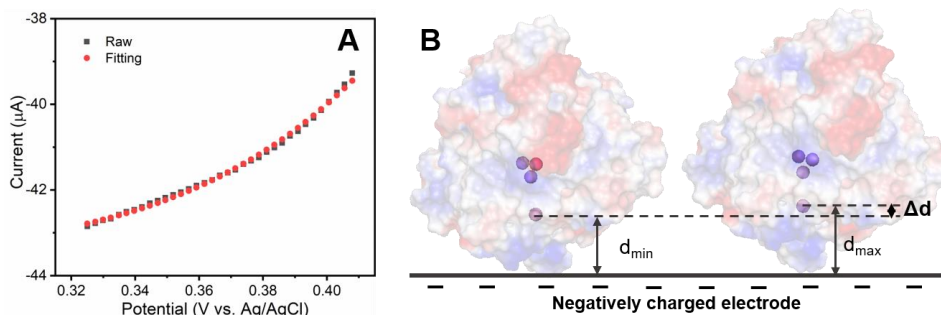


**Figure 5.15** (A) LSV of catalytic reduction of dioxygen at RGO-A/BOx with scan rate of  $1 \text{ mV s}^{-1}$  in dioxygen-saturated PBS (pH 7.0). The black and red dot-lines represent the raw voltammogram and non-linear least square fitted curve, respectively. (B) Schematic illustration of two boundary orientations of BOx on a negatively charged electrode surface, resulting in different tunneling distances  $d$  for interfacial ET from the electrode to the BOx  $\text{Cu}_{\text{T1}}$  site.

### 5.3.5 Stability evaluation of bioelectrodes

The storage and operational stability of the graphene-based bioelectrodes were investigated thoroughly.  $\Delta j_{\text{cat}}$  drops to half its initial value when RGO-A/BOx electrodes are stored for two weeks, while RGO and RGO-A(N) bioelectrodes retain 25% of the initial value, Fig. 5.16A and Fig. 5.17A, highlighting the role of 4-ABA in maintaining the stability. Similar to reported polycyclic aromatic electrode surface modifiers such as phenylalanine, tyrosine and tryptophan,<sup>[302]</sup> grafted 4-ABA binding to the  $\text{Cu}_{\text{T1}}$  site pocket of the enzyme might simultaneously alleviate the desorption and conformational changes of BOx.<sup>[303]</sup> Although freshly prepared RGO-A<sub>ads</sub>/BOx bioelectrodes, where the BOx was physically adsorbed, shows a comparable initial catalytic activity and similar kinetic parameters as covalently bound BOx on RGO-A, Table 5.6, only 35% of the original  $\Delta j_{\text{cat}}$  is retained after two-weeks' storage. This can be explained by BOx leaching from the electrode due to the weak physical interaction, also previously observed when BOx was electrostatically absorbed on GCE modified by MWCNTs.<sup>[89]</sup>

Operational stability is another criterion for stability evaluation, although the operational stability of all the electrodes in the study is lower than the storage stability. RGO-A/BOx shows superior operational stability with a half-lifetime of 55 h compared to RGO/BOx (13 h) and RGO-A<sub>ads</sub>/BOx (40 h), Fig. 5.16B and 5.17B. The high RGO-A/BOx stability is mainly assigned to the amide bonds between BOD lysine residues and the aromatic 4-ABA carboxylic groups on the graphene-based electrode surface, resulting in minimal leakage and activity loss of BOx.<sup>[304]</sup> This could also be attributed to the covalently bonded BOx molecule, less affected by the applied potential (0.2 V) than the

adsorbed one.<sup>[297]</sup> It is noteworthy that RGO-A/BOx with comparable storage stability shows the longest half-lifetime among other reported DET-type BOx bioelectrodes (Table 5.7), indicating its excellent operation stability.

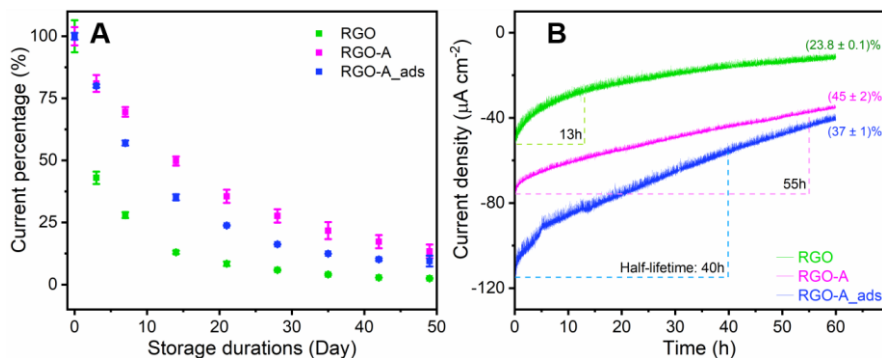


**Figure 5.16** (A) Storage and (B) operational lifetime of the BOx bioelectrodes based on RGO, RGO-A and RGO-A<sub>ads</sub> matrices in dioxygen-saturated and air-bubbling PBS (100 mM, pH 7.0), respectively. For storage lifetime evaluation, the catalytic activity was recorded by CV at a given day during the storage period. The operational stability of BOx bioelectrodes was evaluated by CA with an applied potential of 0.2 V.

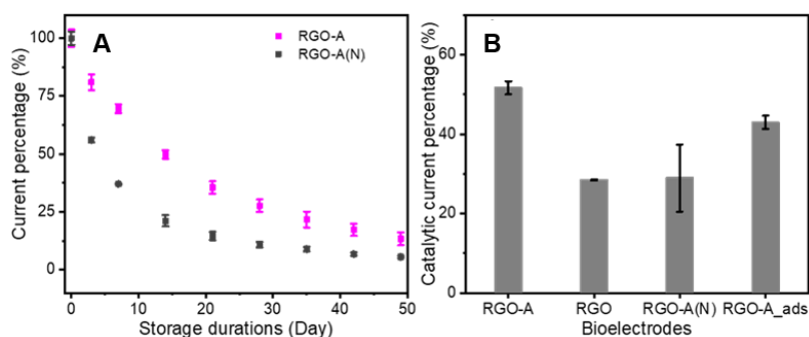


**Figure 5.17** (A) Storage lifetime of the BOx bioelectrodes based on RGO-A(N) and RGO-A matrices in dioxygen-saturated PBS (100 mM, pH 7.0). (B) The catalytic current percentage after the bioelectrodes are continually operated for 50 h at the applied potential of 0.2 V compared to the original catalytic current in air-bubbled PBS (100 mM, pH 7.0).

**Table 5.7** Comparison of the stability of DET-type BO<sub>x</sub> bioelectrode for ORR.

| Matrix                                     | Immobilization technique | Electrolyte              | Storage half-lifetime | No. of measurements (methods) during storage | Operation half-lifetime | Operation conditions                        | Ref.      |
|--|--------------------------|--------------------------|-----------------------|--|-------------------------|---|-----------|
| CPG/RGO-A                                  | Covalent                 | PBS, pH 7.0              | 14 d                  | 2 (CV at 0.20 V)                             | 55 h                    | 0.20 V, air purging                         | This work |
| CPG/RGO-A                                  | Adsorption               | PBS, pH 7.0              | ~10 d                 | 2 (CV at 0.20 V)                             | 40 h                    | 0.20 V, air purging                         | This work |
| GCE/KB-Amine                               | Adsorption               | PBS, pH 7.0              | 6 d                   | 4 (CA at 0 V)                                | -                       | -   | [119]     |
| GCE/KB-PTFE/bilirubin                      | Adsorption               |                          | 7 d (60%)*            | 6 (CA at 0 V)                                | -                       | -   | [305]     |
| NPG-MPA                                    | Covalent                 | PBS, pH 7.4              | 20 d                  | 5 (LSV at 0 V)                               | -                       | -   | [306]     |
| Au/MWCNT-PQQ                               | Covalent                 | citrate-PBS              | 20 d                  | 5 (LSV at 0.25 V)                            | -                       | -   | [307]     |
| GCE/MWCNT-maleimide                        | Covalent                 | PBS, pH 7.0              | ~6 d                  | 5 (- at 0.045 V)                             | -                       | -   | [89]      |
| Mesoporous silica nanotubes-carbon layer   | Encapsulation            | McIlvaine buffer, pH 5.0 | ~15 d (80%)           | fresh (CA at 0 V)                            | -                       | -   | [308]     |
| Porous CF/MWCNT@COOH/chitosan-GA           | Cross-linking            | PBS, pH 7.0              | 120 d (55%)           | 5 (LSV at 0.15 V)                            | -                       | -   | [309]     |
| Carbon fiber/AuNPs/Chitosan-glutaraldehyde | Cross-linking            | PBS, pH 7.0              | ~4 d                  | 0 (CV at 0 V)                                | -                       | -   | [310]     |
| Graphite/AuNPs-MPA                         | Covalent                 | Serum-mimic PBS, pH 7.4  | -                     | -  | ~4 h                    | 0.20 V, 500 rpm rotation                    | [304]     |
| GCE/MWCNT-cellulose                        | Adsorption               | Citrate buffer, pH 5.0   | ~40 d                 | 0  | 45 h (60%)*             | 0.20 V, air purging                         | [14]      |
| Au/CNTs/PANI                               | Adsorption               | PBS, pH 7.4              | -                     | -  | 12 h (78%)              | 0.045 V, Air-saturated, stirring            | [311]     |
| Buckypaper(MWCNT)                          | Adsorption               | PBS, pH 6.0              | -                     | -  | 10 h                    | 0.50 V, O <sub>2</sub> -saturated, stirring | [312]     |

\* The retention percentage of initial electrocatalytic activity. KB: Ketjen Black, a kind of carbon black; MPA: mercaptopropionic acid. All potentials are vs. Ag/AgCl (Sat.).

### 5.3.6 Applications as gas diffusion bioelectrodes and biocathodes

RGO-A/BOx bioelectrodes were finally exploited as a GDBE to demonstrate the versatile nature of our bioelectrode construction methodology.<sup>[313-314]</sup> GDBEs are gaining increasing attention as they accelerate the gaseous substrate supply<sup>[2, 315]</sup>, and offer great potential in portable and wearable EBFCs. GDBEs typically consist of a porous supporting electrode, a gas-diffusion layer, and a biocatalytic layer.<sup>[313]</sup> The consumed gaseous substrate ( $O_2$ ) in the buffer solution for the ORR can be steadily supplied from the gas phase. CPs are suitable as supporting electrodes. A GDBE cell specialized for membrane-less EBFCs was designed and fabricated. RGO-A/BOD in an “air-breathing” configuration with gas phase filling of ambient air shows a  $\Delta j_{cat}$  of  $60 \mu A cm^{-2}$  working at 0.2 V vs. Ag/AgCl, which is higher than the same electrode immersed in the electrolyte only delivering  $40 \mu A cm^{-2}$  (Fig. 5.18). This shows that the GDBE with enhanced dioxygen supply can enhance the catalytic performance, offering considerable potential for practical applications.<sup>[305]</sup>

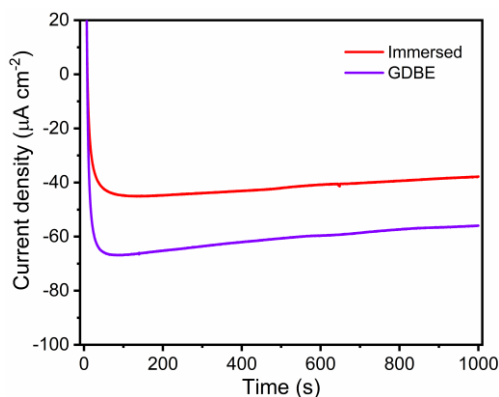


**Figure 5.18** The catalytic performance of the RGO-A/BOx bioelectrode as a GDBE electrode compared to the immersed bioelectrodes, evaluated by CA techniques with an applied potential of 0.2 V after 1000 s.

Finally, the RGO-A in the GDE configurations was assembled with a prepared GOx bioanode for EBFC applications. The constructed glucose/ $O_2$  EBFCs delivered a maximum power density ( $P_{max}$ ) of  $22 \mu W cm^{-2}$  with an OCV of 0.51 V (Fig. 5.19A), which is comparable to other graphene-based glucose/ $O_2$  EBFCs.<sup>[139]</sup> The stability of the constructed EBFC was further tested by continually measuring the current at the potential where the  $P_{max}$  was obtained. Only ~30% current output was retained after the EBFC operating 1 h in a static solution and the lifetime of the EBFC was ~16 h, Fig. 5.19B. Based on the above stability evaluation of BOx stability (half-lifetime: 55 h), it can

be concluded that the decrease in current outputs was mainly due to the instability of the GOx bioanode, suffering redox polymer detachment.

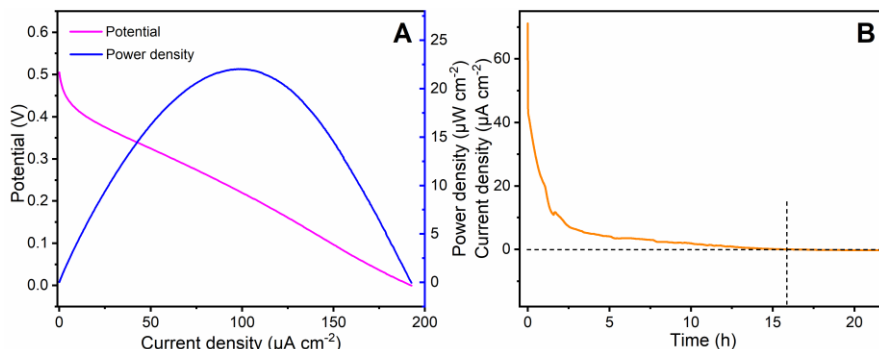


**Figure 5.19** (A) Representative polarization and power density curves obtained from the GOx bioanode and BOx biocathode in air-equilibrated PBS (100 mM, pH 7.0) containing 20 mM glucose. Scan rate:  $1 \text{ mV s}^{-1}$ . (B) Stability of the EBFC in a static solution. The current density in the same electrolyte was recorded at the potential of 0.2 V.

## 5.4 Conclusions

BOx was efficiently covalently bonded on 3D graphene-based electrode with a favorable orientation by inducing negatively charged aromatic linkers on the electrode surface. Both the negative and positive potential pulse improve significantly the bioelectrocatalytic performance of the bioelectrodes toward dioxygen reduction. The bioelectrode with both negative and positive potential pulses shows the highest  $\Delta j_{\text{cat}}$  ( $193 \pm 4 \mu\text{A cm}^{-2}$ ) among other control bioelectrodes. Especially, the importance of the positive potential pulse for electrochemical oxidation of 4-ABA on the produced RGO sheets is concluded. The superior DET-type biocatalytic performance on the RGO-A matrix compared to the RGO matrix is mainly due to better orientation of BOx with the help of negatively charged aromatic groups on the electrode surface. This is also partly attributed to the improved interfacial ET between BOx and the 3D matrix because the RGO aggregation is avoided due to the electrostatic repulsion and thus the high surface area is maintained. The bioelectrode shows outstanding operational stability with the half-lifetime of 55 h significantly higher than the other reported DET-type BOx bioelectrodes, *cf.* Table 5.7, mainly due to the strong covalent bond between the enzyme and electrode surface. The developed graphene-based BOx bioelectrodes, exploited as a GDBE, showed an elevated catalytic response *via* accelerating the gaseous substrate diffusion rate. The BOx bioelectrode was finally utilized as the biocathode in biofuel cells with a well-established GOx bioanode. The fabricated glucose/ $\text{O}_2$  EBFC with an OCV of 0.51 V delivered a  $P_{\text{max}}$  of  $22 \mu\text{A cm}^{-2}$ , comparable to reported values.

# Chapter 6

## Conclusions

---

With the rapidly increasing demands for energy, EBFCs as electrochemical devices hold promise to generate electricity in an environmentally friendly way. However, EBFC applications in wearable, implantable and portable devices remain challenges in terms of stability and power output. With excellent properties such as high surface area, light weight, and high conductivity, graphene as electrode materials shows great potential to promote the performance of bioelectrodes as well as EBFCs.

In this Ph.D. project, first constructed 3D graphene-based CP electrodes (CPG) with large surface area were used as the substrate for further functionalization and enzyme immobilization. CPG was prepared by coating GO onto carbon fibers of porous CP *via* sonication of the CP in GO solutions for optimized period of time. Characterization of the as prepared CPG by SEM confirmed that CPG retained the original 3D structure of CP and thus high surface area. WCA measurements suggested the improved hydrophilicity on CPG compared to the hydrophobic CP. This property ensured uniform loading of nanomaterials and enzymes.

Secondly, a compact sulfite/O<sub>2</sub> EBFC was assembled with a 3D *h*SO graphene-based bioanode and a commercial Pt cathode supported by CP. The 3D *h*SO graphene-based CP bioelectrode was fabricated by first drop-casting graphene-PEI composite, then electrochemically reducing the resulting electrode, and finally casting *h*SO solutions. The introduction of graphene-PEI nanocomposites not only increases the electrode surface area but also provides anchors for *h*SO adsorption *via* electrostatic interactions. Notably, the bioelectrode with electroreduction after the nanomaterial immobilization showed a 9-fold increase of the saturation catalytic current density for sulfite oxidation, reaching 24.4  $\mu\text{A cm}^{-2}$ , compared to the one without electroreduction. Further studies suggested that the electroreduction treatment of GO to RGO on the electrode, leading to accelerated interfacial ET, played a dominating role in the elevated direct catalytic current. The optimized graphene-based *h*SO bioelectrode was successfully exploited as the bioanode in an EBFC with a commercial Pt cathode. The assembled sulfite/O<sub>2</sub> EBFC with an OCV of 0.64 V fed with flowing fuels exhibited a  $P_{\text{max}}$  of 61  $\mu\text{W}$ , exceeding the value for the best reported EBFCs by more than six times. As a compact and portable power generator, the

---

EBFCs hold great potential for extracting electrical energy from body liquids, beverages and food containing sulfite. In addition, the EBFCs can potentially serve as a self-powered biosensor for detecting sulfite.

On the other hand, GO reduced electrochemically onto 3D CPs still leaves residual aggregation. This challenge inspired us to find a better way to avoid the graphene aggregation and retain the high working surface area for enzyme immobilization. Another glucose/O<sub>2</sub> EBFCs was constructed in a GDE configuration by employing an established GOx bioanode and a newly fabricated 3D graphene-based BOx biocathode. The 3D graphene-based BOx biocathode was prepared by first utilizing CPG as support for RGO functionalized with negatively charged aromatic molecules (4-ABA) and then covalently binding BOx with the –COOH groups of 4-ABA on the electrode surface. The production of RGO from GO and grafting of 4-ABA were achieved by applying electrochemical pulses at negative and positive potential, respectively. SEM characterization disclosed that the introduction of 4-ABA during the GO reduction can overcome the aggregation of produced RGO due to the electrostatic repulsion among the graphene sheets and thus preserve the high ESCA. In addition, 4-ABA optimized the orientation of BOx on the electrode surface reaching a highest catalytic current density ( $\Delta j_{\text{cat}}: 193 \pm 4 \mu\text{A cm}^{-2}$ ), confirmed by the model fitting to the electrocatalytic ORR current vs. potential. The dual roles of 4-ABA grafting are thus highlighted. The methodology herein holds promise for further development of graphene-based bioelectrochemical devices. Moreover, the BOx bioelectrode showed very high operation stability (half-lifetime: 55 h) compared to other reported DET-capable BOx bioelectrodes, mainly due to the rigid bonding of enzyme on the electrode surface. The BOx bioelectrode assembled in a GDE cell showed enhanced catalytic activity compared to the one immersed in electrolytes. The BOx/GDE biocathode together with a reported GOx bioanode was combined in a glucose/O<sub>2</sub> EBFC with satisfactory performance ( $P_{\text{max}}: 22 \mu\text{W cm}^{-2}$ , OCV: 0.51 V). The successful exploitation of the bioelectrodes in both GDE and EBFC configurations offers new prospects for electrochemical devices such as biofuel cells or biosensors.

Overall, constructing 3D graphene-based substrates for enzyme immobilization provides great potential to increase the electrocatalytic performance. Furthermore, the 3D graphene-based enzymatic biocatalysts serving as bioelectrodes in EBFCs resulted in high-level power outputs sufficient to power miniaturized and portable devices such as electrochemical sensors. However, the implementation of graphene-based EBFCs in practical applications requires further exploration. The main directions of research in graphene-based EBFCs are (i) miniaturization aiming at implementation in/on human body, (ii) energy generation for portable electrochemical devices and (iii) power sources for the synthesis of valuable chemicals. The following perspectives can be of particular interest for future investigation and possible Ph.D. projects. (1) Dedicated graphene-based materials such as GQDs may be suitable enzyme platforms considering the easy

---

grafting chemistry due to the presence of large amount of carboxylic acid groups at the edges of the GQDs, the likely facilitated electrocatalysis, and the large specific surface areas. (2) Lightweight graphene-based electrodes such as graphene hydrogels for bioanode and biocathode fabrications are promising for portable and wearable EBFCs benefiting from their small weight and high flexibility. (3) CVD derived graphene can serve as integrated electrodes of on-chip enzymatic devices for miniaturized biosensing or bio-powering; (4) and a wide range of fuel molecules such as inorganic molecules or cheap biomass-derived biofuels using new or engineered enzymes provides scope for the construction of stable and efficient graphene-based bioanodes and biocathodes as well as other enzymatic bioelectrodes.

---

## Bibliography

- [1] V. Aravindan, J. Gnanaraj, Y.-S. Lee, S. Madhavi, Insertion-type electrodes for nonaqueous Li-ion capacitors. *Chem. Rev.*, 2014, *114* (23), 11619-11635.
- [2] X. Xiao, H.-q. Xia, R. Wu, L. Bai, L. Yan, E. Magner, S. Cosnier, E. Lojou, Z. Zhu, A. Liu, Tackling the challenges of enzymatic (bio)fuel cells. *Chem. Rev.*, 2019, *119*, 9509-9558.
- [3] H. Moon, I. S. Chang, B. H. Kim, Continuous electricity production from artificial wastewater using a mediator-less microbial fuel cell. *Bioresour. Technol.*, 2006, *97* (4), 621-627.
- [4] B. H. Kim, I. S. Chang, G. Cheol Gil, H. S. Park, H. J. J. B. L. Kim, Novel BOD (biological oxygen demand) sensor using mediator-less microbial fuel cell. *Biotechnol. Lett.*, 2003, *25* (7), 541-545.
- [5] D. R. Bond, D. R. Lovley, Evidence for involvement of an electron shuttle in electricity generation by *Geothrix fermentans*. *Appl. Environ. Microbiol.*, 2005, *71* (4), 2186-9.
- [6] K. Hasan, M. Grattieri, T. Wang, R. D. Milton, S. D. Minteer, Enhanced bioelectrocatalysis of *Shewanella oneidensis* MR-1 by a naphthoquinone redox polymer. *ACS Energy Lett.*, 2017, 1947-1951.
- [7] J. Szczesny, N. Marković, F. Conzuelo, S. Zacarias, I. A. C. Pereira, W. Lubitz, N. Plumeré, W. Schuhmann, A. Ruff, A gas breathing hydrogen/air biofuel cell comprising a redox polymer/hydrogenase-based bioanode. *Nat. Commun.*, 2018, *9* (1), 4715.
- [8] G. T. R. Palmore, H. Bertschy, S. H. Bergens, G. M. Whitesides, A methanol/dioxygen biofuel cell that uses NAD<sup>+</sup>-dependent dehydrogenases as catalysts: application of an electro-enzymatic method to regenerate nicotinamide adenine dinucleotide at low overpotentials. *J. Electroanal. Chem.*, 1998, *443*, 155-161.
- [9] F. Liu, S. Banta, W. Chen, Functional assembly of a multi-enzyme methanol oxidation cascade on a surface-displayed trifunctional scaffold for enhanced NADH production. *Chem. Commun.*, 2013, *49* (36), 3766-8.
- [10] Y. Umasankar, B.-R. Adhikari, A. Chen, Effective immobilization of alcohol dehydrogenase on carbon nanoscaffolds for ethanol biofuel cell. *Bioelectrochemistry*, 2017, *118*, 83-90.
- [11] R. D. Milton, F. Wu, K. Lim, S. Abdellaoui, D. P. Hickey, S. D. Minteer, Promiscuous glucose oxidase: electrical energy conversion of multiple polysaccharides spanning starch and dairy milk. *ACS Catal.*, 2015, *5* (12), 7218-7225.
- [12] P. Bollella, G. Fusco, D. Stevar, L. Gorton, R. Ludwig, S. Ma, H. Boer, A. Koivula, C. Tortolini, G. Favero, R. Antiochia, F. Mazzei, A glucose/oxygen enzymatic fuel cell based on gold nanoparticles modified graphene screen-printed electrode. Proof-of-concept in human Saliva. *Sensor. Actuat. B-Chem.*, 2018, *256*, 921-930.
- [13] X. Xiao, P. Ó. Conghaile, D. Leech, R. Ludwig, E. Magner, An oxygen-independent and membrane-less glucose biobattery/supercapacitor hybrid device. *Biosens. Bioelectron.*, 2017, *98*, 421-427.
- [14] X. Wu, F. Zhao, J. R. Varcoe, A. E. Thumser, C. Avignone-Rossa, R. C. T. Slade, A one-compartment fructose/air biological fuel cell based on direct electron transfer. *Biosens. Bioelectron.*, 2009, *25* (2), 326-331.
- [15] I. Shitanda, K. Takamatsu, A. Niiyama, T. Mikawa, Y. Hoshi, M. Itagaki, S. Tsujimura, High-power lactate/O<sub>2</sub> enzymatic biofuel cell based on carbon cloth electrodes modified with MgO-templated carbon. *J. Power Sources*, 2019, *436*, 226844.
- [16] A. Koushanpour, M. Gamella, E. Katz, A biofuel cell based on biocatalytic reactions of lactate on both anode and cathode electrodes – extracting electrical power from human sweat. *Electroanalysis*, 2017, *29* (6), 1602-1611.
- [17] D. P. Hickey, R. C. Reid, R. D. Milton, S. D. Minteer, A self-powered amperometric lactate

- 
- biosensor based on lactate oxidase immobilized in dimethylferrocene-modified LPEI. *Biosens. Bioelectron.*, 2016, *77*, 26-31.
- [18] T. Zeng, D. Pankratov, M. Falk, S. Leimkühler, S. Shleev, U. Wollenberger, Miniature direct electron transfer based sulphite/oxygen enzymatic fuel cells. *Biosens. Bioelectron.*, 2015, *66*, 39-42.
- [19] D. P. Hickey, F. Giroud, D. W. Schmidtke, D. T. Glatzhofer, S. D. Minteer, Enzyme cascade for catalyzing sucrose oxidation in a biofuel cell. *ACS Catal.*, 2013, *3* (12), 2729-2737.
- [20] C. Liu, S. Alwarappan, Z. Chen, X. Kong, C.-Z. Li, Membraneless enzymatic biofuel cells based on graphene nanosheets. *Biosens. Bioelectron.*, 2010, *25* (7), 1829-1833.
- [21] G. Slaughter, T. Kulkarni, A self-powered glucose biosensing system. *Biosens. Bioelectron.*, 2016, *78*, 45-50.
- [22] A. J. Gross, M. Holzinger, S. Cosnier, Buckypaper bioelectrodes: emerging materials for implantable and wearable biofuel cells. *Energy Environ. Sci.*, 2018, *11* (7), 1670-1687.
- [23] M. Rasmussen, R. E. Ritzmann, I. Lee, A. J. Pollack, D. Scherson, An implantable biofuel cell for a live insect. *J. Am. Chem. Soc.*, 2012, *134* (3), 1458-1460.
- [24] W. Jia, X. Wang, S. Imani, A. J. Bandodkar, J. Ramirez, P. P. Mercier, J. Wang, Wearable textile biofuel cells for powering electronics. *J. Mater. Chem. A*, 2014, *2* (43), 18184-18189.
- [25] I. Jeerapan, J. R. Sempionatto, A. Pavinatto, J.-M. You, J. Wang, Stretchable biofuel cells as wearable textile-based self-powered sensors. *J. Mater. Chem. A*, 2016, *4* (47), 18342-18353.
- [26] W. Gellett, M. Kesmez, J. Schumacher, N. Akers, S. D. Minteer, Biofuel cells for portable power. *Electroanalysis*, 2010, *22* (7-8), 727-731.
- [27] K. P. Prasad, Y. Chen, P. Chen, Three-dimensional graphene-carbon nanotube hybrid for high-performance enzymatic biofuel cells. *ACS Appl. Mater. Inter.*, 2014, *6* (5), 3387-93.
- [28] P. Cinquin, C. Gondran, F. Giroud, S. Mazabrard, A. Pellissier, F. Boucher, J.-P. Alcaraz, K. Gorgy, F. Lenouvel, S. Mathé, P. Porcu, S. Cosnier, A glucose biofuel cell implanted in rats. *PLOS ONE*, 2010, *5* (5), e10476.
- [29] A. T. Yahiro, S. M. Lee, D. O. Kimble, Bioelectrochemistry: I. Enzyme utilizing bio-fuel cell studies. *Biochim. Biophys. Acta*, 1964, *88*, 375-383.
- [30] N. Mano, F. Mao, A. Heller, Characteristics of a miniature compartment-less glucose-O<sub>2</sub> biofuel cell and its operation in a living plant. *J. Am. Chem. Soc.*, 2003, *125*, 6588-6594.
- [31] F. Shen, D. Pankratov, G. Pankratova, M. D. Toscano, J. Zhang, J. Ulstrup, Q. Chi, L. Gorton, Supercapacitor/biofuel cell hybrid device employing biomolecules for energy conversion and charge storage. *Bioelectrochemistry*, 2019, *128*, 94-99.
- [32] X. Xiao, P. Ó. Conghaile, D. Leech, R. Ludwig, E. Magner, A symmetric supercapacitor/biofuel cell hybrid device based on enzyme-modified nanoporous gold: An autonomous pulse generator. *Biosens. Bioelectron.*, 2017, *90*, 96-102.
- [33] I. Jeerapan, N. Ma, Challenges and opportunities of carbon nanomaterials for biofuel cells and supercapacitors: personalized energy for futuristic self-sustainable devices. *C—J. Carbon Res.*, 2019, *5* (4), 62.
- [34] S. C. Barton, H.-H. Kim, G. Binyamin, Y. Zhang, A. Heller, The “wired” laccase cathode: high current density electroreduction of O<sub>2</sub> to water at +0.7 V (NHE) at pH 5. *J. Am. Chem. Soc.*, 2001, *123*, 5802-5803.
- [35] E. Katz, A. F. Bückmann, I. Willner, Self-powered enzyme-based biosensors. *J. Am. Chem. Soc.*, 2001, *123* (43), 10752-10753.
- [36] N. Mano, F. Mao, A. Heller, A miniature biofuel cell operating in a physiological buffer. *J. Am. Chem. Soc.*, 2002, *124*, 12962-12963.
- [37] S. Shleev, A. El Kasmi, T. Ruzgas, L. Gorton, Direct heterogeneous electron transfer reactions of bilirubin oxidase at a spectrographic graphite electrode. *Electrochem. Commun.*, 2004, *6* (9), 934-939.

- 
- [38] N. Yuhashi, M. Tomiyama, J. Okuda, S. Igarashi, K. Ikebukuro, K. Sode, Development of a novel glucose enzyme fuel cell system employing protein engineered PQQ glucose dehydrogenase. *Biosens. Bioelectron.*, 2005, 20 (10), 2145-50.
- [39] S. Shleev, A. Jarosz-Wilkolazka, A. Khalunina, O. Morozova, A. Yaropolov, T. Ruzgas, L. Gorton, Direct electron transfer reactions of laccases from different origins on carbon electrodes. *Bioelectrochemistry*, 2005, 67 (1), 115-24.
- [40] J. T. Holland, C. Lau, S. Brozik, P. Atanassov, S. Banta, Engineering of glucose oxidase for direct electron transfer via site-specific gold nanoparticle conjugation. *J. Am. Chem. Soc.*, 2011, 133 (48), 19262-5.
- [41] S. Xu, S. D. Minteer, Enzymatic biofuel cell for oxidation of glucose to CO<sub>2</sub>. *ACS Catal.*, 2012, 2 (1), 91-94.
- [42] M. Falk, V. Andoralov, Z. Blum, J. Sotres, D. B. Suyatin, T. Ruzgas, T. Arnebrant, S. Shleev, Biofuel cell as a power source for electronic contact lenses. *Biosens. Bioelectron.*, 2012, 37 (1), 38-45.
- [43] R. D. Milton, F. Giroud, A. E. Thumser, S. D. Minteer, R. C. Slade, Hydrogen peroxide produced by glucose oxidase affects the performance of laccase cathodes in glucose/oxygen fuel cells: FAD-dependent glucose dehydrogenase as a replacement. *Phys. Chem. Chem. Phys.*, 2013, 15 (44), 19371-9.
- [44] W. Jia, G. Valdes-Ramirez, A. J. Bandodkar, J. R. Windmiller, J. Wang, Epidermal biofuel cells: energy harvesting from human perspiration. *Angew. Chem. Int. Ed. Engl.*, 2013, 52 (28), 7233-6.
- [45] C. Agnès, M. Holzinger, A. Le Goff, B. Reuillard, K. Elouarzaki, S. Tingry, S. Cosnier, Supercapacitor/biofuel cell hybrids based on wired enzymes on carbon nanotube matrices: autonomous reloading after high power pulses in neutral buffered glucose solutions. *Energy Environ. Sci.*, 2014, 7 (6), 1884-1888.
- [46] E. González-Arribas, O. Aleksejeva, T. Bobrowski, M. D. Toscano, L. Gorton, W. Schuhmann, S. Shleev, Solar biosupercapacitor. *Electrochem. Commun.*, 2017, 74 (Supplement C), 9-13.
- [47] D. Ratautas, L. Tetianec, L. Marcinkeviciene, R. Meskys, J. Kulys, Bioanode with alcohol dehydrogenase undergoing a direct electron transfer on functionalized gold nanoparticles for an application in biofuel cells for glycerol conversion. *Biosens. Bioelectron.*, 2017, 98, 215-221.
- [48] C. Ji, J. Hou, K. Wang, Y. H. Ng, V. Chen, Single-enzyme biofuel cells. *Angew. Chem. Int. Ed. Engl.*, 2017, 56, 1-7.
- [49] R. Yasujima, K. Yasueda, T. Horiba, S. Komaba, Multi-enzyme immobilized anodes utilizing maltose fuel for biofuel cell applications. *ChemElectroChem*, 2018, 5 (16), 2271-2278.
- [50] A. L. Ghindilis, P. Atanasov, E. Wilkins, Enzyme-catalyzed direct electron transfer: Fundamentals and analytical applications. *Electroanalysis*, 1997, 9 (9), 661-674.
- [51] A. Chaubey, B. D. Malhotra, Review: Mediated biosensors. *Biosens. Bioelectron.*, 2002, 17, 441-456.
- [52] J. C. Harper, R. Polsky, D. R. Wheeler, S. M. Brozik, Maleimide-activated aryl diazonium salts for electrode surface functionalization with biological and redox-active molecules. *Langmuir*, 2008, 24, 2206-2211.
- [53] A. K. Sarma, P. Vatsyayan, P. Goswami, S. D. Minteer, Recent advances in material science for developing enzyme electrodes. *Biosens. Bioelectron.*, 2009, 24 (8), 2313-22.
- [54] P. A. Jenkins, S. Boland, P. Kavanagh, D. Leech, Evaluation of performance and stability of biocatalytic redox films constructed with different copper oxygenases and osmium-based redox polymers. *Bioelectrochemistry*, 2009, 76 (1-2), 162-8.
- [55] A. S. N. Murthy, J. Sharma, Electrocatalytic oxidation of ascorbic acid using benzoquinone as a mediator. *Electroanalysis*, 1997, 9 (9), 726-729.

- 
- [56] S. A. Wring, J. P. Hart, Chemically modified, carbon-based electrodes and their application as electrochemical sensors for the analysis of biologically important compounds. A review. *Analyst*, 1992, *117* (8), 1215-1229.
- [57] R. Bourbonnais, D. Leech, M. G. Paice, Electrochemical analysis of the interactions of laccase mediators with lignin model compounds. *BBA-Gen. Subjects*, 1998, *1379* (3), 381-390.
- [58] L. Gorton, A. Torstensson, H. Jaegfeldt, G. Johansson, Electrocatalytic oxidation of reduced nicotinamide coenzymes by graphite electrodes modified with an adsorbed phenoxazinium salt, meldola blue. *J. Electroanal. Chem. Interfacial Electrochem.*, 1984, *161* (1), 103-120.
- [59] K. V. Nguyen, Y. Holade, S. D. Minteer, DNA redox hydrogels: Improving mediated enzymatic bioelectrocatalysis. *ACS Catal.*, 2016, *6* (4), 2603-2607.
- [60] M. T. Meredith, D.-Y. Kao, D. Hickey, D. W. Schmidtke, D. T. Glatzhofer, High current density ferrocene-modified linear poly(ethylenimine) bioanodes and their use in biofuel cells. *J. Electrochem. Soc.*, 2011, *158* (2), B166-B174.
- [61] R. D. Milton, D. P. Hickey, S. Abdellaoui, K. Lim, F. Wu, B. Tan, S. D. Minteer, Rational design of quinones for high power density biofuel cells. *Chem. Sci.*, 2015, *6* (8), 4867-4875.
- [62] S. A. Merchant, M. T. Meredith, T. O. Tran, D. B. Brunski, M. B. Johnson, D. T. Glatzhofer, D. W. Schmidtke, Effect of mediator spacing on electrochemical and enzymatic response of ferrocene redox polymers. *J. Phys. Chem. C*, 2010, *114* (26), 11627-11634.
- [63] S. Xu, S. D. Minteer, Pyrroloquinoline quinone-dependent enzymatic bioanode: incorporation of the substituted polyaniline conducting polymer as a mediator. *ACS Catal.*, 2014, *4* (7), 2241-2248.
- [64] M. J. Cooney, V. Svoboda, C. Lau, G. Martin, S. D. Minteer, Enzyme catalysed biofuel cells. *Energy Environ. Sci.*, 2008, *1* (3), 320.
- [65] M. Rasmussen, S. Abdellaoui, S. D. Minteer, Enzymatic biofuel cells: 30 years of critical advancements. *Biosens. Bioelectron.*, 2016, *76*, 91-102.
- [66] E. E. Ferapontova, T. Ruzgas, L. Gorton, Direct electron transfer of heme- and molybdopterin cofactor-containing chicken liver sulfite oxidase on alkanethiol-modified gold electrodes. *Anal. Chem.*, 2003, *75* (18), 4841-4850.
- [67] S. Abdellaoui, R. D. Milton, T. Quah, S. D. Minteer, NAD-dependent dehydrogenase bioelectrocatalysis: the ability of a naphthoquinone redox polymer to regenerate NAD. *Chem. Commun.*, 2016, *52* (6), 1147-50.
- [68] V. Coman, C. Vaz-Dominguez, R. Ludwig, W. Harreither, D. Haltrich, A. L. De Lacey, T. Ruzgas, L. Gorton, S. Shleev, A membrane-, mediator-, cofactor-less glucose/oxygen biofuel cell. *Phys. Chem. Chem. Phys.*, 2008, *10* (40), 6093-6.
- [69] I. W. Schubart, G. Göbel, F. Lisdat, A pyrroloquinolinequinone-dependent glucose dehydrogenase (PQQ-GDH)-electrode with direct electron transfer based on polyaniline modified carbon nanotubes for biofuel cell application. *Electrochim. Acta*, 2012, *82*, 224-232.
- [70] P. N. Bartlett, F. A. Al-Lolage, There is no evidence to support literature claims of direct electron transfer (DET) for native glucose oxidase (GOx) at carbon nanotubes or graphene. *J. Electroanal. Chem.*, 2018, *819*, 26-37.
- [71] D. Ivnitski, P. Atanassov, C. Apblett, Direct bioelectrocatalysis of PQQ-dependent glucose dehydrogenase. *Electroanalysis*, 2007, *19* (15), 1562-1568.
- [72] N. Lalaoui, N. Means, C. Walgama, A. Le Goff, M. Holzinger, S. Krishnan, S. Cosnier, Enzymatic versus electrocatalytic oxidation of NADH at carbon-nanotube electrodes modified with glucose dehydrogenases: application in a bucky-paper-based glucose enzymatic fuel cell. *ChemElectroChem*, 2016, *3* (12), 2058-2062.
- [73] P. K. Addo, R. L. Arechederra, S. D. Minteer, Towards a rechargeable alcohol biobattery. *J. Power Sources*, 2011, *196* (7), 3448-3451.
- [74] S. Aquino Neto, D. P. Hickey, R. D. Milton, A. R. De Andrade, S. D. Minteer, High current density PQQ-dependent alcohol and aldehyde dehydrogenase bioanodes. *Biosens.*

- 
- Bioelectron.*, 2015, 72, 247-54.
- [75] E. Simon, C. M. Halliwell, C. S. Toh, A. E. G. Cass, P. N. Bartlett, Immobilisation of enzymes on poly(aniline)-poly(anion) composite films. Preparation of bioanodes for biofuel cell applications. *Bioelectrochemistry*, 2002, 55, 13-15.
- [76] Y. Handa, K. Yamagiwa, Y. Ikeda, Y. Yanagisawa, S. Watanabe, N. Yabuuchi, S. Komaba, Fabrication of carbon-felt-based multi-enzyme immobilized anodes to oxidize sucrose for biofuel cells. *Chemphyschem*, 2014, 15 (10), 2145-51.
- [77] D. P. Hickey, M. S. McCamant, F. Giroud, M. S. Sigman, S. D. Minteer, Hybrid enzymatic and organic electrocatalytic cascade for the complete oxidation of glycerol. *J. Am. Chem. Soc.*, 2014, 136 (45), 15917-20.
- [78] M. S. Thorum, C. A. Anderson, J. J. Hatch, A. S. Campbell, N. M. Marshall, S. C. Zimmerman, Y. Lu, A. A. Gewirth, Direct, electrocatalytic oxygen reduction by laccase on anthracene-2-methanethiol-modified gold. *J. Phys. Chem. Lett.*, 2010, 1 (15), 2251-2254.
- [79] E. I. Solomon, R. Sarangi, J. S. Woertink, A. J. Augustine, J. Yoon, S. Ghosh, O<sub>2</sub> and N<sub>2</sub>O activation by Bi-, Tri-, and tetranuclear Cu clusters in biology. *Accounts Chem. Res.*, 2007, 40 (7), 581-591.
- [80] A. S. Campbell, Y. J. Jeong, S. M. Geier, R. R. Koepsel, A. J. Russell, M. F. Islam, Membrane/mediator-free rechargeable enzymatic biofuel cell utilizing graphene/single-wall carbon nanotube cogel electrodes. *ACS Appl. Mater. Inter.*, 2015, 7 (7), 4056-4065.
- [81] M. J. Moehlenbrock, S. D. Minteer, Introduction to the field of enzyme immobilization and stabilization. *Methods Mol. Biol.*, 2017, 1504, 1-7.
- [82] U. Hanefeld, L. Gardossi, E. Magner, Understanding enzyme immobilisation. *Chem. Soc. Rev.*, 2009, 38 (2), 453-468.
- [83] C. Mateo, J. M. Palomo, G. Fernandez-Lorente, J. M. Guisan, R. Fernandez-Lafuente, Improvement of enzyme activity, stability and selectivity via immobilization techniques. *Enzyme Microb. Tech.*, 2007, 40 (6), 1451-1463.
- [84] R. S. Freire, N. Durán, L. T. Kubota, Effects of fungal laccase immobilization procedures for the development of a biosensor for phenol compounds. *Talanta*, 2001, 54 (4), 681-686.
- [85] A. Basso, P. Braiuca, S. Cantone, C. Ebert, P. Linda, P. Spizzo, P. Caimi, U. Hanefeld, G. Degrassi, L. Gardossi, In silico analysis of enzyme surface and glycosylation effect as a tool for efficient covalent immobilisation of CalB and PGA on Sepabeads®. *Adv. Synth. Catal.*, 2007, 349 (6), 877-886.
- [86] C. Di Bari, A. Goñi-Urriaga, M. Pita, S. Shleev, M. D. Toscano, R. Sainz, A. L. De Lacey, Fabrication of high surface area graphene electrodes with high performance towards enzymatic oxygen reduction. *Electrochim. Acta*, 2016, 191, 500-509.
- [87] C. Engelbrekt, K. H. Sørensen, J. Zhang, A. C. Welinder, P. S. Jensen, J. Ulstrup, Green synthesis of gold nanoparticles with starch-glucose and application in bioelectrochemistry. *J. Mater. Chem.*, 2009, 19 (42), 7839-7847.
- [88] Y. Wang, Q. Chi, N. S. Hush, J. R. Reimers, J. Zhang, J. Ulstrup, Scanning tunneling microscopic observation of adatom-mediated motifs on gold-thiol self-assembled monolayers at high coverage. *J. Phys. Chem. C*, 2009, 113 (45), 19601-19608.
- [89] F. A. Al-Lolage, P. N. Bartlett, S. Gounel, P. Staigre, N. Mano, Site-directed immobilization of bilirubin oxidase for electrocatalytic oxygen reduction. *ACS Catal.*, 2019, 9 (3), 2068-2078.
- [90] E. J. Wright, M. Sosna, S. Bloodworth, J. D. Kilburn, P. N. Bartlett, Design of maleimide-functionalised electrodes for covalent attachment of proteins through free surface cysteine groups. *Chem-Eur. J.*, 2014, 20 (19), 5550-5554.
- [91] F. A. Al-Lolage, M. Meneghello, S. Ma, R. Ludwig, P. N. Bartlett, A flexible method for the stable, covalent immobilization of enzymes at electrode surfaces. *Chemelectrochem*, 2017, 4 (6), 1528-1534.
- [92] A. Heller, Miniature biofuel cells. *Phys. Chem. Chem. Phys.*, 2004, 6 (2), 209-216.

- 
- [93] F. Lopez, T. Siepenkoetter, X. Xiao, E. Magner, W. Schuhmann, U. Salaj-Kosla, Potential pulse-assisted immobilization of *Myrothecium verrucaria* bilirubin oxidase at planar and nanoporous gold electrodes. *J. Electroanal. Chem.*, 2018, 812, 194-198.
- [94] J. Chen, Y. Wang, J. Cao, Y. Liu, Y. Zhou, J. H. Ouyang, D. Jia, Facile co-electrodeposition method for high-performance supercapacitor based on reduced graphene oxide/polypyrrole composite film. *ACS Appl. Mater. Inter.*, 2017, 9 (23), 19831-19842.
- [95] N. P. Godman, J. L. DeLuca, S. R. McCollum, D. W. Schmidtke, D. T. Glatzhofer, Electrochemical characterization of layer-by-layer assembled ferrocene-modified linear poly(ethylenimine)/enzyme bioanodes for glucose sensor and biofuel cell applications. *Langmuir*, 2016, 32 (14), 3541-3551.
- [96] M. Christwardana, Y. Kwon, Effects of multiple polyaniline layers immobilized on carbon nanotube and glutaraldehyde on performance and stability of biofuel cell. *J. Power Sources*, 2015, 299 (Supplement C), 604-610.
- [97] X. Yan, J. Chen, J. Yang, Q. Xue, P. Miele, Fabrication of free-standing, electrochemically active, and biocompatible graphene oxide-polyaniline and graphene-polyaniline hybrid papers. *ACS Appl. Mater. Inter.*, 2010, 2 (9), 2521-2529.
- [98] P. Saengdee, C. Promptmas, T. Zeng, S. Leimkühler, U. Wollenberger, Third-generation sulfite biosensor based on sulfite oxidase immobilized on aminopropyltriethoxysilane modified indium tin oxide. *Electroanalysis*, 2017, 29 (1), 110-115.
- [99] S. Frasca, O. Rojas, J. Salewski, B. Neumann, K. Stiba, I. M. Weidinger, B. Tiersch, S. Leimkühler, J. Koetz, U. Wollenberger, Human sulfite oxidase electrochemistry on gold nanoparticles modified electrode. *Bioelectrochemistry*, 2012, 87 (Supplement C), 33-41.
- [100] A. S. Campbell, H. Murata, S. Carmali, K. Matyjaszewski, M. F. Islam, A. J. Russell, Polymer-based protein engineering grown ferrocene-containing redox polymers improve current generation in an enzymatic biofuel cell. *Biosens. Bioelectron.*, 2016, 86 (Supplement C), 446-453.
- [101] C.-e. Zhao, P. Gai, R. Song, Y. Chen, J. Zhang, J.-J. Zhu, Nanostructured material-based biofuel cells: recent advances and future prospects. *Chem. Soc. Rev.*, 2017, 46 (5), 1545-1564.
- [102] X. Kang, J. Wang, H. Wu, I. A. Aksay, J. Liu, Y. Lin, Glucose oxidase-graphene-chitosan modified electrode for direct electrochemistry and glucose sensing. *Biosens. Bioelectron.*, 2009, 25 (4), 901-5.
- [103] T. L. Klotzbach, M. Watt, Y. Ansari, S. D. Minter, Improving the microenvironment for enzyme immobilization at electrodes by hydrophobically modifying chitosan and Nafion® polymers. *J. Membrane Sci.*, 2008, 311 (1-2), 81-88.
- [104] X. Xiao, P. Si, E. Magner, An overview of dealloyed nanoporous gold in bioelectrochemistry. *Bioelectrochemistry*, 2016, 109, 117-126.
- [105] X.-Y. Yang, G. Tian, N. Jiang, B.-L. Su, Immobilization technology: a sustainable solution for biofuel cell design. *Energy Environ. Sci.*, 2012, 5 (2), 5540-5563.
- [106] S. Park, R. S. Ruoff, Chemical methods for the production of graphenes. *Nat. Nanotech.*, 2009, 4 (4), 217-224.
- [107] Y. Si, E. T. Samulski, Synthesis of water soluble graphene. *Nano Lett.*, 2008, 8 (6), 1679-1682.
- [108] Y. Xu, H. Bai, G. Lu, C. Li, G. Shi, Flexible graphene films via the filtration of water-soluble noncovalent functionalized graphene sheets. *J. Am. Chem. Soc.*, 2008, 130 (18), 5856-5857.
- [109] Y. Hernandez, V. Nicolosi, M. Lotya, F. M. Blighe, Z. Sun, S. De, I. T. McGovern, B. Holland, M. Byrne, Y. K. Gun'Ko, J. J. Boland, P. Niraj, G. Duesberg, S. Krishnamurthy, R. Goodhue, J. Hutchison, V. Scardaci, A. C. Ferrari, J. N. Coleman, High-yield production of graphene by liquid-phase exfoliation of graphite. *Nat. Nanotech.*, 2008, 3 (9), 563-568.
- [110] M. D. Stoller, S. Park, Y. Zhu, J. An, R. S. Ruoff, Graphene-based ultracapacitors. *Nano Lett.*, 2008, 8 (10), 3498-3502.
- [111] L. Xu, N. Wei, Y. Zheng, Z. Fan, H.-Q. Wang, J.-C. Zheng, Graphene-nanotube 3D networks:

- 
- intriguing thermal and mechanical properties. *J. Mater. Chem.*, 2012, 22 (4), 1435-1444.
- [112] Y. Yan, W. Zheng, L. Su, L. Mao, Carbon-nanotube-based glucose/O<sub>2</sub> biofuel cells. *Adv. Mater.*, 2006, 18 (19), 2639-2643.
- [113] A. Korani, A. Salimi, High performance glucose/O<sub>2</sub> compartment-less biofuel cell using DNA/CNTs as platform for immobilizing bilirubin oxidase as novel biocathode and integrated NH<sub>2</sub>-CNTs/dendrimer/glucose dehydrogenase/nile blue as bioanode. *Electrochim. Acta*, 2015, 185 (Supplement C), 90-100.
- [114] A. Zebda, C. Gondran, A. Le Goff, M. Holzinger, P. Cinquin, S. Cosnier, Mediatorless high-power glucose biofuel cells based on compressed carbon nanotube-enzyme electrodes. *Nat. Commun.*, 2011, 2, 370.
- [115] T. Miyake, S. Yoshino, T. Yamada, K. Hata, M. Nishizawa, Self-regulating enzyme-nanotube ensemble films and their application as flexible electrodes for biofuel cells. *J. Am. Chem. Soc.*, 2011, 133 (13), 5129-5134.
- [116] F. Gao, L. Viry, M. Maugey, P. Poulin, N. Mano, Engineering hybrid nanotube wires for high-power biofuel cells. *Nat. Commun.*, 2010, 1, 2.
- [117] Y. Kamitaka, S. Tsujimura, N. Setoyama, T. Kajino, K. Kano, Fructose/dioxygen biofuel cell based on direct electron transfer-type bioelectrocatalysis. *Phys. Chem. Chem. Phys.*, 2007, 9 (15), 1793-1801.
- [118] H.-q. Xia, Y. Hibino, Y. Kitazumi, O. Shirai, K. Kano, Interaction between d-fructose dehydrogenase and methoxy-substituent-functionalized carbon surface to increase productive orientations. *Electrochim. Acta*, 2016, 218, 41-46.
- [119] H.-q. Xia, Y. Kitazumi, O. Shirai, K. Kano, Enhanced direct electron transfer-type bioelectrocatalysis of bilirubin oxidase on negatively charged aromatic compound-modified carbon electrode. *J. Electroanal. Chem.*, 2016, 763, 104-109.
- [120] A. Trifonov, K. Herkendell, R. Tel-Vered, O. Yehezkeli, M. Woerner, I. Willner, Enzyme-capped relay-functionalized mesoporous carbon nanoparticles: effective bioelectrocatalytic matrices for sensing and biofuel cell applications. *ACS Nano*, 2013, 7 (12), 11358-11368.
- [121] M. Zhao, Y. Gao, J. Sun, F. Gao, Mediatorless glucose biosensor and direct electron transfer type glucose/air biofuel cell enabled with carbon nanodots. *Anal. Chem.*, 2015, 87 (5), 2615-2622.
- [122] S. Liu, D. Leech, H. Ju, Application of colloidal gold in protein immobilization, electron transfer, and biosensing. *Anal. Lett.*, 2003, 36 (1), 1-19.
- [123] H. Zhang, L. Zhang, Y. Han, Y. Yu, M. Xu, X. Zhang, L. Huang, S. Dong, RGO/Au NPs/N-doped CNTs supported on nickel foam as an anode for enzymatic biofuel cells. *Biosens. Bioelectron.*, 2017, 97, 34-40.
- [124] S. Aquino Neto, T. S. Almeida, L. M. Palma, S. D. Minteer, A. R. de Andrade, Hybrid nanocatalysts containing enzymes and metallic nanoparticles for ethanol/O<sub>2</sub> biofuel cell. *J. Power Sources*, 2014, 259 (Supplement C), 25-32.
- [125] S. Kumar-Krishnan, A. Hernandez-Rangel, U. Pal, O. Ceballos-Sanchez, F. J. Flores-Ruiz, E. Prokhorov, O. Arias de Fuentes, R. Esparza, M. Meyyappan, Surface functionalized halloysite nanotubes decorated with silver nanoparticles for enzyme immobilization and biosensing. *J. Mater. Chem. B*, 2016, 4 (15), 2553-2560.
- [126] D. Rodríguez-Padrón, A. R. Puente-Santiago, A. Caballero, A. M. Balu, A. A. Romero, R. Luque, Highly efficient direct oxygen electro-reduction by partially unfolded laccases immobilized on waste-derived magnetically separable nanoparticles. *Nanoscale*, 2018, 10 (8), 3961-3968.
- [127] D. Cao, P. He, N. Hu, Electrochemical biosensors utilising electron transfer in heme proteins immobilised on Fe<sub>3</sub>O<sub>4</sub> nanoparticles. *Analyst*, 2003, 128 (10), 1268-1274.
- [128] R. Galindo, A. Dector, L. G. Arriaga, S. Gutiérrez, P. Herrasti, Maghemite as a catalyst for glucose oxidation in a microfluidic fuel cell. *J. Electroanal. Chem.*, 2012, 671, 38-43.
- [129] S. Wang, Y. Tan, D. Zhao, G. Liu, Amperometric tyrosinase biosensor based on Fe<sub>3</sub>O<sub>4</sub>

- 
- nanoparticles–chitosan nanocomposite. *Biosens. Bioelectron.*, 2008, *23* (12), 1781-1787.
- [130] H. Teymourian, A. Salimi, S. Khezrian, Fe<sub>3</sub>O<sub>4</sub> magnetic nanoparticles/reduced graphene oxide nanosheets as a novel electrochemical and bioelectrochemical sensing platform. *Biosens. Bioelectron.*, 2013, *49*, 1-8.
- [131] B. Unnikrishnan, S. Palanisamy, S.-M. Chen, A simple electrochemical approach to fabricate a glucose biosensor based on graphene–glucose oxidase biocomposite. *Biosens. Bioelectron.*, 2013, *39* (1), 70-75.
- [132] A.-J. Shen, D.-L. Li, X.-J. Cai, C.-Y. Dong, H.-Q. Dong, H.-Y. Wen, G.-H. Dai, P.-J. Wang, Y.-Y. Li, Multifunctional nanocomposite based on graphene oxide for in vitro hepatocarcinoma diagnosis and treatment. *J. Biomed. Mater. Res.*, 2012, *100A* (9), 2499-2506.
- [133] A. Karimi, A. Othman, A. Uzunoglu, L. Stanciu, S. Andreescu, Graphene based enzymatic bioelectrodes and biofuel cells. *Nanoscale*, 2015, *7* (16), 6909-6923.
- [134] S. Alwarappan, A. Erdem, C. Liu, C.-Z. Li, Probing the electrochemical properties of graphene nanosheets for biosensing applications. *J. Phys. Chem. C*, 2009, *113* (20), 8853-8857.
- [135] L. Tang, Y. Wang, Y. Li, H. Feng, J. Lu, J. Li, Preparation, structure, and electrochemical properties of reduced graphene sheet films. *Adv. Funct. Mater.*, 2009, *19* (17), 2782-2789.
- [136] J. Jia, D. Kato, R. Kurita, Y. Sato, K. Maruyama, K. Suzuki, S. Hirono, T. Ando, O. Niwa, Structure and electrochemical properties of carbon films prepared by a electron cyclotron resonance sputtering method. *Anal. Chem.*, 2007, *79* (1), 98-105.
- [137] C. Soldano, A. Mahmood, E. Dujardin, Production, properties and potential of graphene. *Carbon*, 2010, *48* (8), 2127-2150.
- [138] Y. J. Yun, J. Ju, J. H. Lee, S.-H. Moon, S.-J. Park, Y. H. Kim, W. G. Hong, D. H. Ha, H. Jang, G. H. Lee, H.-M. Chung, J. Choi, S. W. Nam, S.-H. Lee, Y. Jun, Highly elastic graphene-based electronics toward electronic skin. *Adv. Funct. Mater.*, 2017, *27* (33), 1701513.
- [139] F. Shen, D. Pankratov, A. Halder, X. Xiao, M. D. Toscano, J. Zhang, J. Ulstrup, L. Gorton, Q. Chi, Two-dimensional graphene paper supported flexible enzymatic fuel cells. *Nanoscale Adv.*, 2019, *1* (7), 2562-2570.
- [140] Y. Qian, I. M. Ismail, A. Stein, Ultralight, high-surface-area, multifunctional graphene-based aerogels from self-assembly of graphene oxide and resol. *Carbon*, 2014, *68*, 221-231.
- [141] Z. Xu, Y. Zhang, P. Li, C. Gao, Strong, conductive, lightweight, neat graphene aerogel fibers with aligned pores. *ACS Nano*, 2012, *6* (8), 7103-7113.
- [142] Q. Jiang, Y. Zhao, Effects of activation conditions on BET specific surface area of activated carbon nanotubes. *Micropor. Mesopor. Mat.*, 2004, *76* (1), 215-219.
- [143] R. R. Bacsá, C. Laurent, A. Peigney, W. S. Bacsá, T. Vaugien, A. Rousset, High specific surface area carbon nanotubes from catalytic chemical vapor deposition process. *Chem. Phys. Lett.*, 2000, *323* (5), 566-571.
- [144] Z.-X. Cai, X.-H. Song, Y.-Y. Chen, Y.-R. Wang, X. Chen, 3D nitrogen-doped graphene aerogel: a low-cost, facile prepared direct electrode for H<sub>2</sub>O<sub>2</sub> sensing. *Sensor. Actuat. B-Chem.*, 2016, *222*, 567-573.
- [145] B. Wang, S. Yan, Y. Shi, Direct electrochemical analysis of glucose oxidase on a graphene aerogel/gold nanoparticle hybrid for glucose biosensing. *J. Solid State Electr.*, 2015, *19* (1), 307-314.
- [146] J. Filip, J. Tkac, Is graphene worth using in biofuel cells? *Electrochim. Acta*, 2014, *136*, 340-354.
- [147] A. Ambrosi, C. K. Chua, A. Bonanni, M. Pumera, Electrochemistry of graphene and related materials. *Chem. Rev.*, 2014, *114* (14), 7150-7188.
- [148] M. Yi, Z. Shen, A review on mechanical exfoliation for the scalable production of graphene.

- 
- J. Mater. Chem. A*, 2015, 3 (22), 11700-11715.
- [149] W. Yang, G. Chen, Z. Shi, C.-C. Liu, L. Zhang, G. Xie, M. Cheng, D. Wang, R. Yang, D. Shi, K. Watanabe, T. Taniguchi, Y. Yao, Y. Zhang, G. Zhang, Epitaxial growth of single-domain graphene on hexagonal boron nitride. *Nat. Mater.*, 2013, 12, 792.
- [150] M. Losurdo, M. M. Giangregorio, P. Capezzuto, G. Bruno, Graphene CVD growth on copper and nickel: role of hydrogen in kinetics and structure. *Phys. Chem. Chem. Phys.*, 2011, 13 (46), 20836-20843.
- [151] R. Muñoz, C. Gómez-Aleixandre, Review of CVD synthesis of graphene. *Chem. Vapor Depos.*, 2013, 19 (10-11-12), 297-322.
- [152] A. O. Osikoya, O. Parlak, N. A. Murugan, E. D. Dikio, H. Moloto, L. Uzun, A. P. F. Turner, A. Tiwari, Acetylene-sourced CVD-synthesised catalytically active graphene for electrochemical biosensing. *Biosens. Bioelectron.*, 2017, 89, 496-504.
- [153] Y. H. Kwak, D. S. Choi, Y. N. Kim, H. Kim, D. H. Yoon, S.-S. Ahn, J.-W. Yang, W. S. Yang, S. Seo, Flexible glucose sensor using CVD-grown graphene-based field effect transistor. *Biosens. Bioelectron.*, 2012, 37 (1), 82-87.
- [154] D. B. Shinde, J. Debgupta, A. Kushwaha, M. Aslam, V. K. Pillai, Electrochemical unzipping of multi-walled carbon nanotubes for facile synthesis of high-quality graphene nanoribbons. *J. Am. Chem. Soc.*, 2011, 133 (12), 4168-4171.
- [155] Y. Zhang, M. Chu, L. Yang, Y. Tan, W. Deng, M. Ma, X. Su, Q. Xie, Three-dimensional graphene networks as a new substrate for immobilization of laccase and dopamine and its application in glucose/O<sub>2</sub> biofuel cell. *ACS Appl. Mater. Inter.*, 2014, 6 (15), 12808-12814.
- [156] X. Dong, X. Wang, L. Wang, H. Song, H. Zhang, W. Huang, P. Chen, 3D graphene foam as a monolithic and macroporous carbon electrode for electrochemical sensing. *ACS Appl. Mater. Inter.*, 2012, 4 (6), 3129-3133.
- [157] O. C. Compton, S. T. Nguyen, Graphene oxide, highly reduced graphene oxide, and graphene: versatile building blocks for carbon-Based materials. *Small*, 2010, 6 (6), 711-723.
- [158] M. J. Allen, V. C. Tung, R. B. Kaner, Honeycomb carbon: a review of graphene. *Chem. Rev.*, 2010, 110 (1), 132-145.
- [159] W. Chen, L. Yan, P. R. Bangal, Preparation of graphene by the rapid and mild thermal reduction of graphene oxide induced by microwaves. *Carbon*, 2010, 48 (4), 1146-1152.
- [160] C. K. Chua, M. Pumera, Chemical reduction of graphene oxide: a synthetic chemistry viewpoint. *Chem. Soc. Rev.*, 2014, 43 (1), 291-312.
- [161] Y. Li, K. Sheng, W. Yuan, G. Shi, A high-performance flexible fibre-shaped electrochemical capacitor based on electrochemically reduced graphene oxide. *Chem. Commun.*, 2013, 49 (3), 291-293.
- [162] A. Koushanpour, N. Guz, M. Gamella, E. Katz, Graphene-functionalized 3D-carbon fiber electrodes – preparation and electrochemical characterization. *Electroanalysis*, 2016, 28 (9), 1943-1946.
- [163] X. Wang, J. Wang, H. Cheng, P. Yu, J. Ye, L. Mao, Graphene as a spacer to layer-by-layer assemble electrochemically functionalized nanostructures for molecular bioelectronic devices. *Langmuir*, 2011, 27 (17), 11180-11186.
- [164] S. Wei, Y. Hao, Z. Ying, C. Xu, Q. Wei, S. Xue, H.-M. Cheng, W. Ren, L.-P. Ma, Y. Zeng, Transfer-free CVD graphene for highly sensitive glucose sensors. *J. Mater. Sci. Technol.*, 2019,
- [165] M. Zhou, Y. Zhai, S. Dong, Electrochemical sensing and biosensing platform based on chemically reduced graphene oxide. *Anal. Chem.*, 2009, 81 (14), 5603-5613.
- [166] N. Lalaoui, A. Le Goff, M. Holzinger, M. Mermoux, S. Cosnier, Wiring laccase on covalently modified graphene: carbon nanotube assemblies for the direct bio-electrocatalytic reduction of oxygen. *Chem-Eur. J.*, 2015, 21 (8), 3198-3201.
- [167] L. Dai, Graphene: Tunable superdoping. *Nat. Energy*, 2016, 1 (4), 16041.

- 
- [168] K. Gong, F. Du, Z. Xia, M. Durstock, L. Dai, Nitrogen-doped carbon nanotube arrays with high electrocatalytic activity for oxygen reduction. *Science*, 2009, *323* (5915), 760-764.
- [169] L. S. Panchakarla, K. S. Subrahmanyam, S. K. Saha, A. Govindaraj, H. R. Krishnamurthy, U. V. Waghmare, C. N. R. Rao, Synthesis, structure, and properties of boron- and nitrogen-doped graphene. *Adv. Mater.*, 2009, *21* (46), 4726-4730.
- [170] Y. Wang, Y. Shao, D. W. Matson, J. Li, Y. Lin, Nitrogen-doped graphene and its application in electrochemical biosensing. *ACS Nano*, 2010, *4* (4), 1790-1798.
- [171] P. Gai, Y. Ji, Y. Chen, C. Zhu, J. Zhang, J.-J. Zhu, A nitrogen-doped graphene/gold nanoparticle/formate dehydrogenase bioanode for high power output membrane-less formic acid/O<sub>2</sub> biofuel cells. *Analyst*, 2015, *140* (6), 1822-1826.
- [172] A. Ahmadian Yazdi, J. Xu, Nitrogen-doped graphene approach to enhance the performance of a membraneless enzymatic biofuel cell. *Front. Energy*, 2018, *12* (2), 233-238.
- [173] J. Han, L. L. Zhang, S. Lee, J. Oh, K.-S. Lee, J. R. Potts, J. Ji, X. Zhao, R. S. Ruoff, S. Park, Generation of B-doped graphene nanoplatelets using a solution process and their supercapacitor applications. *ACS Nano*, 2013, *7* (1), 19-26.
- [174] S. Gong, Q. Wang, Boron-doped graphene as a promising anode material for potassium-ion batteries with a large capacity, high rate performance, and good cycling stability. *J. Phys. Chem. C*, 2017, *121* (44), 24418-24424.
- [175] C. Zhang, N. Mahmood, H. Yin, F. Liu, Y. Hou, Synthesis of phosphorus-doped graphene and its multifunctional applications for oxygen reduction reaction and lithium ion batteries. *Adv. Mater.*, 2013, *25* (35), 4932-4937.
- [176] T. Van Tam, S. G. Kang, K. F. Babu, E.-S. Oh, S. G. Lee, W. M. Choi, Synthesis of B-doped graphene quantum dots as a metal-free electrocatalyst for the oxygen reduction reaction. *J. Mater. Chem. A*, 2017, *5* (21), 10537-10543.
- [177] M. Li, C. Liu, H. Zhao, H. An, H. Cao, Y. Zhang, Z. Fan, Tuning sulfur doping in graphene for highly sensitive dopamine biosensors. *Carbon*, 2015, *86*, 197-206.
- [178] V. Urbanová, F. Karlický, A. Matěj, F. Šembera, Z. Janoušek, J. A. Perman, V. Ranc, K. Čépe, J. Michl, M. Otyepka, R. Zboril, Fluorinated graphenes as advanced biosensors – effect of fluorine coverage on electron transfer properties and adsorption of biomolecules. *Nanoscale*, 2016, *8* (24), 12134-12142.
- [179] F. Shahzad, S. A. Zaidi, C. M. Koo, Synthesis of multifunctional electrically tunable fluorine-doped reduced graphene oxide at low temperatures. *ACS Appl. Mater. Inter.*, 2017, *9* (28), 24179-24189.
- [180] V. Georgakilas, M. Otyepka, A. B. Bourlinos, V. Chandra, N. Kim, K. C. Kemp, P. Hobza, R. Zboril, K. S. Kim, Functionalization of graphene: covalent and non-covalent approaches, derivatives and applications. *Chem. Rev.*, 2012, *112* (11), 6156-6214.
- [181] A. Sinitskii, A. Dimiev, D. A. Corley, A. A. Fursina, D. V. Kosynkin, J. M. Tour, Kinetics of diazonium functionalization of chemically converted graphene nanoribbons. *ACS Nano*, 2010, *4* (4), 1949-1954.
- [182] S. Niyogi, E. Bekyarova, M. E. Itkis, H. Zhang, K. Shepperd, J. Hicks, M. Sprinkle, C. Berger, C. N. Lau, W. A. deHeer, E. H. Conrad, R. C. Haddon, Spectroscopy of covalently functionalized graphene. *Nano Lett.*, 2010, *10* (10), 4061-4066.
- [183] Z. Xu, S. Wang, Y. Li, M. Wang, P. Shi, X. Huang, Covalent functionalization of graphene oxide with biocompatible poly(ethylene glycol) for delivery of paclitaxel. *ACS Appl. Mater. Inter.*, 2014, *6* (19), 17268-17276.
- [184] C. Shan, H. Yang, D. Han, Q. Zhang, A. Ivaska, L. Niu, Water-soluble graphene covalently functionalized by biocompatible poly-L-lysine. *Langmuir*, 2009, *25* (20), 12030-12033.
- [185] S. Park, D. A. Dikin, S. T. Nguyen, R. S. Ruoff, Graphene oxide sheets chemically cross-linked by polyallylamine. *J. Phys. Chem. C*, 2009, *113* (36), 15801-15804.
- [186] H. J. Salavagione, M. A. Gómez, G. Martínez, Polymeric modification of graphene through esterification of graphite oxide and poly(vinyl alcohol). *Macromolecules*, 2009, *42* (17), 6331-

- [187] S. Korkut, M. S. Kilic, S. Uzuncar, B. Hazer, Novel graphene-modified poly(styrene-b-isoprene-b-styrene) enzymatic fuel cell with operation in plant leaves. *Anal. Lett.*, 2016, 49 (14), 2322-2336.
- [188] N. Kaur, A. Bharti, S. Batra, S. Rana, S. Rana, A. Bhalla, N. Prabhakar, An electrochemical aptasensor based on graphene doped chitosan nanocomposites for determination of Ochratoxin A. *Microchem. J.*, 2019, 144, 102-109.
- [189] E. E. Tkalya, M. Ghislandi, G. de With, C. E. Koning, The use of surfactants for dispersing carbon nanotubes and graphene to make conductive nanocomposites. *Curr. Opin. Colloid In.*, 2012, 17 (4), 225-232.
- [190] Z. Kang, K. Jiao, X. Xu, R. Peng, S. Jiao, Z. Hu, Graphene oxide-supported carbon nanofiber-like network derived from polyaniline: A novel composite for enhanced glucose oxidase bioelectrode performance. *Biosens. Bioelectron.*, 2017, 96, 367-372.
- [191] A. Halder, M. Zhang, Q. Chi, Electroactive and biocompatible functionalization of graphene for the development of biosensing platforms. *Biosens. Bioelectron.*, 2017, 87, 764-771.
- [192] M. Fang, J. Long, W. Zhao, L. Wang, G. Chen, pH-Responsive chitosan-mediated graphene dispersions. *Langmuir*, 2010, 26 (22), 16771-16774.
- [193] D. Wang, Y. Li, P. Hasin, Y. Wu, Preparation, characterization, and electrocatalytic performance of graphene-methylene blue thin films. *Nano. Res.*, 2011, 4 (1), 124-130.
- [194] H. Liu, J. Gao, M. Xue, N. Zhu, M. Zhang, T. Cao, Processing of graphene for electrochemical application: noncovalently functionalize graphene sheets with water-soluble electroactive methylene green. *Langmuir*, 2009, 25 (20), 12006-12010.
- [195] B. Liang, X. Guo, L. Fang, Y. Hu, G. Yang, Q. Zhu, J. Wei, X. Ye, Study of direct electron transfer and enzyme activity of glucose oxidase on graphene surface. *Electrochem. Commun.*, 2015, 50, 1-5.
- [196] G.-X. Wang, Y. Qian, X.-X. Cao, X.-H. Xia, Direct electrochemistry of cytochrome c on a graphene/poly (3,4-ethylenedioxythiophene) nanocomposite modified electrode. *Electrochem. Commun.*, 2012, 20, 1-3.
- [197] Y. Song, C. Chen, C. Wang, Graphene/enzyme-encrusted three-dimensional carbon micropillar arrays for mediatorless micro-biofuel cells. *Nanoscale*, 2015, 7 (16), 7084-7090.
- [198] V. Mani, R. Devasenathipathy, S.-M. Chen, J.-A. Gu, S.-T. Huang, Synthesis and characterization of graphene-cobalt phthalocyanines and graphene-iron phthalocyanine composites and their enzymatic fuel cell application. *Renew. Energ.*, 2015, 74, 867-874.
- [199] Á. Torrinha, M. C. B. S. M. Montenegro, A. N. Araújo, Conjugation of glucose oxidase and bilirubin oxidase bioelectrodes as biofuel cell in a finger-powered microfluidic platform. *Electrochim. Acta*, 2019, 318, 922-930.
- [200] A. Koushanpour, M. Gamella, N. Guz, E. Katz, A biofuel cell based on biocatalytic reactions of glucose on both anode and cathode electrodes. *Electroanalysis*, 2017, 29 (4), 950-954.
- [201] A. Koushanpour, M. Gamella, Z. Guo, E. Honarvarfard, A. Poghossian, M. J. Schöning, K. Alexandrov, E. Katz, Ca<sup>2+</sup>-switchable glucose dehydrogenase associated with electrochemical/electronic interfaces: applications to signal-controlled power production and biomolecular release. *J. Phys. Chem. B*, 2017, 121 (51), 11465-11471.
- [202] A. Koushanpour, N. Guz, M. Gamella, E. Katz, Biofuel cell based on carbon fiber electrodes functionalized with graphene nanosheets. *ECS J. Solid State Sc.*, 2016, 5 (8), M3037-M3040.
- [203] K. Hoshi, K. Muramatsu, H. Sumi, Y. Nishioka, Graphene-coated carbon fiber cloth for flexible electrodes of glucose fuel cells. *Jpn. J. Appl. Phys.*, 2016, 55 (2S), 02BE05.
- [204] N. Maleki, S. Kashanian, M. Nazari, N. Shahabadi, A novel and enhanced membrane-free performance of glucose/O<sub>2</sub> biofuel cell, integrated with biocompatible laccase nanoflower biocathode and glucose dehydrogenase bioanode. *IEEE Sens. J.*, 2019, 1-1.
- [205] Y. Yu, H. Y. Y. Nyein, W. Gao, A. Javey, Flexible electrochemical bioelectronics: the rise of

- 
- in situ bioanalysis. *Adv. Mater.*, 2019, 1902083.
- [206] X. Huang, L. Zhang, Z. Zhang, S. Guo, H. Shang, Y. Li, J. Liu, Wearable biofuel cells based on the classification of enzyme for high power outputs and lifetimes. *Biosens. Bioelectron.*, 2018, 124-125, 40-52.
- [207] X. Peng, T. Hu, T. Bao, L. Zhao, X. Zeng, W. Wen, X. Zhang, S. Wang, A label-free electrochemical biosensor for methyltransferase activity detection and inhibitor screening based on graphene quantum dot and enzyme-catalyzed reaction. *J. Electroanal. Chem.*, 2017, 799, 327-332.
- [208] T. Chen, S. C. Barton, G. Binyamin, Z. Gao, Y. Zhang, H.-H. Kim, A. Heller, A miniature biofuel cell. *J. Am. Chem. Soc.*, 2001, 123 (35), 8630-8631.
- [209] T. Miyake, K. Haneda, N. Nagai, Y. Yatagawa, H. Onami, S. Yoshino, T. Abe, M. Nishizawa, Enzymatic biofuel cells designed for direct power generation from biofluids in living organisms. *Energy Environ. Sci.*, 2011, 4 (12), 5008-5012.
- [210] L. Halamkova, J. Halamek, V. Bocharova, A. Szczupak, L. Alfonta, E. Katz, Implanted biofuel cell operating in a living snail. *J. Am. Chem. Soc.*, 2012, 134 (11), 5040-3.
- [211] N. Mano, A. de Poulpique, O<sub>2</sub> reduction in enzymatic biofuel cells. *Chem. Rev.*, 2017,
- [212] M. Cadet, S. Gounel, C. Stines-Chaumeil, X. Brilland, J. Rouhana, F. Louerat, N. Mano, An enzymatic glucose/O<sub>2</sub> biofuel cell operating in human blood. *Biosens. Bioelectron.*, 2016, 83 (Supplement C), 60-67.
- [213] D. Pankratov, L. Ohlsson, P. Gudmundsson, S. Halak, L. Ljunggren, Z. Blum, S. Shleev, Ex vivo electric power generation in human blood using an enzymatic fuel cell in a vein replica. *RSC Advances*, 2016, 6 (74), 70215-70220.
- [214] G. Göbel, M. L. Beltran, J. Mundhenk, T. Heinlein, J. Schneider, F. Lisdat, Operation of a carbon nanotube-based glucose/oxygen biofuel cell in human body liquids—Performance factors and characteristics. *Electrochim. Acta*, 2016, 218 (Supplement C), 278-284.
- [215] Z. Kang, K. Jiao, J. Cheng, R. Peng, S. Jiao, Z. Hu, A novel three-dimensional carbonized PANI1600@CNTs network for enhanced enzymatic biofuel cell. *Biosens. Bioelectron.*, 2018, 101 (Supplement C), 60-65.
- [216] M. Falk, Z. Blum, S. Shleev, Direct electron transfer based enzymatic fuel cells. *Electrochim. Acta*, 2012, 82, 191-202.
- [217] H. Sakai, T. Nakagawa, Y. Tokita, T. Hatazawa, T. Ikeda, S. Tsujimura, K. Kano, A high-power glucose/oxygen biofuel cell operating under quiescent conditions. *Energy Environ. Sci.*, 2009, 2 (1), 133-138.
- [218] Y. Ogawa, K. Kato, T. Miyake, K. Nagamine, T. Ofuji, S. Yoshino, M. Nishizawa, Organic transdermal iontophoresis patch with built-in biofuel cell. *Adv. Healthc. Mater.*, 2015, 4 (4), 506-510.
- [219] J. Cheng, Y. Han, L. Deng, S. Guo, Carbon nanotube–bilirubin oxidase bioconjugate as a new biofuel cell label for self-powered immunosensor. *Anal. Chem.*, 2014, 86 (23), 11782-11788.
- [220] F. Conzuelo, J. Vivekananthan, S. Pöller, J. M. Pingarrón, W. Schuhmann, Immunologically controlled biofuel cell as a self-powered biosensor for antibiotic residue determination. *ChemElectroChem*, 2014, 1 (11), 1854-1858.
- [221] D. Sokic-Lazic, S. D. Minter, Pyruvate/air enzymatic biofuel cell capable of complete oxidation. *Electrochim. Solid St.*, 2009, 12 (9), F26-F28.
- [222] M. J. Moehlenbrock, T. K. Toby, A. Waheed, S. D. Minter, Metabolon catalyzed pyruvate/air biofuel cell. *J. Am. Chem. Soc.*, 2010, 132, 6288-6289.
- [223] I. Wheeldon, S. D. Minter, S. Banta, S. C. Barton, P. Atanassov, M. Sigman, Substrate channelling as an approach to cascade reactions. *Nat. Chem.*, 2016, 8 (4), 299-309.
- [224] D. Pankratov, Z. Blum, D. B. Suyatin, V. O. Popov, S. Shleev, Self-charging electrochemical bio capacitor. *ChemElectroChem*, 2014, 1 (2), 343-346.

- 
- [225] D. Pankratov, Z. Blum, S. Shleev, Hybrid electric power biodevices. *ChemElectroChem*, 2014, 1 (11), 1798-1807.
- [226] S. Aguayo, L. Bozec, Mechanics of bacterial cells and initial surface colonisation. In *Biophysics of Infection*, Leake, M. C., Ed. Springer International Publishing: Cham, 2016; pp 245-260.
- [227] H. Hölscher, AFM, tapping mode. In *Encyclopedia of Nanotechnology*, Bhushan, B., Ed. Springer Netherlands: Dordrecht, 2012; pp 99-99.
- [228] F.-Y. Zhu, Q.-Q. Wang, X.-S. Zhang, W. Hu, X. Zhao, H.-X. Zhang, 3D nanostructure reconstruction based on the SEM imaging principle, and applications. *Nanotechnology*, 2014, 25 (18), 185705.
- [229] R. A. Young, R. V. Kalin, Scanning electron microscopic techniques for characterization of semiconductor materials. In *Microelectronics Processing: Inorganic Materials Characterization*, American Chemical Society: 1986; Vol. 295, pp 49-74.
- [230] D. F. Swinehart, The Beer-Lambert Law. *J. Chem. Educ.*, 1962, 39 (7), 333.
- [231] R. S. Khandpur, *Handbook of Analytical Instruments, Second Edition*. McGraw-Hill: New York, USA, 2007.
- [232] J. Shang, L. Ma, J. Li, W. Ai, T. Yu, G. G. Gurzadyan, The origin of fluorescence from graphene oxide. *Sci. Rep.*, 2012, 2 (1), 792.
- [233] D. Li, M. B. Müller, S. Gilje, R. B. Kaner, G. G. Wallace, Processable aqueous dispersions of graphene nanosheets. *Nat. Nanotechnol.*, 2008, 3, 101.
- [234] L. H. Yahia, L. K. Mireles, 4 - X-ray photoelectron spectroscopy (XPS) and time-of-flight secondary ion mass spectrometry (ToF SIMS). In *Characterization of Polymeric Biomaterials*, Tanzi, M. C.; Farè, S., Eds. Woodhead Publishing: 2017; pp 83-97.
- [235] T. Schmid, P. Dariz, Raman microspectroscopic imaging of binder remnants in historical mortars reveals processing conditions. *Heritage*, 2019, 2 (2), 1662-1683.
- [236] G. Kothleitner, M. J. Neish, N. R. Lugg, S. D. Findlay, W. Grogger, F. Hofer, L. J. Allen, Quantitative elemental mapping at atomic resolution using X-ray spectroscopy. *Phys. Rev. Lett.*, 2014, 112 (8), 085501.
- [237] D. Pletcher, R. Greff, R. Peat, L. M. Peter, J. Robinson, *Instrumental methods in electrochemistry*. Woodhead Publishing Limited, Cambridge: 2001.
- [238] M. Winter, R. J. Brodd, What are batteries, fuel cells, and supercapacitors? *Chem. Rev.*, 2004, 104 (10), 4245-4270.
- [239] N. Mano, A. de Poulpiquet, O<sub>2</sub> reduction in enzymatic biofuel cells. *Chem. Rev.*, 2018, 118 (5), 2392-2468.
- [240] Gamry Instruments. Basics of electrochemical impedance spectroscopy. <https://www.gamry.com/application-notes/EIS/basics-of-electrochemical-impedance-spectroscopy/> accessed. 2007,
- [241] G. Pankratova, D. Pankratov, K. Hasan, H.-E. Åkerlund, P.-Å. Albertsson, D. Leech, S. Shleev, L. Gorton, Supercapacitive photo-bioanodes and biosolar cells: A novel approach for solar energy harnessing. *Adv. Energy Mater.*, 2017, 7 (12), 1602285.
- [242] D. Pankratov, G. Pankratova, T. P. Dyachkova, P. Falkman, H.-E. Åkerlund, M. D. Toscano, Q. Chi, L. Gorton, Supercapacitive biosolar cell driven by direct electron transfer between photosynthetic membranes and CNT networks with enhanced performance. *ACS Energy Lett.*, 2017, 2 (11), 2635-2639.
- [243] S. M. Mostafavi, 3D graphene biocatalysts for development of enzymatic biofuel cells: a short review. *J. Nanoanalysis*, 2015, 2, 57-62.
- [244] H.-J. Qiu, Y. Guan, P. Luo, Y. Wang, Recent advance in fabricating monolithic 3D porous graphene and their applications in biosensing and biofuel cells. *Biosens. Bioelectron.*, 2017, 89, 85-95.
- [245] I. Mazurenko, A. de Poulpiquet, E. Lojou, Recent developments in high surface area

- 
- bioelectrodes for enzymatic fuel cells. *Curr. Opin. Electrochem.*, 2017, 5 (1), 74-84.
- [246] S. Gan, L. Zhong, T. Wu, D. Han, J. Zhang, J. Ulstrup, Q. Chi, L. Niu, Spontaneous and fast growth of large-area graphene nanofilms facilitated by oil/water interfaces. *Adv. Mater.*, 2012, 24 (29), 3958-3964.
- [247] N. Seselj, C. Engelbrekt, Y. Ding, H. A. Hjuler, J. Ulstrup, J. Zhang, Tailored electron transfer pathways in Au<sub>core</sub>/Pt<sub>shell</sub>-Graphene nanocatalysts for fuel cells. *Adv. Energy Mater.*, 2018, 8 (13), 1702609.
- [248] Y. Zhu, S. Murali, M. D. Stoller, A. Velamakanni, R. D. Piner, R. S. Ruoff, Microwave assisted exfoliation and reduction of graphite oxide for ultracapacitors. *Carbon*, 2010, 48 (7), 2118-2122.
- [249] Y. Hu, W. Chen, T. Lei, B. Zhou, Y. Jiao, Y. Yan, X. Du, J. Huang, C. Wu, X. Wang, Y. Wang, B. Chen, J. Xu, C. Wang, J. Xiong, Carbon quantum dots-modified interfacial interactions and ion conductivity for enhanced high current density performance in lithium-sulfur batteries. *Adv. Energy Mater.*, 2019, 9 (0), 1802955.
- [250] V. Wernert, C. Lebouin, V. Benoit, R. Gadiou, A. de Poulpiquet, E. Lojou, R. Denoyel, Direct electron transfer of bilirubin oxidase at a carbon flow-through electrode. *Electrochim. Acta*, 2018, 283, 88-96.
- [251] E. Frackowiak, F. Béguin, Carbon materials for the electrochemical storage of energy in capacitors. *Carbon*, 2001, 39 (6), 937-950.
- [252] C. A. Temple, T. N. Graf, K. V. Rajagopalan, Optimization of expression of human sulfite oxidase and its molybdenum domain. *Arch. Biochem. Biophys.*, 2000, 383 (2), 281-287.
- [253] R. Hille, The mononuclear molybdenum enzymes. *Chem. Rev.*, 1996, 96 (7), 2757-2816.
- [254] C. Feng, R. V. Kedia, J. T. Hazzard, J. K. Hurley, G. Tollin, J. H. Enemark, Effect of solution viscosity on intramolecular electron transfer in sulfite oxidase. *Biochemistry*, 2002, 41 (18), 5816-5821.
- [255] L. A. Coury, B. N. Oliver, J. O. Egekeze, C. S. Sosnoff, J. C. Brumfield, R. P. Buck, R. W. Murray, Mediated, anaerobic voltammetry of sulfite oxidase. *Anal. Chem.*, 1990, 62 (5), 452-458.
- [256] A. Pacheco, J. T. Hazzard, G. Tollin, J. H. Enemark, The pH dependence of intramolecular electron transfer rates in sulfite oxidase at high and low anion concentrations. *J. Biol. Inorg. Chem.*, 1999, 4 (4), 390-401.
- [257] T. Zeng, S. Leimkühler, U. Wollenberger, V. Fourmond, Transient catalytic voltammetry of sulfite oxidase reveals rate limiting conformational changes. *J. Am. Chem. Soc.*, 2017, 139 (33), 11559-11567.
- [258] C. S. Pundir, R. Rawal, Determination of sulfite with emphasis on biosensing methods: A review. *Anal. Bioanal. Chem.*, 2013, 405 (10), 3049-3062.
- [259] S. J. Elliott, A. E. McElhaney, C. Feng, J. H. Enemark, F. A. Armstrong, A voltammetric study of interdomain electron transfer within sulfite oxidase. *J. Am. Chem. Soc.*, 2002, 124 (39), 11612-11613.
- [260] M. Sezer, R. Spricigo, T. Utesch, D. Millo, S. Leimkühler, M. A. Mroginski, U. Wollenberger, P. Hildebrandt, I. M. Weidinger, Redox properties and catalytic activity of surface-bound human sulfite oxidase studied by a combined surface enhanced resonance Raman spectroscopic and electrochemical approach. *Phys. Chem. Chem. Phys.*, 2010, 12 (28), 7894-7903.
- [261] T. Zeng, S. Leimkühler, J. Koetz, U. Wollenberger, Effective electrochemistry of human sulfite oxidase immobilized on quantum-dots-modified indium tin oxide electrode. *ACS Appl. Mater. Inter.*, 2015, 7 (38), 21487-21494.
- [262] R. Spricigo, R. Dronov, K. V. Rajagopalan, F. Lisdat, S. Leimkühler, F. W. Scheller, U. Wollenberger, Electrocatalytically functional multilayer assembly of sulfite oxidase and cytochrome c. *Soft Matter*, 2008, 4 (5), 972-978.
- [263] M.-H. Wang, B.-W. Ji, X.-W. Gu, H.-C. Tian, X.-Y. Kang, B. Yang, X.-L. Wang, X. Chen, C.-

- 
- Y. Li, J.-Q. Liu, Direct electrodeposition of graphene enhanced conductive polymer on microelectrode for biosensing application. *Biosens. Bioelectron.*, 2018, *99*, 99-107.
- [264] A. Kaplan, Z. Yuan, J. D. Benck, A. Govind Rajan, X. S. Chu, Q. H. Wang, M. S. Strano, Current and future directions in electron transfer chemistry of graphene. *Chem. Soc. Rev.*, 2017, *46* (15), 4530-4571.
- [265] S. Pei, H.-M. Cheng, The reduction of graphene oxide. *Carbon*, 2012, *50* (9), 3210-3228.
- [266] Y. Shao, J. Wang, M. Engelhard, C. Wang, Y. Lin, Facile and controllable electrochemical reduction of graphene oxide and its applications. *J. Mater. Chem.*, 2010, *20* (4), 743-748.
- [267] Z. Li, T. Huang, W. Gao, Z. Xu, D. Chang, C. Zhang, C. Gao, Hydrothermally activated graphene fiber fabrics for textile electrodes of supercapacitors. *ACS Nano*, 2017, *11*, 11056-11065.
- [268] R. Spricigo, S. Leimkühler, L. Gorton, F. W. Scheller, U. Wollenberger, The electrically wired molybdenum domain of human sulfite oxidase is bioelectrocatalytically active. *Eur. J. Inorg. Chem.*, 2015, *2015* (21), 3526-3531.
- [269] R. Spricigo, C. Richter, S. Leimkühler, L. Gorton, F. W. Scheller, U. Wollenberger, Sulfite biosensor based on osmium redox polymer wired sulfite oxidase. *Colloid. Surface. A.*, 2010, *354* (1), 314-319.
- [270] Z. Lu, M. Sun, T. Xu, Y. Li, W. Xu, Z. Chang, Y. Ding, X. Sun, L. Jiang, Superaerophobic electrodes for direct hydrazine fuel cells. *Adv. Mater.*, 2015, *27* (14), 2361-2366.
- [271] C. Zhang, R. Hao, H. Liao, Y. Hou, Synthesis of amino-functionalized graphene as metal-free catalyst and exploration of the roles of various nitrogen states in oxygen reduction reaction. *Nano Energy*, 2013, *2* (1), 88-97.
- [272] W. Huang, H. Sun, H. Shanguan, X. Cao, X. Xiao, F. Shen, K. Mølhav, L. Ci, P. Si, J. Zhang, Three-dimensional iron sulfide-carbon interlocked graphene composites for high-performance sodium-ion storage. *Nanoscale*, 2018, *10* (16), 7851-7859.
- [273] G. K. Ramesha, S. Sampath, Electrochemical reduction of oriented graphene oxide films: an in situ Raman spectroelectrochemical study. *J. Phys. Chem. C*, 2009, *113* (19), 7985-7989.
- [274] M. A. Raj, S. A. John, Fabrication of electrochemically reduced graphene oxide films on glassy carbon electrode by self-assembly method and their electrocatalytic application. *J. Phys. Chem. C*, 2013, *117* (8), 4326-4335.
- [275] Y. Wang, H. Sauriat-Dorizon, H. Korri-Youssoufi, Direct electrochemical DNA biosensor based on reduced graphene oxide and metalloporphyrin nanocomposite. *Sensors Actuat. B-Chem.*, 2017, *251*, 40-48.
- [276] T. Zeng, S. Frasca, J. Rumschöttel, J. Koetz, S. Leimkühler, U. Wollenberger, Role of conductive nanoparticles in the direct unmediated bioelectrocatalysis of immobilized sulfite oxidase. *Electroanalysis*, 2016, *28* (10), 2303-2310.
- [277] C. Mateo, O. Abian, R. Fernandez - Lafuente, J. M. Guisan, Reversible enzyme immobilization via a very strong and nondistorting ionic adsorption on support - polyethylenimine composites. *Biotechnol. Bioeng.*, 2000, *68* (1), 98-105.
- [278] T. Utesch, M. Sezer, I. M. Weidinger, M. A. Mroginski, Adsorption of sulfite oxidase on self-assembled monolayers from molecular dynamics simulations. *Langmuir*, 2012, *28* (13), 5761-5769.
- [279] E. R. Sartori, H. H. Takeda, O. Fatibello-Filho, Glassy carbon electrode modified with functionalized carbon nanotubes within a poly(allylamine hydrochloride) film for the voltammetric determination of sulfite in foods. *Electroanalysis*, 2011, *23* (11), 2526-2533.
- [280] B. Ganai, A. Masood, M. Zargar, M. Syed, Kinetics of sulfite oxidase purified from *Malva sylvestris*. *J. Ind. Pollut. Contr.*, 2006, *22*, 77-82.
- [281] A. J. Gross, X. Chen, F. Giroud, C. Travelet, R. Borsali, S. Cosnier, Redox-active glyconanoparticles as electron shuttles for mediated electron transfer with bilirubin oxidase in solution. *J. Am. Chem. Soc.*, 2017, *139* (45), 16076-16079.

- 
- [282] T. Samejima, C.-S. C. Wu, K. Shiboya, H. Kaji, S. Koikeda, K. Ando, J. T. Yang, Conformation of bilirubin oxidase in native and denatured states. *J. Protein Chem.*, 1994, *13* (3), 307-313.
- [283] I. Mazurenko, K. Monsalve, J. Rouhana, P. Parent, C. Laffon, A. L. Goff, S. Szunerits, R. Boukherroub, M.-T. Giudici-Orticoni, N. Mano, E. Lojou, How the intricate interactions between carbon nanotubes and two bilirubin oxidases control direct and mediated O<sub>2</sub> reduction. *ACS Appl. Mater. Inter.*, 2016, *8* (35), 23074-23085.
- [284] J. A. Cracknell, T. P. McNamara, E. D. Lowe, C. F. Blanford, Bilirubin oxidase from *Myrothecium verrucaria*: X-ray determination of the complete crystal structure and a rational surface modification for enhanced electrocatalytic O<sub>2</sub>reduction. *Dalton Trans.*, 2011, *40* (25), 6668-6675.
- [285] R. J. Lopez, S. Babanova, Y. Ulyanova, S. Singhal, P. Atanassov, Improved interfacial electron transfer in modified bilirubin oxidase biocathodes. *ChemElectroChem*, 2014, *1* (1), 241-248.
- [286] P. Olejnik, B. Palys, A. Kowalczyk, A. M. Nowicka, Orientation of laccase on charged surfaces. mediatorless oxygen reduction on amino- and carboxyl-ended ethylphenyl groups. *J. Phys. Chem. C*, 2012, *116* (49), 25911-25918.
- [287] A. Le Goff, M. Holzinger, S. Cosnier, Recent progress in oxygen-reducing laccase biocathodes for enzymatic biofuel cells. *Cell. Mol. Life Sci.*, 2015, *72* (5), 941-952.
- [288] N. Lalaoui, A. Le Goff, M. Holzinger, S. Cosnier, Fully oriented bilirubin oxidase on porphyrin-functionalized carbon nanotube electrodes for electrocatalytic oxygen reduction. *Chem. Eur. J.*, 2015, *21* (47), 16868-16873.
- [289] G. Zhao, L. Jiang, Y. He, J. Li, H. Dong, X. Wang, W. Hu, Sulfonated graphene for persistent aromatic pollutant management. *Adv. Mater.*, 2011, *23* (34), 3959-3963.
- [290] X. Xiao, E. Magner, A quasi-solid-state and self-powered biosupercapacitor based on flexible nanoporous gold electrodes. *Chem. Commun.*, 2018, *54* (46), 5823-5826.
- [291] E. M. Kober, J. V. Caspar, B. P. Sullivan, T. J. Meyer, Synthetic routes to new polypyridyl complexes of osmium(II). *Inorg. Chem.*, 1988, *27* (25), 4587-4598.
- [292] R. J. Forster, J. G. Vos, Synthesis, characterization, and properties of a series of osmium- and ruthenium-containing metallopolymers. *Macromolecules*, 1990, *23* (20), 4372-4377.
- [293] X. Chen, L. Yin, J. Lv, A. J. Gross, M. Le, N. G. Gutierrez, Y. Li, I. Jeerapan, F. Giroud, A. Berezovska, R. K. O'Reilly, S. Xu, S. Cosnier, J. Wang, Stretchable and flexible buckypaper-based lactate biofuel cell for wearable electronics. *Adv. Funct. Mater.*, 2019, *29* (46), 1905785.
- [294] B. Barbier, J. Pinson, G. Desarmot, M. Sanchez, Electrochemical bonding of amines to carbon fiber surfaces toward improved carbon - epoxy composites. *J. Electrochem. Soc.*, 1990, *137* (6), 1757-1764.
- [295] G. Yang, Y. Shen, M. Wang, H. Chen, B. Liu, S. Dong, Copper hexacyanoferrate multilayer films on glassy carbon electrode modified with 4-aminobenzoic acid in aqueous solution. *Talanta*, 2006, *68* (3), 741-747.
- [296] Jmol: an open-source Java viewer for chemical structures in 3D. <http://www.jmol.org/>.
- [297] C. Gutierrez-Sanchez, A. Ciaccavava, P. Y. Blanchard, K. Monsalve, M. T. Giudici-Orticoni, S. Lecomte, E. Lojou, Efficiency of enzymatic O<sub>2</sub> reduction by *Myrothecium verrucaria* bilirubin oxidase probed by surface plasmon resonance, PMIRRAS, and electrochemistry. *ACS Catal.*, 2016, *6* (8), 5482-5492.
- [298] R. D. Milton, F. Giroud, A. E. Thumser, S. D. Minter, R. C. T. Slade, Bilirubin oxidase bioelectrocatalytic cathodes: the impact of hydrogen peroxide. *Chem. Commun.*, 2014, *50* (1), 94-96.
- [299] C. Léger, A. K. Jones, S. P. J. Albracht, F. A. Armstrong, Effect of a dispersion of interfacial electron transfer rates on steady state catalytic electron transport in [NiFe]-hydrogenase and other enzymes. *J. Phys. Chem. B*, 2002, *106* (50), 13058-13063.

- 
- [300] A. Christenson, S. Shleev, N. Mano, A. Heller, L. Gorton, Redox potentials of the blue copper sites of bilirubin oxidases. *BBA-Bioenergetics*, 2006, *1757* (12), 1634-1641.
- [301] C. C. Moser, J. M. Keske, K. Warncke, R. S. Farid, P. L. Dutton, Nature of biological electron transfer. *Nature*, 1992, *355* (6363), 796-802.
- [302] C. F. Blanford, C. E. Foster, R. S. Heath, F. A. Armstrong, Efficient electrocatalytic oxygen reduction by the 'blue' copper oxidase, laccase, directly attached to chemically modified carbons. *Faraday Discussions*, 2009, *140* (0), 319-335.
- [303] N. Lalaoui, R. David, H. Jamet, M. Holzinger, A. Le Goff, S. Cosnier, Hosting adamantane in the substrate pocket of laccase: Direct bioelectrocatalytic reduction of O<sub>2</sub> on functionalized carbon nanotubes. *ACS Catal.*, 2016, *6* (7), 4259-4264.
- [304] C. Gutiérrez-Sánchez, M. Pita, M. D. Toscano, A. L. De Lacey, Bilirubin oxidase-based nanobiocathode working in serum-mimic buffer for implantable biofuel cell. *Electroanalysis*, 2013, *25* (6), 1359-1362.
- [305] K. So, S. Kawai, Y. Hamano, Y. Kitazumi, O. Shirai, M. Hibi, J. Ogawa, K. Kano, Improvement of a direct electron transfer-type fructose/dioxygen biofuel cell with a substrate-modified biocathode. *Phys. Chem. Chem. Phys.*, 2014, *16* (10), 4823-4829.
- [306] T. Siepenkoetter, U. Salaj-Kosla, X. Xiao, P. Ó. Conghaile, M. Pita, R. Ludwig, E. Magner, Immobilization of redox enzymes on nanoporous gold electrodes: Applications in biofuel cells. *ChemPlusChem*, 2017, *82* (4), 553-560.
- [307] G. Göbel, F. Lisdat, Organic interlayers for oxygen reducing electrodes based on bilirubin oxidase and MWCNT modified gold. *Electrochem. Commun.*, 2008, *10* (11), 1691-1694.
- [308] T. Itoh, Y. Shibuya, A. Yamaguchi, Y. Hoshikawa, O. Tanaike, T. Tsunoda, T.-a. Hanaoka, S. Hamakawa, F. Mizukami, A. Hayashi, T. Kyotani, G. D. Stucky, High-performance bioelectrocatalysts created by immobilization of an enzyme into carbon-coated composite membranes with nano-tailored structures. *J. Mater. Chem. A*, 2017, *5* (38), 20244-20251.
- [309] T. X. H. Le, V. Flaud, M. Bechelany, M. Cretin, S. Tingry, Optimal direct electron transfer between MWCNTs@COOH/BOD/chitosan layer and porous carbon felt for dioxygen reduction. *Electrochim. Acta*, 2017, *230*, 373-381.
- [310] T. X. H. Le, M. Bechelany, A. B. Engel, M. Cretin, S. Tingry, Gold particles growth on carbon felt for efficient micropower generation in a hybrid biofuel cell. *Electrochim. Acta*, 2016, *219*, 121-129.
- [311] Y. M. Parunova, S. O. Bushnev, E. Gonzalez-Arribas, P. Falkman, A. V. Lipkin, V. O. Popov, S. V. Shleev, D. V. Pankratov, Potentially implantable biocathode with the function of charge accumulation based on nanocomposite of polyaniline/carbon nanotubes. *Russian J. Electrochem.*, 2016, *52* (12), 1166-1171.
- [312] C. Walgama, A. Pathiranaage, M. Akinwale, R. Montealegre, J. Niroula, E. Echeverria, D. N. McIlroy, T. A. Harriman, D. A. Lucca, S. Krishnan, Buckypaper-bilirubin oxidase biointerface for electrocatalytic applications: Buckypaper thickness. *ACS Appl. Bio. Mater.*, 2019, *2* (5), 2229-2236.
- [313] K. So, K. Sakai, K. Kano, Gas diffusion bioelectrodes. *Curr. Opin. Electrochem.*, 2017, *5* (1), 173-182.
- [314] S. R. Higgins, C. Lau, P. Atanassov, S. D. Minteer, M. J. Cooney, Hybrid biofuel cell: Microbial fuel cell with an enzymatic air-breathing cathode. *ACS Catal.*, 2011, *1* (9), 994-997.
- [315] H.-q. Xia, K. So, Y. Kitazumi, O. Shirai, K. Nishikawa, Y. Higuchi, K. Kano, Dual gas-diffusion membrane- and mediatorless dihydrogen/air-breathing biofuel cell operating at room temperature. *J. Power Sources*, 2016, *335*, 105-112.



---

# Appendix

Contributions made during the Ph.D. project are included.

## International Journals:

J. Tang, R. M. L. Werchmeister, L. Preda, W. Huang, Z. Zheng, S. Leimkühler, U. Wollenberger, X. Xiao, C. Engelbrekt, J. Ulstrup, J. Zhang, Three-dimensional sulfite oxidase bioanodes based on graphene functionalized carbon paper for sulfite/O<sub>2</sub> biofuel cells, *ACS Catal.*, **2019**, *9* (7), 6543-6554.

R. M. L. Werchmeister, J. Tang, X. Xiao, U. Wollenberger, H. A. Hjuler, J. Ulstrup, J. Zhang, Three-dimensional bioelectrodes utilizing graphene based bioink, *J. Electrochem. Soc.*, **2019**, *166* (16), G170-G177.

J. Tang, X. Yan, C. Engelbrekt, J. Ulstrup, E. Magner, X. Xiao, J. Zhang, Development of graphene-based enzymatic biofuel cells: A minireview, submitted to *Bioelectrochemistry* (January **2020**).

J. Tang, X. Yan, W. Huang, C. Engelbrekt, J. Ulstrup, X. Xiao and J. Zhang, Direct electron transfer of orientated bilirubin oxidase on three-dimensional carbon paper with reduced graphene aggregation (in preparation).

## Oral presentations at national and international conferences

J. Tang, R. M. L. Werchmeister, L. Preda, W. Huang, Z. Zheng, S. Leimkühler, U. Wollenberger, X. Xiao, J. Ulstrup, J. Zhang, Graphene-sulfite oxidase bioanodes for enzymatic biofuel cells, XXV International Symposium on Bioelectrochemistry and Bioenergetics, May **2019**, Limerick, Ireland.

## Poster presentations at national and international conferences:

J. Tang, R. M. L. Werchmeister, C. Engelbrekt, J. Zhang, Graphene-glucose oxidase bioanodes for enzymatic biofuel cells, *Sustain Conference*, December **2017**, Kgs. Lyngby, Demark.

J. Tang, R. M. L. Werchmeister, L. Preda, W. Huang, Z. Zheng, S. Leimkühler, U. Wollenberger, X. Xiao, J. Zhang, Graphene-sulfite oxidase bioanodes for enzymatic biofuel cells, *Sustain Conference*, November **2018**, Kgs. Lyngby, Demark.

---

J. Tang; R. M. L. Werchmeister, U. Wollenberger, C. Engelbrekt, J. Zhang, Graphene-sulfite oxidase bioanodes for enzymatic biofuel cells, *The Danish Chemical Society Annual Meeting*, June **2019**, Copenhagen, Demark.

**Attended workshops or seminars:**

*PhD Workshop on Bioanalysis*, workshop, November **2017**, Potsdam, Germany.